

# ANALYSIS OF THE GEOMAGNETIC FIELD IN ANTARCTICA FROM NEAR-SURFACE AND SATELLITE DATA

Thesis by  
Luis R. Gaya-Piqué

\* \* \* \* \*

Observatori de l'Ebre  
Universitat Ramon Llull  
2004

## Acknowledgements

Foremost I would like to record my thanks to Dr. Joan Miquel Torta Margalef at Observatori de l'Ebre (OE, Spain) and to Dr. Angelo De Santis at Istituto Nazionale di Geofisica e Vulcanologia (INGV, Italy). Some years ago they had the original idea of doing this study, and I am sincerely proud that they placed their trust in me to develop the work. The experience they have on geomagnetism in general, on spherical cap harmonic analysis in particular, and their continuous encouragement and follow-up, led to this complete thesis.

I would specially like to thank all people who provided the data used to develop this work. First of all, I would like to thank all the people who spent several months of their lives in Antarctica doing the magnetic measurements with which the observatory annual means were obtained. These data were downloaded from the World Data Centers for Geomagnetism in Edinburgh (<http://www.geomag.bgs.ac.uk>) and Copenhagen (<http://web.dmi.dk/projects/wdcc1>). Other ground data (observatory monthly and minute means, etc.) were obtained from the Institut de Physique du Globe de Paris (IPGP; <http://www.ipgp.jussieu.fr>), and from the Space Physics Interactive Data Resource server of the National Oceanic and Atmospheric Administration (NOAA; <http://spidr.ngdc.noaa.gov>).

I would like to express my gratitude to Dr. Giovanni Romeo at INGV for supplying the magnetic data from Boomerang experiment; to Dr. Nils Olsen at the Danish Space Research Institute (DSRI), Copenhagen, for providing and making a first selection of the POGO, Ørsted, and Champ satellites data; I would like to thank also Dr. Olsen for his help and friendship during the five weeks spent in Copenhagen in 2002; to Dr. Mioara Mandea at Institut de Physique du Globe de Paris for her constructive comments and suggestions that helped to improve this thesis; to Dr. Michael Purucker at the Geodynamics Branch of the Goddard Space Flight Center (GSFC) for providing Magsat satellite data and for helpful discussions; to Dr. Erwan Thébaud at Ecole et Observatoire des Sciences de la Terre (EOST), Strasbourg, for his help and assistance in the computation of the Legendre functions; to Dr. Roberta Tozzi at INGV for the autoregressive calculus of Mirny observatory annual means; to José Germán Solé at OE for the Ebre observatory sunspot numbers; to Dr. Alfons Eckstaller at Alfred Wegener Institut, Bremerhaven, for the Georg von Neumayer observatory monthly means; to Dr. Alexander Golynsky at VNIIOkeangeologia, St. Petersburg, for the Riiser-Larsen Sea magnetic marine data; to Marta Ghidella at Instituto Antártico Argentino, Buenos Aires, for the Antarctic Peninsula – Weddell Sea aeromagnetic data; and to Dr. Dhananjay Ravat at Southern Illinois University for providing

the software for the equivalent source inversion and for his help in the processing of the marine and aeromagnetic data. Similar thanks are also due to Dr. Gerry V. Haines (first at the Geological Survey of Canada, presently retired) for facilitating the original software to develop the spherical cap harmonic analysis, and to Dr. Terence J. Sabaka at GSFC for the Comprehensive Model CM3 code. Some of the figures and maps in this work were produced employing the Generic Mapping Tools free-distribution package developed by Paul Wessel at Hawaii University and Walter H.F. Smith at NOAA. I express my heartfelt gratitude towards Dr. James B. Arokiasamy at INGV, who read the manuscript and improved the way in which it was written.

We are grateful for the support of the Ørsted Science Data Centre at the Danish Meteorological Institute, and the Champ Information System and Data Center at the GeoForschungsZentrum, Potsdam. The Ørsted Project is funded by the Danish Ministry of Transport, Ministry of Research and Information Technology, and Ministry of Trade and Industry. Additional support was provided by NASA, ESA, CNES, and DARA. The Champ satellite project is supported by grants from the German Space Agency (DLR) under contract FKZ 50 EP 9587. Both Ørsted and Champ International Science Teams were joined through two different projects.

Some periods of this research were supported by projects, grants and contracts from the Observatori de l'Ebre, the Spanish *Programa Nacional de Recursos Naturales – Investigación en la Antártida*, the INGV (through the Italian *Programma Nazionale di Ricerche in Antartide*), and by the INTAS program.

Finally, I would like to express my gratitude to Dr. Luis Felipe Alberca at OE, who gave me the opportunity to begin my career as a scientist at Ebre observatory that far-off summer in 1996.

My sincere thanks are also due in no small measure to all people who gave me their love and friendship during all this time, those who showed me that home is the place where you have a friend.

*To my parents, my brother, and my fiancée.*

## Contents

Contents	3
I. Introduction	5
I.1. The Magnetic Field at the Earth's surface	5
I.2. The main field and its secular variation	8
Expression of the field in terms of spherical harmonics	8
Properties of the Associated Legendre Functions and Spherical Harmonics	13
I.3. The crustal field	15
I.4. The necessity of a reference field for Antarctica	16
II. Harmonic Analysis on a Spherical Cap	23
II.1. Introduction	23
II.2. Applications of SCHA	28
Main and anomaly field models	28
Secular variation models	31
Main field and secular variation models	32
External field models and other studies	33
Theoretical works	36
II.3. Limitations of SCHA	38
II.4. Calculus of the associated Legendre functions	41
III. Data Description and Selection	48
III.1. Introduction	48
III.2. Observatory data	48
Introduction	48
Geomagnetic Observatories South of 60°	49
III.3. Stratospheric balloon data	59
Introduction	59
Boomerang experiment	61
III.4. Satellite data	68
Introduction	68
Satellite missions	71
Criteria for the selection of satellite data	72
Satellite Data used	76
IV. The Antarctic Reference Model	85



IV.1. Data weighting	85
IV.2. Model parameterisation	86
IV.3. Results	91
Fit to observatory data	93
Fit to satellite data	97
Secular variation of the model	105
V. Applications of the Antarctic Reference Model	117
V.1. Online computation of the Antarctic Reference Model	117
V.2. Magnetic maps	117
V.3. Location of the magnetic pole	130
V.4. Study of magnetic jerks	132
V.5. Application to magnetic surveys	133
Marine surveys from the Riiser-Larsen Sea and the Cooperation Sea	135
Aeromagnetic surveys over the Antarctic Peninsula and Weddell Sea areas	140
VI. Conclusions	146
VII. References	150
Analytical index	161

## I. Introduction

### I.1. *The Magnetic Field at the Earth's surface*

The magnetic field is an intrinsic property of our planet. The existence of a planetary magnetic field seems to be the rule and not the exception in our Solar System: among those planets in our neighbourhood, only Venus lacks any magnetism, whereas the others have, or have had (as in the case of our Moon) dynamo fields in the past [Stevenson, 1983].

The sources of the magnetic field recorded at the Earth's surface (or geomagnetic field) are located both inside and outside our planet. When the geomagnetic field is measured at or near the surface of the Earth, a superposition of contributions from several origins is obtained: internal fields produced in the outer core of the Earth (known as main field) or by magnetisation of the rocks located at the crust (known as crustal field); external fields due to currents flowing in the magnetosphere (the enveloping region of the Earth where the magnetic field exclude the solar wind) and ionosphere (the layer of the upper atmosphere that is partially ionised by radiation and energetic particles from space); and other internal fields induced by the effect of the changing external currents on the Earth's interior.

The main field of the Earth is produced by electric currents inside the outer core, which is located between 2,900 km and 5,100 km deep and mainly composed of iron. Figure I.1 shows a schematic view of the Earth's interior. The knowledge of this main field is incomplete because of the large attenuation due to the distance (the field decreases mostly as  $r^{-3}$ ) and to the presence of the terrestrial mantle, which has a small but non-zero conductivity. It is because of this small conductivity, slow convection movements, and still high temperatures (higher than the Curie point, the temperature at which an element loses its magnetic properties) that there is no any magnetic field generated in the mantle, with probable exception of the upper layers (the upper mantle, cooler than the deep mantle, forms together with the overlying crust the layer called lithosphere). The Earth's crust is more accessible than the core or the mantle, and parameters like temperature, pressure, composition are better known for this layer. The study of the crust allows the distinction between zones or rocks with remanent magnetisation (when a magnetic field exists even without an ambient field) from those with induced magnetisation (the only field is that induced by the presence of an external field).

The sources for the external fields can be found in the magnetosphere and the ionosphere. The interaction of the solar wind (the plasma that expands from the solar atmosphere) with the

geomagnetic field leads to a compression of the field lines near the Earth, creating the magnetosphere (figure I.2). The solar wind flows around the Earth, dragging the field with it and forming the magnetotail. The magnetosheath is the region that separates the front shock from the boundary of the magnetosphere (called magnetopause), whereas the neutral sheet is a region where the field is very weak because field lines of opposite senses cancel along the middle of the magnetotail. The solar wind particles can penetrate into the ionosphere through the polar cusps, the region where the solar wind folds down the magnetospheric field, separating the lines of force that belong to the magnetotail or to the front side of the Earth. The plasma inside the magnetosphere causes the appearance of the Van Allen belts, ring currents along close field lines associated with movements of ionised gas of different sign. The temporal changes in these currents are the main source of the magnetic storms.

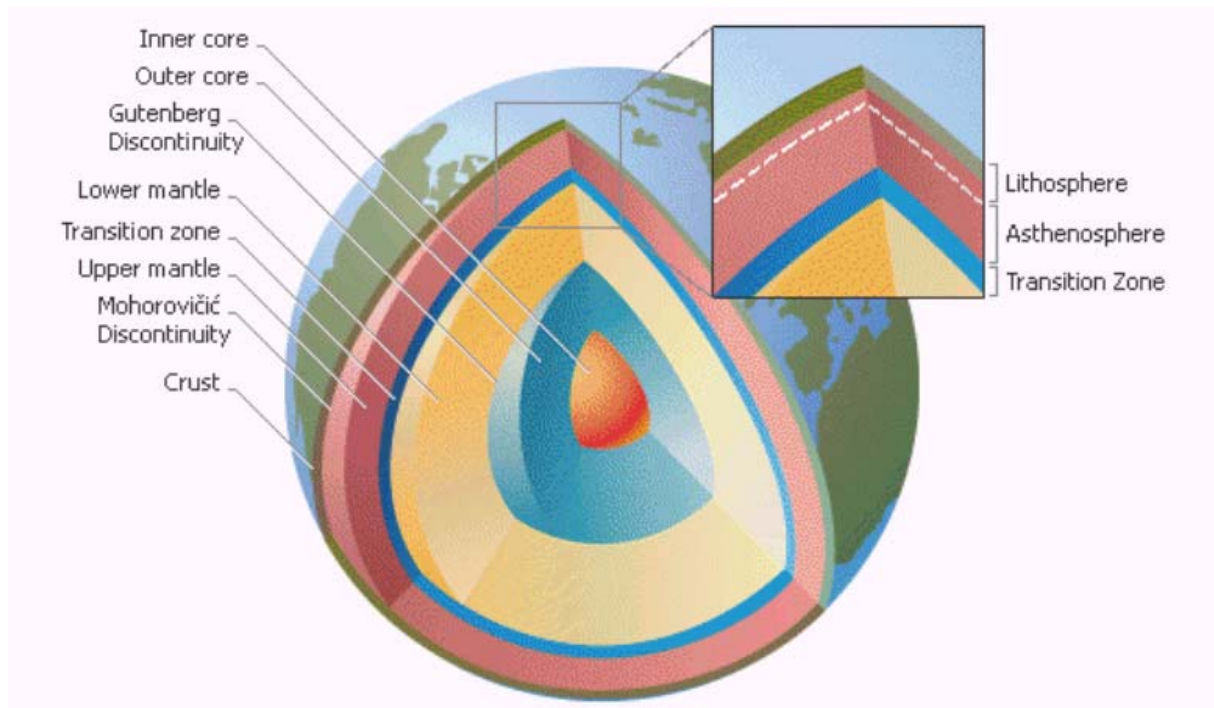


**Figure I.1.** Schematic representation of the Earth's interior showing the names of the most important layers and discontinuities found.

The electric currents present in the ionosphere are due to thermal effects, and also due to tidal forces from the Moon and the Sun. The solar particles able to penetrate inside the magnetosphere can also interact with the atmospheric plasma, so it is sometimes difficult to find the correct source for a measured event. Ionospheric currents are stronger during the daytime and in the summer hemisphere, due to the solar radiation, resulting in an increase of the conductivity in the

commonly known as ionospheric E layer [e.g. Campbell, 1997]. Thermal winds cause global scale currents, with a vortex for each hemisphere. For periods of low external (solar) magnetic activity, it creates the solar quiet-day variations in the magnetic field (Sq). The enhancement of this variation in a narrow band along the magnetic equator (due to a greater conductivity) is called the equatorial electrojet. The so-called coupling currents connect the Sq current systems of both hemispheres, when the electric potential in both hemispheres is unbalanced, i.e. specially during the solstices. Another important current system is the auroral electrojet, a flow of charged particles that moves from dawn to dusk in the high latitude upper ionosphere. At these high latitudes, ionosphere and magnetosphere are connected by currents that are trapped by the magnetic field lines and aligned to them. A representation of the main current systems in the ionosphere is shown in figure I.3.

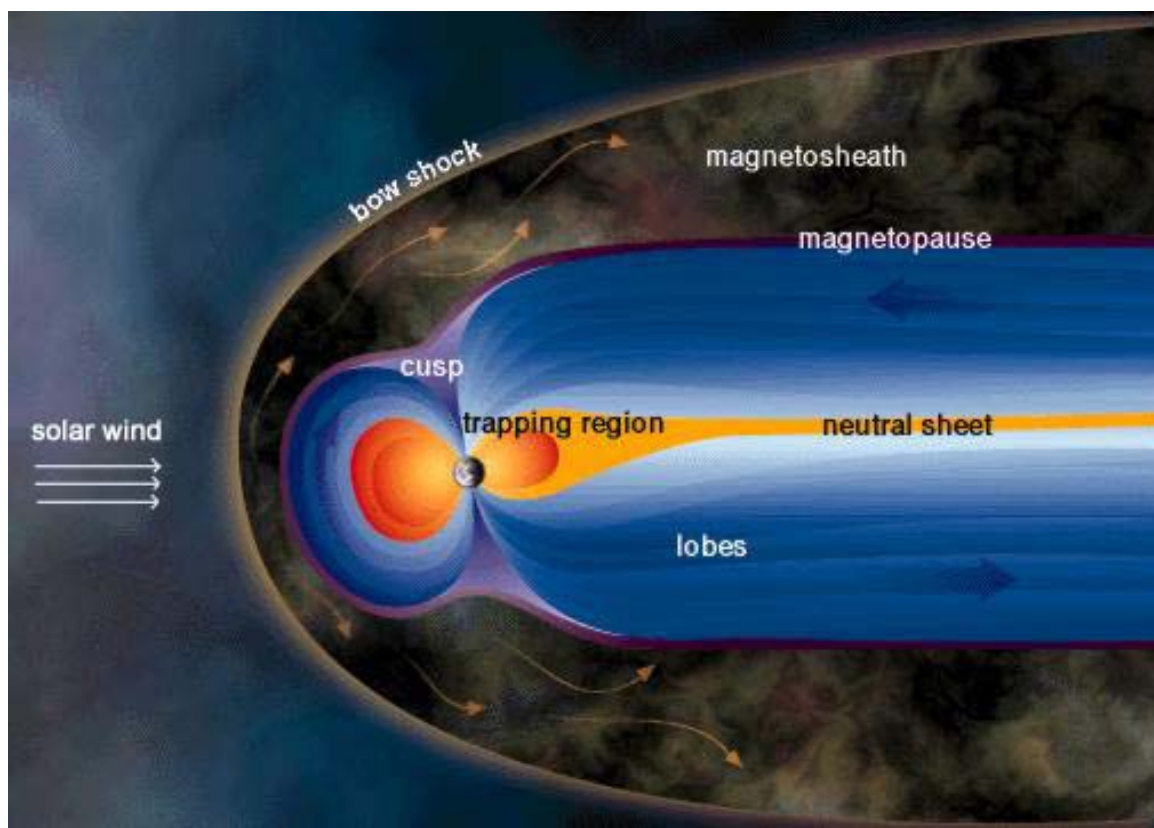


**Figure I.2.** A view of the Earth's magnetosphere. Picture taken from the website *Windows to the Universe* [<http://www.windows.ucar.edu/>], University Corporation for Atmospheric Research.

To end with this brief enumeration of the contributions to the magnetic field measured near the Earth's surface, the variation of these external currents creates current systems in the Earth's interior that induce secondary magnetic fields, whose intensity is related to the size of the inducing fields and the conductivity of the Earth's interior.

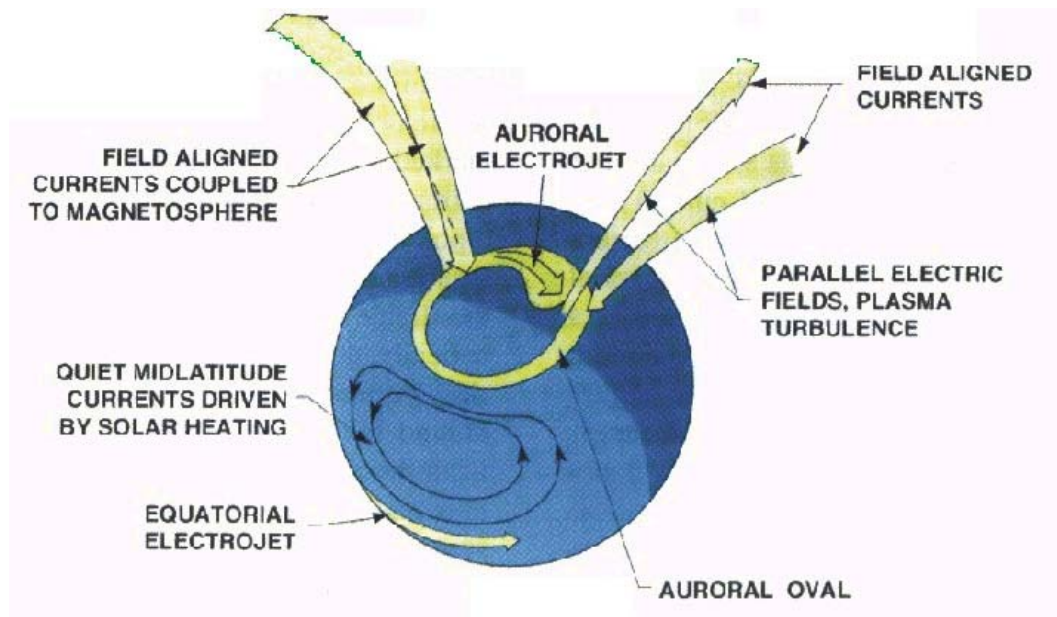


**Figure I.3.** Schematic view of the main current systems found in the ionosphere. Figure adapted from T.Moretto, GSFC/NASA, after Lanzerotti *et al.* [1993].

## 1.2. The main field and its secular variation

If we want to analyse the magnetic field of the Earth, it is necessary to individualise the different contributions before commented: main, crustal, external, and induced fields. All these contributions have different properties (time scale, magnitude, wavelength) that help in their discrimination. A table with the main features of these different fields can be found in Parkinson [1983, p. 6].

The magnetic field measured at the Earth's surface is mainly of core origin. The main field changes its strength in space and in time (the secular variation). The maximum intensity is around 60,000 nT (where 1 nT is equivalent to  $0.1 \text{ Wb} \cdot \text{m}^{-2}$ ) near the magnetic poles, and around 25,000 nT near the magnetic equator (values at year 2000). The mechanism that is able to produce and sustain this magnetic field is the thermal and compositional convection that produces the movement of the liquid core. The interactions between these flowing charges and the geomagnetic field, following the theory of the geodynamo, maintain the field and produce its secular variation.

### Expression of the field in terms of spherical harmonics

The geomagnetic field, as any vector, can be defined by its direction and intensity. All magnetic fields have an associated electric field. The quantities that outline an electromagnetic field are: the magnetic induction or flux density **B**; the intensity of the geomagnetic field **H**; the

intensity of the electrical field  $\mathbf{E}$ ; the electric displacement  $\mathbf{D}$ ; and the electric current density  $\mathbf{J}$ . These quantities are related through the Maxwell equations:

$$\nabla \times \mathbf{E} = -\frac{\partial \mathbf{B}}{\partial t} \quad (\text{I.1})$$

$$\nabla \times \mathbf{H} = \frac{\partial \mathbf{D}}{\partial t} + \mathbf{J} \quad (\text{I.2})$$

$$\nabla \cdot \mathbf{D} = q \quad (\text{I.3})$$

$$\nabla \cdot \mathbf{B} = 0 \quad (\text{I.4})$$

where  $q$  is the charge density. Assuming negligible electric field changes (i.e.,  $\mathbf{D}$  is constant) and keeping in mind that the magnetic induction is related to the field intensity through the permeability of the medium  $\mu$ , then:

$$\nabla \times \mathbf{B} = \mu \mathbf{J} \quad (\text{I.5})$$

In a current-free space, like the region from the Earth's surface up to 50-60 km, the current density is negligible, so the curl of the geomagnetic field is annulled. This fact allows the magnetic induction to be written as the gradient of a scalar potential  $V$ :

$$\mathbf{B} = -\nabla V \quad (\text{I.6})$$

Based on (I.4), the gradient of the induction is also zero, so the geomagnetic potential must satisfy Laplace equation:

$$\nabla^2 V = 0 \quad (\text{I.7})$$

Equation (I.7) is not valid for heights close to the ionospheric E layer (around 95 km) and above, where electric currents flow through the magnetic field lines [e.g. Langel *et al.*, 1996]. Taking into account that the geomagnetic potential can be separated as the sum of a potential due to sources internal to the Earth's surface and another potential caused by external sources, the geomagnetic field measured in the ionosphere can be expressed as:

$$\mathbf{B} = \mathbf{B}_i + \mathbf{B}_e + \mathbf{B}_j \quad (\text{I.8})$$

The data used to determine the potential are chosen in order to minimise the field due to sources placed into the ionosphere ( $\mathbf{B}_j$ ), so the final potential is a good approximation of the internal ( $\mathbf{B}_i$ ) and external ( $\mathbf{B}_e$ ) fields. As said before, this potential satisfies equations (I.6) and (I.7). A potential of this kind can be expressed as an expansion of spherical harmonic functions,

as described by Gauss [1839]. The potential can be described as a sum of contributions corresponding to the internal and external fields:

$$V = V_i + V_e \quad (\text{I.9})$$

Developing equation (I.7) in spherical coordinates  $(r, \theta, \phi)$  and solving through separation of variables [e.g., Jackson, 1962], the internal ( $V_i$ ) and external ( $V_e$ ) potential take the form:

$$V_i(r, \theta, \phi) = a \sum_{n=1}^{\infty} \sum_{m=0}^n \left(\frac{a}{r}\right)^{n+1} \{g_n^m \cos m\phi + h_n^m \sin m\phi\} P_n^m(\cos \theta) \quad (\text{I.10})$$

$$V_e(r, \theta, \phi) = a \sum_{n=1}^{\infty} \sum_{m=0}^n \left(\frac{r}{a}\right)^n \{q_n^m \cos m\phi + s_n^m \sin m\phi\} P_n^m(\cos \theta) \quad (\text{I.11})$$

where  $a$  is the Earth's mean radius,  $\{g_n^m, h_n^m\}$  are the spherical harmonic coefficients or Gauss coefficients with both integer order  $m$  and degree  $n$  for the internal field,  $\{q_n^m, s_n^m\}$  are the Gauss coefficients for the external field, and  $P_n^m(\cos \theta)$  are the associated Legendre functions. It is common in Geomagnetism to use these polynomials in their partially Schmidt-normalised form [e.g. Chapman and Bartels, 1940]. The products of these functions by sines or cosines receive the name of spherical harmonics, while the expressions (I.10) and (I.11) are called spherical harmonic expansion of the potential. The radial term is defined so that the internal potential vanishes at infinite distance from the Earth's surface, whereas the external potential is zero at the origin of the coordinate system (i.e., at the centre of the Earth).

The potential  $V$  is not a measurable quantity. Datasets from observatories, satellites, magnetic surveys, etc., are formed by values of the different geomagnetic field elements, which are directly or afterwards transformed to  $X$ ,  $Y$ , and  $Z$  components. These components are related to the geomagnetic potential through the partial derivatives in spherical coordinates:

$$\begin{aligned} X \equiv -B_\theta &= \frac{1}{r} \frac{\partial V}{\partial \theta} = \\ &= \sum_{n=1}^{\infty} \sum_{m=0}^n \left[ \left(\frac{a}{r}\right)^{n+2} \{g_n^m \cos m\phi + h_n^m \sin m\phi\} + \left(\frac{r}{a}\right)^{n-1} \{q_n^m \cos m\phi + s_n^m \sin m\phi\} \right] \frac{dP_n^m(\cos \theta)}{d\theta} \end{aligned} \quad (\text{I.12})$$

$$\begin{aligned} Y \equiv B_\phi &= \left( -\frac{1}{r \sin \theta} \right) \frac{\partial V}{\partial \phi} = \\ &= \frac{1}{\sin \theta} \sum_{n=1}^{\infty} \sum_{m=1}^n m \left[ \left(\frac{a}{r}\right)^{n+2} \{g_n^m \sin m\phi - h_n^m \cos m\phi\} + \left(\frac{r}{a}\right)^{n-1} \{q_n^m \sin m\phi - s_n^m \cos m\phi\} \right] P_n^m(\cos \theta) \end{aligned} \quad (\text{I.13})$$

$$\begin{aligned}
Z &\equiv -B_r = \frac{\partial V}{\partial r} = \\
&= -\sum_{n=1}^{\infty} \sum_{m=0}^n \left[ (n+1) \left( \frac{a}{r} \right)^{n+2} \{g_n^m \cos m\phi + h_n^m \sin m\phi\} - n \left( \frac{r}{a} \right)^{n-1} \{q_n^m \cos m\phi + s_n^m \sin m\phi\} \right] P_n^m(\cos \theta)
\end{aligned} \tag{I.14}$$

Equations (I.10) and (I.11) contain only a spatial dependence. A temporal dependence can also be included; for the particular case of the representation of the main field, an expression like the following can be added to the potential to give account for the secular variation:

$$V_{SV}(\vec{r}, t) = a \sum_{n=1}^{L_{max}} \sum_{m=0}^n \left( \frac{a}{r} \right)^{n+1} \{ \dot{g}_n^m \cos m\phi + \dot{h}_n^m \sin m\phi \} \cdot (t - t_0) \cdot P_n^m(\cos \theta) \tag{I.15}$$

where  $\{ \dot{g}_n^m, \dot{h}_n^m \}$  are the Gauss coefficients for the secular variation (i.e. the time derivative of  $\{ g_n^m, h_n^m \}$ ), and  $t_0$  is the epoch of the main-field model (or reference epoch). This is for example the expression for the secular variation of the International Geomagnetic Reference Field [IGRF; Mandea and Macmillan, 2000], a model accepted as standard to represent the global main field and its temporal change. The Working Group 8 of the International Association of Geomagnetism and Aeronomy (IAGA), Division V, produces a set of Gauss coefficients at five-year intervals to compute the values of the main field for a particular location and epoch. For example the last up to date proposed version for IGRF, known as IGRF 9<sup>th</sup> generation (IGRF-9) and released at the IUGG XXIII General Assembly in July 2003 [IAGA, 2003], includes models of the main field from 1900 to 2000 and a secular variation model for 2000-2005.

The parameter  $L_{max}$  in equation (I.15) is the maximum degree of the coefficients that represent the secular variation given by the model. As reflected in equations (I.10) and (I.11), the general solution for the potential (and also for the magnetic components) becomes a sum of an infinite number of terms. In practice, when the field is computed from a finite input dataset, the summation is truncated to a maximum degree  $n_{max}$ , obtaining a set of coefficients sufficient to represent in a realistic way the observed geomagnetic field. Therefore, it is supposed that the field is properly represented by a set of coefficients up to degree  $n_{max}$ . For the particular case of the IGRF, the value of  $n_{max}$  was equal to 10 (that is, 120 coefficients) until the IGRF 8<sup>th</sup> generation (named IGRF-8); the IGRF-9 includes coefficients up to degree  $n=13$  for year 2000 (i.e., the number of IGRF-9 coefficients for 2000 is 195).

The potential up to degree 13 or 14 is considered to be due mainly to the magnetic field produced in the Earth's core, whereas for higher degrees the field is accepted to be mostly of crustal origin [Langel and Estes, 1982]. This transition is reflected in the change of slope found



when representing the logarithm of the geomagnetic field power spectrum as a function of  $n$ , where the spectrum is defined as [Lowes, 1966]:

$$R_n = (n+1) \sum_{m=0}^n \{(g_n^m)^2 + (h_n^m)^2\} \quad (\text{I.16})$$

Figure I.4 shows this change in slope when representing the logarithm of the spatial power spectrum of the field defined by the coefficients of the model developed by Olsen *et al.* [2000] using the first measurements obtained from the Ørsted satellite [Neubert *et al.*, 2001]. This common behaviour has been found by several authors when analysing different geomagnetic models [e.g. Langel, 1987].

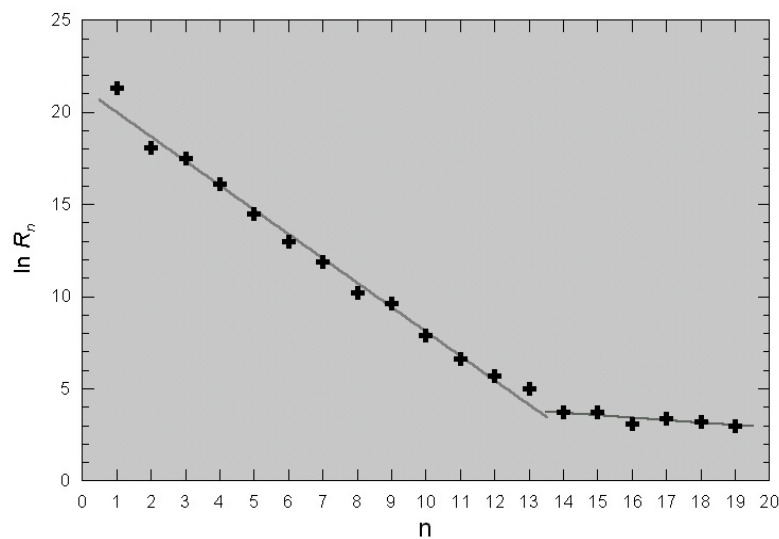


**Figure I.4.** Logarithm of the spatial power spectrum of the geomagnetic field (crosses) computed through the relation (I.16) for the set of coefficients of the Ørsted Initial Field Model [Olsen *et al.*, 2000]. Best fits (lines) are computed for  $2 \leq n \leq 13$  and  $14 \leq n \leq 19$ .

The individual terms in the expression for the development of the potential can be interpreted as due to equivalent sources placed at the Earth's centre. In this way, the terms with  $n=1$  would represent the magnetic field due to a dipole, those with  $n=2$  would symbolise a quadrupole, those corresponding to  $n=3$  would be associated to the field generated by an octupole, and so on [e.g. again Chapman and Bartels, 1940]. A good approximation to give an account of the main field is to consider it as produced by a dipole placed at the centre of the Earth and tilted about  $11^\circ$  with regard to the rotation axis of the planet. It represents nearly 90% of the field measured at the surface. The points where the axis of this imaginary dipole would intersect the surface are called the geomagnetic poles; due to the secular variation, the position of these poles varies with time, and they are nowadays roughly located at West Greenland and at the East coast of Antarctica.

## Properties of the Associated Legendre Functions and Spherical Harmonics

As seen in equation (I.10) and thereafter, the geomagnetic field potential (and so the magnetic components) can be expressed as a function of associated Legendre functions  $P_n^m(z)$  with Schmidt normalization. Many of the properties satisfied by the geomagnetic field are therefore consequence of the mathematical properties of these functions. They are related to the ordinary Legendre polynomials in the form:

$$P_n^m(z) = (1 - z^2)^{m/2} \frac{d^m P_n(z)}{dz^m} \quad (\text{I.17})$$

where the polynomials can be computed in a general way through the relation:

$$P_n(z) = \sum_{j=0}^k (-1)^j \frac{(n-2j)! z^{n-2j}}{2^n j! (n-j)! (n-2j)!}, \quad k \equiv \text{integer} = \begin{cases} n/2 \\ (n-1)/2 \end{cases} \quad (\text{I.18})$$

Values for the first associated Legendre functions computed using equations (I.17) and (I.18) can be found in table I.1, and a graphical representation of those functions for some given degrees  $n$  is shown in figure I.5.

n	m	$P_n^m(\cos \theta)$
1	0	$\cos \theta$
1	1	$\sin \theta$
2	0	$1/2 (\cos^2 \theta - 1)$
2	1	$3 \sin \theta \cos \theta$
2	2	$3 \sin^2 \theta$
3	0	$1/2 (5 \cos^3 \theta - 3 \cos \theta)$
3	1	$1/2 \sin \theta (15 \cos^2 \theta - 3)$
3	2	$15 \sin^2 \theta \cos \theta$
3	3	$15 \sin^3 \theta$

**Table I.1.** Associated Legendre functions for the first values of  $m, n$

One of the main properties of the associated Legendre functions is their orthogonality over the interval  $[-1, 1]$ . This property is expressed as:

$$\int_{-1}^1 P_n^m(z) \cdot P_k^m(z) \cdot dz = \begin{cases} 0 & \text{for } k \neq n \\ \frac{2}{2n+1} \frac{(n+m)!}{(n-m)!} & \text{for } k = n \end{cases} \quad (\text{I.19})$$

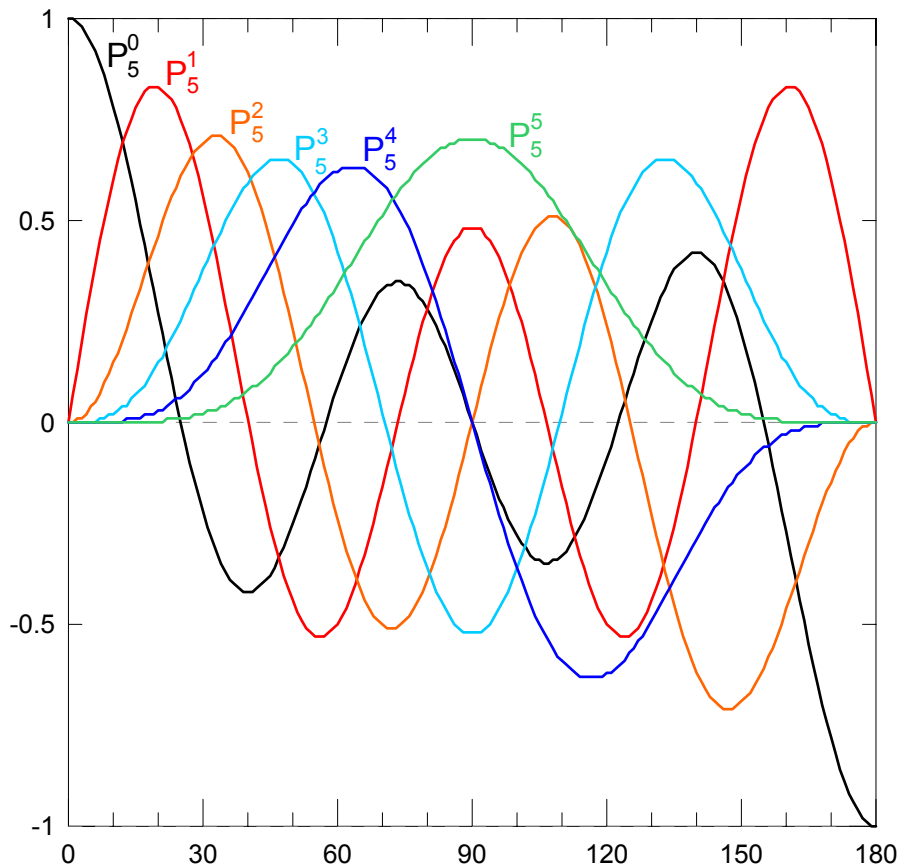


**Figure I.5.** Associated Legendre functions of degree five as a function of colatitude.

Analogously, spherical harmonics  $P_n^m(\cos\theta)\cos m\phi$  and  $P_n^m(\cos\theta)\sin m\phi$  are orthogonal over the sphere. The orthogonality of these functions implies that the coefficients of a spherical expansion (like that for the potential) can be determined independently, regardless of the number of terms in the expansion. Since the expanded function (e.g. a magnetic component) is only known at discrete points, the orthogonality of the spherical harmonics will be preserved depending on the rightness in the distribution of the data [Langel, 1987].

Spherical harmonics are zero  $n-m$  times along the parallels of the sphere (due to the fact that the associated Legendre functions cancel), and also along the meridians  $2m$  times (because of the trigonometric functions). This fact divides the sphere into cells where the sign of the corresponding spherical harmonic is positive or negative: when  $m=0$  the sphere is divided into fringes limited only by parallels, when  $m = n$  harmonics do not vanish for any latitude. Figures I.6a and I.6b show some examples of the shape of the spherical harmonics over the surface of a sphere. It is evident the presence of regions in which the sign of the spherical harmonics alternates, depending on the values of  $m$  and  $n$ .

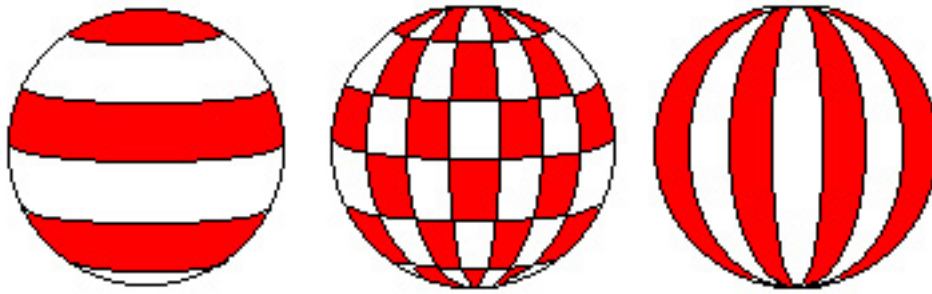


**Figure I.6a.** Zonal (left), tesseral (center), and sectorial (right) forms of spherical harmonics, where the constant sign of the spherical harmonic is represented by zones of same color.

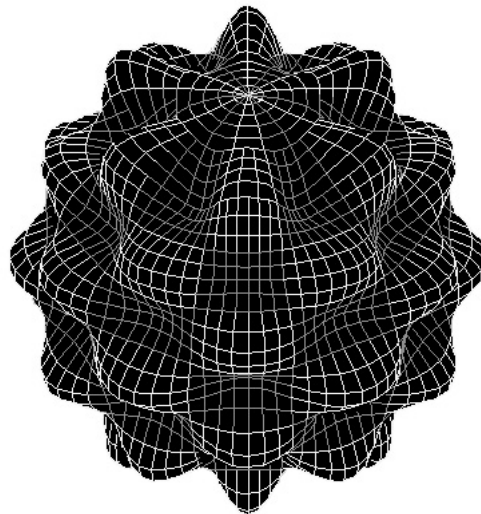


**Figure I.6b.** Legendre polynomial surface with degree  $n=12$  and order  $m=6$ . Figure generated from a program by P. McFadden, AGSO.

### I.3. The crustal field

The magnetic deviations found during quiet geomagnetic periods (i.e. when external fields are weak) when comparing a real measurement with the value of a reference model receive the name of magnetic anomalies. Depending on the area under study, local and regional anomalies blend. The intensity of the crustal field can reach values as high as several thousands of nanotesla at the Earth's surface, for example near volcanic areas [e.g. Blanco-Montenegro *et al.*, 2003, and references therein], but usually the anomaly values are around few tens or hundreds of nanotesla.

The anomaly field is highly variable in space due to the magnetisation contrasts between rocks. These contrasts have the origin in the different ages of the structures, their different geological history and lithology, or the difference in temperature. As said before, almost the totality of the mantle (and in some cases, the lower layer of the crust) is above the Curie temperature, so the magnetic anomalies can be considered as produced by the crustal field. The

information that can be obtained through the study of the crustal field is therefore restricted to the depth of the Curie isotherm or to the crust-mantle discontinuity, depending on which one is nearer the surface. However, the role of the upper mantle with regard to its contribution to the geomagnetic field has to be clarified, because some works have demonstrated that the upper mantle can present significant magnetisation, especially in oceanic regions.

The study of the crustal magnetic field began as a tool to locate ore beds. The first available documents tell that, in the 17<sup>th</sup> century Scandinavians conducted magnetic surveys to locate hidden iron deposits. At present crustal mapping is not only used for petroleum and mineralogy exploration, but the knowledge of the magnetic anomaly field in geophysical studies has become of indubitable importance. The study of lineated magnetic anomalies close to oceanic ridges and their correlation with the geomagnetic field reversal time scale provided an evidence to the seafloor spreading and the theory of plate tectonics (see Harrison [1987] for a review). The study of the continental anomalies has provided information about the structure of the lithosphere which were not available from direct geological prospecting. Moreover, the remanent magnetisation present in some rocks due to their magnetic properties is on the basis of the study of the paleomagnetic field. The magnetic anomalies detected in near-surface surveys are in most cases due to the induced magnetisation [Langel and Hinze, 1998]; it can be checked looking at the pattern of the anomalies and the direction of the present magnetic field. Magnetic anomalies related to remanent magnetisation are nevertheless evident, and this is the predominant kind of magnetisation in the oceanic basis. Rocks with a high Königsberger ratio (i.e. the remanent magnetisation is more important than the induced one) are for example basalt and granite, while for limestone the induced magnetisation dominates.

Under magnetic disturbed conditions, the external fields can mask the crustal contribution, reaching values up to several hundreds of nanotesla during strong geomagnetic storms. Because of this, many indices have been created to give account of the geomagnetic (quiet or disturbed) conditions (see e.g. Siebert and Meyer [1996] for a review). As it will be shown further on (see Chapter III), the effects of the external fields can be minimised if the analysed data are selected according to different criteria, with the use of the geomagnetic indices as a threshold. It is beyond the scope of this work the modelling of the external fields.

#### **1.4. *The necessity of a reference field for Antarctica***

The analysis of magnetic anomalies is essential in regions where the Earth's surface is not reached by other means, like in the case of the Antarctic continent, where almost all the surface



(except some coastal regions) is covered by a thick layer of ice. Hence, several near-surface magnetic surveys have been carried out in the region specially for the last 45 years, and a big effort has been made to produce a compilation of the data from all these surveys under the framework of the Antarctic Digital Magnetic Anomaly Project [ADMAP; Chiappini *et al.*, 1998, 1999]. Figure I.7 shows the coverage of the different near-surface surveys compiled by the ADMAP group. These kind of studies contribute to a better understanding of Antarctic geology, and the role of Antarctica in the tectonic and geological evolution of Gondwana [e.g. Lawver *et al.*, 1987]. Figure I.8 shows a map of the main tectonic features of the Antarctic continent.

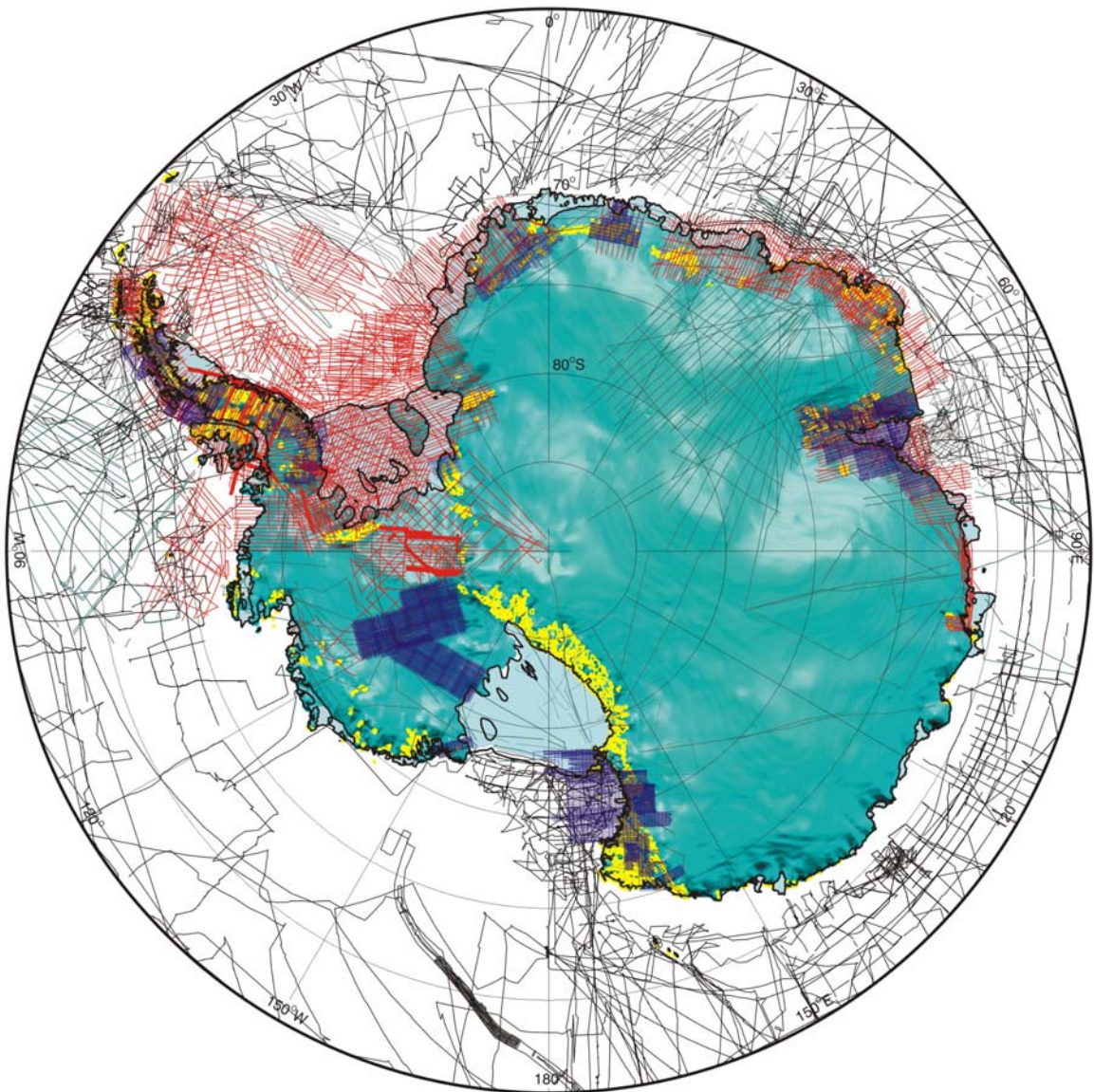


**Figure I.7.** Spatial coverage of the different near-surface Antarctic magnetic surveys compiled by the ADMAP group. Blue, red, and cyan lines represent aeromagnetic tracks with line spacing around 5, 20, and 50 km respectively, whereas violet lines correspond to marine surveys. From Golinsky *et al.* [2001].



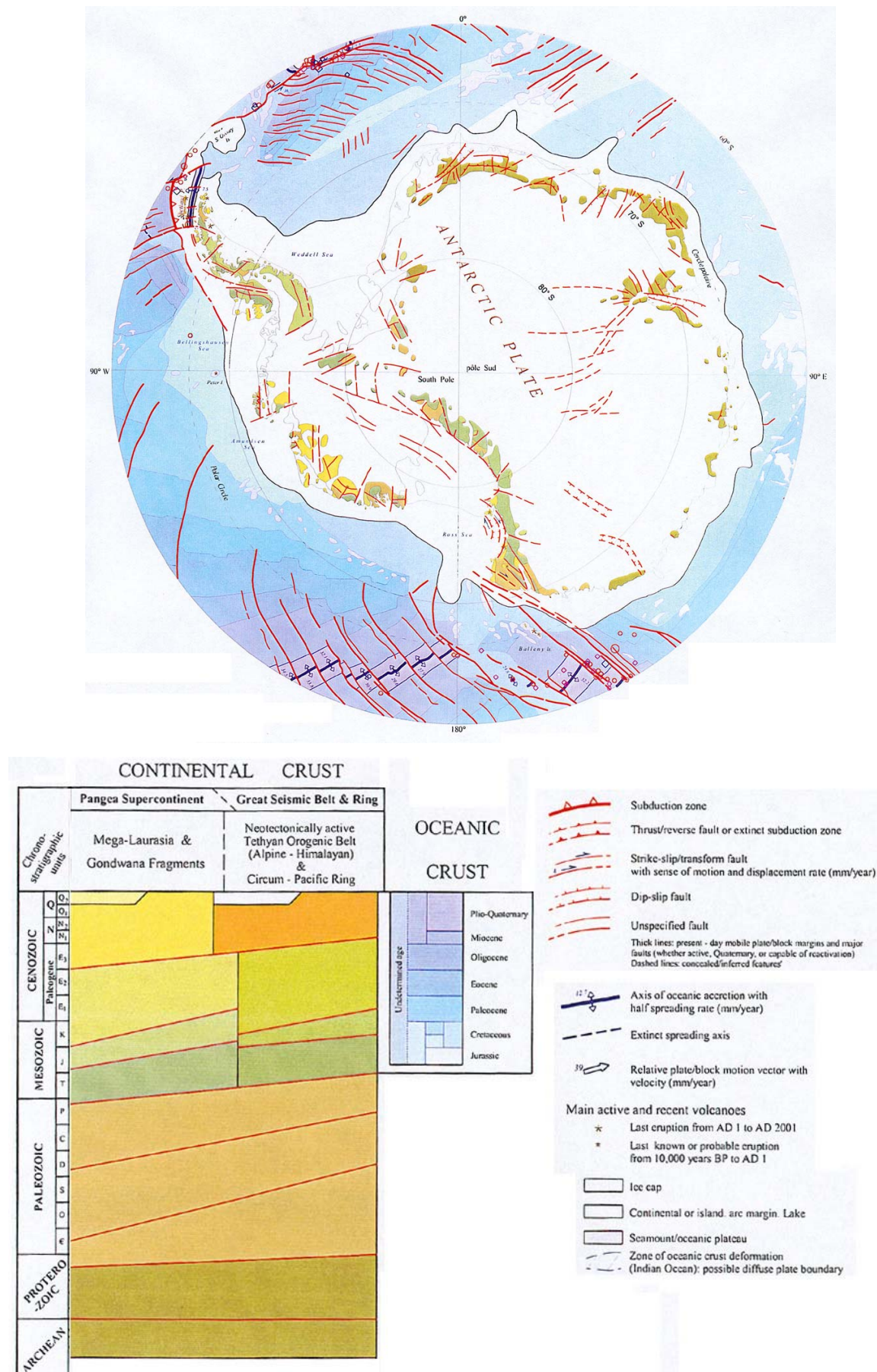


Figure I.8. Seismotectonic map of the Antarctic Region (adapted from Haghypour [2001]).

To study separately the different contributions to the magnetic field measured in any location, it is fundamental to remove the magnetic signatures that are not interesting for the desired study. For example, if we want to study the crustal field, the collected data must be previously processed in order to make sure of the removal of the main and external fields.

Let's suppose a set of magnetic measurements without external field perturbations, i.e. the values include only main and crustal fields (in order to eliminate the external contributions, the measurements taken at a fixed station placed near the area of the geomagnetic survey are used to correct the data from diurnal and other external variations). A tool to isolate both internal contributions as accurately as possible is needed. A proper definition of the main field allows the reduction of the magnetic survey data to a reference epoch and to a common height; the combination of magnetic surveys taken in very different situations (years, altitudes); and therefore the study of the morphology of the field.

The procedure to eliminate the main field from a measurement is thus to subtract a reference field, usually the IGRF model calculated for a given epoch. This procedure is based on the consideration of the different wavelengths represented by the different contributions. The sources placed within the outer core are supposed to produce a magnetic field with much longer wavelengths than those produced by the crustal field. These long wavelengths are removed when correcting by IGRF models (that can represent wavelengths up to 4,000 km).

The main errors when analysing the magnetic anomalies arise however from errors in the core field estimation [Alsdorf *et al.*, 1994a], and these errors increase in the case of Antarctica, where the International Geomagnetic Reference Field often does not represent the main field with the needed accuracy. Moreover, the use of IGRF to represent the secular variation can also lead to errors when applied to restricted regions of the Earth's surface, due to the assumption of a constant variation pattern over five-year intervals. Logistic difficulties limit human presence in Antarctica, as well as the capability of operating geomagnetic observatories for a regular and continuous recording of the field: the scarcity of continuous ground-based recordings makes the achievement of a good approximation for the secular variation even more difficult. Furthermore, Antarctic geomagnetic observatories are often those that present the highest bias values with respect to main field models [Sabaka and Baldwin, 1993; Mande and Langlais, 2002], models that are usually not designed to represent the long wavelength crustal field. Lithospheric local and regional contributions are usually mixed and what can be sometimes needed (as the case may be) is a model able to represent not only the main field but also the longest wavelength part of the lithospheric field.



To illustrate these facts, we can consider the aeromagnetic surveys carried out between 1971 and 1973 by the United States program over Ross Island and the Dry Valleys, in Antarctica. As shown by Chiappini *et al.* [2002] in the ambit of a compilation of aeromagnetic anomalies for the Transantarctic Mountains - Ross Sea sector, some problems arose when reducing to a same epoch the different surveys realised under this program. The reference field removed from the data to obtain the magnetic anomaly map was the DGRF 1990 (when the coefficients of a particular IGRF model are not supposed to change because they will not undergo further revision, the model has been traditionally called DGRF). The first map obtained was that in top of figure I.9, and some features were not consistent with the regional rock susceptibility data found in the literature. A constant value was manually added to the survey with lowest apparent resolution to shift its base level, and the bottom map in figure I.9 was obtained. The major changes are noted over the Wilson Piedmont Glacier region, and the basement at the Ross Sea coast seems to be nonmagnetic, while the high frequency magnetic anomalies over the Olympus and Asgaard Ranges are preserved. The major differences between both maps were therefore found in the overlapping common region. The differences between both surveys would probably not appear if the secular variation given by the removed reference field had been more accurate. Another example can be found in von Frese *et al.* [1999], where after the removal of a reference field from Magsat satellite data over the southern cap, a residual core field component was found in the expected anomaly field map.

The necessity of a regional model more accurate than the IGRF to represent the geomagnetic field over Antarctica led De Santis *et al.* [1999a], in the framework of the ADMAP project, to propose the development of a Laplacian regional model. The geomagnetic potential would be computed by means of Spherical Cap Harmonic Analysis (SCHA) [Haines, 1985a], the natural solution of the Laplace's equation over a restricted region of the Earth's surface.

The objective of this work is therefore the development of a model capable of representing the main field on the Antarctic continent and adjacent seas, useful not only for crustal studies but also to improve our understanding of the magnetic field in this particular region of the Earth. By means of a proper definition of the main field, a clear and unambiguous interpretation of the found magnetic anomalies will be achieved. A well-parameterised secular variation will make easier the reduction of individual surveys, so data from old campaigns could be combined with new data without problems on the overlapping regions. Finally, a reliable model will contribute to improve our knowledge of the most important features of the geomagnetic field in Antarctica.

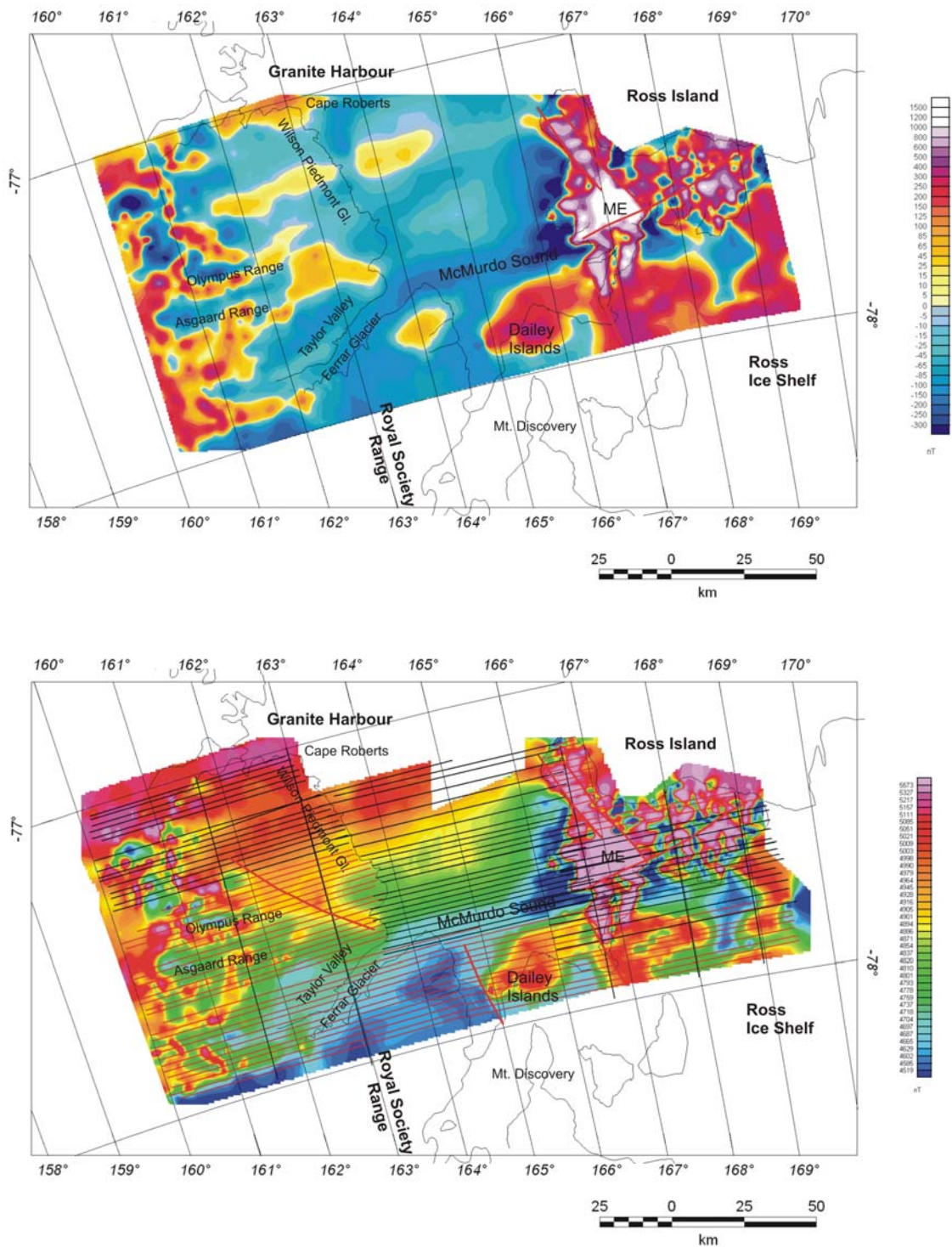


**Figure I.9.** Anomaly maps obtained from an aeromagnetic survey over Ross Island and the Dry Valleys, Antarctica. The top map shows a fictitious structure oriented in a NW direction separating the Wilson Piedmont Glacier from the high frequency anomalies over Olympus and Asgaard Range. The bottom map was obtained after applying a hand levelling. The previous region appears now nonmagnetic, so the fictitious anomaly probably arose when the DGRF90 was applied to reduce the different surveys. Maps taken from Chiappini *et al.* [2002].

The contents of this work are as follows. In Chapter II the spherical cap harmonic analysis theory applied to develop the model is revisited. A summary of the studies that previously used the same approach is detailed. The advantages and drawbacks of the modelling technique are discussed, as well as the modifications and improvisations since the introduction of the technique in its original form. Attention will be paid to the features of the technique adopted in this thesis, as well as to the improvement in the computation of the associated Legendre functions.

Chapter III deals with the data used in the development of the model. The imposed criteria to select the different datasets (from surface, near-surface, or satellite campaigns) are presented, together with information about the pre-processing of the measurements. Data from a stratospheric balloon mission will be presented and analysed for the first time in this chapter.

On Chapter IV the model in a strict sense is proposed. Different models are discussed, and the selection of the most appropriate candidate is made on the basis of different considerations (fit to real data, either used or not in the development of the model; behaviour in regions without measurements, etc.). The validity of the model is demonstrated comparing its behaviour with that of global models.

Chapter V discusses about the physical and geological applications that can be extracted from the model (determination of the location of the magnetic pole; study of geomagnetic jerks; etc.). The reduction of magnetic surveys carried out in different periods to obtain merged anomaly maps confirms the utility of the model. Finally and after the conclusions, a list of the references consulted to develop this work is provided.

Each chapter has been conceived as an independent unit, but at the same time it follows a logical sequence to connect all the sections. In this way, a reader interested in the present state of the spherical cap harmonic analysis can just consult the second Chapter, or the reading of Chapter III will be enough for those interested only in the data selection process. Those readers who are familiar with the study and modelling of the magnetic field can avoid the introductions present at the beginning of each section.

## II. Harmonic Analysis on a Spherical Cap

### II.1. Introduction

Some advantages of the representation of the potential in terms of spherical harmonics, as shown before, are the possibility to separate the field into internal and external contributions, the availability to make a vertical (upward or downward) continuation of the field, and the representation of the different contributions as a function of multipolar terms, obtaining a contribution to the spectral content from each one of the harmonics. Nevertheless, development of the potential as given in (I.10) is not reliable when measurements from only restricted regions of the Earth surface are available. Global spherical harmonics lose their orthogonality in a limited region, so the determination of the coefficients of the model, usually by using the least squares method, is numerically unstable. In spite of this fact Haines [1985a] showed that, there is a specific solution for Laplace equation for the situation of a spherical cap when the boundary conditions are appropriate. It was defined in this way the concept of Spherical Cap Harmonic Analysis (SCHA).

For the whole sphere, the equation (I.10) must satisfy continuity conditions in longitude, that is, both the potential and its derivative must have the same values when  $\phi = 0$  as well as when  $\phi = 2\pi$ . With regard to the colatitude, potential and derivative are forced to be zero at the poles depending on the value of the order  $m$ :

$$\begin{aligned} \left. \frac{\partial V_n^m(r, \theta, \phi)}{\partial \theta} \right|_{\theta=0, \pi} &= 0 \quad \text{for } m = 0 \\ V_n^m(r, \theta, \phi) \Big|_{\theta=0, \pi} &= 0 \quad \text{for } m \neq 0 \end{aligned} \quad (\text{II.1})$$

These conditions force the degree  $n$  to be an integer. When restricting the analysis to a spherical cap of half-angle  $\theta_0 \neq \pi$  (centred or not at the pole), we have the same boundary conditions in longitude but different conditions at the border of the cap. Potential and derivative can take any value different from zero when  $\theta = \theta_0$ . In general, they can be represented by functions in longitude and radial distance:

$$V(r, \theta_0, \phi) = f(r, \phi) \quad (\text{II.2})$$

$$\frac{\partial V(r, \theta_0, \phi)}{\partial \theta} = g(r, \phi) \quad (\text{II.3})$$

Equation (II.2) is valid when the degree  $n_k$  takes such a value that the derivative in colatitude of the potential is zero at the border of the cap. Keeping in mind the expression for the magnetic potential, this condition is equivalent to impose the derivative of the associated Legendre function to be zero:

$$\frac{dP_{n_k}^m(\cos \theta_0)}{d\theta} = 0 \quad (\text{II.4})$$

Equation (II.3) is on the other hand satisfied for those values of  $n_k$  such that the potential is zero at the border of the cap, that is:

$$P_{n_k}^m(\cos \theta_0) = 0 \quad (\text{II.5})$$

So, the only acceptable values for  $n_k$  will be those for which the Legendre functions or their derivatives are zero at the border of the cap. In contrast to the case of the sphere, these degrees  $n_k$  that satisfy expressions (II.4) and (II.5) are not necessarily integer values.

With the idea of ordering the set of solutions for both boundary equations, an integer index  $k$  is defined to numerate the different roots of  $n$  for each  $m$ . Thus, given an order  $m$ , the possible degree values  $n_k$  (ordered as crescent  $k$ ) are alternate solutions of (II.4) or (II.5), being  $n_0$  the first solution of (II.4). When the difference between the index  $k$  and the order  $m$  is even (both of them begin with the value zero) the values for  $n_k(m)$  satisfy equation (II.4), while when  $k-m$  takes odd values the values for  $n_k(m)$  are roots of equation (II.5). The two sets of  $P_{n_k}^m$ , those with  $k-m=\text{even}$  and with  $k-m=\text{odd}$ , define two complete sets of basis functions that are orthogonal inside each set [De Santis and Torta, 1997a]. They are analogous to the case of Legendre polynomials in the harmonic analysis for the global case, but with the  $k-m=\text{even}$  set of functions not orthogonal to those of the  $k-m=\text{odd}$  set. This fact is reflected in a scalar product different from zero:

$$\int_0^{\theta_0} P_{n_j(m)}^m(\cos \theta) P_{n_k(m)}^m(\cos \theta) \sin \theta d\theta = \frac{\sin \theta_0 \cdot P_{n_j(m)}^m(\cos \theta_0)}{(n_k(m) - n_j(m)) \cdot (n_k(m) + n_j(m) + 1)} \left\{ \frac{dP_{n_k(m)}^m(\cos \theta_0)}{d\theta} \right\} \quad (\text{II.6})$$

when  $j-m=\text{even}$  and  $k-m=\text{odd}$ .

In this way, the potential over the surface of a spherical cap of half-angle  $\theta_0$  due to internal sources can be written as:

$$V_i(r, \theta, \phi) = a \sum_{k=0}^{KINT_{max}} \sum_{m=0}^k \left( \frac{a}{r} \right)^{n_k(m)+1} \{ g_k^m \cos m\phi + h_k^m \sin m\phi \} P_{n_k(m)}^m(\cos \theta) \quad (\text{II.7})$$

whereas for the case of external sources we have:

$$V_e(r, \theta, \phi) = a \sum_{k=1}^{KEXT_{\max}} \sum_{m=0}^k \left(\frac{r}{a}\right)^{n_k(m)} \{q_k^m \cos m\phi + s_k^m \sin m\phi\} P_{n_k(m)}^m(\cos \theta) \quad (\text{II.8})$$

Analogously, equation (I.9) is still valid and the total potential is the sum of those potentials of internal and external origin with respect to the cap surface.  $KINT_{\max}$  and  $KEXT_{\max}$  are the maximum indices on the expansion for internal and external sources respectively,  $P_{n_k(m)}^m(\cos \theta)$  are the associated Legendre functions with non integer degree  $n_k(m)$ , being  $\{g_k^m, h_k^m\}$  ( $\{q_k^m, s_k^m\}$ ) the spherical harmonic coefficients of the expansion representing internal (external) sources. As it can be seen, the index  $k$  also numerates these spherical cap harmonic coefficients, being  $[(KINT_{\max}+1)^2 + (KEXT_{\max}+1)^2 - 1]$  the number of coefficients that define the model.

As in the global case, a temporal dependence can also be added to represent the variation of the geomagnetic field. Related to the choice of the temporal series, different options can be considered. For example, Haines and Torta [1994] used in their study power series, Legendre series, and Fourier series. The coefficients are therefore expressed as a temporal series expansion in the form:

$$g_k^m(t) = \sum_{q=0}^{L_{\max}} g_{k,q}^m F_q\left(\frac{t-t_0}{T}\right), \quad h_k^m(t) = \sum_{q=0}^{L_{\max}} h_{k,q}^m F_q\left(\frac{t-t_0}{T}\right) \quad (\text{II.9})$$

where  $t_0$  and  $T$  are the translation and scaling parameters, and  $F_q(t)$  is the  $q^{\text{th}}$  temporal basis function chosen. In case of a power series, the temporal basis functions result in the expansion:

$$F_q(t) = t^q \quad (\text{II.10})$$

i.e. a polynomial that multiplies the terms of the expansion with a maximum temporal degree  $L_{\max}$ .

To improve the modelling of the secular variation, Haines [1993] proposed the method of main field differences. For a certain epoch  $t$  and given a location  $\vec{r}$  (in spherical coordinates,  $\vec{r}$  denoting longitude, latitude and altitude), the vector field  $\vec{B}$  can be expressed as a temporal expansion of functions in the form:

$$\vec{B}(\vec{r}, t) = \vec{b}_0(\vec{r}) + \vec{b}_1(\vec{r})t + \vec{b}_2(\vec{r})t^2 + \dots + \vec{b}_q(\vec{r})t^q + \vec{\delta}(\vec{r}) \quad (\text{II.11})$$

where  $\vec{\delta}(\vec{r})$  is the crustal field bias (i.e., the magnetic anomaly for that position).  $\vec{b}_0(\vec{r})$  is the main field at the zero epoch of the model, and the terms  $\vec{b}_1(\vec{r})t, \dots, \vec{b}_q(\vec{r})t^q$  represent the secular variation. Usually (e.g. for the IGRF models) the crustal field is considered a noise term when

modelling the main field, although the most recent models, those called comprehensive models [Sabaka *et al.*, 2002] and that will be introduced in the next chapter, try to represent also these crustal contributions.

The main parameter when analysing the secular variation is the difference in field values for a given location between two epochs  $t_1$  and  $t_2$ :

$$\vec{B}(\vec{r}, t_2) - \vec{B}(\vec{r}, t_1) = \vec{b}_1(\vec{r})(t_2 - t_1) + \vec{b}_2(\vec{r})(t_2 - t_1)^2 + \dots + \vec{b}_q(\vec{r})(t_2 - t_1)^q \quad (\text{II.12})$$

As can be seen in the above equation, both the main field at epoch  $\vec{b}_0(\vec{r})$  and the crustal bias  $\vec{\delta}(\vec{r})$  disappeared. So this method presents two clear advantages: first, it is not necessary to make a differentiation of equation (II.11) to obtain the secular variation field (it is often computed as  $\dot{\vec{B}}$ ); and second, the contamination introduced by the crustal anomaly field disappears when computing the secular variation. The main field differences method is therefore a more robust way to model the secular variation than fitting variations obtained by numerical differentiation. If one takes differences relative to the mean over a series of observations at the same location, the mean value for a certain component  $E$  of the field is:

$$\bar{E} = \beta_0 + \beta_1 \bar{t} + \beta_2 \bar{t}^2 + \dots + \beta_q \bar{t}^q + \delta_E \quad (\text{II.13})$$

then the method can also be used as solution for the main field. To finish with this parenthesis about the modelling of the secular variation, it is obvious that the vectors  $\vec{b}_q$  can be developed using spherical cap harmonic analysis.

The Gauss coefficients for the conventional harmonic analysis are related to those for the SCHA, as shown by De Santis *et al.* [1999b]. Imposing that the field deduced from a regional harmonic analysis on a spherical cap must be equal to that one deduced from a global analysis, and assuming  $r = a$  in the expression for the potential, the following relation is obtained:

$$\begin{Bmatrix} G_k^m \\ H_k^m \end{Bmatrix} = \sum_{n=m}^{\infty} T_k^{m,n} \begin{Bmatrix} g_n^m \\ h_n^m \end{Bmatrix} \quad (\text{II.14})$$

where  $\{G_n^m, H_n^m\}$  are the coefficients for the regional case and  $\{g_n^m, h_n^m\}$  is the set for the global analysis,  $T_k^{m,n}$  being the transformation matrix between coefficients. From the above equation it can be deduced that, given a global potential there is a unique possible representation for a chosen cap, whereas for the inverse situation (i.e., given a potential on a spherical cap) the number of functions showing a different value for the potential beyond the cap is infinite.

The associated Legendre functions with integer order  $m$  and real degree  $n_k(m)$  (written here as  $n$  for simplicity) can be computed from the relationship:

$$P_n^m(\cos \theta) = \sum_{j=0}^{\infty} A_j(m, n) \cdot \sin^{2j}(\theta/2) \quad (\text{II.15})$$

where the terms  $A_j(m, n)$  are defined as:

$$\begin{aligned} A_0(m, n) &= K_n^m \sin^m \theta & \text{for } j = 0 \\ A_j(m, n) &= \left( \frac{(j+m-1)(j+m) - n(n+1)}{j(j+m)} \right) \cdot A_{j-1}(m, n) & \text{for } j > 0 \end{aligned} \quad (\text{II.16})$$

$K_n^m$  is a constant that depends on the chosen normalisation for the associated Legendre functions. For a Schmidt normalisation:

$$\begin{aligned} K_n^m &= 1 & \text{for } m = 0 \\ K_n^m &= \frac{2^{1/2}}{m! 2^m} \left( \frac{(n+m)!}{(n-m)!} \right)^{1/2} & \text{for } m > 0 \end{aligned} \quad (\text{II.17})$$

In spite of the infinite number of addends in (II.15), this series can be truncated when the sum reaches the desired level of convergence. The  $\theta$ -derivative of  $P_n^m(\cos \theta)$  is obtained by deriving expression (II.15):

$$\begin{aligned} \frac{dP_n^m(\cos \theta)}{d\theta} &= \frac{\sin \theta}{2} \sum_{j=1}^{\infty} j \cdot A_j(m, n) \cdot \sin^{2(j-1)}(\theta/2) & \text{for } m = 0 \\ \frac{dP_n^m(\cos \theta)}{d\theta} &= \frac{m \cos \theta}{\sin \theta} P_n^m + \frac{\sin \theta}{2} \sum_{j=1}^{\infty} j \cdot A_j(m, n) \cdot \sin^{2(j-1)}(\theta/2) & \text{for } m > 0 \end{aligned} \quad (\text{II.18})$$

In this way, the associated Legendre functions and their derivatives with respect to the colatitude can be computed through relationships (II.15) and (II.18), using which it is possible to solve equations (II.4) and (II.5) for the appropriate root values.

As it has been shown, one of the main advantages presented by SCHa unlike other regional analysis methods is that the technique satisfies Laplace's equation, and most of the properties that were satisfied by the ordinary spherical harmonics approximation are also accomplished by the spherical cap harmonics [De Santis *et al.*, 1999b; Lowes, 1999a]. This fact, together with the relatively small number of coefficients to represent short wavelength features of the geomagnetic field and a usually proper fit to the input data, has converted SCHa into the favourite technique



when compared with other regional modelling techniques [Haines, 1990; Düzgit and Malin, 2000].

## II.2. Applications of SCHA

By definition, the spherical cap harmonic analysis allows the inclusion of data taken at different heights to obtain the model coefficients, such as observatory data, ground, marine, and aeromagnetic surveys, and satellite measurements. Since 1985, when the theory was first introduced by Haines, several works have been developed using SCHA: models for the main geomagnetic field, its secular variation, or both of them; anomaly field models; studies of electrical ionospheric currents; etc. In what follows we present some applications that can be found in the literature involving the use of SCHA. An exhaustive compilation of such works [J.M. Torta, personal communication] can be found in table II.1.

### Main and anomaly field models

The first application of SCHA to a real case was proposed by Haines [1985b]. Using data from Magsat satellite above 40° North latitude for magnetically quiet periods, Haines modelled the vertical anomaly field by using the derivative of the magnetic potential expressed as (II.7) with respect to the radial component. For a set of 5087 input measurements, the selected model was represented by an expansion of maximum index  $K_{\max}=22$ , resulting in a set of 190 internal coefficients statistically significant for an  $F$ -level equal to 3. This  $F$ -test is based on a stepwise procedure in which the coefficients are added or removed from the regression according to their significance [e.g. Draper and Smith, 1966]: a given coefficient is only considered if its value is  $\sqrt{F}$  times greater than its standard deviation [Haines and Torta, 1994]. The procedure will be explained in detail in chapter IV. The model was able to fit the input data with an error of 3.6 nT, representing wavelengths down to 1000 km, according to the expression for the minimum representable wavelength of a spherical harmonic model:

$$\lambda_{\min} = \frac{2\pi r}{n} \quad (\text{II.19})$$

where  $n$  is the degree of the Legendre functions ( $n_k$  for the case of SCHA). Since the vertical component was the only one which was modelled (due to the contamination of the horizontal components by field-aligned currents), it was not compulsory for the potential to be differentiable in latitude, so the model was formed by only one set of basis functions completely orthogonal on the cap.

## ABOUT THE TECHNIQUE

- Haines, *J. Geophys. Res.* 90, 2583, 1985  
Haines, *HHI-Rep.* 21, 27, 1987  
Haines, *Comput. Geosc.* 14, 413, 1988  
Haines, *J. Geomag. Geoelectr.* 42, 1001, 1990  
Haines, *Phys. Earth Planet. Inter.* 65, 231, 1991  
De Santis, *Geophys. J. Int.* 106, 253, 1991  
De Santis, *Geophys. Res. Lett.* 19, 1065, 1992  
Torta et al., *Phys. Earth Planet. Inter.* 74, 209, 1992  
Haines, *Geophys. J. Int.* 114, 490, 1993  
De Santis & Falcone, *Proc. II Hot.-Marus. Symp.*, 1994  
Torta & De Santis, *Geophys. J. Int.* 127, 441, 1996  
De Santis et al., *Phys. Earth Planet. Inter.* 97, 15, 1996  
De Santis et al., *J. Geomag. Geoelectr.* 49, 359, 1997  
De Santis & Torta, *J. Geodesy* 71, 526, 1997  
De Santis et al., *Annali di Geofisica* 40, 1161, 1997  
Lowes, *Geophys. J. Int.* 136, 781, 1999  
De Santis et al., *Phys. Chem. Earth A* 24, 935, 1999  
Düzgüt & Malin, *Geophys. J. Int.* 141, 829, 2000  
Korte & Holme, *Geophys. J. Int.* 153, 253, 2003

## REFERENCE FIELD MODELS

- Haines & Newitt, *J. Geomag. Geoelectr.* 38, 895, 1986  
Nevanlinna et al., *Deut. Hydro. Zeits.* 41, 177, 1988  
Newitt & Haines, *J. Geomagn. Geoelectr.* 41, 249, 1989  
De Santis et al., *J. Geomagn. Geoelectr.* 42, 1019, 1990  
Newitt & Haines, *Curr. Res. E, G.S.C.*, 275, 1991  
Nevanlinna & Rynö, *HHI-Rep.* 22, 106, 1991  
Torta et al., *J. Geomag. Geoelectr.* 45, 573, 1993  
An et al., *J. Geomag. Geoelectr.* 46, 789, 1994  
An et al., *Geomagn. Aeron.* 34, 581, 1995  
Haines & Newitt, *J. Geomag. Geoelectr.* 49, 317, 1997  
Kotzé & Barraclough, *J. Geomag. Geoelectr.* 49, 452, 1997  
Chiappini et al., *Phys. Chem. Earth* 24, N.5, 433, 1999  
Kotzé, *Earth Planets Space* 53, 357, 2001  
De Santis et al., *Geophys. Res. Lett.* 29, N. 8, 33-1, 2002

## SECULAR VARIATION MODELS

- Haines, *J. Geophys. Res.* 90, 12563, 1985  
García et al., *Phys. Earth Planet. Inter.* 68, 65, 1991  
Miranda et al., *J. Geomag. Geoelectr.* 49, 373, 1997  
Torta et al., *Tectonophysics* 347, 179, 2002

## DETERMINATION OF THE NORTH MAGNETIC POLE

- Newitt & Niblett, *Can. J. Earth Sci.* 23, 1062, 1986  
Newitt & Barton, *J. Geomag. Geoelectr.* 48, 221, 1996  
Newitt et al., *EOS* 83, 381, 2002

## ANOMALY FIELD MODELS

- Haines, *J. Geophys. Res.* 90, 2593, 1985  
De Santis et al., *NATO ASI Series C* 261, 1, 1989  
Torta et al., *Cahi. Cent. Eur. Geod. Seis.* 4, 179, 1991  
An et al., *J. Geomag. Geoelectr.* 44, 243, 1992  
Duka, *Annali di Geofisica* 41, 49, 1998  
Zhen-chang et al., *Chin. J. Geophys.* 41, 42, 1998  
Rotanova & Odintsov, *Phys. Chem. Earth A* 24, 455, 1999  
Rotanova et al., *Acta Geophys. Pol.* 48, 223, 2000  
Korte & Haak, *Phys. Earth Planet. Inter.* 122, 205, 2000  
Kotzé, *Geophys. Res. Lett.* 29, N. 15, 5-1, 2002

## GEOMAGNETIC VARIATIONS OF EXTERNAL ORIGIN

- Walker, *J. Atmos. Terr. Phys.* 51, 67, 1989  
Newitt & Walker, *J. Geomag. Geoelectr.* 42, 937, 1990  
Haines & Torta, *Geophys. J. Int.* 118, 499, 1994  
Torta et al., *J. Geophys. Res.* 102, 2483, 1997  
Walker et al., *J. Atmos. Sol. Terr. Phys.* 59, 1435, 1997  
Amm, *Ann. Geophys.* 16, 413, 1998

## IONOSPHERIC PARAMETERS

- De Santis et al., *Ann. Geophys.* 9, 401, 1991  
De Santis et al., *Adv. Space Res.* 12, N. 6, 279, 1992  
De Santis et al., *Comput. Geosc.* 20, 849, 1994  
El-Arini et al., *Proc. Int. Beacon Sat. Symp.* 358, 1994  
Dremukhina et al., *J. Atmos. Sol. Terr. Phys.* 60, 1517, 1998

## GEODESY

- Jiancheng et al., *Manuscr. Geod.* 20, 265, 1995  
Hwang & Chen, *Geophys. J. Int.* 129, 450, 1997

**Table II.1.** List of works (including only those written in English) related to the spherical cap harmonic analysis technique as of December 2003 [J.M. Torta, personal communication]

Thanks to the almost total coverage of the Earth's surface, the measurements of the geomagnetic field during Magsat and Ørsted missions have been used to develop other regional anomaly field models, at national or continental scale. As example, vectorial data from Magsat satellite were used to model the anomaly field by means of SCHA over Spain [Torta, 1992], China [An *et al.*, 1992], Italy [De Santis *et al.*, 1990], Poland [Rotanova *et al.*, 2000], and over the complete European continent [De Santis *et al.*, 1989; Rotanova and Odintsov, 1999], whereas field values from Ørsted mission have been recently modelled over Southern Africa [Kotzé, 2001]. Haines [1985b] modelled also the vertical field measured by Magsat for latitudes above 40°N. In all cases, after a wide pre-process of the data to avoid different non-desired contributions to the measured field (those coming from the main, the external, and induced fields), the anomaly field was expressed as an expansion in spherical harmonics. Table II.2 shows a comparison of main features of all these models.

Author	Region	Half-angle $\theta_0$	$K_{\max}$	# coef.	$\lambda_{\min}$
An <i>et al.</i> [1992]	China	35°	12	169	1300 km
De Santis <i>et al.</i> [1989]	Europe	35°	15	256	1000 km
De Santis <i>et al.</i> [1990]	Italy	7°	9	100	330 km
Haines [1985b]	Lat > 40°N	50°	22	190	1000 km
Kotzé [2001]	South Africa	20°	7	58	1200 km
Rotanova and Odintsov [1999]	Europe	40°	18	361	1000 km
Rotanova <i>et al.</i> [2000]	Poland	12°	6	49	850 km
Torta [1992]	Spain	16°	10	88	685 km

**Table II.2.** Main features of different magnetic anomaly field models developed by using SCHA

Main field models often mix with those models for magnetic anomalies. This is due to the fact that, as pointed out by Haines [1985a,b], it is physically and mathematically advantageous to remove a global reference field (for example, the IGRF model) to the input data before modelling. From the first viewpoint, removing the contribution of the longer wavelengths means to minimise the loss of contribution of the highest degree harmonics to the field power spectrum. In practice it guarantees a faster convergence of the model to the input data. It is also used for

avoiding extremely high values with alternate sign of the coefficients of the model, as in An *et al.* [1994], where the modelling of observatory and repeat station values in Southeast Asia without previous subtraction of a reference field led to absolute values of the coefficients  $g_k^m, h_k^m$  up to  $10^6$  nT. In fact, these so-called “main field models” are often models of the residuals obtained after removing a reference field to an input data set. For example, this is the case of the model by De Santis *et al.* [1990] for Italy and surrounding areas where, previously to the modelling of near-surface and satellite data, the IGRF computed at 1985.0 was removed. The chosen cap for that model had a half-angle of  $7^\circ$  and the maximum spatial index  $K_{\max}$  was equal to 9, so the model was able to represent wavelengths as short as 330 km.

### Secular variation models

Secular variation models are necessary to reduce to a common epoch magnetic measurements from magnetic surveys carried out in different epochs, or to attempt to forecast the future (or past) values of the geomagnetic field. When developing a secular variation model, two are the strategies that can be adopted: the first consists in modelling the main field for several fixed epochs to compute afterwards the secular variation with these models; the second approximation is based on the modelling of the variation itself. This last procedure was adopted by Haines [1985c] to model the secular variation from the first differences of the North American observatory and repeat station annual means for 20 years. In this way a secular variation model formed by 39 statistically significant coefficients for a fourth-degree maximum spatial expansion and a second-degree temporal expansion was obtained, using a  $30^\circ$  half-angle cap. Korte and Haak [2000] used the same technique to model the first differences on the measurements taken from a set of European repeat stations, in the search for temporal variations in the magnetic anomalies (it is shown that anomaly values can change with time due to induced magnetic fields caused by the interaction between the variable magnetic field and the upper mantle [e.g., Rikitake, 1966]). Their model was developed for a  $18^\circ$  cap with  $K_{\max}=4$  and  $L_{\max}=0$ , and different models were developed starting from various sets of field differences at five-year intervals. Finally, Torta *et al.* [2002] used a  $30^\circ$  cap with  $K_{\max}=L_{\max}=4$  to obtain a set of 100 coefficients to represent the change of the geomagnetic field from 1960 to 1998 for Antarctica, using as input data the annual means from 25 observatories below  $60^\circ$  South latitude. The aforementioned main-field differences technique was used to generate this model.

The modelling of the secular variation field (or the main field itself) from a regional approach represents a problem since the secular change consists in a large-scale component, whereas the

regional techniques are designed to represent small-scale features. De Santis *et al.* [1996] proposed a way to reduce this inconvenient. They forced the gradient in colatitude of the secular variation described by the regional models to fit the values given by global models. Colatitude was chosen because global models like IGRF show a smooth behaviour with regard to the corresponding gradient. The validity of the approach was demonstrated by fitting three-component secular variation data over the Italian region. The authors showed therefore that a realistic regional model could be obtained when global constraints were introduced.

### Main field and secular variation models

Haines and Newitt [1986] developed the first complete model (in the sense of main field plus secular variation) using SCHA as the modelling technique. However the derivation of both fields was not simultaneous. The secular variation was fit independently to avoid the effect of crustal anomalies, and the main field model was obtained by integration later. Magsat satellite and aeromagnetic survey data were used after subtracting the IGRF 3<sup>rd</sup> generation model evaluated at 1985. The resulting model presented a maximum spatial index equal to 16 for the fixed main field and to 4 for the secular variation field, the last one with temporal degrees 1 to 3, using a spherical cap of 30° of half-angle.

A similar approach was that adopted by Torta *et al.* [1993] to model the field over Spain, since a preliminary secular variation model was computed to reduce all data to the same epoch, and the main field model was thereafter developed. The model was based on both satellite (Magsat) and ground (observatory and repeat station) data. The secular variation model was developed on a 45° half-angle spherical cap (the data were limited to a 16° cap), with maximum spatial index  $K_{\max}=4$  and temporal degree  $L_{\max}=2$ . The main field was previously modelled on a 8° half-angle spherical cap, but the non-uniform data distribution suggested the application of the translated origin spherical cap analysis approach (TOSCA, see next section for details), so the model was finally derived for a  $K=9$  expansion on a 30° half-angle translated origin cap.

The large size of the cap where the secular variation model was developed (45°) is a consequence of the results found by Torta *et al.* [1992]. The minimum degree  $n_k$  of a SCHA expansion for a small cap is higher than those typical of the secular variation field. There is therefore a lack of long wavelengths represented by the model. When the size of the cap is increased, lower values of  $n_k$  can be achieved and the resulting model presents a suitable harmonic content.

The updating of the Canadian geomagnetic reference field led Haines and Newitt [1997] to introduce several innovations in the model development. In this case both main and secular variation fields were modelled simultaneously by applying the main field differences method (see preceding section). The order of the temporal expansion was allowed to change depending on the spatial degree: in this way,  $L=7$  was taken for  $K=0$  and 1;  $L=3$  for  $K=2$  to 5;  $L=1$  for  $K=6$  and 7; and no temporal variation was applied to the coefficients with  $K=8$  to 16. This approach is in some way similar to the development of a model in which the coefficients that contribute to the main field can change with time (i.e. they present a secular variation) but not those related to the crustal field. Moreover, cosine functions were used as temporal functions instead of simple polynomials, since they have zero derivative at the limits of the time interval and extrapolation problems related to the high-order polynomials are so reduced.

The same approach as in Haines and Newitt [1997] was adopted by De Santis *et al.* [2002a] (and subsequently by Gaya-Piqué *et al.* [2004]) to introduce the first regional reference model for Antarctica. These models will be widely discussed in the next chapters, since they represent the starting point of this thesis.

### External field models and other studies

The works until now presented are related to the application of SCHA to the modelling of the internal fields. As seen in equations (II.7) and (II.8), the spherical cap harmonic analysis provides the theoretical possibility of an internal-external field separation, so the technique can give account of the currents that induce magnetic variations on the Earth's surface.

We can consider the work by Haines and Torta [1994] the first one in which SCHA is used to model the equivalent currents (i.e. those ionospheric and induced currents able to represent the measured variations of the geomagnetic field). A previous work by Walker [1989] contained some errors when deriving the SCHA formulations, and no mathematical development was given in other earlier study by Langel [1993]. The authors modelled the variations for a very quiet geomagnetic day to demonstrate the validity of the approach.

Torta *et al.* [1997] used at a later stage SCHA to separate the internal and the external parts of the field variation in order to investigate the behaviour of the solar quiet currents over Europe. As in Haines and Torta [1994], the regional pattern of the Sq focus and its temporal and spatial variations were properly represented. The movement of the ionospheric currents system was monitored in detail through the surface of the cap with temporal continuity.

Related to these studies, Torta and De Santis [1996] showed that even though SCHA demonstrated to be useful when representing the dynamics of the ionospheric current system at a regional scale (the overall contour pattern was well defined over the cap), the results were sometimes not reliable in the sense of a proper internal-external discrimination. In this way, SCHA turns to be only a mathematical tool when wavelengths of a given pattern are modelled using wavelengths with different inherent characteristics. That work proposed nevertheless the use of SCHA when the cap under study has a size similar to that of the area in which the geomagnetic variations take place.

Kotzé [2002] used recently SCHA to identify the external field when analysing Ørsted satellite total intensity field data over southern Africa. The external contributions were modelled as a general function in longitude and colatitude over the surface of the spherical cap. Satellite data were selected according to the external magnetic activity (to obtain a dataset perturbed as low as possible). IGRF-8 (based mainly on Ørsted measurements) was removed from the data, assuming therefore the resultant residuals to be largely due to external currents. The SCHA expansion of the function was truncated at  $K=1$ , so four coefficients were derived to give account of the external field at each satellite measurement location.

Despite the results obtained in the previously commented works, great care must be taken when using spherical cap harmonics to separate internal from external fields. The physical meaning and validity of the coefficients has to be checked, i.e. it is necessary to control if the internal (external) coefficients represent appropriately the internal (external) contribution of the field.

As an example for these facts, consider the situation in which a field with some known external contribution is to be modelled. With this aim, a grid of values for the magnetic field components, with well-known internal and external contributions, can be synthesised using the comprehensive model CM3 proposed by Sabaka *et al.* [2002]. A grid of 568 points located at the Earth's surface was built. The points were separated  $1^\circ$  in latitude and equally spaced in longitude. The magnetic field values, with known crustal and magnetospheric contributions, were computed at these points. A SCHA model can be therefore developed on a  $30^\circ$  half-angle cap using both internal and external coefficients. Since the crustal field of CM3 was defined by coefficients with degree  $n$  up to 45, a  $K=15$  is needed for the maximum expansion of the proposed spherical cap model, taking into account that for a  $30^\circ$  cap it represents a maximum degree value  $n_k=46.01$ . In this way both input data and SCHA model contain similar

wavelengths. The results of the fit of the different models to the input data in terms of root mean squares (RMS) are shown in table II.3.

Each model has been computed as follows. The input data in case A contained only crustal field without any external contribution, so the model developed was only formed by internal coefficients up to  $K_{\max}=15$ . Residuals (computed with regard to the same input file) are very low. For cases B-E the input crustal values were contaminated with a magnetospheric contribution, assuming a constant value for the Dst index [Mayaud, 1980] equal to 10. RMS fit is referred to the total values of the input data (internal plus external contributions) in scenarios B-C, but considering only internal coefficients for the case B, and internal and external coefficients with  $K_{\max}=2$  for the case C when synthesising the field. The fit is better for the case C, so it could be concluded that the inclusion of the external coefficients improved the model.

Case	Input data	Coefficients of the model	Fit to data	Fit using coefficients	RMS <sub>X</sub> (nT)	RMS <sub>Y</sub> (nT)	RMS <sub>Z</sub> (nT)
A	int	int	int	int	4.2	6.4	7.7
B	int+ext	int	int+ext	int	5.5	6.9	8.8
C	int+ext	int+ext	int+ext	int+ext	4.7	6.6	8.2
D	int+ext	int+ext	ext	ext	56.6	20.7	61.2
E	int+ext	int+ext	int	int	60.4	24.6	63.1

**Table II.3.** Root mean squares fit of different SCHA models to X, Y, and Z synthetic geomagnetic field values generated using CM3 [Sabaka *et al.*, 2002]. *int* refers to internal (data, coefficients), *ext* to external. See text for details.

Scenarios D and E were proposed using internal and external coefficients as in case C, but only external coefficients were used in case D and only internal coefficients for case E to synthesise the field. For the case D the model was directly compared to the known external contribution present in the input values, whereas for the case E the model was compared to the crustal part of the input data set. As can be seen in table II.3, the fits are dramatically worst than in the case in which both internal and external coefficients were considered as a whole. It means that the internal (external) coefficients are not representing properly the internal (external) field separately, but it is necessary to consider the total set of coefficients to represent accurately the data.



Examples like this must be taken into account when separating the different field contributions by means of spherical cap harmonic analysis. A similar result was previously found by Torta and De Santis [1996] when modelling the internal and external equivalent current functions over Europe: the internal and external parts of the regular geomagnetic daily variation were not properly separated by SCHA, in spite of a good representation of the overall field. Torta *et al.* [1992] also found that the use of internal and external coefficients improved the fit to the input data set that consisted in only dipolar (i.e. internal) data. As it will be shown in the next section, the internal-external separation can be improved if some considerations are taken into account when computing the associated Legendre functions.

To finish with this review about the practical applications of spherical cap harmonic analysis, De Santis and Torta [1997a] proposed SCHA to model the local gravity field. It followed a paper by Jiancheng *et al.* [1995] in which the application of SCHA to the gravity field was firstly proposed, but in an incorrect way.

### Theoretical works

As seen in table II.1, many papers have been written about the SCHA technique from a theoretical viewpoint. Lowes [1999a] demonstrated the orthogonality over the cap of the vector fields derived from spherical cap harmonic analysis with the same  $k - m$  parity, giving also expressions for their mean squares. It was also shown that any internal field is orthogonal to any external field for the SCHA case if the basis functions were both odd or both even.

A very interesting theoretical approach was that of De Santis *et al.* [1999b]. The authors discussed the relationship between the ordinary Legendre functions of the global harmonic analysis and the associated Legendre functions of non-integer degree. In this sense, the connection between ordinary and spherical cap coefficients was previously shown in equation (II.14). A special attention was given to the role of the term  $G_0^0$  of the SCHA expansion (the nomenclature given by the authors is followed here). The presence of the term  $g_0^0$  is not possible in ordinary spherical harmonics (it would imply the existence of magnetic monopoles). It is not the case for SCHA, so we can express this leading coefficient as an expansion in terms of zonal ( $m=0$ ) coefficients:

$$G_0^0 = \sum_{n=n_{min}}^{\infty} T_0^{0,n} g_n^0 \quad (\text{II.20})$$

Usually the summation is done from  $n_{\min}=1$  to a finite value. The removal of a reference model as IGRF before the application of SCHA corresponds to removing the terms from  $n=1$  to 10 (in case that a model previous to IGRF-9 is used), so  $n_{\min}=11$  in (II.20) and  $G_0^0$  is close to zero. An inadequate removal of long wavelengths can drive to too high values of this coefficient.

Two drawbacks arise from the lack of orthogonality of the basis functions in SCHA: it is in principle not feasible the application of any other numerical quadrature procedure than the least squares method [e.g. Press *et al.*, 1986] in the inversion procedure; and the impossibility to find an analogous expression to (I.16) for the power spectrum of the geomagnetic field.

Regarding the first problem, De Santis and Torta [1997b] (refined successively by De Santis *et al.* [in preparation]) introduced an integral matrix based approach to estimate the spherical cap harmonic coefficients from a uniform distribution of the vertical component of the geomagnetic field over a spherical cap. When the results are compared with those obtained by the use of the least squares inversion method, this integral approach seems to show a better stability and efficiency, especially when some Gaussian noise is added to the data.

For the second problem, De Santis [1998] proposed an approach based on an iterative application of the spherical cap harmonic analysis technique, taking advantage of the orthogonality of the basis functions inside each set of functions. The potential is thus defined in an iterative way, taking each time only one set of basis functions, and approximating the residual of the solution by using the other set of basis functions recursively in successive steps. This iterative approach is continued until the residual is small enough, moment in which the final potential can be approximated by a sum of the two sets of coefficients used (even and odd). As the functions inside each one of these summations are orthogonal, it can be introduced the concept of regional power spectrum of the geomagnetic field using an expression similar to (I.16). Implications that can be for example derived are the knowledge of the power spectrum content of North and South hemispheres in search of an hemispheric asymmetry that could be related to turbulent movements in the outer core, or the possibility to compute the total energy content for a given surface from a regional model.

The extrapolation of a spherical cap harmonic model outside the boundary of the cap leads to large errors in the determination of the field values, because by definition the basis functions of the potential expansion are only orthogonal within each even or odd set into the spherical cap. Problems can also appear at the edge of the region of validity if the distribution of data inside the cap is far from uniform. To solve these difficulties, De Santis [1991] proposed a translated origin

spherical cap harmonic analysis (TOSCA). This method consists of an ordinary spherical cap harmonic analysis in which the origin of coordinates has been moved from the centre of the Earth to another location along the vertical axis. The application of this approach for the case of Italy corrected some spurious border effects that appeared in a previous model [De Santis *et al.*, 1990] when normal SCHA technique was used. TOSCA was also successfully applied by Torta *et al.* [1993] to overcome fictitious oscillations of the modelled field components over Spain due to the non-uniform ground data distribution.

Another improvement to the conventional SCHA technique was introduced to adjust conventional spherical harmonics to a spherical cap after an artificial enlargement of the colatitude to that of a hemisphere is done. This innovation was called adjusted spherical harmonic analysis [ASHA; De Santis, 1992].

Finally another study about the late developments proposed to improve SCHA and about the main limitations of the method was carried by De Santis and Falcone [1995]. In addition to the discussion of some of the innovations to the original technique just detailed, the main point of this work was the study of the radial dependence of the field values in SCHA. Following this study, it is shown that there is a sort of expansion in the radial function, considering the expansion in SCHA similar to that one in ordinary spherical harmonics:

$$f(r) = \sum_{k=0}^{\infty} \sum_{m=0}^k a_k^m \left( \frac{R}{r} \right)^{n_k(m)+1} = \sum_{n=0}^{\infty} a_n \left( \frac{R}{r} \right)^{n+1} \quad (\text{II.21})$$

The authors proposed that a deep investigation of the radial variation of the field would be fundamental to separate accurately the internal and external contributions to the magnetic field.

### II.3. Limitations of SCHA

Although SCHA has been widely used to model potential fields at a regional scale because of the many advantages offered by the technique and the good results obtained, there are nevertheless some limitations inherent in SCHA. The main problems, besides the lack of orthogonality of the basis functions before commented, are found for the representation of wavelengths longer than the area covered by the data, the radial extrapolation of the field, and the theoretical aspects involved in the internal-external separation.

The modelling of long-wavelength fields (secular variation field, solar quiet variation) using small caps becomes difficult, as shown by Torta [1992]. As said in section II.2 when discussing about the main field and secular variation models, the lowest values of  $n_k$  for small caps lead to

wavelengths lower than those which are intrinsic to the field to be modelled. The fit of a field with low harmonic content by using higher harmonics would be only possible in case of an infinite expansion of terms. Since this is not possible, and taking into account that the minimum  $n_k$  values decrease as the half-angle of the spherical cap increases, the usual solution adopted has been to increase the size of the cap [e.g. Torta *et al.*, 1992], so the resulting model has a reliable spectral content. The cap can not be nevertheless enlarged ad infinitum: the non-orthogonality of the basis functions and the numerical instabilities when solving the least-squares matrix to obtain the model coefficients limit the size of the cap [Torta and De Santis, 1996].

The high values of  $n_k$  can also affect the radial variation of the SCHA. As pointed out by F.J. Lowes [personal communication], the fact that the potential depends on the radial distance as  $r^{-(n_k+1)}$  for internal fields and as  $r^{n_k}$  for external contributions means that an intrinsically slow varying field is fitted with rapid varying functions for high  $n_k$  values. Regarding the problem of the upward continuation of the field, Haines [1985a] showed that the fit of a SCHA model to a synthetic input dataset deteriorated with altitude. Moreover, the differences increased inward from the border to the centre of the cap with increasing heights. The misfit is important outside the height range of the input data, since the SCHA represents the best least-squares solution inside the dominion of the data.

The third main problem raises in the separation of the fields from internal and external origins. As remarked by Lowes [1999b], the internal-external separation involves essentially a separate analysis for the horizontal and vertical parts of the field. Since the X and Y components of the magnetic field are obtained as the derivatives with respect to the colatitude and longitude, respectively, the fit to the horizontal components is equivalent to the fit to the scalar potential, whereas the analysis of the vertical component Z, obtained as the radial derivative of the field, involves a fit to the radial derivative of the potential. Mathematically these relationships are expressed (at Earth's surface, i.e.  $r = a$ ) as:

$$\begin{aligned} X &= \frac{1}{a} \frac{\partial V}{\partial \theta} = \sum_{n=1}^N \sum_{m=0}^n [(g_n^{m,int} + g_n^{m,ext}) \cos m\phi + (h_n^{m,int} + h_n^{m,ext}) \sin m\phi] \frac{dP_n^m(\cos \theta)}{d\theta} \equiv \\ &\equiv \sum_{n=1}^N \sum_{m=0}^n [g_n^m \cos m\phi + h_n^m \sin m\phi] \frac{1}{n} \frac{dP_n^m(\cos \theta)}{d\theta} \end{aligned} \quad (\text{II.22})$$

$$\begin{aligned} Y &= -\frac{1}{a \sin \theta} \frac{\partial V}{\partial \phi} = \sum_{n=1}^N \sum_{m=0}^n [(g_n^{m,int} + g_n^{m,ext}) \sin m\phi - (h_n^{m,int} + h_n^{m,ext}) \cos m\phi] \frac{m P_n^m(\cos \theta)}{\sin \theta} \equiv \\ &\equiv \sum_{n=1}^N \sum_{m=0}^n [g_n^m \sin m\phi - h_n^m \cos m\phi] \frac{m}{n} \frac{P_n^m(\cos \theta)}{\sin \theta} \end{aligned} \quad (\text{II.23})$$

$$\begin{aligned}
 Z = \frac{\partial V}{\partial r} &= \sum_{n=1}^N \sum_{m=0}^n \left[ (ng_n^{m,ext} - (n+1)g_n^{m,int}) \cos m\phi + (nh_n^{m,ext} - (n+1)h_n^{m,int}) \sin m\phi \right] P_n^m(\cos \theta) \equiv \\
 &\equiv \sum_{n=1}^N \sum_{m=0}^n \left[ G_n^m \cos m\phi + H_n^m \sin m\phi \right] P_n^m(\cos \theta)
 \end{aligned} \tag{II.24}$$

where the new coefficients are expressed as:

$$g_n^m \equiv n(g_n^{m,int} + g_n^{m,ext}), \quad h_n^m \equiv n(h_n^{m,int} + h_n^{m,ext}) \tag{II.25}$$

$$G_n^m \equiv ng_n^{m,ext} - (n+1)g_n^{m,int}, \quad H_n^m \equiv nh_n^{m,ext} - (n+1)h_n^{m,int} \tag{II.26}$$

Therefore, the Gauss coefficients that describe the internal and external parts of the field can be expressed as:

$$g_n^{m,int} = \frac{(g_n^m - G_n^m)}{2n+1}, \quad h_n^{m,int} = \frac{(h_n^m - H_n^m)}{2n+1} \tag{II.27}$$

$$g_n^{m,ext} = \frac{(n+1)g_n^m + nG_n^m}{n(2n+1)}, \quad h_n^{m,ext} = \frac{(n+1)h_n^m + nH_n^m}{n(2n+1)} \tag{II.28}$$

The Gauss internal and external coefficients would be also obtained by a combined analysis of all three components. For small caps, it is not possible to represent simultaneously the horizontal and the vertical parts of the field with the same accuracy [Torta, 1992]. Moreover, the solution of this double analysis does not satisfy necessary the Laplace equation, since SCHA would give different solutions for both analysis. On the other hand, the common fit of all three XYZ components gives a potential solution of Laplace equation, but this fit is usually less precise than the separate fit of the horizontal and vertical components; for example, it has been shown in table II.3 that the inclusion of external coefficients improved the fit to only internal data. So it is obvious that the errors can be too significant when doing an internal-external separation.

The three main theoretical problems presented in this subsection do not have too much significance in the development of the model presented in this thesis. The size of the cap where the model was developed is large enough to avoid the problems related to the spectral content represented by the coefficients. The data used is distributed from sea level to satellite altitudes, and the model presents a smooth behaviour in that range, as it will be shown in next chapters. Finally, the present model does include only internal coefficients. However, although good results were presented in the last section, the drawbacks presented here have to be always kept in mind when using spherical cap harmonic analysis.

#### II.4. Calculus of the associated Legendre functions

Though it is not a drawback inherent in the SCHA theory, the computation of the associated Legendre functions presents a problem when using the original approach proposed by Haines [1988]. The calculation of  $P_n^m(\cos\theta)$  through relation (II.15) becomes difficult due to the large range in the size of the power series, specially for large values of colatitude or degree, so it is not an easy task to achieve the desired accuracy when developing the summation. The code proposed in the original form of SCHA, in Fortran language, encountered often failures due to overflow and underflow when computing the summation. Figure II.1 shows an example of the kind of problems we can find when the required accuracy is not reached. In figure II.1a there is an error on the computation of the Legendre functions, given a degree  $n$ , for high values of the colatitude. On the other hand, figure II.1b shows how high values of the degree can lead to inconsistent values of the associated Legendre functions for a fixed colatitude.

As suggested by Thébault *et al.* [2002], a more stable way to compute the values of the associated Legendre functions is the one proposed by Olver and Smith [1983]. This algorithm was developed employing extended-range arithmetic subroutines, a software extension of ordinary floating-point arithmetic that greatly increases the exponent range of the represented numbers. The increased exponent range is achieved by allocating a separate integer storage location to the exponent of each floating-point number, and subsequently the computed associated Legendre function values are returned to ordinary floating-point values when possible. A demonstration of the validity of this method is shown in figures II.2a and II.2b, which are equivalent to II.1a and II.1b but generated using the Olver and Smith procedure.

The improvement in the computation of the associated Legendre functions has great implications. As said before, the maximum degree of a SCHA expansion depends both on the maximum spatial index of the expansion and on the size of the cap. Given an order  $m$ , the root  $n_k(m)$  is bigger for small caps. On the other hand,  $n_k$  increases as the maximum index for the spatial expansion does (for a spherical cap of fixed size). The possibility of computing the values of the spherical harmonics for any colatitude or degree  $n_k$  can be of big utility when separating the geomagnetic field in its internal and external parts, avoiding the problems previously shown.

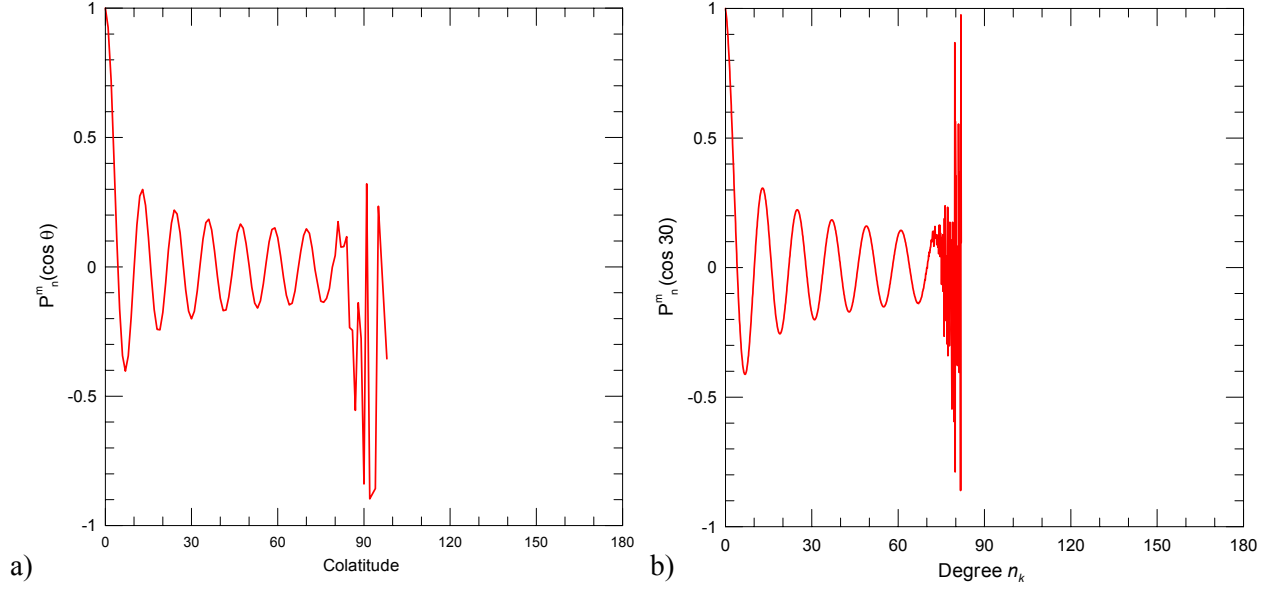


**Figure II.1.** Associated Legendre functions computed following Haines [1988] subroutines a) as a function of colatitude for  $m=0$ ,  $n_k=30.9606$ , and b) as a function of the degree  $n_k$  given a colatitude  $\theta=30^\circ$ . There is a lack of convergence of the series in both cases that leads to incorrect values of  $P_{n_k}^m$ .

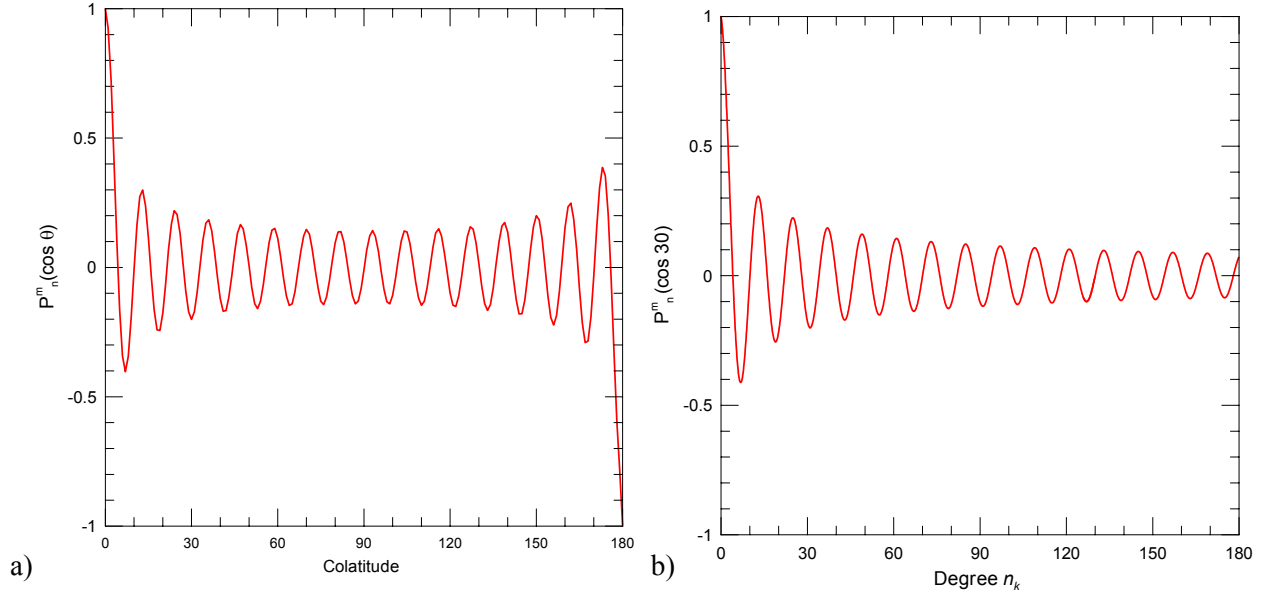


**Figure II.2a and II.2b.** As figure II.1a and II.1b but the associated Legendre functions being now computed following Olver and Smith [1983] subroutines.

The use of the Olver and Smith method and the increase in the precision when computing the values of  $n_k$  (the original Fortran code for the spherical cap analysis of Haines [1988] used single precision, whereas double precision has been actually adopted), are the starting point for the improvement of the SCHA computation. In what follows two examples are presented to check the validity of this affirmation.

The first test was done using as input data a snapshot of the crustal and primary (not induced) ionospheric and magnetospheric contributions of the CM3 model for a fixed time. A grid of 568 points was created, equivalent to that introduced in the last section to check the ability of SCHA to fit independently the internal and external fields. Magnetic field values were synthesised at these points for a common epoch and time. The spherical cap model, developed using a  $30^\circ$  half-angle cap, presented a good fit to the total input data and also a good internal-external separation when going up to  $K_{\max}=60$  for the internal expansion of the potential and  $L_{\max}=20$  for the external one. Only one set of basis functions was used (it means that the basis functions are completely orthogonal), and the value of the maximum degree  $n_k$  implied was around 180. The use of high values of  $K_{\max}$  allows for a good internal-external separation when the cap is large or the field is highly structured, which can imply better horizontal and vertical extrapolations. The fit was rather good for all three components of the field and for all contributions, as can be seen in figures II.3 to II.5.

The second test was a revision of the work from Torta and De Santis [1996]. A synthetic grid of 50 values equally distributed on a  $18^\circ$  cap was created using the Sq model from Malin and Gupta [1977]. For each point an hourly value was computed, so 1200 input values (50 points x 24 values per point) were synthesised to give account of the diurnal variation of this field over the European region. Fits to input data were approximately the same as found by Torta and De Santis for the case of a  $18^\circ$  cap with  $K_{\max}=L_{\max}=5$  for both internal and external expansions (see figure 1 from their paper).

As in the case of the 1996 paper, the results improved dramatically when enlarging the cap, and the separation of the internal and external contributions reached an acceptable accuracy; a cap of  $60^\circ$  (with data only for the most internal  $18^\circ$ ) thus provided a good internal-external separation. The equivalent currents presented a more similar pattern to that obtained by gridding the input data, without oscillations at the border of the  $18^\circ$  area in which input data were available. Moreover, on the contrary to Torta and De Santis [1996] paper, bigger the cap better the fit. A cap of  $180^\circ$  (i.e. an SHA) with data from only the first  $18^\circ$  gave a percentual error lower than 10% for the external data, lower than 20% for the internal contribution, and near to zero for the total field for a  $K_{\text{int}} = K_{\text{ext}} = 8$ , expansion with temporal degree equal to 8 using Fourier series as temporal basis functions.



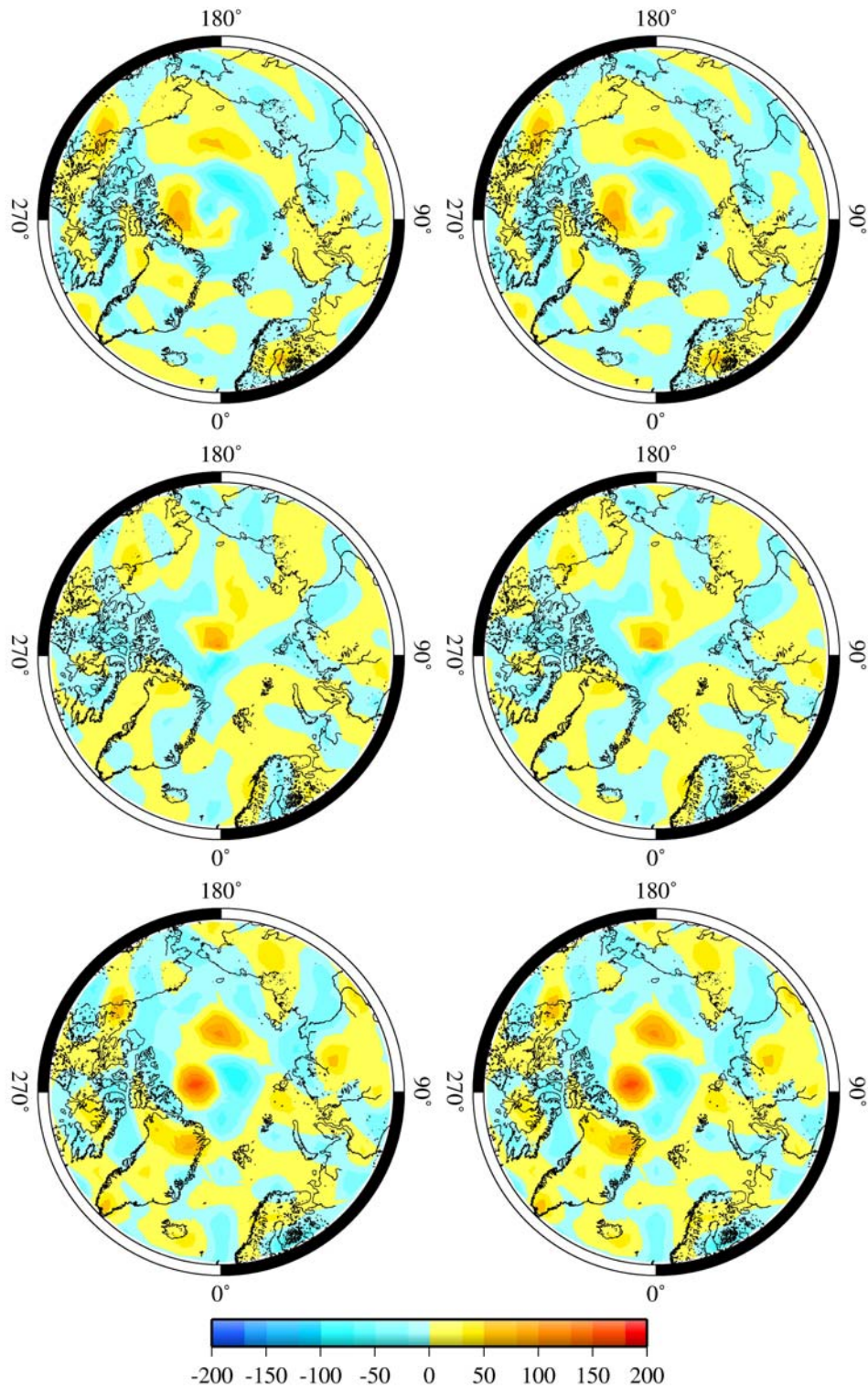


**Figure II.3.** Left: X (top), Y (center), and Z (bottom) components of the crustal and external magnetic fields given by CM3 model for a fixed time, and used as input data for the development of a SCHA model. Right: as left but for the field computed using the SCHA model. See text for details.

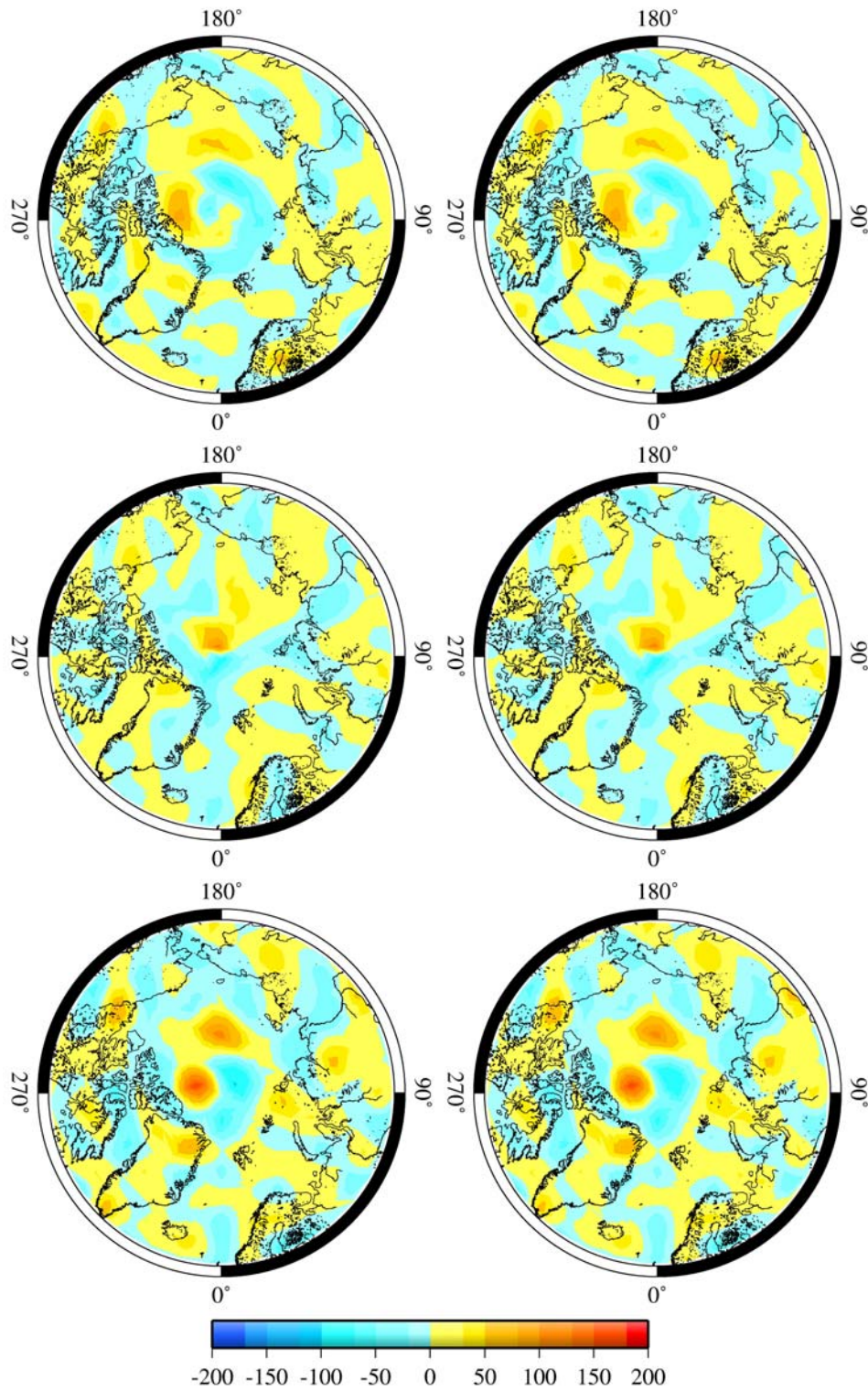


**Figure II.4.** Left: X (top), Y (center), and Z (bottom) components of the crustal magnetic field given by CM3 model, and used as input data for the development of a SCHA model. Right: as left but for the field computed using the SCHA model. See text for details.



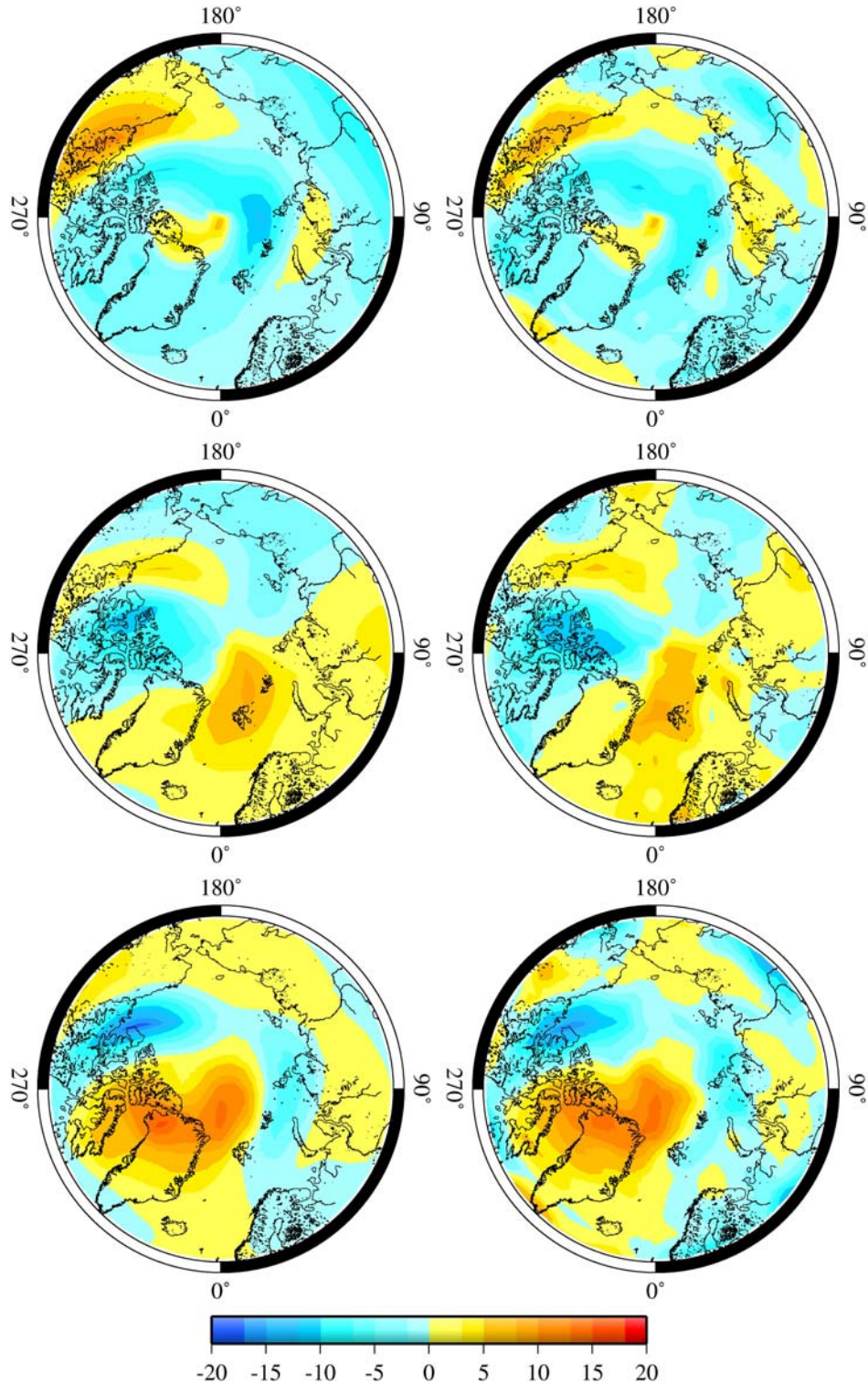


**Figure II.5.** Left: X (top), Y (center), and Z (bottom) components of the primary (not induced) external magnetic field produced by CM3 model for a fixed time, and used as input data for the development of a SCHA model. Right: as left but for the field computed using the SCHA model. See text for details.

The in-depth review of the SCHA made in this chapter has consented for a better understanding of the technique. The description of the main problems presented by the technique has been useful to put some light on the limitations that the developed model could present. The thorough study of the virtues and drawbacks of SCHA has allowed, for instance, to test procedures for the development of harmonic expansions on spherical cap to higher degrees than those presently reached. This fact means in practice that the fit to an input field can be improved, for example, in case an internal-external separation is needed. At the moment and in what follows, and due to the different nature of the data used (see next section), it was preferred to develop a SCHA model using only internal expansion for the potential, leaving for the close future the use of both internal and external coefficients.

### **III. Data Description and Selection**

#### **III.1. Introduction**

As discussed in the previous chapters, spherical cap harmonic analysis allows surface data (from ground observatories and repeat stations) to be combined with near-surface surveys (aeromagnetic or balloon) and with satellite measurements, without the necessity of reduce the data to a common altitude before modelling. This was decisive in choosing this regional technique of analysis as the approach to model the geomagnetic field, together with the fact that the Antarctic region has an almost circular form, and data taken at different altitudes resemble a spherical cap.

The main problems with the Antarctic observatory database are the lack of temporal continuity and the inhomogeneous spatial distribution of the observatories. Although the East Antarctic sector (Indian Ocean) has been well covered, at least near the coastline, by several observatories in operation during overlapping periods during the last forty years, they are scarce in the Southwest sector (Pacific Ocean - Amundsen Sea); and the situation is extreme for the South polar cap. In oceanic regions only regional and restricted in time measurements from marine surveys are sometimes available. Magnetic data collected during satellite missions bridge all these gaps.

The Antarctic reference model developed using a combination of different satellite missions with surface and near-surface data will be presented in the next chapter. Since one of the main utility of the model is the reduction of magnetic surveys to a common epoch, data coming from aeromagnetic or marine campaigns were not included to develop the model in order to guarantee its independence. On the contrary, data coming from a stratospheric balloon have been considered. Special attention will be paid to this mission since it constitutes an unknown set of data. In what follows, description of the data used and the different criteria adopted to select these data sets are discussed.

#### **III.2. Observatory data**

##### **Introduction**

The deployment and maintenance of manned observatories in Antarctica are difficult due to the logistic problems coming from the weather conditions and the remoteness of the continent. The situation is particularly difficult for geomagnetic observatories. The hostile conditions keep

scientists from running and maintenance of a conventional observatory, and in this way most of the Antarctic observatories can not be considered as a standard Intermagnet observatory [e.g. Kerridge, 2001]. For example, the fact that several Antarctic bases are only in operation during Austral summer limits the development of absolute magnetic measurements to few months per year, as in the case of the Livingston observatory in the neighbourhood of the Juan Carlos I Spanish Antarctic Base [Torta *et al.*, 1999], so the determined baselines are sometimes not completely reliable. In most cases the location where a geomagnetic observatory is installed is not the best site possible, but the only available option within a poor range of possibilities, limited usually to the Antarctic coast. Moreover, observatories on the ice shelf must be relocated periodically due to the motion of the site, so it is not surprising to find geomagnetic stations with a number attached to the IAGA code [McLean *et al.*, 1995] to identify the spatial shifting of the same observatory.

Nevertheless, the arrival of the International Geophysical Year (IGY) in 1957-1958 asked for an effort to increase the human presence in Antarctica. The IGY was designated to collect and share data on the Earth's natural phenomena, between them the geomagnetic field. The 1957-1958 interval was selected because in this way scientists could study the geophysical phenomena during a period in which the solar activity was known to be maximum. More than 10,000 scientists from 67 countries participated in the program, and as a result more than 40 stations were established on the Antarctic Continent and sub-Antarctic islands, some of them supporting a geomagnetic observatory to give account of the geomagnetic field at the South polar cap. The main importance of this ensemble of observatories is therefore the capability of monitoring the geomagnetic secular variation almost for the last forty-five years.

### Geomagnetic Observatories South of 60°

Around 25 geomagnetic observatories (without considering relocations of a same observatory) have been operating below 60° South latitude since 1960 to date. 1960 was selected as the beginning year of this study because in this way the model gives account of the secular variation for the years immediately after the IGY, when the number of magnetic surveys also increased. The amount of Antarctic data before 1960 is poor, as can be seen in the big compilation of the near-surface magnetic surveys developed in Antarctica done by Golinsky *et al.* [2001] in the framework of the ADMAP project. The only magnetic data in this compilation before 1960 correspond to a marine survey in the Southwest Indian Ocean in 1958, and the measurements from the Project Magnet of the US Navy are very few [Chiappini *et al.*, 1999].

The geographical distribution of the observatories used in this work is shown (using the 3-letter IAGA code) in figure III.1, and more details for each observatory are given in table III.1. The observatories presented in this table are ordered following their geographic latitude. The respective geomagnetic coordinates were obtained for epoch 2000.0 using the first three coefficients of the IGRF-8 to compute the position of the geomagnetic poles and then obtaining the corresponding geomagnetic latitudes and longitudes. The data intervals correspond to the first and last available annual means (dated January 2003) for each observatory at the World Data Center (WDC) for Geomagnetism in Edinburgh. The WDC system was also a result of the IGY, intended to acquire, store, and distribute several kinds of environmental data [Rishbeth, 1991]. The Edinburgh WDC, supported by the British Geological Survey, appears to present the most up to date data with respect to other Centers.

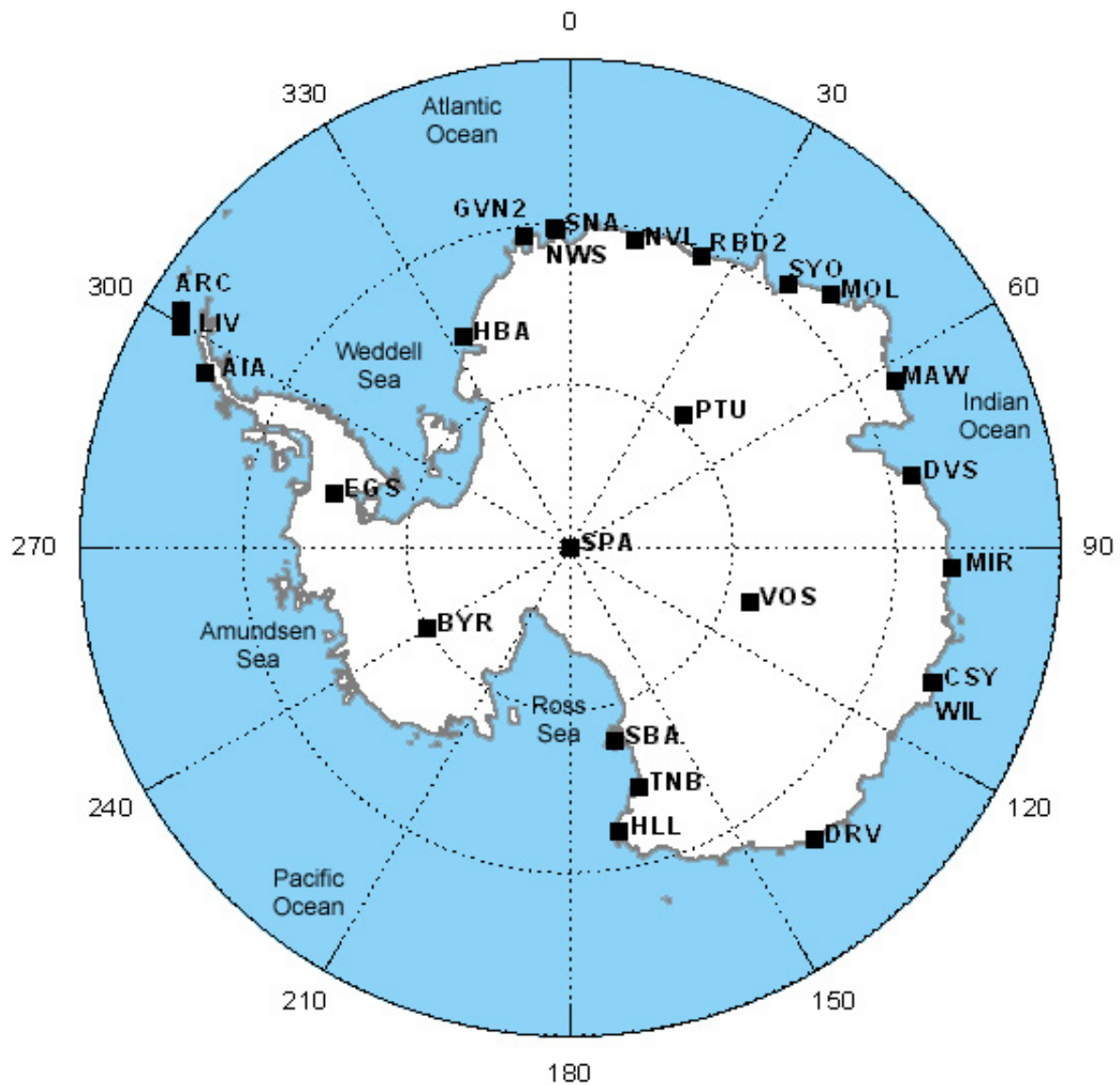


**Figure III.1.** Geographical distribution of the studied observatories (identified by 3-letter IAGA codes).

IAGA code	Observatory	Geographic (°)		Geomagnetic (°)		Altitude (m)	Data Interval
		Latitude	Longitude	Latitude	Longitude		
ARC	Arctowski	-62.167	301.517	-51.913	9.870	16	1978.8-1995.5
LIV	Livingston	-62.667	299.600	-52.357	8.376	19	1997.0-2002.0
AIA	Argentine Islands	-65.250	295.733	-54.853	5.306	10	1960.5-2000.5
WIL	Wilkes	-66.250	110.583	-76.695	183.773	10	1960.5-1966.5
CSY	Casey	-66.283	110.533	-76.729	183.689	40	1978.5-2001.5
MIR	Mirny	-66.550	93.017	-76.362	153.352	20	1960.5-2000.5
DRV	Dumont D'Urville	-66.667	140.017	-74.624	231.486	30	1960.5-2002.5
MAW	Mawson	-67.600	62.883	-73.262	109.182	3	1960.5-2001.5
MOL	Molodyozhnaya	-67.667	45.850	-70.286	89.288	854	1965.5-1998.5
DVS	Davis	-68.583	77.967	-76.560	127.206	0	1979.4-2000.5
SYO	Syowa	-69.000	39.583	-70.313	82.791	15	1960.5-2001.5
SNA1	Sanae 1	-70.300	357.633	-64.703	47.519	50	1962.7-1970.5
SNA2	Sanae 2	-70.300	357.417	-64.675	47.362	50	1971.7-1978.5
SNA3	Sanae 3	-70.317	357.417	-64.690	47.346	50	1980.5-1989.5
RBD2	Roi Baudouin 2	-70.433	24.300	-68.878	67.597	39	1964.7-1966.5
NWS	Norway Station	-70.500	357.467	-64.865	47.212	80	1960.5-1961.5
GVN2	Neumayer Station	-70.667	351.733	-64.282	42.968	0	1993.6-2000.5
NVL	Novolazarevskaya	-70.767	11.817	-67.164	57.473	460	1961.5-1987.5
HLL	Hallett	-72.300	170.317	-74.331	-83.186	0	1960.5-1962.5
TNB	Terranova Bay	-74.683	164.117	-77.287	-82.523	28	1987.1-1999.0
EGS	Eights	-75.233	282.833	-64.805	-3.347	450	1963.7-1965.4
HBA	Halley Bay	-75.517	333.400	-66.929	26.812	30	1960.5-1980.5
SBA	Scott Base	-77.850	166.783	-78.933	-68.979	10	1964.5-2002.5
VOS	Vostok	-78.450	106.867	-88.868	163.969	3500	1960.5-2001.5
PTU	Plateau	-79.250	40.500	-78.196	57.670	3620	1966.5-1968.5
BYR1	Byrd Station 1	-79.983	240.000	-71.342	-24.002	1515	1960.5-1961.5
BYR2	Byrd Station 2	-80.000	240.512	-71.320	-23.728	1515	1962.5-1968.3
SPA	Amundsen-Scott	-90.000	346.683	-79.542	0.000	2800	1960.5-1971.5

**Table III.1.** Geographic and geomagnetic coordinates of the Antarctic observatories used to develop the model ordered according to the geographic latitude, and interval for which annual means are available.



The data used to generate the model that will be presented in the next chapter as the final result of this work are the annual means. The use of annual mean values guarantees a minimal contamination of the observatory data by external field: rapid variations disappear, and the effect of diurnal variations is minimised. In order to reduce even more the contribution of ionospheric and magnetospheric currents from the observatory values, other modellers proposed another kind of approach in the use of surface data. For example, Olsen *et al.* [2002a] used local midnight data during geomagnetic quiet days, a similar approach to that one of Sabaka *et al.* [2002] for the CM3, and Olsen [2002] proposed a linear estimation from local midnight observatory values during quiet periods to constrain the secular variation. Langlais and Manda [2000] used observatory monthly means to propose a candidate secular variation model for the IGRF 8<sup>th</sup> generation. Unfortunately, the lack of most of the Antarctic observatory monthly data makes almost compulsory the use of annual means, as will be shown later.

The observatories presented in table III.1 were not working simultaneously; it is moreover difficult to find a temporal overlapping of two or more observatories for many regions of Antarctica. The temporal distribution of the annual means used to generate the model is shown in figure III.2, where the observatories geographical latitude increases as the Y axis decreases.

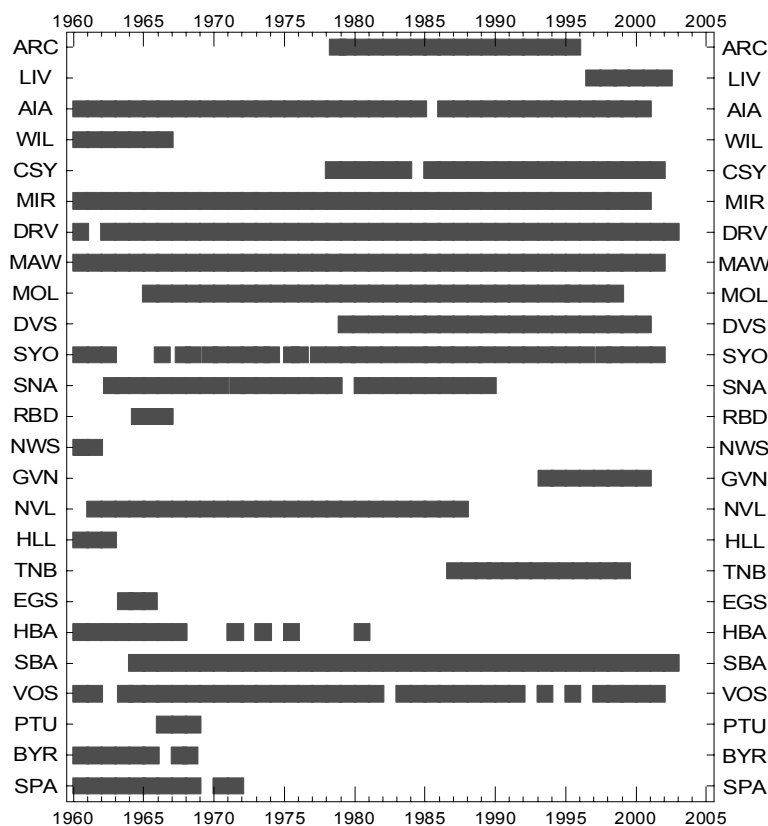


**Figure III.2.** Temporal distribution of the observatory annual means used to develop the model.

From the last table and figure, it is clear that the data distribution is not so good as would be desirable. The Antarctic continent can be divided into four longitudinal sectors to discuss in detail the distribution of annual means:

- a) East Antarctica – Indian Ocean sector (longitudes between  $0^{\circ}$  and  $90^{\circ}$  East): the coastline is well covered by three observatories that worked during almost the whole interval of the study (MAW, MOL, and SYO), and two stations that operated for more than 20 years (NVL from the sixties to the end of the eighties, and DVS from the eighties and still in operation). Only three annual means are available from RBD2 (1964.7 to 1966.5), whereas the inner continent is poorly represented by just one observatory, Plateau (PTU), which operated for only three years at the end of the sixties.
- b) East Antarctica – Australian sector (longitudes between  $90^{\circ}$  and  $180^{\circ}$  East): it is the best-covered sector, since three well-spaced observatories along the coastline (MIR, DRV, and SBA) and one inner observatory (VOS) present approximately 40 annual means. Other four observatories (CSY, WIL, HLL, and TNB) contribute with series of data that go from 3 (HLL) to 24 (CSY) annual mean values.
- c) Amundsen Sea - Pacific Ocean sector (longitudes between  $180^{\circ}$  and  $270^{\circ}$  East): only one observatory, Byrd, is located at this sector. It suffered a spatial relocation, so only two annual means (1960.5 and 1961.5) for BYR1, and other six for BYR2 the years immediately after are available for the considered period. It is thus the worst covered sector.
- d) Weddell Sea – Atlantic Ocean sector (longitudes between  $270^{\circ}$  East and  $0^{\circ}$ ): the sub-Antarctic islands near the Antarctic Peninsula house three observatories that jointly cover the whole period of study (ARC, AIA, and LIV; the last one is operated by Ebre observatory [e.g. Torta *et al.*, 2001]). The most Eastern part of this sector presents other three observatories (NWS, GVN, and SNA, these last two with their respective relocations) that gives account of the complete time interval. The situation is not so good for Southern latitudes, being only available three annual means for EGS and 12 for HBA, all them before the eighties.

To end with this review of the available data, the observatory placed at the South Pole, SPA, contributes to the model with 11 annual means from 1960.5 to 1971.5. The inhomogeneous distribution of the annual means and the lack of continuity of the temporal series recommend the

use of a method like that of main field differences presented in section II.1 to represent the secular variation field.

All the series of annual mean values were visually inspected to avoid erroneous values. The most common problems were the presence of some spurious values, or spikes, due to different causes. As an example, we can consider the Australian geomagnetic station Casey (CSY). The annual means from 1978.5 to 1991.5 were computed only using absolute measurements (i.e., without a variograph or an automatic station). This fact implies that the annual means do not follow a more or less regular secular variation pattern before 1992, as reflected in figure III.3, where the values of X, Y, Z, and F magnetic elements for CSY are presented. The final decision was not to consider the annual mean values for 1981.5 and 1989.5, because they differed too much from the trends described by the other values.

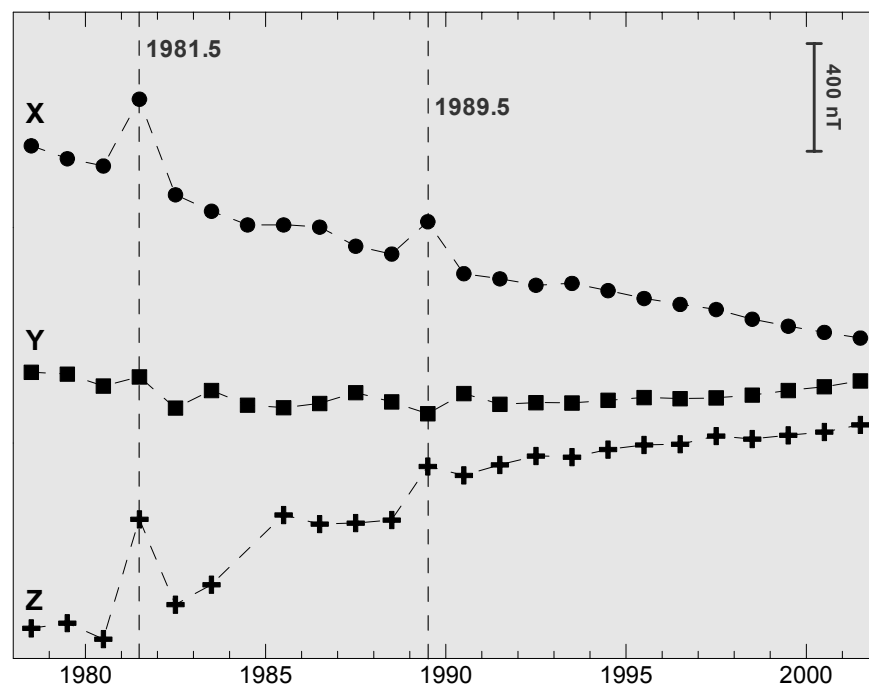


**Figure III.3.** Temporal behaviour of the annual means of X, Y, and Z magnetic components for Casey observatory. Note the spurious values for 1981.5 and 1989.5 annual means.

A different problem was the one related to Mirny Station (MIR). This observatory was relocated in December 1988, but the coordinates of the new location were not given to the WDC, and no information has been obtained after direct contact with the responsible of the observatory. The problem represents an analogous situation to that of a hypothetical existence of a different observatory before (we can say, MIR1) and after (MIR2; values in grey in figure III.4) year 1989, but with the same spatial coordinates for both of them.

To solve the problem, the annual mean values for 1989.5 for each element were computed by extrapolation assuming an autoregressive secular variation approach. This method was preferred to the usual way of connecting both series (those before and after the change epoch), i.e. the addition of a constant quantity (usually computed as a mean value) to all the measurements after the epoch to join both temporal series in a reasonable way. The autoregressive method seems to provide a good estimation of the secular variation applied to many temporal series from different observatories [e.g. De Santis *et al.* 2003].

In this method, the annual mean of a given element for a certain epoch,  $E_t$ , is related to the  $m$  previous annual means by imposing the following equality:

$$E_t = k_0 + k_1 \cdot E_{t-1} + k_2 \cdot E_{t-2} + \dots + k_m \cdot E_{t-m} \quad (\text{III.1})$$

where coefficients  $k_0, k_1, \dots, k_m$  are estimated by least squares. Regressions of different order  $m$  were made for the case of Mirny observatory, and  $m=4$  was finally decided because the corresponding autoregressive model showed a better *rms* fit with respect to the data before 1989. After obtaining this synthetic value for 1989.5, the difference between it and the real value was applied to the real data after 1989 for all components. The final results obtained for the values of Mirny are shown in figure III.4.

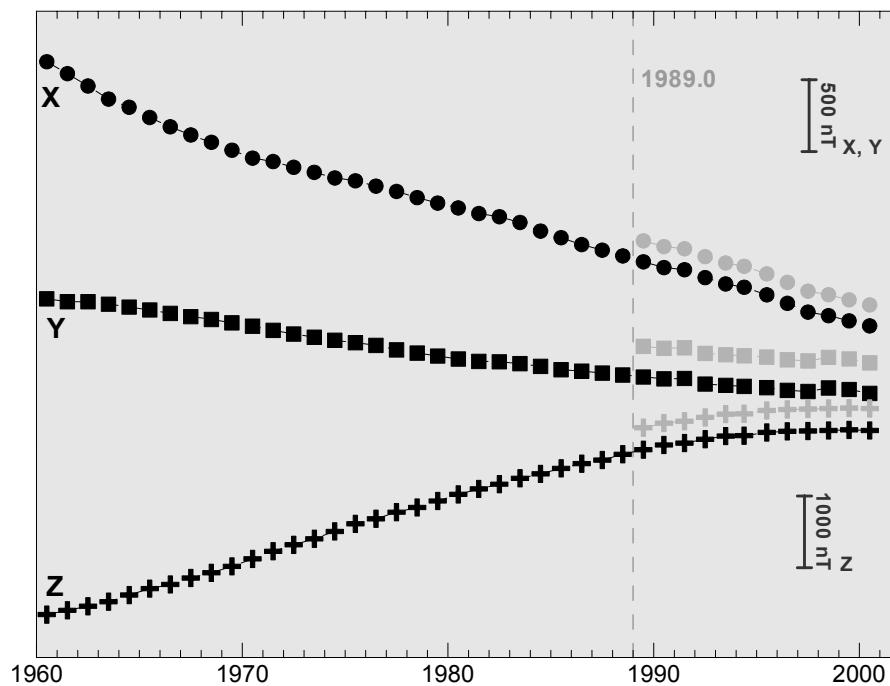


**Figure III.4.** Temporal behaviour of the corrected annual means of X, Y, and Z magnetic components (black) for Mirny observatory. The jump in the original values (grey) for 1989 is disappeared.

The use of observatory monthly means instead of annual means has also been checked. It must be kept in mind that most of the Antarctic territory is illuminated by the sunlight for half of the year in Austral summer. Ionospheric and magnetospheric field amplitudes are therefore seasonal dependent, being the external field influences more important for summer season. The selection of monthly means corresponding only to the Austral winter can help in this manner to individuate the magnetic signature of this seasonal variation [Olsen *et al.*, 2002a]. Unfortunately the temporal and spatial distribution of the monthly means is worst than that of the annual means. Monthly means were available from the Institut de Physique du Globe de Paris [Alexandrescu, 1998] and the World Data Center for Geomagnetism in Copenhagen. Table III.2 shows, for each previously mentioned observatory, the interval in which these values are available. Strictly speaking, data coming from the WDC in Copenhagen were not monthly means but hourly mean values, so monthly means were computed from the hourly values when necessary. To homogenise both data sets from IGP and WDC, monthly means were computed from all days, instead of using only the magnetic quiet days as proposed by Olsen *et al.* [2002a].

As can be seen in table III.2, there are observatories in which monthly means are not available, making even more difficult the modelling task. The worst cases are found for CSY, MOL, DVS, GVN2, NVL, and TNB, all them located at the East Antarctic sector. For these six observatories an average of 10 years of data are lost when considering monthly means compared with the available annual means. The extreme case is that of Syowa, which presented a complete coverage of annual mean values but no monthly means are on the other hand disposable.

IAGA code	Data Interval	IAGA code	Data Interval	IAGA code	Data Interval
ARC	1978.45-1995.96	DVS	1988.21-2000.96	TNB	<i>no monthly means</i>
LIV	1996.96-2002.16	SYO	<i>no monthly means</i>	EGS	1964.12-1965.71
AIA	1960.04-1999.96	SNA1	1962.54-1970.96	HBA	1960.04-1967.96
WIL	1964.71-1966.04	SNA2	1971.04-1978.96	SBA	1964.21-2001.96
CSY	1989.21-2001.96	SNA3	1979.04-1989.96	VOS	1960.29-1998.96
MIR	1960.04-1997.96	RBD2	1964.54-1966.96	PTU	1966.21-1968.87
DRV	1960.62-2001.96	NWS	<i>no monthly means</i>	BYR1	1960.04-1962.96
MAW	1964.04-2001.96	GVN2	<i>no monthly means</i>	BYR2	1963.04-1968.37
MOL	1965.04-1977.96	NVL	1961.21-1978.96	SPA	1960.00-1971.92
		HLL	<i>no monthly means</i>		

**Table III.2.** Time period in which monthly means are available for each observatory. Observatories are ordered according to the geographic latitude and represented by their IAGA code.

The monthly means were also visually inspected, and problems analogous to those of the annual means were found. Figure III.5 shows for example the temporal behaviour of the monthly means for Dumont D'Urville. This particular observatory suffered a big list of changes during its operation (changes in instrumentation, relocation, etc.). These changes are well detailed for the annual mean values, so a uniform reconstruction of the data series can be done. This is not the case however for the monthly mean values. There is a sharp change of baseline between the years before and after 1973, which is clearly visible for the Z component. Comparing with the annual mean values, the values before 1973 seem to present an irregular behaviour. Hence the autoregressive method was again applied, in this case to predict the secular variation back to the past. To do this, the time scale was simply inverted to observe the phenomenon in the opposite direction. Similar situations were found for VOS, SNA3, and NVL, but unfortunately the lack of information about relocations, etc. forced in some cases the data to be cancelled because of the difficulty to decide which series of measurements was the correct and which the shifted one.

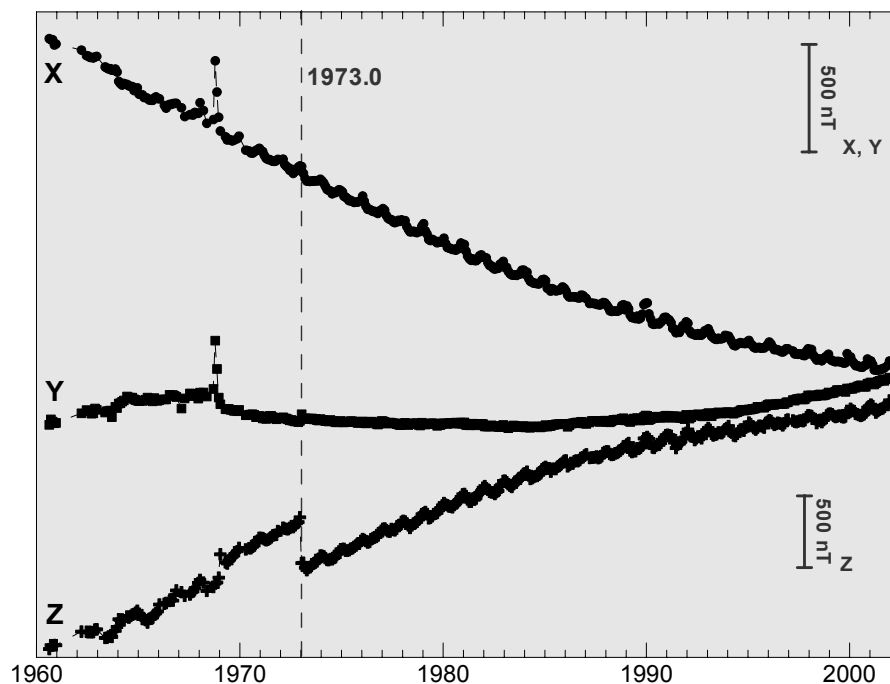


**Figure III.5.** Temporal behaviour of the monthly means of X, Y, and Z magnetic components for Dumont D'Urville observatory. Note the irregular behaviour of the data before 1973.

A particular problem was found for Vostok hourly mean values. The WDC format uses a daily tabular base value for each component of the magnetic field that must be added to the hourly values to obtain the real field value for that hour. The base values for the Z component of VOS corresponding to years 1978 and 1979 presented a change in sign when downloaded from

the WDC in Copenhagen, so values were completely wrong. The error was communicated to the responsables of the WDC to avoid an improper use of Vostok data by other researchers.

The relevance of the choice between annual or monthly means is clearly manifested in figure III.6, where the temporal behaviour of the total intensity field for Scott Base station for both annual and monthly mean values are presented. A clear correlation can be found comparing the temporal evolution of the monthly means with the sunspot numbers registered at Ebre observatory from 1980 to 2002. The sunspot (or Wolf) number is an index formulated by Rudolf Wolf in 1848 to estimate the solar activity by counting the number of individual spots and groups of spots that can be daily found on the face of the sun. The higher the sunspot number, the more important is the solar magnetic activity registered: as can be seen, the amplitudes of the seasonal variation are larger when the sunspot number is high, indicating a strong contribution of the external field from solar origin.

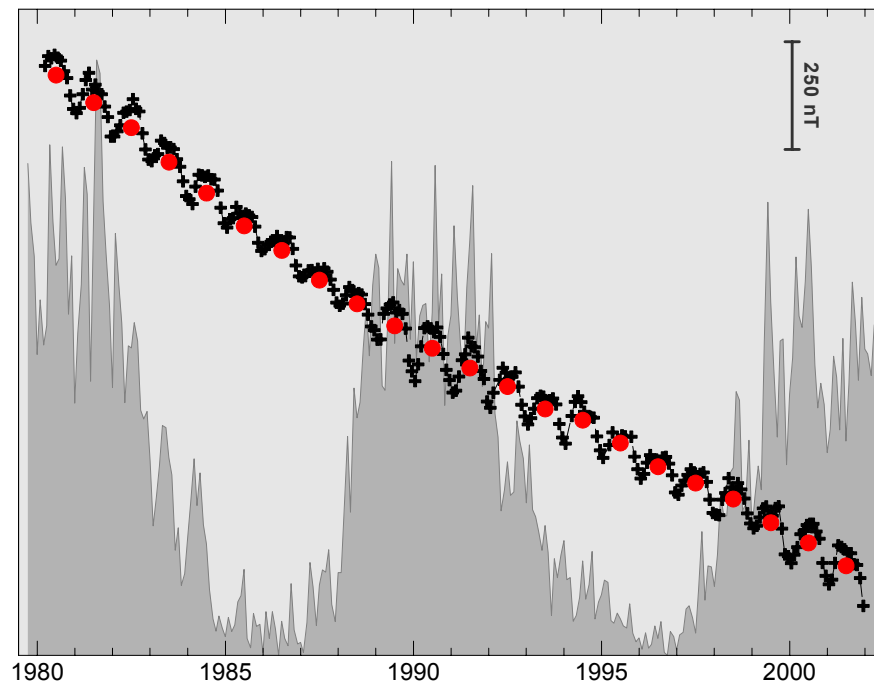


**Figure III.6.** Temporal behaviour of the annual (red dots) and monthly (black crosses) means of total magnetic intensity for Scott Base observatory. The background figure represents the Wolf numbers as measured at Ebre observatory.

The computation of the annual means as an average of values from all the year can thus drive to an inadequate consideration of the 11-year cycle of solar activity. For the years in which the Wolf number is small (i.e. low solar activity), we can say from 1983 to 1988 and from 1993 to 1998 in figure III.6, the annual means approximate the Austral winter monthly values; whereas

for a high sunspot number (before 1983 and after 1998, and from 1988 to 1993) the annual means take into account the high amplitude of the Austral summer variation. The use of only monthly means from the Austral winter season could contribute to remove this solar-cycle effect.

As it has been shown, the main problem with the available monthly means is their bad temporal distribution. The case of SBA shown in figure III.6, with a good temporal coverage, would be an exception. The usual situation is that in which several time gaps are present in the set of monthly values, so linear interpolation is necessary to reconstruct the series with the consequent introduced error. Hence, the final decision was the use of annual means to develop the model. This means that summer season data have been also included in the model, and this fact might explain the bad fit of the model to the observatory data, when comparing it with models that take into account external contributions, as it will be shown in Chapter IV.

### **III.3. Stratospheric balloon data**

#### **Introduction**

The observatory data used to develop the different Antarctic models subject of this work were presented in the last section; next section will deal with the measurements taken during different satellite missions. In the present section, and in order to follow an imaginary upward continuation, data coming from a stratospheric balloon mission are presented.

The magnetic measurements taken onboard a stratospheric balloon are not just an alternative to the aeromagnetic surveys and satellite missions but a necessary complement to them. The poor coverage of the Earth's surface given by ground observatories is improved by campaigns that spread over a more or less vast region of the Earth's surface. Satellite magnetic measurements are distributed nowadays over the entire globe (except a small region near the geographical poles; see next section for details about satellite missions), providing information about that part of the geomagnetic spatial spectrum of long wavelength (the threshold wavelength depending on the satellite altitude). On the other hand, aeromagnetic surveys cover a smaller region of the Earth's surface, but the proximity to the sources allows the achievement of information about magnetic anomalies of very low wavelengths. As pointed out by Cohen *et al.* [1986] the combination of different overlapping campaigns is often not a way to improve the knowledge of higher wavelengths, because of the difficulty to reduce different surveys to a common scenario (precisely due to the misestimation of the main field models).



There exists therefore a gap in the geomagnetic spectrum that can be studied through the use of aeromagnetic and satellite measurements. Magnetic measurements taken at an intermediate height would help in filling this gap: this is the role of the magnetic instrumentation that stratospheric balloons carry. The altitude of this kind of experiments is such that the shorter wavelengths are almost cancelled, and the longer ones are only attenuated with the distance to the ground level but enhanced with respect to the satellite level. In this way, the part of the spectrum between, we can say, 200 and 1000 km is monitored, giving key information about geological and tectonic features, and the possibility to penetrate deep in the crust to reach the upper mantle.

Depending on the flight time, two kinds of balloon experiments can be done: those involving conventional or long duration flights [Needleman, 1996]. In the first case, the typical flight duration is from some hours to few days; this is for example the kind of flight discussed by Cohen *et al.* [1986] for a balloon that on June 26<sup>th</sup>, 1984 flew from Sicily to Southern Spain in 18 hours at an altitude between 36 and 40 km. In the second case, the balloon can fly for a time interval that depends on the regional wind regime of the surveyed region, but it can last for two or three weeks.

Antarctica is a privileged area to carry on these kind of long-duration balloon flights. During the weeks close to the Austral summer solstice, the Antarctic stratospheric winds follow a quasi-circular pattern around the pole. A balloon launched from an Antarctic Station about 1200 km away from the South Pole returns approximately to the place of origin along a parallel in a time period between one and three weeks. Typical Antarctic balloon trips are shown in Wilkes [1998], as well as a description of the representative characteristics of balloon flights in Antarctica.

One of the main advantages of the Antarctic balloon flights is that the vertical displacements are reduced with respect to other latitudes because of the continuous sunlight, whereas one of the points to be taken into account is the thermal protection of the payload sensors due to the high albedo. In spite of the limited coverage of a stratospheric balloon compared to that of a spacecraft mission, the cost of a flight makes it an interesting choice to study the crustal field. Based on all the above reasons, the launch of Antarctic circumpolar balloon flights has become a routine from McMurdo Station since 1989 [Wilkes, 2000], with very different motivations, often related to the study of the deep space but sometimes also devoted to geophysical studies, as when magnetometers are carried pickaback. As in the case of satellite missions, magnetometers are usually placed at the end of a long beam to reduce the magnetic perturbations due to other electronic equipment. This is the best solution while waiting for the development of high-altitude

aeromagnetic surveys [Hildenbrand *et al.*, 1996] able to map the regional anomalies at a bigger scale and not only limited to a latitudinal circle or to a linear flight path.

### Boomerang experiment

The Boomerang experiment [Balloon Observations Of Millimetric Extragalactic Radiation ANd Geophysics; Crill, 2001] was designed to study the cosmic background radiation by means of a microwave telescope carried by a stratospheric balloon [De Bernardis *et al.*, 2000]. The balloon was launched on December 29<sup>th</sup>, 1998 from McMurdo Station (166.66° East longitude, 77.85° South latitude) for a 259-hours trip that concluded 50 km away from the origin point. Figure III.7 shows the route followed by the balloon, which covered a region with a lack of magnetic observatories. The mean height of the flight was around 38 km.

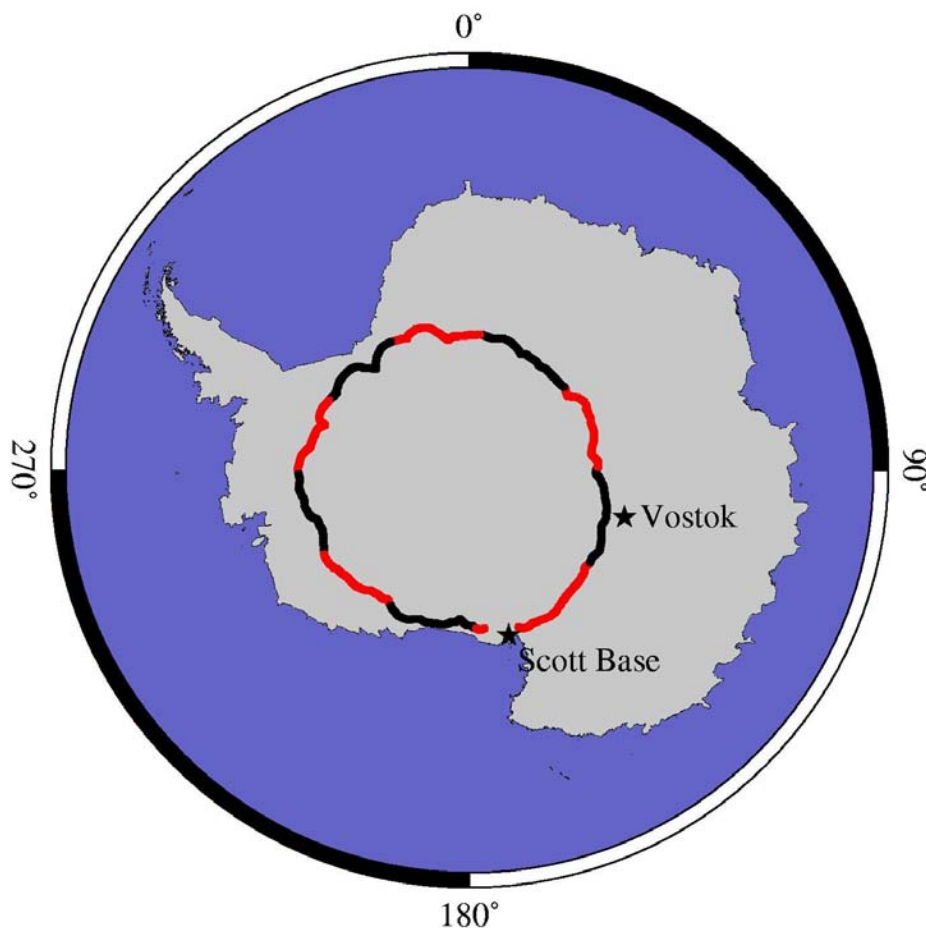


**Figure III.7.** Path followed by the balloon (anticlockwise sense) carrying the magnetic instrumentation during the Boomerang experiment. Alternate colors mean different days. The locations of Scott Base and Vostok are indicated since they represent respectively the starting point of the flight and the nearest geomagnetic observatory met by the balloon during the flight time.

The magnetic field was measured using a three-axial magnetometer. No absolute magnetic instruments were carried because at the moment of the experiment only a vectorial magnetometer was available. This was in fact one of the major problems found when analysing the data, since the usual way to calibrate the vectorial magnetometer is the comparison of the total field computed from the magnetic components and that given by a scalar instrument. Measurements were taken at approximately 10 Hz. The position of the balloon was furnished by a differential Global Positioning System (GPS) array, while a two-axis Sun sensor provided the azimuth of the whole system. The true azimuth was obtained after correcting the attitude of the gondola by the data from a gyroscope.

The big amount of data (around 870,000 measurements per day) was reduced at a first stage by computing minute means. After checking the similarities with this data set, half-hour means were obtained and used in what follows. The mean distance travelled by the balloon in half hour was around 15 km, so there is no necessity for using minute means to study the field of the area surveyed by the balloon. Means were computed for all three components of the magnetic field X, Y, and Z, starting from December 30<sup>th</sup> at 0 hours UT, since the measurements taken the previous day (when the balloon was still going towards a stable cruise height) presented not reliable values.

A problem arose when considering the horizontal components individually. As can be seen in figure III.8, a shifting seemed to be present between both (real and synthetic) data sets for X and Y components. It could be due to the fact that the magnetometer was placed at the end of a boom, and it could be possible that the boom was not perpendicular with the gondola. There is therefore an extra angle to be added to the azimuth of the system (Sun plus gondola azimuth) to find the real orientation of the magnetometer. After many tests, the angle which provided the best correlation (i.e. the angle for which the shifting roughly disappeared) between the X and Y components and the IGRF-8 model was around 20 degrees.

To ensure that the shift was due to the orientation of the magnetometer and not to other physical reasons, the horizontal value of the magnetic field H, computed as the square root of the sum of the squared horizontal components, was obtained. No shifting was appreciated between the real H and that computed through the IGRF-8, confirming the instrumental origin of the previous disagreement. The amplitude of the periodic oscillations diminished, so that we can assume that the remaining signal is due to the diurnal variation of the magnetic field and the effects of the external fields. The suitability of the comparison allows us to think that the

instruments were properly protected against the high albedo coming from the Antarctic ice surface, so thermal protection of the payload sensors was properly achieved.

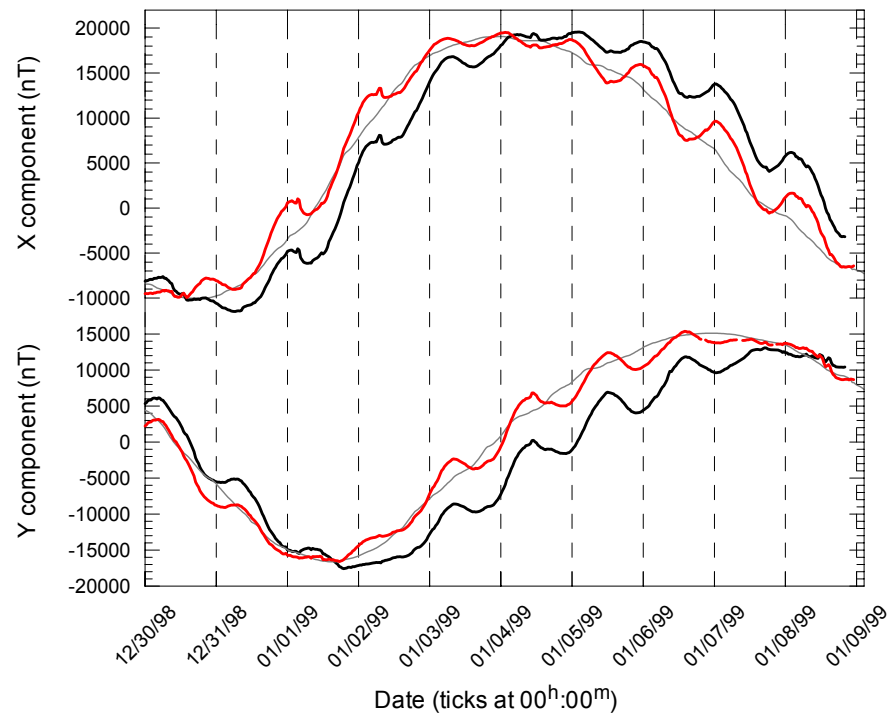


**Figure III.8.** Temporal variation of the X and Y components of the magnetic field measured by the balloon magnetometer (black lines) together with those provided by the IGRF-8 model (grey lines). The application of an extra angle of  $20^\circ$  to the azimuth when converting from the system reference frame to a frame oriented to the real north cancelled the shifting between IGRF-8 and balloon values (red lines).

Once the horizontal H and the vertical Z elements were known, the total intensity F was obtained (figure III.9). This is the most interesting element since it can be compared with the measurements taken during aeromagnetic or marine campaigns (usually scalar surveys). Moreover, even though no satellite missions were in course during the period of flight of the Boomerang experiment, data can be compared with synthetic data generated by using the CM3 model. This model was developed using satellite data from different missions, and it gives account of the ionospheric and magnetospheric contributions.

The differences found when comparing the data with a reference model are not only due to the crustal field, but to the diurnal variation of the magnetic field and to the different degree of external magnetic activity. It must be kept in mind that the balloon changed its position during the day with respect to the auroral oval, the flow of charged particles that moves from dawn to dusk in the high latitude upper ionosphere.

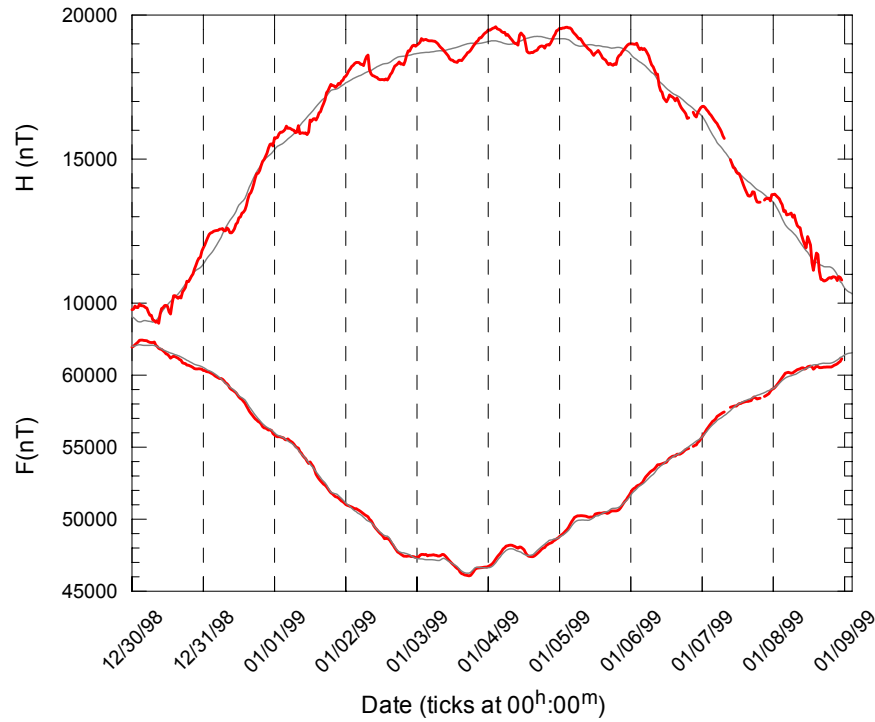


**Figure III.9.** Temporal variation of the H and F elements of the magnetic field measured by the balloon magnetometer (red lines) together with those provided by the IGRF-8 model (grey lines).

The importance of the external contribution can be estimated by means of the values of the magnetic activity indices [Mayaud, 1980]. The behavior of the  $K_p$ , provisional AE, and PC indices is shown in figure III.10. The importance of the PC index, a dimensionless parameter to monitor the state of the magnetosphere [Troshichev *et al.*, 1979; see below for details], lies in the fact that it is deduced from measurements at Vostok magnetic observatory, the nearest station to the balloon flight. According to the criteria applied by other authors when selecting satellite data,  $K_p \leq 1$  – following Coles [1985] and  $AE \leq 50 nT$  as imposed by Ravat *et al.* [1995], only data from the first two days of the flight and few hours between January the 5<sup>th</sup> and the 7<sup>th</sup> are under geomagnetic quiet conditions. The values of the PC index were also low only during those periods. The f10.7 index, which gives account of the solar radio flux activity at a 10.7 cm wavelength, was high for all the considered period (130.9 sfu for December 1998 and 124.3 sfu for January 1999), since the experiment took place during the rising part of the 22<sup>nd</sup> cycle of solar activity. From all the above indicators, strong influence from external fields can be expected to be present especially in the horizontal components.

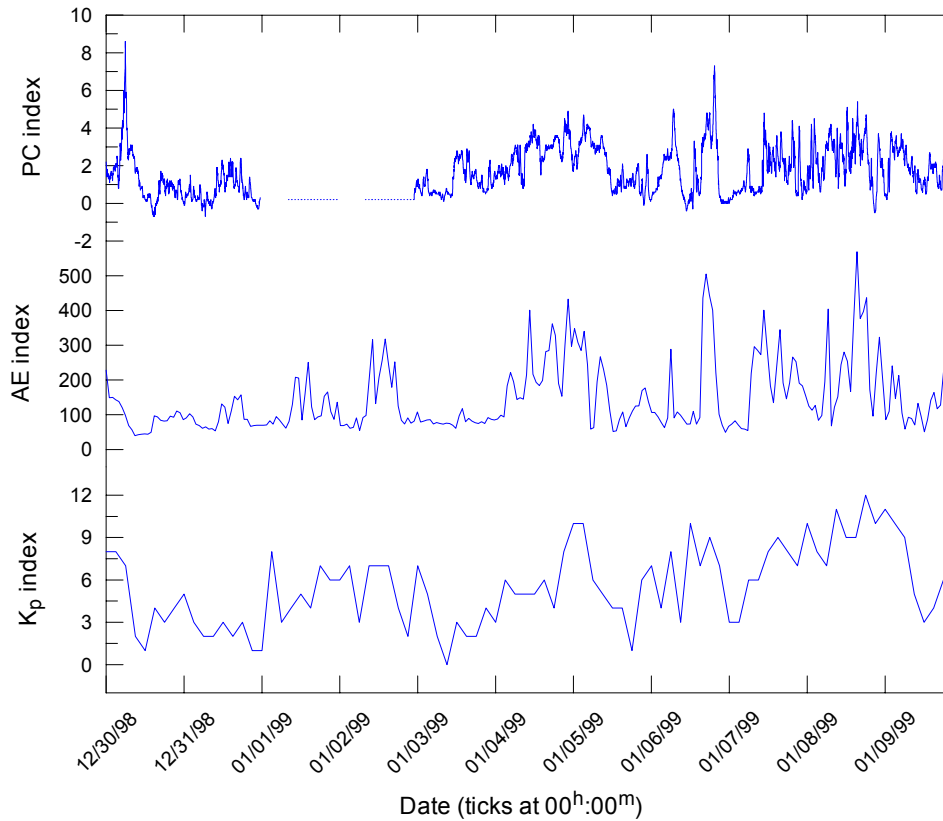


**Figure III.10.** Temporal variation of PC (top), AE (middle), and Kp (bottom) indices during the flight period of Boomerang experiment. The usual nomenclature has been followed to represent the  $Kp$  ( $Kp = 0o$  equals to value 0,  $Kp = 0+$  corresponds to value 1,  $Kp = 1-$  to value 2, ...,  $Kp = 9o$  to value 27).

Figure III.11 shows the residuals of the measured and computed magnetic elements with respect to the CM3 model. In this case the crustal contribution of the model has not been added, since it is just the spectral content to be isolated, so only contributions from the main field (up to degree 13), and from sources placed in the ionosphere and the magnetosphere were considered. The presence of a remaining diurnal variation signal in these data is evident. Unfortunately it is not possible to apply the typical procedure to remove this variation, that is the use of data measured at a base station or observatory, since the balloon flight covered a too large area to be monitored by a base magnetometer. Only four Antarctic geomagnetic observatories below 65° South latitude provided minute values during the epoch of the experiment: Dumont D'Urville, Mawson, Davis, and Scott Base, all four near the coastline between 0 and 180° East longitude. The comparison of the measured total intensity values as a function of local time shows important discrepancies for the four stations (figure III.12), making more difficult the choice of one of these observatories as reference level to remove the diurnal signal from Boomerang data.

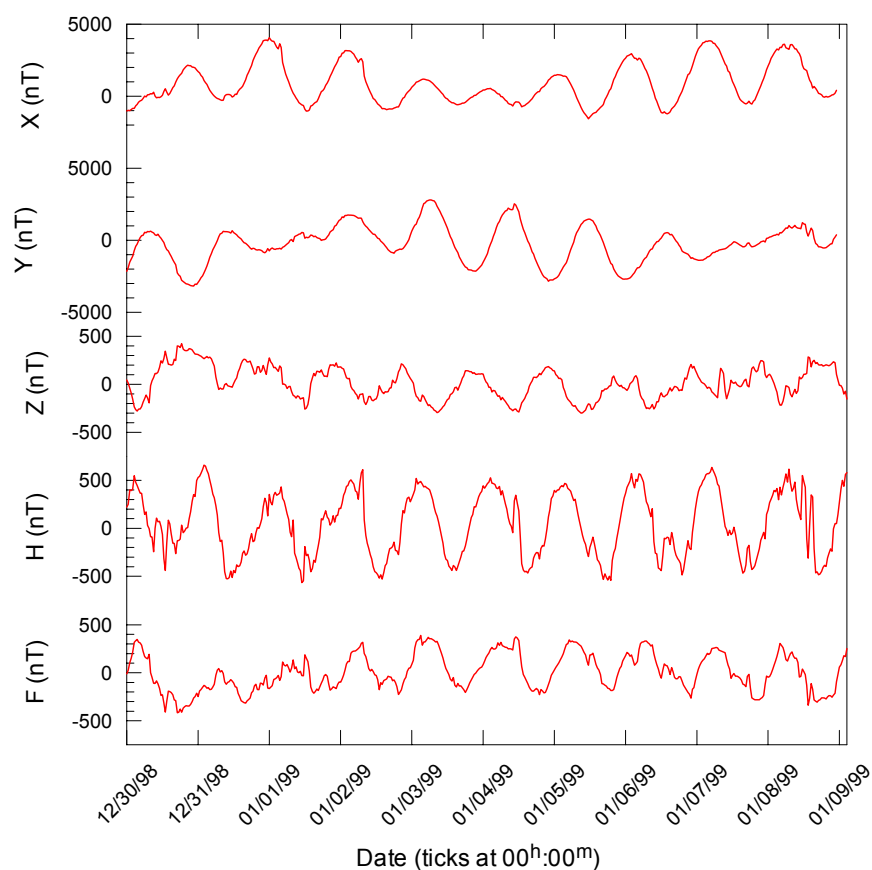


**Figure III.11.** Residuals of the magnetic data measured by Boomerang with respect to the CM3 model [Sabaka *et al.*, 2002], in which crustal contribution has not been considered.

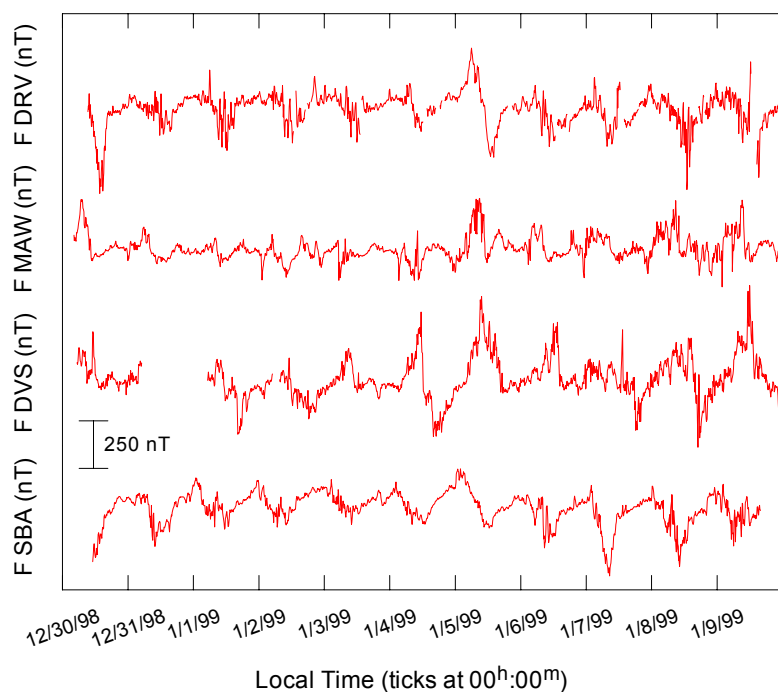


**Figure III.12.** Total intensity as a function of local time measured at the four geomagnetic observatories placed below  $65^\circ$  South latitude which provided minute data during the period of the balloon flight.

As can be seen from figure III.11, the amplitude in the daily oscillations of the X and Y components measured by Boomerang are about 5000 nT. These values are too high to be created by a source with natural origin, despite the proximity of the balloon to the ionospheric sources and the important effects of the field aligned currents at those latitudes. On the other hand, the amplitudes for H element are much lower, and for example the diurnal variation of the total intensity field is of the same order than that recorded at the ground observatories like Scott Base. There is therefore every indication that something was disturbing the measurements made by the magnetometer, probably a field created by the other instrumentation carried by the balloon that affected the horizontal components record. These results have been discussed with the team responsible for the magnetic part of the Boomerang experiment, in order to take into account these problems in future stratospheric missions.

In the light of these considerations, only the total intensity F has been used for the development of the model. In order to eliminate the remaining diurnal variation from the data once the external contribution from CM3 was removed, a spectral analysis procedure was adopted. The study of the power spectrum (the distribution of energy of the signal per unit time, figure III.13) of the total intensity field shows a clear periodicity for the signal between 23 and 24 hours (the periodicity is lower than 24 hours since Boomerang is moving following its circular trip around the geographic Pole). A high-pass filter was applied to remove this unwanted part of the signal. Figure III.14 shows the remaining signal.

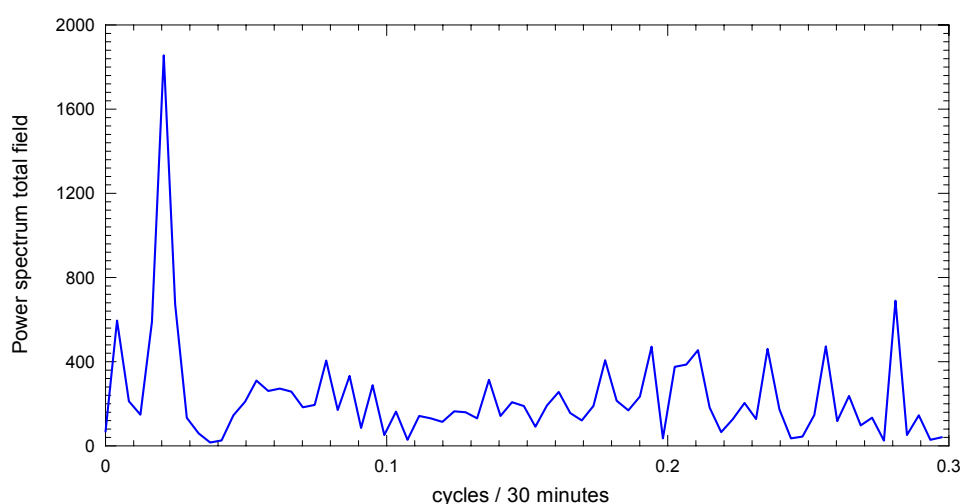


**Figure III.13.** Power spectrum of the total intensity field measured by Boomerang. The main peak corresponds to a frequency equal to 0.021 cycles per 30 minutes, i.e. a period of 23.8 hours.



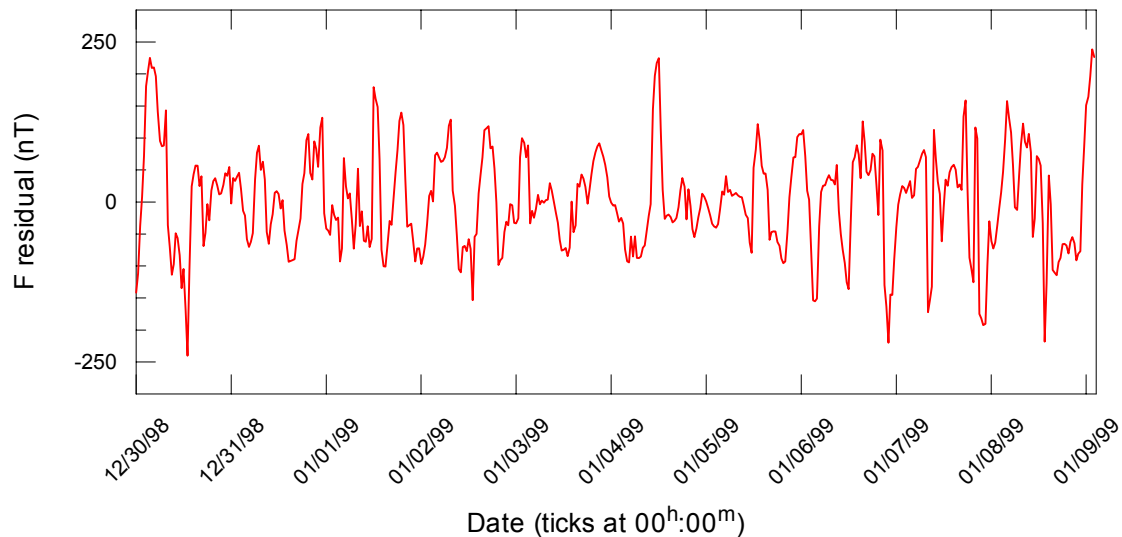


**Figure III.14.** Total field measured by Boomerang magnetometer after subtracting the main and external contributions given by CM3 and a high-pass filter to remove the diurnal variation.

A comparison of figure III.14 and the previous figure III.10 shows a clear correlation between some of the sharp peaks that appear in the residual of the total field measured by Boomerang (after removing the main and external contributions using CM3 and the application of the high-pass filter), and the indices of magnetic activity. The wide amplitude high frequency oscillations during the first half of December 30<sup>th</sup>, and January 4<sup>th</sup>, 6<sup>th</sup>, 7<sup>th</sup>, and 8<sup>th</sup> correspond to episodes of high external magnetic activity, as denoted by PC and AE indices. According to these indices, a set of 163 values was finally selected and used in the development of the model, corresponding to measurements taken during the second half of December 30<sup>th</sup>, December 31<sup>st</sup>, the first half of January 1<sup>st</sup>, January 3<sup>rd</sup>, and the first half of January 6<sup>th</sup>. The longitudes covered by the selected data are between 140° and 70°, 5° and -40°, and -120° and -135°, so information about the behaviour of the magnetic field at stratospheric altitude will be included in the model for some arcs that spread along the circle followed by the balloon path. The previously removed CM3 contributions were added to this residual field in order to model the total intensity field values.

### III.4. Satellite data

#### Introduction

We have described until this point the surface or near-surface data used in this study. Observatory data are appropriate to model the secular variation and to impose a constraint at ground level, whereas balloon data improve our knowledge of the intermediate wavelengths of the geomagnetic spectrum. Nevertheless there is a poor coverage of the Antarctic continent, and

more data, covering the complete territory and distributed in height, are necessary if we want to model properly the geomagnetic field.

The uniform coverage of the satellite observations and the negligible secular variation of the core field (if measurements are taken in a relatively short time), both characteristics help to describe long wavelength anomalies that often disappear or are badly discriminated when combining disparate near-surface campaigns. This restriction of the satellite measurements near a given epoch, however, impulses several researchers to affirm that observatory data is the most proper (if not unique) way to model the secular variation of the geomagnetic field [e.g. Langlais and Manda, 2000]. Following these authors' point of view, occasional satellite missions can not define properly the secular variation, because the temporal change of the geomagnetic field presents a behaviour far from linear [e.g. De Santis *et al.*, 2002b].

The necessity of geomagnetic satellite missions to a better understanding of the magnetic field registered on our planet can not be nevertheless put to doubt. The quantity, and more important, the quality of the geomagnetic field models has increased with the arrival of the International Decade of Geopotential Field Research. This was an initiative of IAGA to take advantage of the several planned satellite missions for the end of the last century and the beginning of the present. The increase in the number of spacecraft missions gives high hopes for the study of the Earth from high altitude [Ravat and Purucker, 1999]. A report of recent global magnetic field models developed using latest satellite missions data can be found in Purucker [2002].

The instrumentation onboard a satellite can be designed to measure the vector field, the total intensity field, or both of them. The reason to measure the scalar field when it can be in principle obtained as the square root of the sum of the quadratic components is because of the intrinsic difficulties to measure the vector field on a satellite. The errors that one can find on the satellite data can be divided into two blocks: usual errors that can be found in any kind of measurements, and errors inherent to satellites. The first include those errors that are related to the instrumentation and to contaminating fields (nevertheless, the proximity of the satellites to the magnetospheric sources can increase these last errors). The second group is composed by errors on the determination of the exact time and position, the magnetometer orientation (called also magnetometer attitude), and the magnetic fields induced by the own satellite.

The spacecraft fields are eliminated by deploying the magnetic sensor at the end of a non-magnetic boom some meters long. The position and timings determination have improved considerably thanks to the use of the GPS. It must be taken into consideration that an uncertainty

of 36 meters in the radial position can lead to errors up to 1 nT; and a drift of 10 milliseconds in time, considering a constant orbital velocity of  $7 \text{ km}\cdot\text{s}^{-1}$ , can produce errors of nearly 2 nT. Finally, a star imager is used to determine the orientation of both the magnetometer and the satellite. If we are using a triaxial fluxgate magnetometer to measure the components of the geomagnetic field, an error of 20 arc seconds in the orientation of one of the axis would result in 5 nT error in the field perpendicular to that axis, whereas the scalar field is not affected by a deterioration of the orientation accuracy.

A satellite describes an ellipse around the Earth (although the orbit can be also circular) with closest (perigee) and farthest (apogee) points from the Earth. The angle of the orbit plane with the Earth's equatorial plane is called the inclination of the satellite's orbit. The satellite orbital plane can be imagined as a nearly fixed frame in which the satellite is moving around. Each complete orbit takes from 90 to 200 minutes for apogees between 200 and 2000 km. The Earth would be turning around its axis under this fixed geometry, so each longitude passes beneath the orbit of the satellite and the data are well distributed all over the world. If the orbital plane frame is fixed with regard to the Sun, then a given latitude will see the satellite passing above at nearly the same local time, in what is called a sun-synchronous orbit.

The longitudinal and temporal distribution of the satellite tracks (projection of the orbit onto the Earth's surface) can be set choosing appropriately the orbital parameters. Depending on the inclination, height, ellipticity of the orbit, etc., tracks can therefore overlies after a given number of orbits (this configuration implies the appearance of gaps in longitude), or be never repeated. The possibility of having adjacent satellite passes is a helpful tool to remove fields of external origin [Alsdorf *et al.*, 1994a; von Frese *et al.*, 1999]. Nearest tracks should present the same main and crustal field signatures if the distance between them is negligible compared to the distance to the Earth's surface, so pass-to-pass correlation filtering could in principle remove the external field contributions. A proper determination of the external currents behaviour will be however possible only when multi-satellite missions will go on. More than one satellite measuring simultaneously the magnetic field of the Earth at different orbits and heights would enable the determination of the temporal changes of the geomagnetic field. This is the object of the *swarm* proposal, a constellation of satellites to study the dynamics of the Earth's magnetic field and its interaction with the Earth system [Friis-Christensen *et al.*, 2002]. This mission will facilitate the study of the spatial and temporal change of the geomagnetic field at medium and long wavelengths, and for periods between seconds and years [Olsen *et al.*, 2002a].

Until the upcoming of this multi-satellite constellation, the geomagnetic field modellers will continue using past and present spacecraft missions to improve the knowledge of the Earth's interior. A summary of modelling methods together with an extensive list of the use of satellite magnetic anomalies in the past, are given in the impressive book by Langel and Hinze [1998]. On the other hand, the approach proposed by Sabaka *et al.* [2002] represents the new generation of comprehensive models in which all contributions are modelled individually thanks to the satellite data availability.

### Satellite missions

There have been four satellite missions from which data have been used in this study: POGO, Magsat, Ørsted, and Champ, each one of them with their particular orbital parameters and magnetic instrumentation characteristics. A list of the main parameters for the satellite missions used in this work can be found in table III.3. A description of the first satellite missions (until mid of the nineties) that have contributed to measure the magnetic field can be found in Langel and Hinze [1998], whereas a detailed summary of the present, upcoming and proposed magnetic field satellites is given at the web site of Purucker [2003].

Satellite	Date	Altitude (km)	Inclination	Local Time	Instrumentation
OGO-2	Oct 1965 to Sep 1967	413 – 1510	87°	All local times	Rubidium (scalar)
OGO-4	Jul 1967 to Jan 1969	412 – 908	86°	All local times	Rubidium (scalar)
OGO-6	Jun 1969 to Jul 1971	397 – 1098	82°	All local times	Rubidium (scalar)
Magsat	Nov 1979 to May 1980	325 – 550	97°	06:00 / 18:00	Fluxgate (vector) and Cesium (scalar)
Ørsted	Feb 1999 to present	620 – 850	96°	All local times	Fluxgate (vector) and Overhauser (scalar)
Champ	Jul 2000 to present	300 – 460	87°	All local times	Fluxgate (vector) and Overhauser (scalar)

**Table III.3.** Main features of the magnetic satellite missions considered in this work.

The Orbiting Geophysical Observatory (OGO) was the first mission to deploy satellites for a high accuracy measurement of the geomagnetic field [Cain *et al.*, 1967]. Previous satellite missions, like *Sputnik 3* in 1958 and *Cosmos 49* in 1964, presented problems like the presence of

large magnetic disturbances or poor data accuracy. The OGO satellites, which operated between 1965 and 1971, were divided in two groups: three of them were moving around the Earth in orbits of very high eccentricity to study the magnetosphere, and other three were placed in a near-polar orbit (the name POGO stands for Polar OGOs). Measurements were taken for all local times at altitudes between 400 to 1,500 km.

Unfortunately POGO satellites carried only a rubidium-vapor magnetometer to measure the scalar magnetic field (however, with an accuracy better than 6 nT never reached before). Magsat satellite was the first satellite, from November 1979 to May 1980, to monitor both magnetic components and scalar field [Langel *et al.*, 1982a]. The scalar magnetometer was a cesium-vapor instrument with accuracy of 1.5 nT, whereas the vector magnetometer consisted of three fluxgate sensors accurate to 3 nT for each axis. For the first time, these vector data helped to describe the different contributions contained in the near-Earth magnetic field [Langel, 1982].

Magsat mission presented however three disadvantages with respect to POGO satellites, concerning flight time and spatial distribution. First, POGO covered all local times whereas Magsat flew in a dawn-dusk orbit. This is an important difference keeping in mind that the ionospheric dynamo varies as a function of the local time. Second, Magsat covered almost only the Antarctic summer, when there is continuous sunlight and therefore the ionospheric magnetic activity is increased, in contrast with POGO, which flew during all seasons. Finally, POGO satellites covered more space near the geographic South Pole than Magsat satellite (which covered the Polar Regions up to 83° South latitude), because of the different inclination of the orbits.

It has been necessary to wait for almost 20 years for new high precision magnetic satellites. The Danish Ørsted [Olsen *et al.*, 2000] and the German Champ [Holme *et al.*, 2000] missions represent the beginning of a new era in geomagnetic research from space. The improvement of the instrumentation with respect to previous missions will be fundamental not only for the development of the main field models, but also for the knowledge of the Earth's crust (the altitude of Champ satellite is less than 300 km in its nearest approach to the surface). The possibility of having simultaneous measurements from more than one spacecraft must be an important point to define also the fields of external origin.

### Criteria for the selection of satellite data

The amount of available magnetic satellite measurements is actually huge. POGO satellites flights lasted a total time of almost six years, Magsat another half year, and Ørsted and Champ

are still flying at present. Not all these data are nevertheless useful for all kind of geomagnetic purposes: for example, if we want to study only the internal (main and crustal) fields, it is necessary to remove those data sets with a high contribution from external and induced currents.

The usual method to remove undesired external contributions from the input data set has been the selection of periods during quiet magnetic conditions. Based on geomagnetic activity indices and (or) on the interplanetary field conditions, modellers decide if a particular measurement can be chosen to contribute to the development of the magnetic model, or on the other hand if it is too contaminated to be considered.

When considering the data selection procedure, the characteristics of the region under study have to be taken into account. Some indices and procedures are more adequate than others to select the data depending on the latitude where the measurement was done. For example, the solar daily variation Sq and the equatorial electrojet fields will be always present during sunlight hours, whereas field-aligned currents and auroral currents will contribute to the measurements at any time, but their importance is related almost exclusively to the polar regions. One can choose only data from the dark hemisphere to avoid the first kind of diurnal currents. On the other hand, applying simultaneously a selection criterion based on the values of some magnetic indices would be also useful to remove contaminated data.

A proper index to begin with the selection of data at mid latitudes is the Kp index. This three-hour index is computed from the measurements of a series of observatories (11 northern and 2 southern stations) out of the auroral regions. Kp values vary in a scale that goes from 0o for minimum magnetic activity to 9o for maximum perturbation (with one-third unit sublevels indicated by adding the symbol -, +, or o). The choice of a threshold value means an improvement in the quality of the data (in terms of avoiding external contributions): data with Kp index higher than this threshold value is simply not considered. As we are dealing with an index averaged over a long temporal range, restrictions are often also imposed on the value of the Kp index previous to the considered time interval. Another useful index to describe the situation at equatorial latitudes is the Dst index, which is obtained using data from four observatories placed at low latitudes near the geomagnetic equator.

Olsen *et al.* [2000] used, together with other criteria, both Kp and Dst indices to select data for the development of the Ørsted initial magnetic field model. Kp was chosen to be lower or equal to 1+ for the time of observation and to 2o for the previous interval, whereas the maximum absolute value of Dst was fixed in 10 nT with a maximum temporal variation of 3 nT/h. As only

scalar data were selected for latitudes  $|90^\circ - \theta_{dip}| \geq 50^\circ$  (where  $\theta_{dip}$  was given by the first three coefficients of the IGRF-8 model), the restriction criteria provided a selected subset of 303 scalar measurements below  $60^\circ$  South latitude. These data were used in the development of the first version of the Antarctic reference model [De Santis *et al.*, 2002a].

For high latitudes a selection based on the value of the Kp value is important, but it does not represent the best solution to isolate the quietest data. Even when Kp has a low value, a big magnetic activity can be found in the auroral regions, so another kind of indices are also needed to give account of the polar activity. A useful parameter for these cases is the AE index, computed from the deviations on the horizontal component of the magnetic field at a series of observatories distributed along the northern auroral zone. For example, Ravat *et al.* [1995] imposed a limit value of 50 nT for the AE index to consider data when evaluating the Magsat scalar data at polar latitudes.

The presence of a strong interplanetary field is also a criterion used to reject data. During periods of high magnetic activity, the Z component of the interplanetary magnetic field (IMF) turns southward. As IMF was adopted to be negative when directed to the South, periods with a high interplanetary magnetic activity present more negative vertical IMF values. The choice of data from periods with  $IMF > 0$  for the vertical component would contribute to ensure a low contribution of the substorm activity.

Troshichev *et al.* [1979] proposed a new magnetic activity index, called Polar Cap index (PCI), to give account of the magnetic activity related to the IMF vertical component. This index is derived from a single near pole station for both hemispheres, Thule ( $290.766^\circ$  longitude,  $77.466^\circ$  latitude) for the North and Vostok ( $106.867^\circ$  longitude,  $-78.45^\circ$  latitude) for the South Polar cap, unlike AE that is derived only for the Northern Hemisphere. Vennerstrøm *et al.* [1991] found a good correlation between both PCI and AE indices, gradually decreasing with increasing level of activity. By own definition, the Polar Cap index would be more related to the interactions between the solar wind and the magnetosphere (e.g. the field aligned currents), so PCI is a good indicator of the regional activity in the auroral oval and not only of local disturbances.

Both for high and low latitudes, the effects of ionospheric currents can be minimised if only data from the nightside hemisphere are selected. Moreover, Olsen *et al.* [2002b] imposed a more restrictive method based on the Sun's height: measurements carried on when the Sun was higher than  $5^\circ$  below the horizon were not considered. This more restrictive approach, that can be done

when the amount of data is high, demonstrated to be more useful than the traditional division of data between night and day hemispheres. A new procedure by Chambodut *et al.* [2003] was recently proposed, based on the selection of measurements made in the “real shadow side” of the Earth; it will be taken into account in future data selection processes.

Also for all latitudes, a posterior step to improve the data selection would be the comparison between adjacent passes. This technique is based in the fact that the external contribution is of dynamic nature compared to the internal field, so discrepancies found in neighbour tracks can be interpreted as due to external currents. The profiles for which the variance is lower are those considered less contaminated by external fields. For example, Alsdorf *et al.* [1994a] applied the pass-to-pass correlation technique when separating the internal from the external contributions contained into the satellite scalar field measurements over the South Pole.

A visual inspection of two adjacent passes helps also to clarify the importance of the magnetic indices criteria for the data selection. Figure III.15 shows the residuals of the measured magnetic field components with respect to the internal contribution of the CM3 for two adjacent passes of Ørsted satellite over the Antarctic. These passes were selected in order to give a picture of the field during a magnetically disturbed day (January 11<sup>th</sup>, 2000, black points in figure III.15), and during a quiet day (January 21<sup>st</sup>, 2000, red points). Ørsted satellite spends approximately 16 minutes for a passage over the Antarctic continent like the one shown in the figure. Kp index was equal to 3o for January 11<sup>th</sup> (qualified as one of the five most disturbed days of the month), and equal to 1- for January 21<sup>st</sup> (one of the five quietest days). In the same way, AE index values were equal to 130 nT and 69 nT, respectively. Major discrepancies between both passes can be specially appreciated for the horizontal components X and Y. The representation of the vertical component Z shows clearly the difference between January 21<sup>st</sup>, which presents a smooth behaviour of the field, and January 11<sup>th</sup>, with some sharp changes. The most important dissimilarities are found in this case for the lower geographical longitudes, which correspond (see the figure with the location of the passes) to the positions closest to the magnetic pole, sign that a contribution from magnetic external fields is present.

The fulfilment of the selection criteria above presented does not guarantee a set of data completely clean from external fields to develop an internal field model. The perturbation can be nevertheless minimised if more than one of these criteria is applied at the same time. For instance, the appropriate selection at high latitudes would be based on the Kp and Dst index, but also on the AE and PC indices, the strength of the vertical component of the interplanetary field, the Sun’s height, and the coherence between adjacent passes.



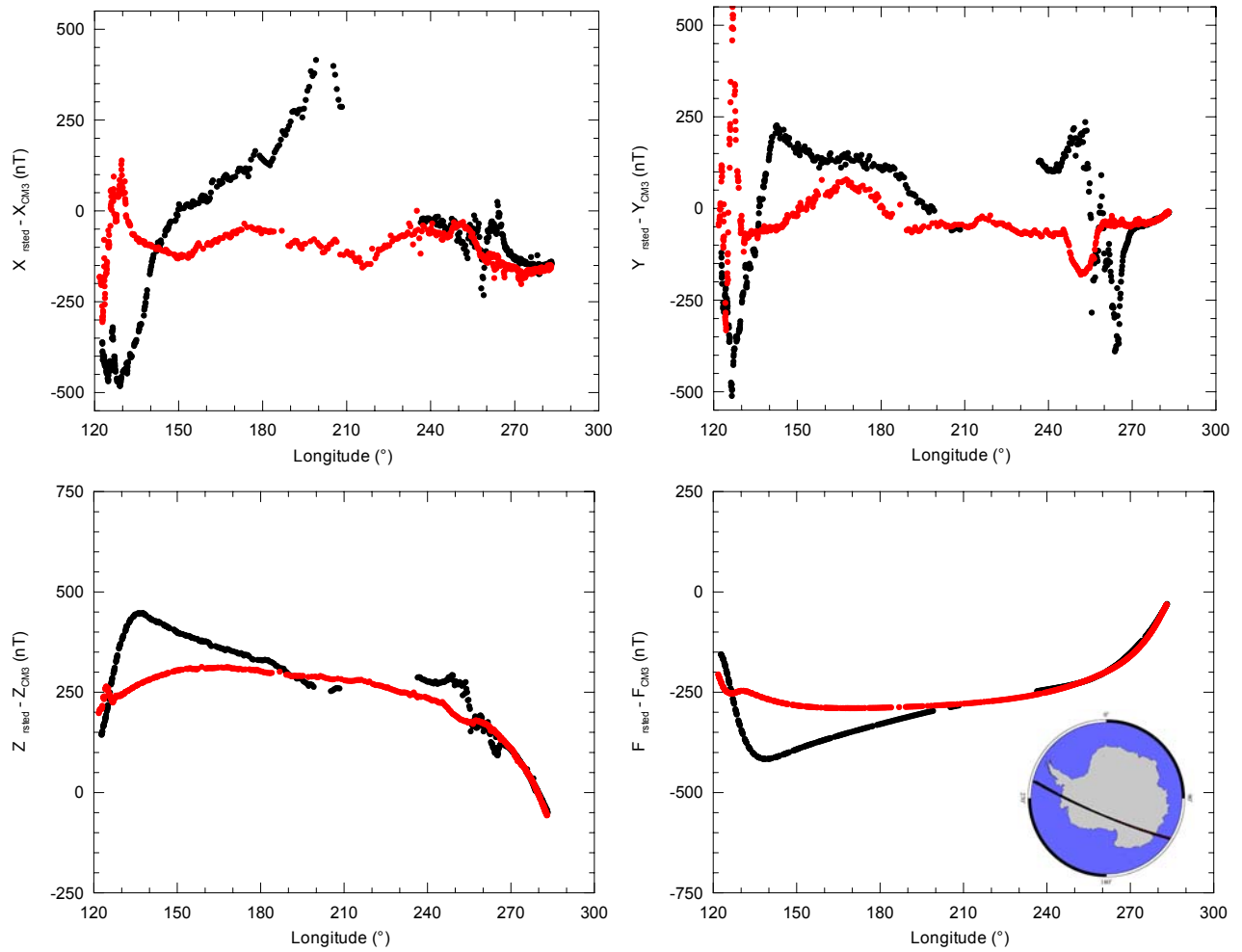


**Figure III.15.** Residuals of the magnetic field values measured during two adjacent passes of Ørsted satellite with respect to the internal field given by CM3. January 11<sup>th</sup>, 2000 pass (black) corresponds to a disturbed day, whereas January 21<sup>st</sup>, 2000 pass (red) represents a quiet day.

### Satellite Data used

Table III.4 shows the original number of available total intensity values for each one of the six satellites used in this study, together with the temporal interval at which the measurements were done and the height range in which these data were taken. These original data sets, provided by Nils Olsen from the Danish Space Research Institute, were selected considering a solar height lower than 5° below the horizon and according to the value of the Kp index. Therefore, threshold values of Kp=1+ at the time of the measurement and Kp=2o for the previous 3-hour interval were adopted. The number of measurements varies from less than 1000 data for the OGO-2 satellite to more than 20000 for OGO-6, Ørsted, and Champ missions. No decimation was applied to put on the same level all six missions, because it is convenient to apply previously the data selection based on the magnetic activity indices and compare thereafter the final data sets.

Satellite	Date interval	Altitude range (km)	# F values
OGO-2	1966.2 – 1967.7	430 – 1,500	828
OGO-4	1967.6 – 1968.8	420 – 910	3,972
OGO-6	1969.4 – 1971.3	400 – 1,100	23,606
Magsat	1980.2 – 1980.3	330 – 460	1,723
Ørsted	1999.9 – 2002.6	650 – 870	20,033
Champ	2000.6 – 2002.5	400 – 500	21,558

**Table III.4.** Original number of total intensity values for each one of the magnetic satellite missions considered in this work, selected considering the Sun's height and the Kp index, together with the temporal and height ranges in which data were collected.

The use of scalar data instead of vectorial measurements avoids errors like the magnetometer misorientation or the anisotropy in the attitude accuracy of the rotation and pointing directions of the satellite, as in the case of Ørsted satellite [Holme, 2000]. These scalar values are not affected by the sensor orientation, and the Backus effect [Backus, 1970] is not present because we are in polar regions. This effect, which is important near the dip-equator [Stern and Bredekamp, 1975], would prevent the derivation of a unique solution for the potential from scalar data because the orientation of the field is not known. Moreover, the presence of large amplitude variations in the horizontal components due to the field-aligned currents is avoided when using only the total intensity, very similar to the vertical component at polar areas.

A figure similar to the previous III.15 can help to make clear the fact that only scalar data have been considered. We can compare two adjacent passes realised during two of the quietest days of January 2000, the 8<sup>th</sup> and the 18<sup>th</sup>. Residuals for the magnetic elements with respect to the CM3 for these two days are shown in figure III.16. Whereas both Z and F magnetic elements are similar in both cases, the horizontal components present several disparities. It is therefore clear from this figure that, the inclusion of vectorial data into the model could lead to some inconsistencies in the evaluation of the field, since the magnetic field horizontal components at a similar location and almost the same epoch could take different values.

There is nevertheless a problem associated to the inclusion of scalar data to develop a geomagnetic field model, that is the non-linearity of the total field in the coefficients that represent the magnetic components. To overcome this problem, an iterated linearisation was applied: a Taylor series expansion of the total field was developed, and only the linear terms

were considered. As pointed by Cain *et al.* [1965], any component of the magnetic field,  $F$  in particular, can be approximated by the series expansion:

$$F \cong F_0 + \sum_{j=1}^J \left( \frac{\partial F}{\partial g_j} \right)_0 \Delta g_j \quad (\text{III.2})$$

where  $F_0$  is an approximate initial value of the total field,  $(\partial F / \partial g_j)_0$  is the derivative with respect to  $g_j$  evaluated using an approximate value for the coefficient, and  $\Delta g_j$  is an appropriate correction to the given coefficient. In our case, a global reference field provides the starting value for the iteration, which continues until the changes in the model coefficients are negligible.

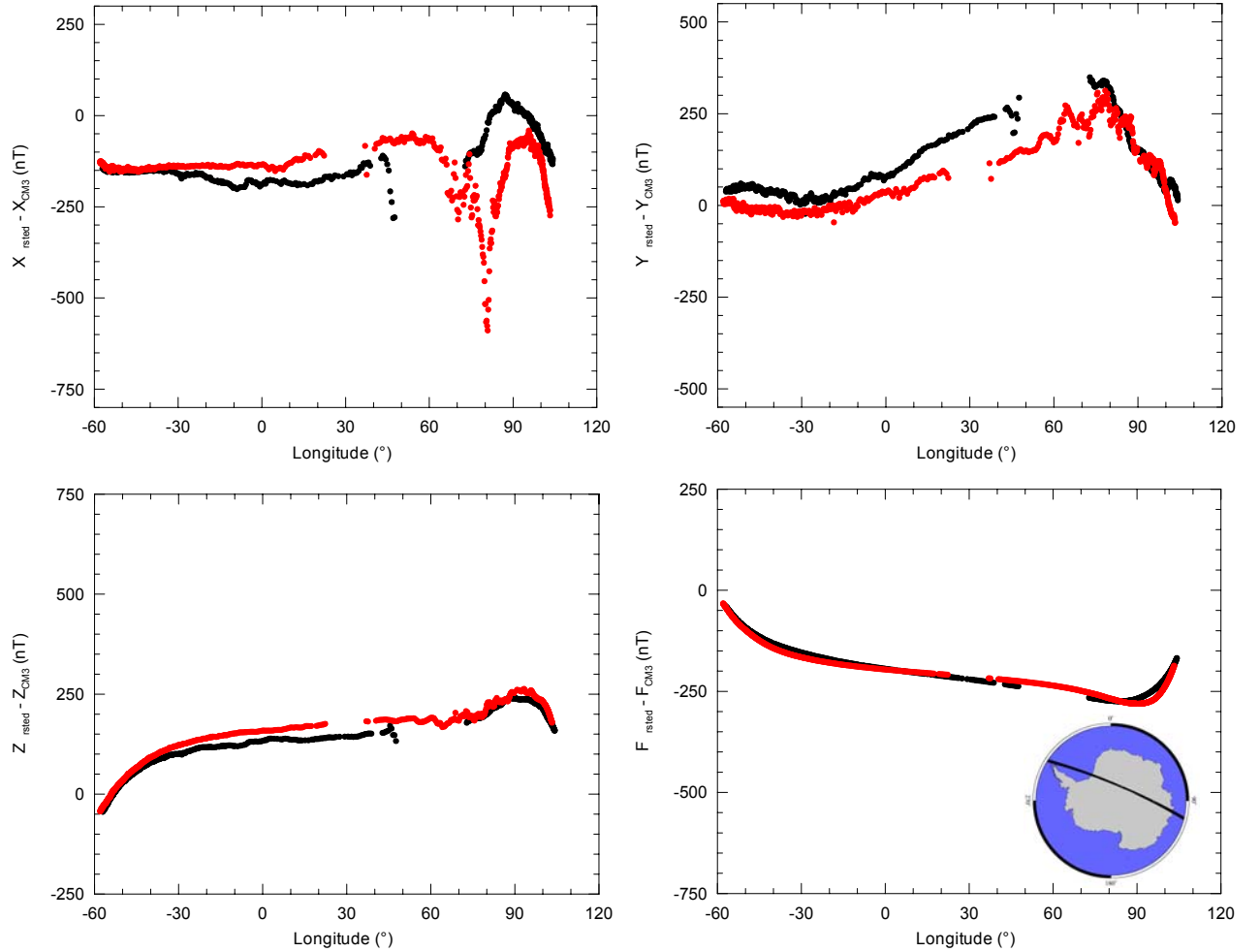


**Figure III.16.** Residuals of the magnetic field values measured during two adjacent passes of Ørsted satellite with respect to the internal field given by CM3. Both January 8<sup>th</sup>, 2000 (black) and January 21<sup>st</sup>, 2000 (red) passes correspond to magnetic quiet days.

The first step in the satellite data selection consisted in a more restrictive selection based on the Kp index, to avoid as much as possible the disturbances from ionospheric and magnetospheric fields. Coles [1985], as said before, proposed a maximum value of 1- for this planetary index when analysing the Magsat data at high latitudes. After this selection, the percentage of measurements not considered with respect to the original data sets was around the 50% for POGO and Magsat satellites, and around 60% for Ørsted, and Champ missions.

Since Kp index does not report the activity in Polar regions, the next step was the selection following an auroral index like AE. The maximum absolute value allowed for AE was 50 nT, as in Ravat *et al.* [1995]. The values for AE were nevertheless not available for 2002 at the moment in which this work was developed, so no AE selection was applied for Ørsted and Champ missions from epoch 2002.0.

Problems with the AE index however arise in case of a persistent positive value of the vertical component of the interplanetary magnetic field. In that situation, the auroral oval moves towards the pole reducing its size, so AE values can be small (because the AE observatories will be outside the auroral range) as if no disturbance was indicated in the polar cap [Langel and Hinze, 1998]. By this reason, another selection was applied based on the PC index. Unfortunately, this index is only available from 1978 for Vostok observatory (i.e., for the South Polar cap), and no values are computed for 1980, so the selection based on the PCI was only applied to Ørsted and Champ missions. In some way, PCI provides some indication of the activity in the auroral zone for both these satellites since (as said before) AE index was not available for year 2002. A threshold value of 0.3 for the absolute value of the PCI was therefore adopted, contributing also to make the number of data from each different satellite mission of the same order.

After all these selections based on the different indices, the remaining data were selected imposing a maximum height for the satellite measurement. A maximum limit was chosen for 900 km height, since only OGO-4 presented a significant number of values above this altitude. The final number of data after each one of the different selections is listed in table III.5. It can be seen from the comparison between table III.5 and table III.4 that, after the application of all the selection criteria the original data sets have been reduced around a 90% for OGO-2, OGO-4, Ørsted, and Champ missions, and around a 80% for OGO-4 and Magsat satellites. The distribution of the final data for each mission is shown in figure III.17. Magnetic measurements are available for almost the whole Antarctic continent, except the region near the geographic pole due to the orbital parameters of the different missions. The size of this region without data depends on the satellite, being smaller for Champ and OGO-4 missions (6° and 8°, respectively),

and going up to  $16^\circ$  for the OGO-6 and  $13^\circ$  for the Ørsted missions. On the other hand, figure III.18 represents the distribution in height of the total field data points used for each mission.

Satellite	$K_p \leq 1 -$	$AE \leq 50 \text{ nT}$	$ PC  \leq 0.3$	height $\leq 900 \text{ km}$
OGO-2	462	259	PCI not available	66
OGO-4	1,872	1,138	PCI not available	1,116
OGO-6	12,539	4,916	PCI not available	3,414
Magsat	876	341	PCI not available	341
Ørsted	8,064	5,929	2,077	2,077
Champ	8,871	5,811	2,256	2,256

**Table III.5.** Number of remaining total intensity values for each one of the magnetic satellite missions considered in this work after the application of the different selection criteria.

The proper satellite coverage of the region under study, despite the different restrictive criteria imposed, confirms that it is not necessary to use data from the dayside interval for the development of the model, reducing in this way the contribution of the external currents. The importance of this choice is reflected if two different data sets, one containing data from the dayside Hemisphere and another containing data from the nightside Hemisphere, are modelled independently. In order to produce these models, 2,716 dayside total intensity measurements from Ørsted satellite were selected according to the  $K_p$ ,  $AE$ , and  $PC$  indices imposing the same criteria presented before for the selection of the 2,077 Ørsted nightside values. Two different SCHA models were therefore developed in a separate way, one for each data set. Both models considered only an internal expansion with  $K_{\max}=12$  and  $L_{\max}=2$  for the two years and a half covered by the data. The root mean squares with respect to the input data were 9.8 nT for the day data, and 5.5 nT for the nightside data, indicating that the diurnal data are more contaminated than the night set. Figure III.19 shows the differences found between both models synthesised for epoch 2000 at 700 km height. The maximum differences are found on the vicinity of the Geomagnetic South Pole, and it demonstrates that the inclusion of dayside data could introduce an important external contamination into the model.

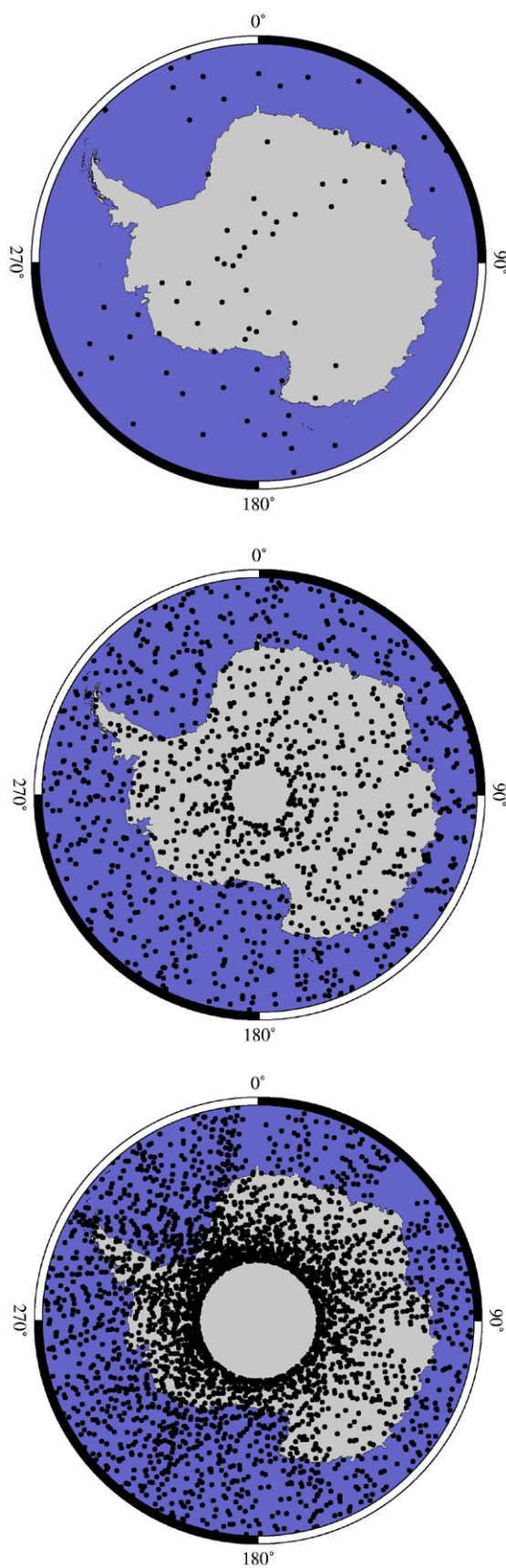


**Figure III.17.** Spatial distribution of the magnetic measurements from OGO-2 (top), OGO-4 (centre), and OGO-6 (bottom) missions used to develop the Antarctic Reference model.

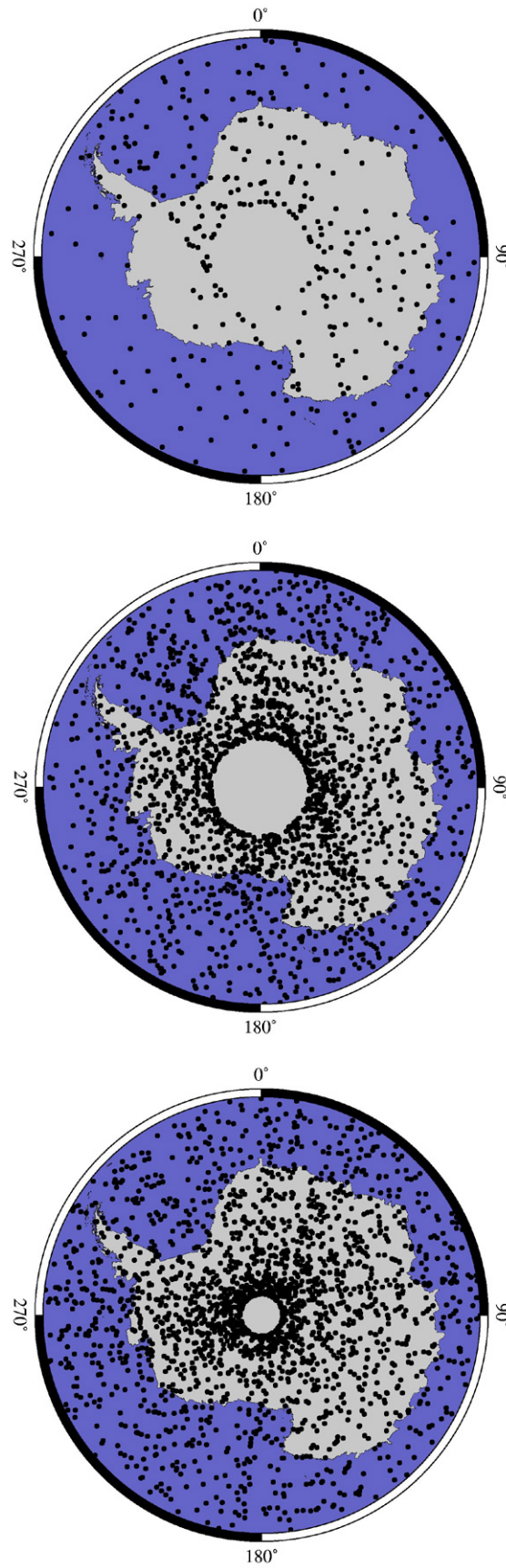


**Figure III.17 (continued).** Spatial distribution of the magnetic measurements from Magsat (top), Ørsted (centre), and Champ (bottom) missions used to develop the Antarctic Reference model.

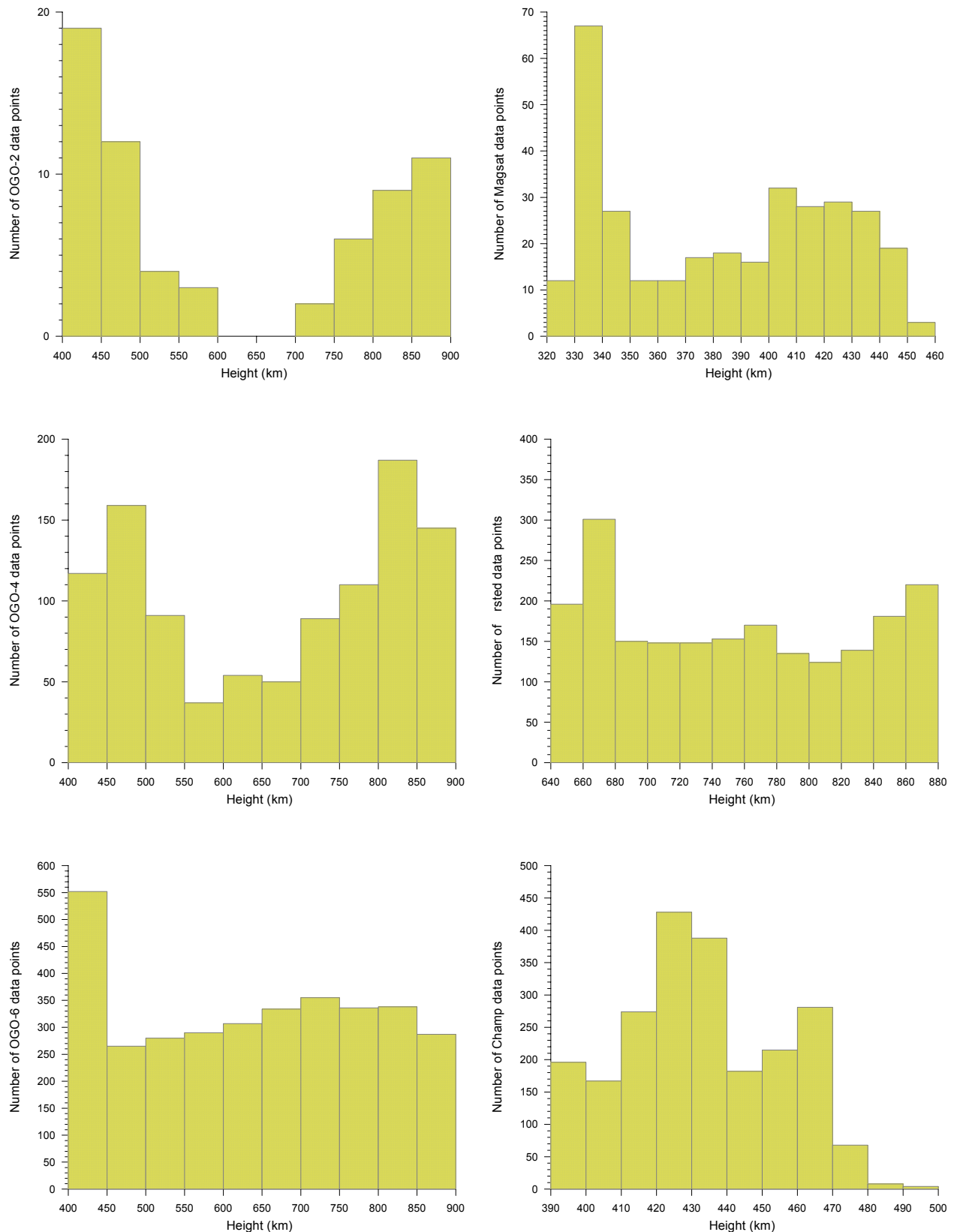


**Figure III.18.** Distribution in height of the total field measurements used from each satellite mission, from top to bottom and from left to right, OGO-2, OGO-4, OGO-6, Magsat, Ørsted, and Champ. Note that the axis ranges change for each histogram.



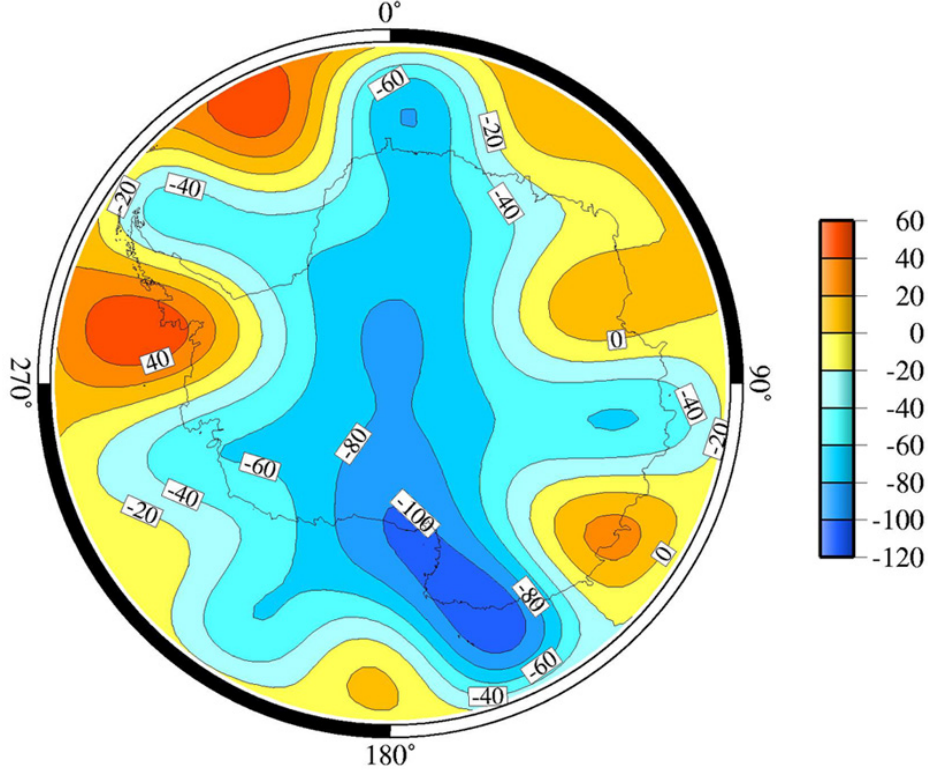


**Figure III.19.** Differences found between a SCHA model developed from dayside total field Ørsted data and another one from nightside values, for epoch 2000 at 700 km height. Contour lines each 20 nT.

To finish with the description of the criteria used to select the satellite datasets, no restriction was applied regarding the Dst index. Olsen *et al.* [2000], for example, imposed that the maximum value allowed for the index during the time of the measurement was  $|Dst| \leq 10$  nT, with a maximum temporal variation  $|dDst/dt| \leq 3$  nT/h with regard to the previous 3-hour value. This criteria is nevertheless useful when dealing with data taken at low latitudes, far from the region considered in this work, so it was not applied for our data since the criteria imposed were considered to be restrictive enough.

## IV. The Antarctic Reference Model

Once the data sets have been selected and the mathematical approach defined, the Antarctic Reference model is presented in this chapter. Several tests were applied in an attempt to improve the model. The parameters that define the model were chosen in order to give account of all the necessities expressed at the beginning of this work: the reference model must be a proper representation of the magnetic field of core origin and also of the longest wavelengths of the crustal field below 60° South latitude; it has to be a compromise between a good fit of the input data and an accurate representation of the field in those places without data (i.e., overfitting has to be avoided); and its temporal validity takes into account the former magnetic surveys carried out in Antarctica.

### IV.1. Data weighting

The different data sets included in the model were weighted according to the reciprocal of the variance of the total error of the measurement, so a weighted least squares regression was applied [Draper and Smith, 1966]. Each variance was computed as the sum of two contributions, one for the error associated to the measurement (instrumental errors, etc.),  $\sigma_m$ , and the other related to the part of the crustal field not represented by the model,  $\sigma_c$ .

Different errors were assigned to each set of data. The higher the altitude at which measurements were carried on, the lower the value of the crustal error, so  $\sigma_c$  is supposed to change depending on the altitude at which data were taken. On the other hand, the different reliability of the various data sets makes compulsory the choice of diverse values of  $\sigma_m$ . From a mathematical point of view, weighting is required to satisfy the conditions to apply the method of least squares, that is, the variances of the observations have to be equal. As pointed out by Haines [1993], some assumptions have to be made about the crustal field bias  $\bar{\delta}(\vec{r})$  in equation (II.11) to achieve this requirement. Besides a variance value equal to  $\sigma_c$ , the covariance has to be zero for different observatories. This hypothesis is true if the data come from no too close observation points. This fact, that is reasonable for ground data, can be questioned for satellite measurements, affecting the uncertainty in the least squares coefficients.

The values for the different variances were given according to the estimations made in previous papers. In this sense, following Haines and Newitt [1997] a value  $\sigma_c=200$  nT was chosen for the observatory data, taking into account that the Antarctic observatories present high bias values because of the anomalous areas in which they are usually forced to be deployed. For

the satellite data,  $\sigma_c=0$  nT was chosen for the satellite missions flights at highest altitudes, i.e. POGO and Ørsted missions, whereas  $\sigma_c=5$  nT was decided for Magsat and Champ. Finally,  $\sigma_c=50$  nT was fixed for the Boomerang stratospheric measurements. Regarding the measurement error,  $\sigma_m=10$  nT was selected for the observatory and the balloon data, and also for Magsat, Ørsted, and Champ satellites, whereas  $\sigma_m=25$  nT was decided for POGO missions because of the lower accuracy of the instruments carried by these satellites.

## IV.2. Model parameterisation

The spherical, and spherical cap, harmonic methods intrinsically permit to undertake the joint inversion of diverse data sets with different spatial resolution as, in our case, the combination of satellite data with ground or near ground data. However they suffer at some level from the frequency overlap between the spectra of the various source fields, both in the spatial and temporal domains. Satellite data provide small-scale spatial information, but only for short durations, while observatory annual means cover in some way the entire domain, but only provide broad-scale spatial information [Sabaka *et al.*, 2002]. Nevertheless, if the model parameterisation is efficient such a limitation can be taken into account. In the following it will be shown how for the Antarctic Reference Model the class of chosen basis functions and their particular parameters are restricted in order to achieve optimal results.

The least squares method assumes that the regression model (i.e., the determined spherical harmonic series) fits properly the input data. This is not completely true since the expansion is finite, so the higher harmonics can contaminate the lower ones, phenomenon called aliasing. A method to minimize this effect avoiding the filtering of data, is the expansion up to high enough degrees of the harmonic expansion of the potential, so the contribution from the non accepted harmonics is negligible.

The spherical cap in which the model was defined, centred at the geographic South Pole, was chosen with a half-angle of  $30^\circ$ , enough to cover the Antarctic territory and surrounding marine areas. The temporal coverage of the model was decided between 1960.0 and 2005.0, approximately the epochs for the first and the last input data. The temporal expansion was computed through the method of main field differences presented in section II.1. Cosine functions were chosen to represent the temporal variation of the model, since these functions have derivative equal to zero at the edges of the temporal interval of the model, reducing the problems related to extrapolation. A visual evidence of the kind of problems that can be encountered for a model developed using polynomials as temporal functions is shown in figure

IV.1. Due to the few observatory annual means available for the beginning of the time range studied, a total intensity map for epoch 1960.0 can be considered like a sort of extrapolation. The contour lines for a constant value of  $F$  present fictitious oscillations. These undulations disappear when cosine functions are used, as it will be shown in the maps presented in the next chapter.

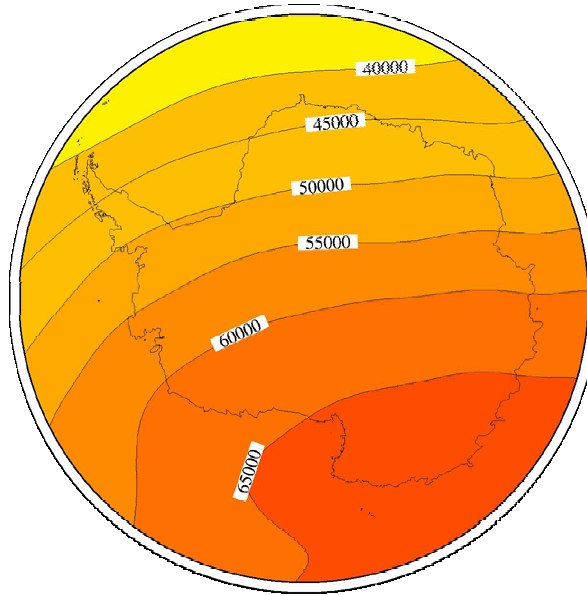


**Figure IV.1.** Map for the total intensity field (in nT) computed for 1960.0 at sea level by using a previous SCHA model, which considered polynomials as temporal functions. Fictitious oscillations can be noted in the different contour lines.

Different models were developed using only internal coefficients with a maximum index up to  $K=16$  in the spherical cap spatial expansion (II.7) for the potential of the magnetic field. A variable maximum temporal order was decided depending on the value of the spatial index:  $L=4$  was assigned for  $K=0$  to 4,  $L=1$  for  $K=5$  to 7, and  $L=0$  was given to the functions with spatial index  $K=8$  or higher. In this way, the temporal variation of the higher degree harmonics was avoided. No improvement was obtained when moving to higher temporal degrees. Table IV.1 shows the fit of the model to the input observatory data, and table IV.2 that to the satellite and Boomerang data, for some of the generated models. The fits of the global models IGRF 9<sup>th</sup> generation and CM3 with respect to the input data sets are also presented for comparison (all the IGRF-9 coefficients up to degree  $n=13$  for year 2000 were used to obtain the misfit values). The accuracy of the fit can be enhanced by going to higher values for the spatial expansion (it is clearly shown in the case of the stratospheric data), but overfit will make the model unrealistic. For example, it can be appreciated in table IV.1 an improvement in the root mean square of the fit to the observatory data for models with  $K=12$  or higher. Nevertheless, the field contours show fictitious oscillations in those regions without data when representing the values of the magnetic

components for a given epoch and height using high degree models. Figure IV.2 shows for example the maps for the X, Y, Z, and F elements computed at sea level for epoch 2000.0 using a SCHA model with K=16. IGRF-9 computed at 1980.0 has been removed to emphasize the undulations involved in a model with such a high degree for the spatial expansion.

		RMS (nT)			
Model		X	Y	Z	F
SCHA mdoels	K=4	673	611	1369	1409
	K=6	684	620	1365	1406
	<b>K=8</b>	<b>678</b>	<b>612</b>	<b>1359</b>	<b>1399</b>
	K=10	678	611	1357	1397
	K=12	677	609	1351	1391
	K=14	678	606	1344	1385
	K=16	678	607	1360	1399
IGRF-9		694	600	1372	1411
CM3 <sub>internal</sub>		690	611	1365	1403

**Table IV.1.** Misfit in terms of root mean square of some developed models (with changing index for the spatial expansion) to the observatory data. Fits of IGRF-9 and CM3 (only internal contributions) are shown for comparison. The results for the final SCHA model adopted are highlighted.

		RMS (nT)						
Model		OGO-2	OGO-4	OGO-6	Magsat	Champ	Ørsted	Boomerang
SCHA models	K=4	43.3	25.9	18.0	15.2	13.8	12.1	72.4
	K=6	30.7	18.6	13.0	13.8	11.0	9.6	72.7
	<b>K=8</b>	<b>22.9</b>	<b>13.4</b>	<b>11.4</b>	<b>13.2</b>	<b>9.8</b>	<b>9.4</b>	<b>74.2</b>
	K=10	23.6	13.8	11.5	12.9	9.9	9.4	69.5
	K=12	23.6	13.9	11.7	13.1	9.7	9.3	62.3
	K=14	21.4	13.6	11.4	13.9	10.1	9.6	56.7
	K=16	20.5	13.1	11.2	12.6	10.2	9.5	54.2
IGRF-9		21.9	21.7	22.5	14.7	19.0	19.7	60.4
CM3 <sub>internal</sub>		16.6	22.3	22.2	21.4	24.8	24.5	51.0
CM3 <sub>int+ext</sub>		6.3	5.8	5.3	3.7	4.6	3.3	51.0

**Table IV.2.** Misfit of some developed models (with changing index for the spatial expansion) to the satellite and Boomerang data. Fits of IGRF-9 and CM3 (only internal, and internal plus external contributions) are shown for comparison. The results for the final SCHA model adopted are highlighted.

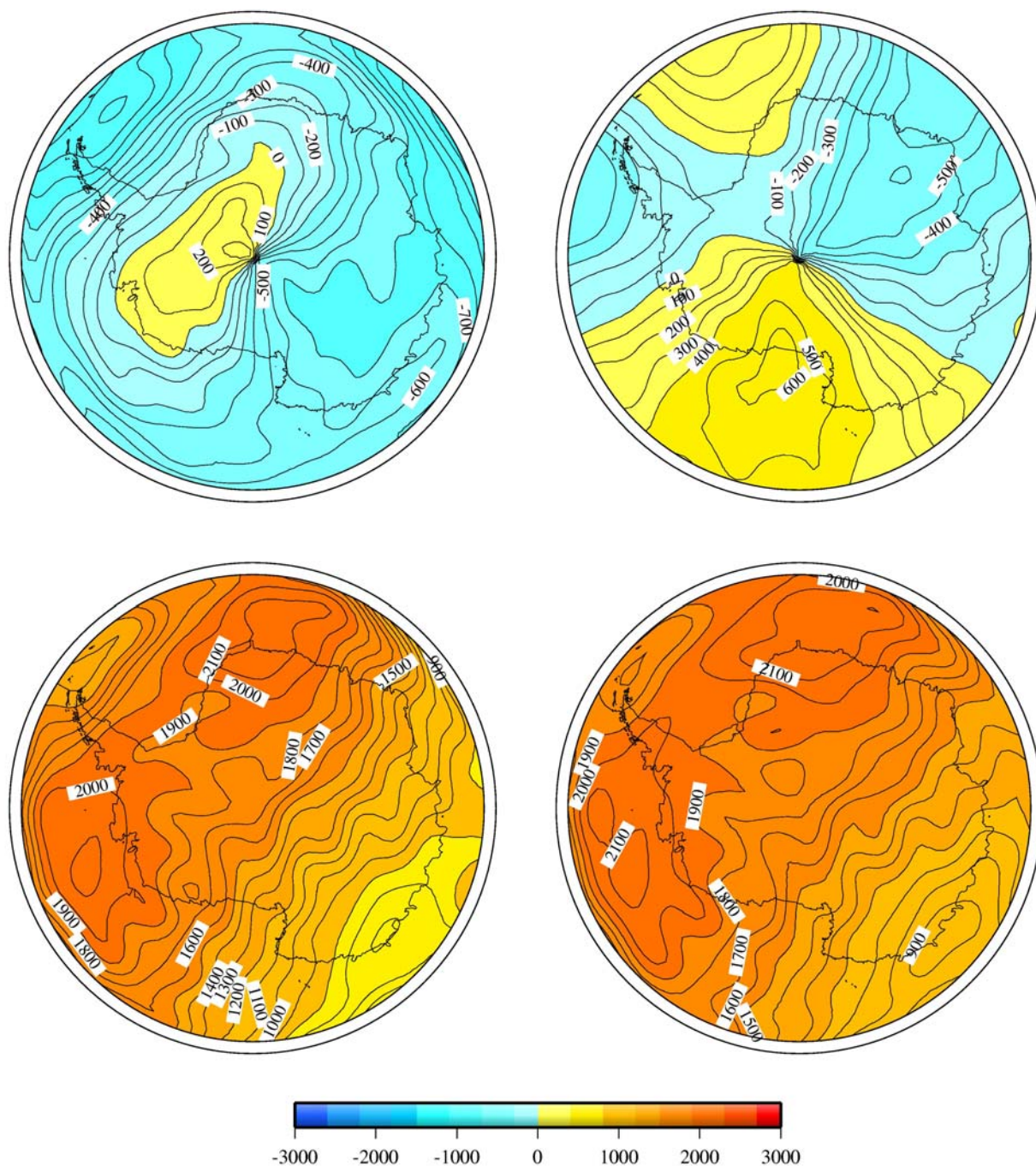


**Figure IV.2.** Magnetic maps, in nT, produced by using a SCHA model with  $K=16$  at epoch 2000.0 (sea level) for X (top left), Y (top right), Z (bottom left), and F (bottom right) magnetic elements. IGRF-9 computed at 1980.0 has been removed to highlight the fictitious oscillations in the contour lines given by such a model.

Another aspect to be taken into account is the theoretical wavelength supposed to be represented by the model. For example, the maximum value of the degree  $n_k$  that is root of equations (II.4) and (II.5) is equal to 24.95 for the model with  $K=8$ . It means that the spectral content of this spherical cap model is equivalent to that of an ordinary spherical harmonic model



of approximately degree 25. Hence following equation (II.19) the model can represent features of the geomagnetic field of wavelengths down to 1,600 km. For comparison, a model like IGRF ( $n_{\max}=10$ , except for the year 2000 coefficients for IGRF 9<sup>th</sup> generation, in which case  $n_{\max}=13$ ) can represent wavelengths down to 4,000 km; for the comprehensive model CM3 the maximum degree for the expansion of the field considered to be of nuclear origin is  $n=13$ , whereas the crustal field reaches the value  $n_{\max}=65$ , corresponding to features of wavelengths down 600 km.

In the previous secular variation model developed by Torta *et al.* [2002], the fit to synthetic input data was also used to decide the degree of the spatial expansion. A truncation index  $K=5$  was established on the basis of the fit to a regular grid of IGRF values. A similar approach has been followed here to have complementary information for the choice of the maximum  $K$  value. The decision was to synthesise the model values at the real input data locations, i.e. the observatory positions, and the Boomerang and satellite places where  $F$  values were measured; in this way, the particular configuration of the real data distribution was preserved. The synthetic values were obtained through the CM3 up to degree  $n=13$ , and the misfit to synthetic data was computed using models with maximum expansion  $K=4$  to  $K=16$ . The results are shown in figure IV.3, for observatory and satellite data. It can be seen how the rms fit values are high for low values of  $K$ , the inflexion point being around  $K=7-8$ . All the models were developed using cosine series for the temporal expansion, but the results are similar when using polynomials.

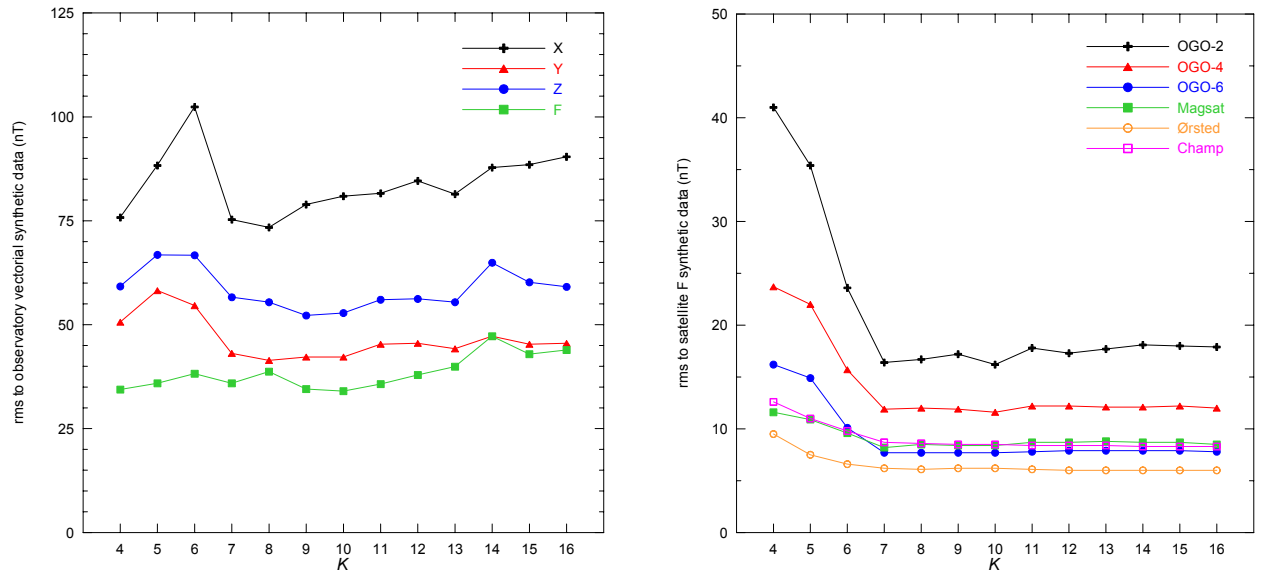


**Figure IV.3.** Misfit in terms of root mean square of some SCHA models to the synthetic input data sets, as a function of the maximum  $K$  index of the spatial expansion for each model. The synthetic values were computed using the CM3 at the real locations of the data used in the development of the ARM.

### IV.3. Results

Keeping all the above considerations in mind (fit to real input data, no overfitting, minimum wavelength represented, fit to synthetic input data, etc.), the model with  $K=8$  was finally chosen as the Antarctic Reference Model (ARM). A value of  $F=4$  was applied for the F-level in the stepwise regression procedure to obtain the coefficients of the model. This procedure includes variables in turn into the inversion process, to check the significance of each given coefficient until a convergence in the solution is reached [Draper and Smith, 1966]. If the contribution from a given coefficient is nonsignificant, that variable is removed and the appropriate regression is computed using the remaining coefficients. A new coefficient is then checked: if it passes the F entry test, it is entered and all the variables in are checked; if it fails, a further removal is attempted. Since the relationship between variables change at each regression, the best coefficient at a given step can be negligible at another stage. The process stops when no coefficients can be removed and no other variables are significant enough to be included.

Some objections can be made to this variable rejection method, since small but well-determined coefficients are removed from the regression, and large poor resolved coefficients can be accepted. As pointed in Haines and Torta [1994], the use of this method, as well as of the least squares procedure, is just a choice to determine the coefficients of the model. It is expected that the regularisation approach recently presented by Korte and Holme [2003] will improve the inversion method (see the conclusions chapter for more details).

From the set of 405 possible coefficients in a model with  $K=8$  for the spatial and  $L=4$  for the temporal expansions, the restriction  $F=4$  reduces the number of coefficients to 163. For example, the IGRF model needs 120 coefficients at five-year intervals to define the main field, so in such a long period like that considered in this work (45 years), the number of coefficients required is more than one thousand. The coefficients that define the Antarctic reference model are presented in table IV.3.

It must be considered that the model was developed using as input data not the data sets discussed in the last chapter, but their residuals with respect to a previous main-field model: the IGRF-9 evaluated at 1980.0 (approximately the mid-point of the temporal interval) was removed from each observation before doing the inversion to obtain the coefficients. In this way, the number of iterations to obtain the coefficients of the model was reduced, because of the faster convergence to the input data. There is also a statistical motivation, this is, the removal of a global reference model is equivalent to the strengthening of the power spectrum from high wave numbers, since aliasing from long wavelength fields is minimized. Hence the final model is the



combination of the spherical cap harmonic coefficients and the DGRF coefficients for 1980. In order to compute the value of the SCHA model for a given epoch and location, it is therefore necessary to add to the spherical cap model the value of the IGRF-9 for that location at 1980.0.

$k$	$m$	$n_k(m)$	$g_{k,q=0}^m$	$h_{k,q=0}^m$	$g_{k,q=1}^m$	$h_{k,q=1}^m$	$g_{k,q=2}^m$	$h_{k,q=2}^m$	$g_{k,q=3}^m$	$h_{k,q=3}^m$	$g_{k,q=4}^m$	$h_{k,q=4}^m$
0	0	.000000	200.463		464.645		-43.103		213.761		-157.998	
1	0	4.083687	-78.931		712.558		30.524		-61.019		35.477	
1	1	3.119597	.000	76.134	-55.282	-49.673	-47.753	9.462	.000	-31.341	-22.300	.000
2	0	6.835398	89.574		-571.613		17.398		71.606		.000	
2	1	6.835398	.000	-57.410	-96.534	-81.008	47.614	33.078	.000	-9.220	20.203	26.373
2	2	5.492825	-6.033	-76.981	5.314	-199.231	-26.870	11.912	12.458	-7.267	.000	31.481
3	0	10.038550	-54.333		453.079		-32.043		-39.419		-24.228	
3	1	9.712069	-1.035	42.028	124.557	127.876	-29.240	-28.181	-10.415	9.677	-7.003	-27.318
3	2	9.373283	.000	93.238	.000	198.499	13.252	-7.930	-9.295	.000	.000	-21.448
3	3	7.752442	4.127	1.552	-74.491	107.311	18.201	12.684	-1.985	-4.994	15.364	14.624
4	0	12.908284	17.641		-379.878		15.235		16.039		12.552	
4	1	12.908284	2.556	.000	-111.649	-142.087	14.337	13.076	5.750	-7.761	3.972	16.716
4	2	12.372043	-8.301	-89.862	-5.783	-232.408	-11.586	-2.178	-2.644	.832	1.145	4.548
4	3	11.807398	-5.617	.000	74.561	-106.729	-6.116	.000	-3.371	5.095	-7.558	-4.521
4	4	9.958907	-4.569	-1.093	39.605	-9.551	3.564	-5.204	-1.490	.000	5.245	-1.350
5	0	16.024836	.000		242.550							
5	1	15.821528	.000	-38.071	77.568	116.284						
5	2	15.615372	2.380	59.061	.000	168.669						
5	3	14.918042	.000	.000	-74.433	93.204						
5	4	14.177771	.000	.000	-27.113	-9.928						
5	5	12.133388	1.511	-3.749	2.512	.000						
6	0	18.936446	.000		-110.423							
6	1	18.936446	.000	44.637	-25.777	-49.497						
6	2	18.583016	.000	-24.039	.000	-85.265						
6	3	18.221949	.000	.000	43.508	-53.551						
6	4	17.390980	.000	.000	20.449	12.841						
6	5	16.504141	.000	1.492	-1.307	-1.337						
7	0	22.018287	-2.227		27.331							
7	1	21.870167	.000	-28.424	.000	10.243						
7	2	21.720958	.000	.000	.000	19.313						
7	3	21.246148	2.105	.000	-14.486	18.498						
7	4	20.758775	.000	.000	-9.235	-7.848						
7	5	19.812087	.000	.000	.000	3.609						
7	6	18.797908	.000	-.715	-2.223	.000						
7	7	16.422823	.000	-1.066	1.161	.000						
8	0	24.951381	3.019									
8	1	24.951381	-2.884	7.821								
8	2	24.685780	.000	2.722								
8	3	24.417002	-2.570	1.454								
8	4	23.838976	-2.129	-1.172								
8	5	23.243683	.000	.966								
8	6	22.194042	-1.067	.000								
8	8	18.547237	1.211	.000								

**Table IV.3.** Coefficients for the Antarctic Reference Model.  $g_{k,q}^m, h_{k,q}^m$  are the spherical cap harmonic coefficients of order  $m$  and degree  $n_k(m)$  for the degree  $q$  of the temporal expansion.

### Fit to observatory data

Once the model has been presented its validity has to be checked. Table IV.I detailed the root mean square fit to the input observatory data for different models compared to those given by IGRF-9 and CM3. Although the differences are statistically unimportant, ARM improves the fit to X, Z, and F elements of the magnetic field with respect to the global models, whereas it is a bit worst in the case of the Y component measured at the Antarctic geomagnetic observatories.

Once the coefficients of the model are determined, the anomaly vector bias from the solution can be computed for each one of the observatories used as input data. This kind of bias is estimated as in Langel *et al.* [1982b] as the mean difference between the real value of each component and the value predicted by the model for all annual means for a given observatory. In recent models like the CM3 the observatory biases are among the parameters to be determined. Table IV.4. shows the bias estimated through the ARM together with the anomaly vector values given by Langel *et al.* [1982b], and Sabaka *et al.* [2002] for some of the observatories used.

It can be seen that the biases estimated by the ARM mostly agree with those given by Langel *et al.* [1982b]. Some similarities are also found when comparing to the bias determined by the CM3. There are nevertheless some discrepancies for certain observatories. Important disagreements can be for example found for HBA (an observatory with data available only for the first part of the temporal range covered by the model, and without any other observatory close to it), and for the X component of MAW and MOL. Nevertheless the differences between the ARM biases and those computed by the other models do not follow any clear correlation. Figure IV.4 shows for example the evolution of the differences between ARM biases and the biases from Sabaka *et al.* [2002] with the magnetic latitude: no clear dependence is observed. On the other hand, high bias like those for SBA, SPA, or for the Z component of DRV are given by all three models. There is also agreement with the biases presented in Manda and Langlais [2002] for the three Antarctic magnetic observatories considered in that work, i.e. DRV, MAW (again, except for the X component of this observatory), and SBA. The differences can be therefore due to the diverse methods applied by each author to obtain the biases values, and to the different datasets used to compute the models with which biases were obtained.

Observatory	Bias (nT)			Observatory	Bias (nT)		
	X	Y	Z		X	Y	Z
AIA	-44.2	-86.8	305.6	SNA2	-27.6	-21.5	-20.2
	69.3	-83.5	512.8		-51.4	-19.1	28.6
	106.9	-36.4	564.7		48.1	38.8	45.1
WIL	718.7	-314.7	74.6	NVL	-358.1	-46.8	127.4
	619.2	-296.5	29.4		-310.9	72.4	194.6
	683.1	-394.8	128.3		-202.6	64.3	195.3
MIR	-115.6	12.1	-441.8	HBA	210.3	315.2	-295.8
	-135.1	50.2	-428.5		-26.3	400.2	-7.4
	-44.9	13.0	-410.3		72.3	449.9	-137.9
DRV	-74.9	-439.0	-2823.2	SBA	-2158.7	-1008.7	-3766.7
	-172.8	-389.2	-2687.6		-2276.1	-936.6	-3766.9
	-237.1	-391.2	-2662.4		-2232.1	-922.3	-3812.2
MAW	145.3	19.0	174.8	BYR2	-28.2	33.6	-36.4
	16.7	25.0	197.7		-24.2	37.5	-147.2
	13.0	-39.1	131.6		81.0	68.5	-74.9
MOL	173.4	-91.2	-288.8	SPA	-1282.8	-3416.4	146.6
	-40.6	-95.5	-207.4		-1342.7	-3469.6	79.8
	-28.7	-90.8	-165.3		-1300.6	-3576.7	-76.8

**Table IV.4.** Anomaly vector bias as estimated through the Antarctic Reference Model (top value inside each cell), together with the values found by Langel *et al.*, [1982b] (middle) and those computed by Sabaka *et al.* [2002] (bottom).

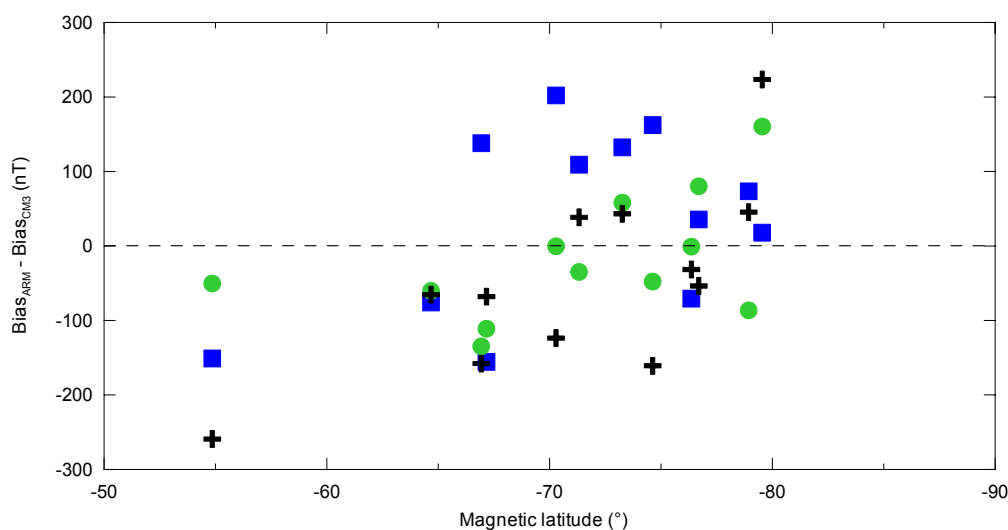


**Figure IV.4.** Evolution of the differences between ARM biases and those given by Sabaka *et al.* [2002] with respect to the magnetic latitude of each observatory, for X (blue squares), Y (green circles), and Z (black crosses) magnetic components.

Still more important than the fit to observatory data used in the development of the model, it is necessary to check how the model predicts (historical or future) data which were not considered. Torta *et al.* [2002] checked the secular variation model for Antarctica excluding Vostok data from the analysis and developing a second model, in order to compare the new model with the excluded observatory data set. The authors adopted this strategy due to the impossibility to obtain new Antarctic magnetic data sets. In spite of all the aforementioned difficulties, it has been possible to obtain an old data set for Georg von Neumayer Station (GVN, -70.617°S, 351.633° E) [A. Eckstaller, personal communication]. It consists of a set of total intensity field monthly means from April 1983 to February 1992. Since this dataset was obtained at the late stage of development of the model, it was decided to not consider it in the development of the model but to use GVN data to check its validity.

Annual means for GVN were computed from 1983 to 1991 for the central epoch of each year (for 1983.75 for the first year, since only monthly values from April were available), and the total intensity values were estimated using ARM model as well as IGRF-9 and CM3 (considering main and crustal fields for the latter). As can be seen from figure IV.5, ARM is the model which provides the best fit to the real data in terms of both absolute value and secular variation of the magnetic field. Numerically, the rms values for the fit to the total intensity field are 12.7 nT for the ARM, 53.0 nT for IGRF-9, and 51.1 nT for CM3. With respect to the secular variation, we can fit a straight line to the total field values predicted by each model (reasonable hypothesis looking at the figure) and compare the slopes of the different fits to that of the real data. The slope of the fit for the ARM values (-108.9 nT/year) is more similar to that of the real data (-107.1 nT/year) than the slopes found for IGRF (-97.5 nT/year) or CM3 (-102.6 nT/year). We can therefore affirm that ARM is able to predict data not used in its development.

Though Georg von Neumayer observatory changed location in 1992 [Eckstaller *et al.*, 1997], it could be argued that GVN position is almost identical to that of GVN2 station, whose data were used to develop the ARM. Hence the results presented in figure IV.5 could be just interpreted as a prove that ARM secular variation can be extrapolated in time for the considered stations, being an irrelevant test to check the reliability of the model in space. In order to verify the consistency of the model, data coming from a traverse between the French base Dumont D'Urville (DRV) and the Italian-French Concordia Station were obtained. The data correspond to nine total intensity field values taken between January and February 1994 in the George V – Adelie Land area, a region empty of measurements for the development of ARM. They were

downloaded from the website of the Ecole et Observatoire des Sciences de la Terre (Louis Pasteur University, <http://eost.u-strasbg.fr/obsmag/accueil.html>).

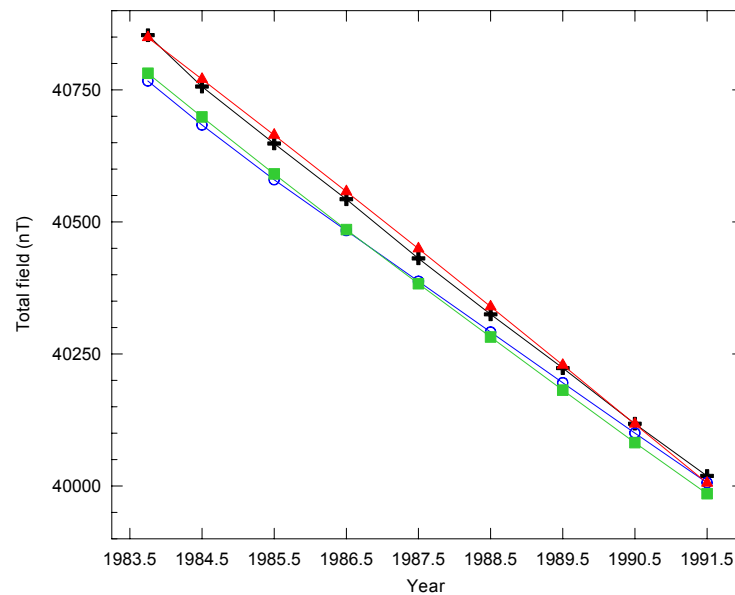


**Figure IV.5.** Total intensity field annual means measured at GVN observatory (black crosses), together with the values predicted by ARM (red triangles), IGRF-9 (blue circles), and CM3 (green squares) models.

Figure IV.6 shows the locations of these measurements, and table IV.5 the misfit of IGRF-9, CM3, and ARM to these data. Different fits are shown in the case of the Comprehensive Model, depending on whether just internal (up to degree  $n=13$  or  $n=65$ ) or internal plus magnetospheric contributions are considered for the model. It can be seen that the values predicted by ARM are closer to the real measurements than IGRF-9 values. ARM is equivalent to CM3 when only the internal (main plus crustal) field is considered for the latter, and the CM3 is slightly better only when the magnetospheric contribution is included. The spatial interpolation given by ARM can therefore be considered as reliable also in those regions devoid of magnetic observatories.

Model	RMS (nT)
IGRF-9	271.2
CM3 <sub><math>n=13</math></sub>	273.7
CM3 <sub><math>n=65</math></sub>	232.6
CM3 <sub><math>n=65</math>+magnetospheric</sub>	227.0
ARM	233.3

**Table IV.5.** Misfit of the different models to the total intensity field measured at the locations shown in figure IV.6.

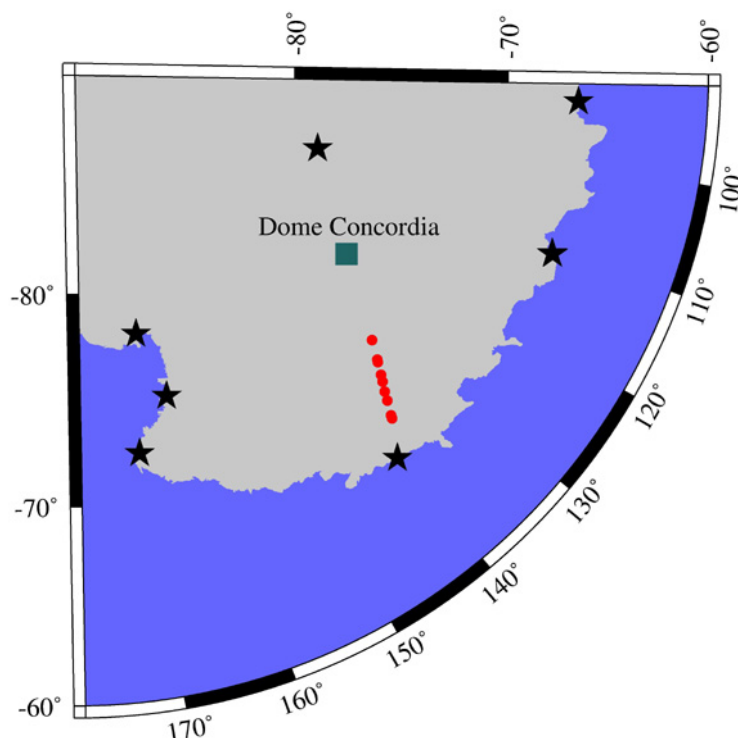


**Figure IV.6.** Location of the total field measurements made during an Antarctic traverse in 1994 (red points) together with the nearest Antarctic magnetic observatories (black stars).

#### Fit to satellite data

It was also shown in table IV.2 that ARM fits better the satellite data than IGRF-9 and CM3 when only the internal contributions for the latter one are considered. The improvement of ARM is more important than in the case of the observatory data, in some cases being greater than 50%. The only exception is the fit to OGO-2 satellite data, probably due to the few points from this mission (66) included in the development of the model. CM3 is superior when it is allowed to take into account the external field through the (previously known) values of Dst and f10.7 indices. As said before, the inclusion of external field contributions has not been considered in the ARM. In any case, the comparison of the magnetic field values predicted by all three models for some given satellite tracks (figure IV.7) shows that differences between ARM and CM3 (including all internal and external contributions) are lower than between IGRF-9 and the Comprehensive Model, independently of the region covered by the track and the epoch of the mission, except again for OGO-2. It is also remarkable, the proper fit of IGRF to Magsat data, since the IGRF coefficients for 1980 were mainly based on data from this mission.

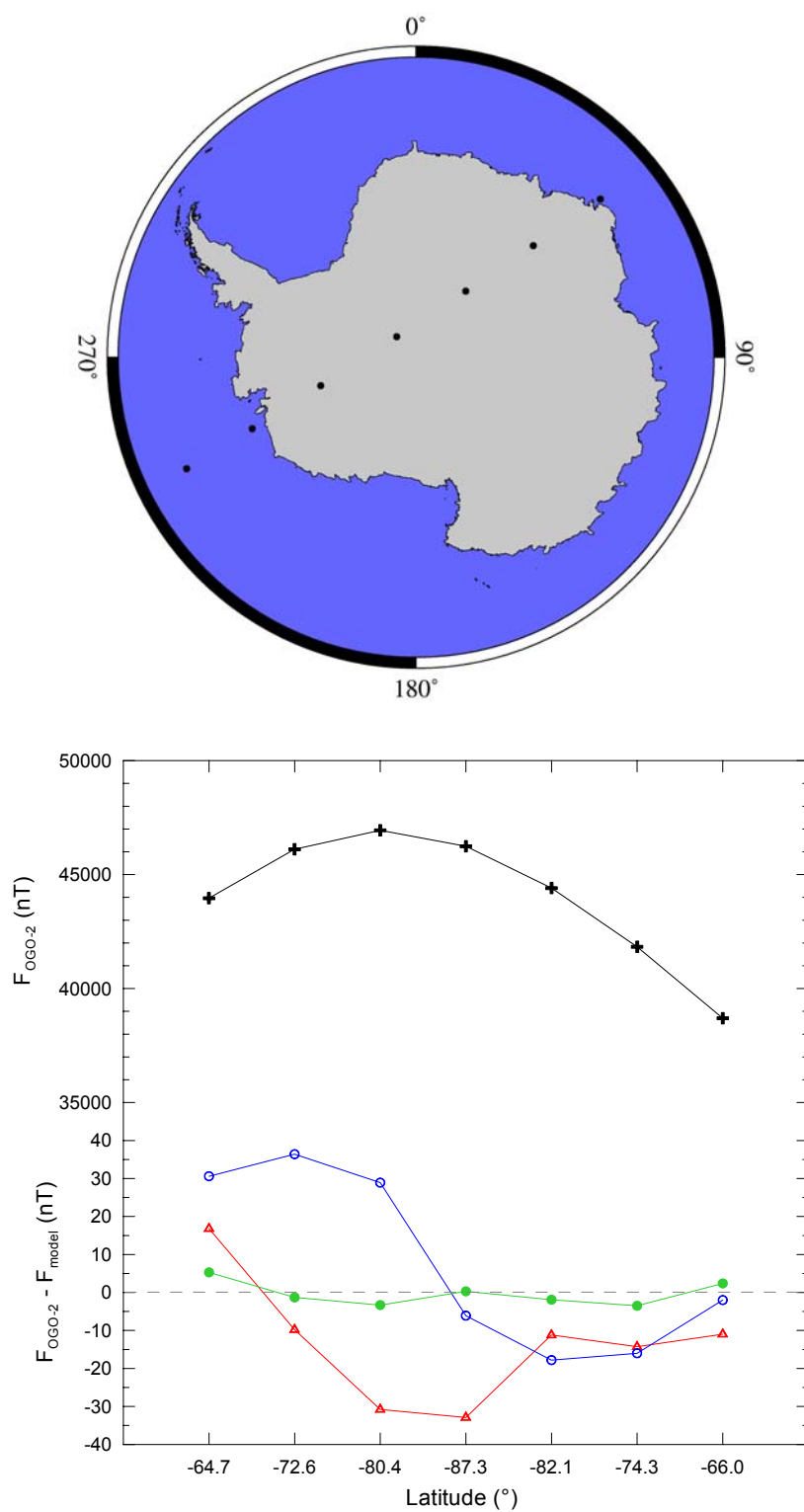


**Figure IV.7.** Total intensity measured during a track of OGO-2 satellite mission (black crosses), and its differences with respect to the ARM (red triangles), IGRF (blue open circles), and CM3 (green solid circles) models. Track shown in the top half of the figure.

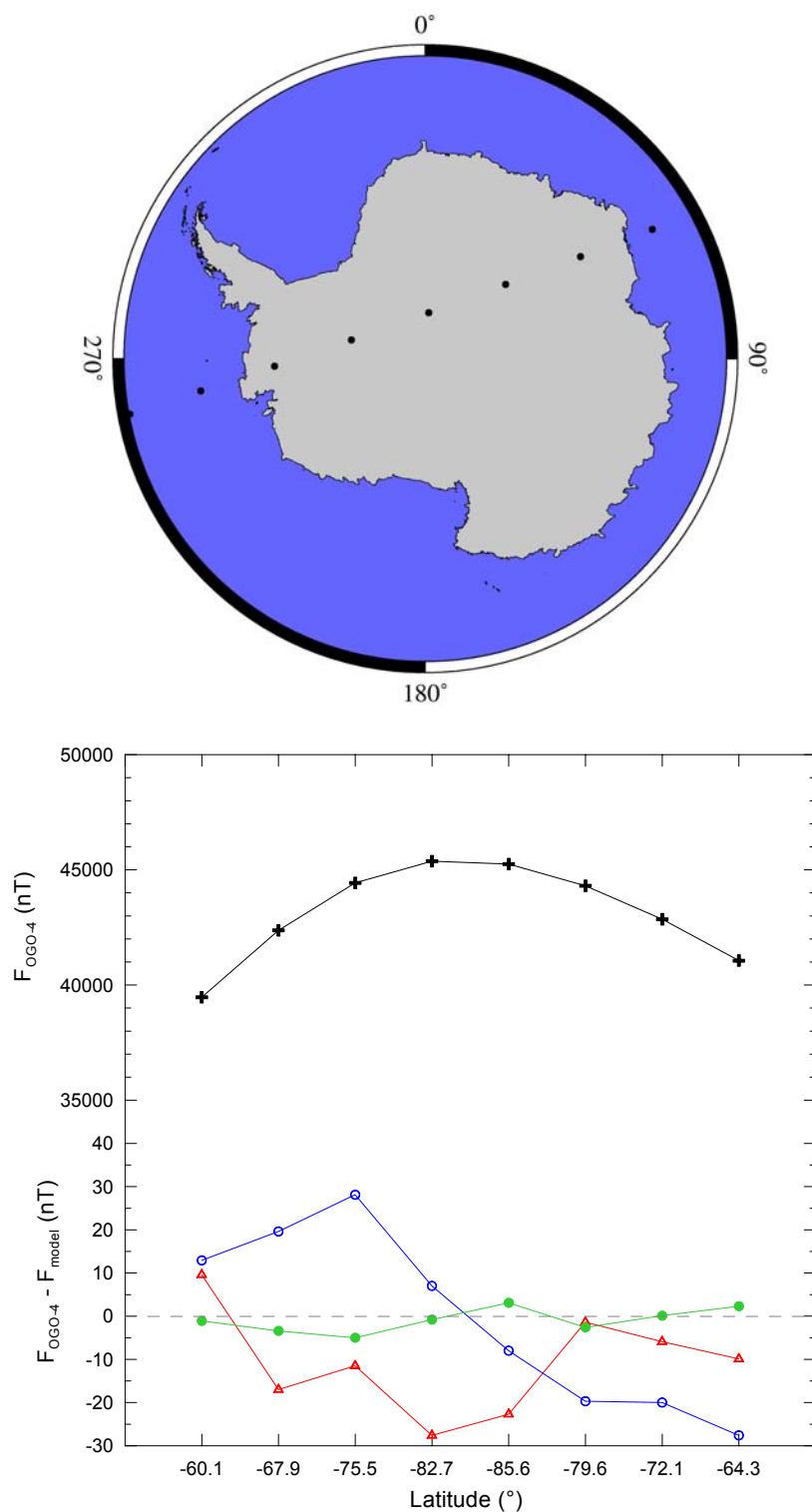


**Figure IV.7 (continued).** Total intensity measured during a track of OGO-4 satellite mission (black crosses), and its differences with respect to the ARM (red triangles), IGRF (blue open circles), and CM3 (green solid circles) models. Track shown in the top half of the figure.



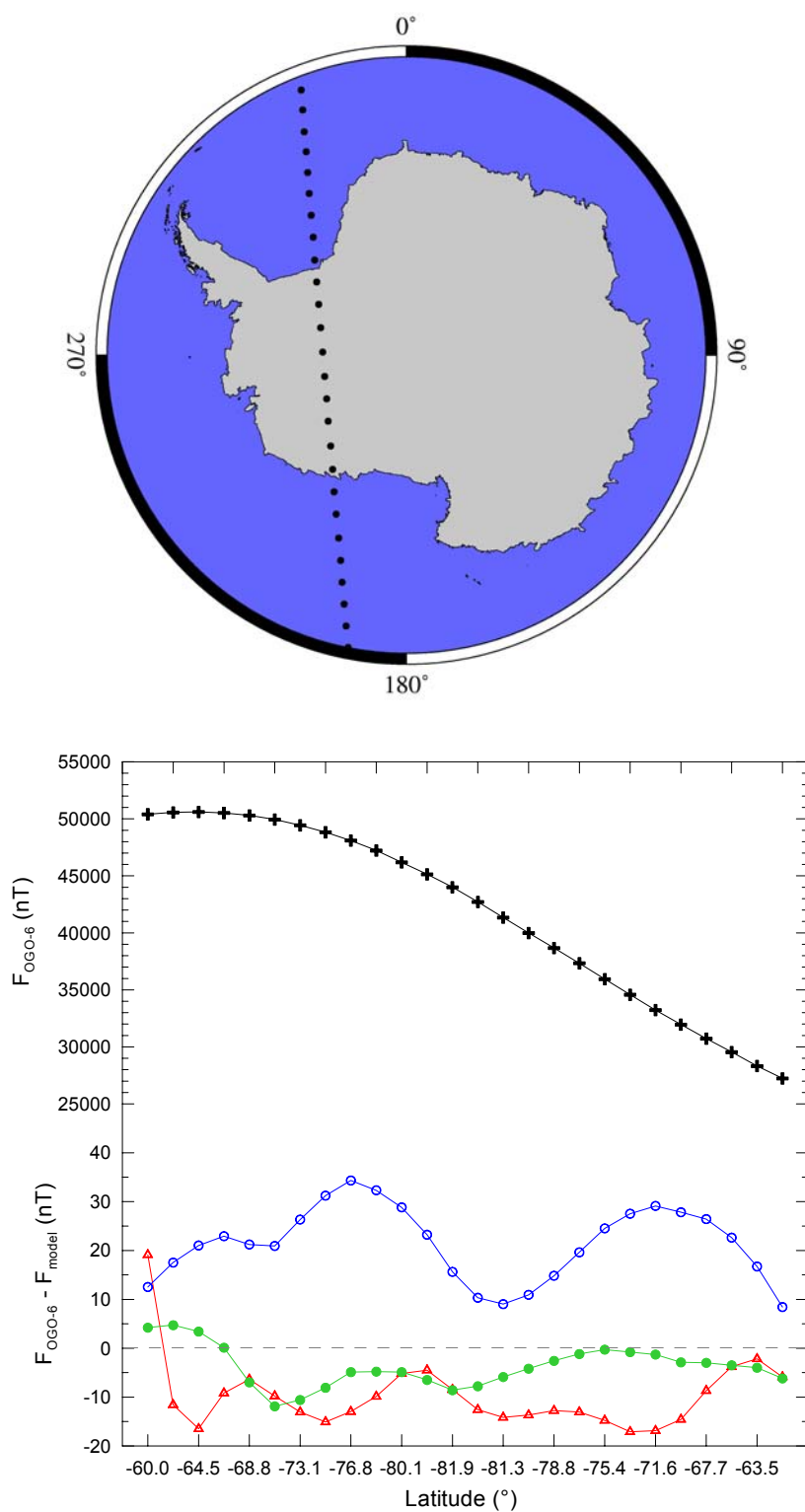


**Figure IV.7 (continued).** Total intensity measured during a track of OGO-6 satellite mission (black crosses), and its differences with respect to the ARM (red triangles), IGRF (blue open circles), and CM3 (green solid circles) models. Track shown in the top half of the figure.

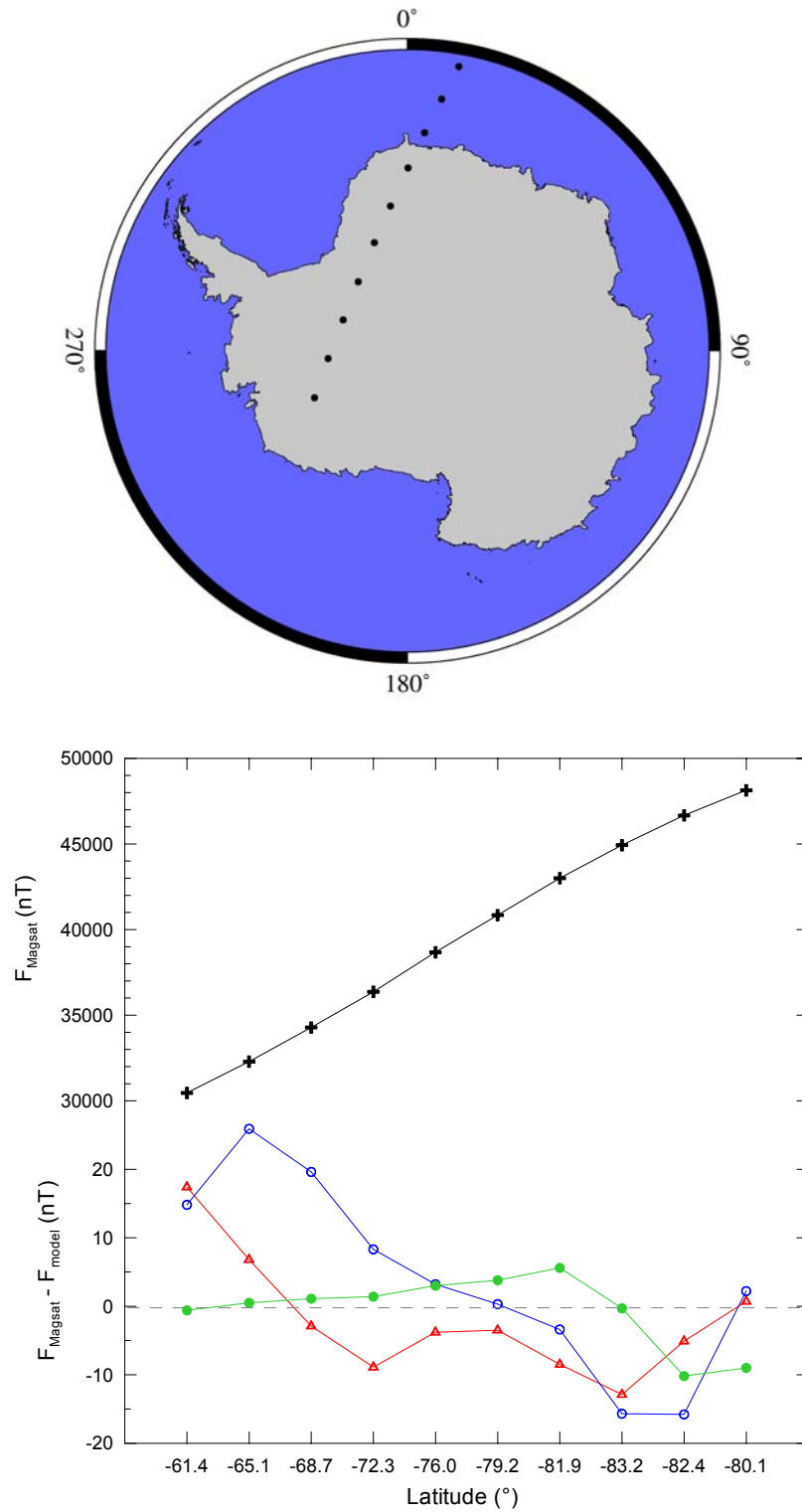


**Figure IV.7 (continued).** Total intensity measured during a track of Magsat satellite mission (black crosses), and its differences with respect to the ARM (red triangles), IGRF (blue open circles), and CM3 (green solid circles) models. Track shown in the top half of the figure.

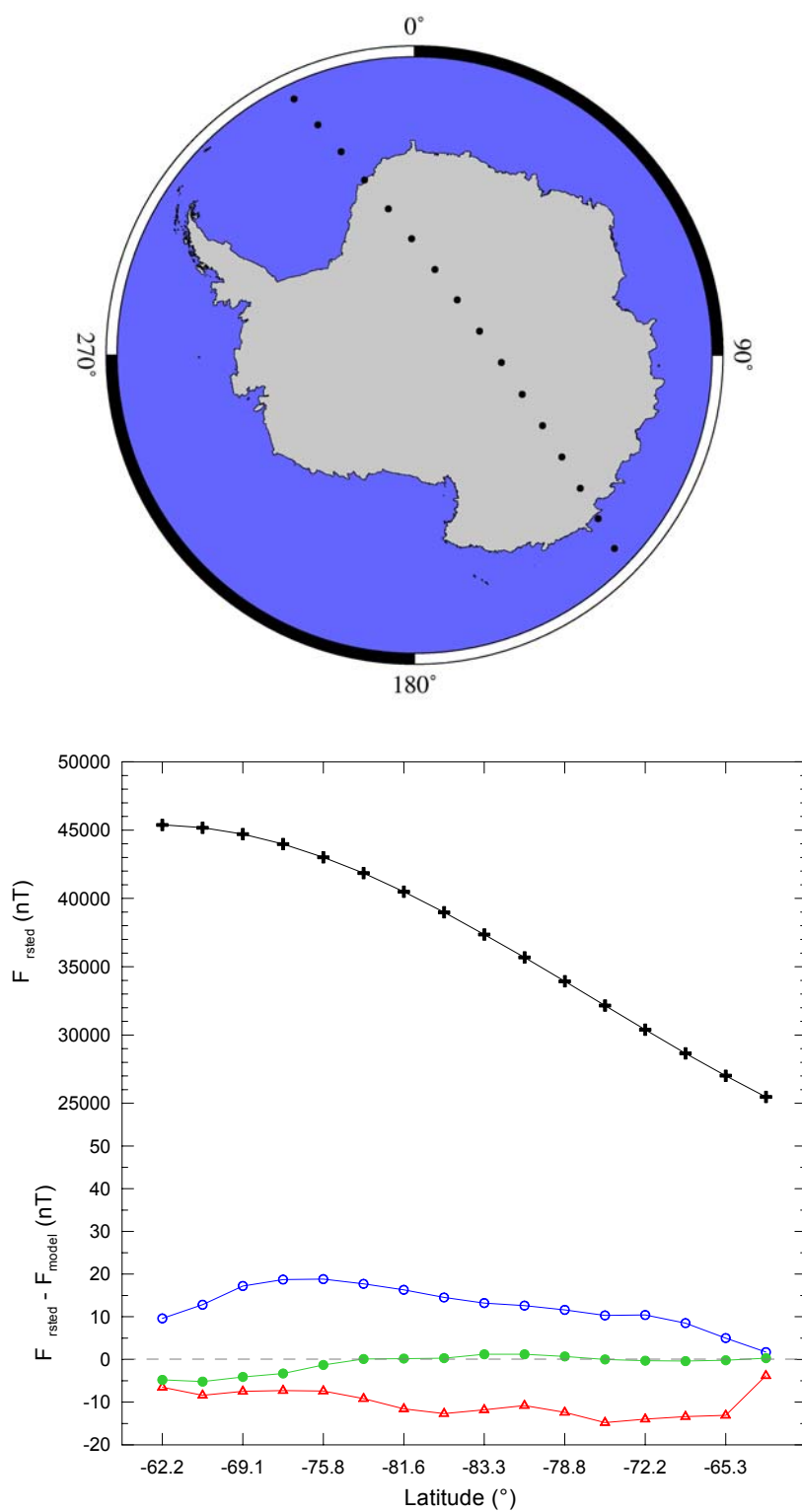


**Figure IV.7 (continued).** Total intensity measured during a track of Ørsted satellite mission (black crosses), and its differences with respect to the ARM (red triangles), IGRF (blue open circles), and CM3 (green solid circles) models. Track shown in the top half of the figure.

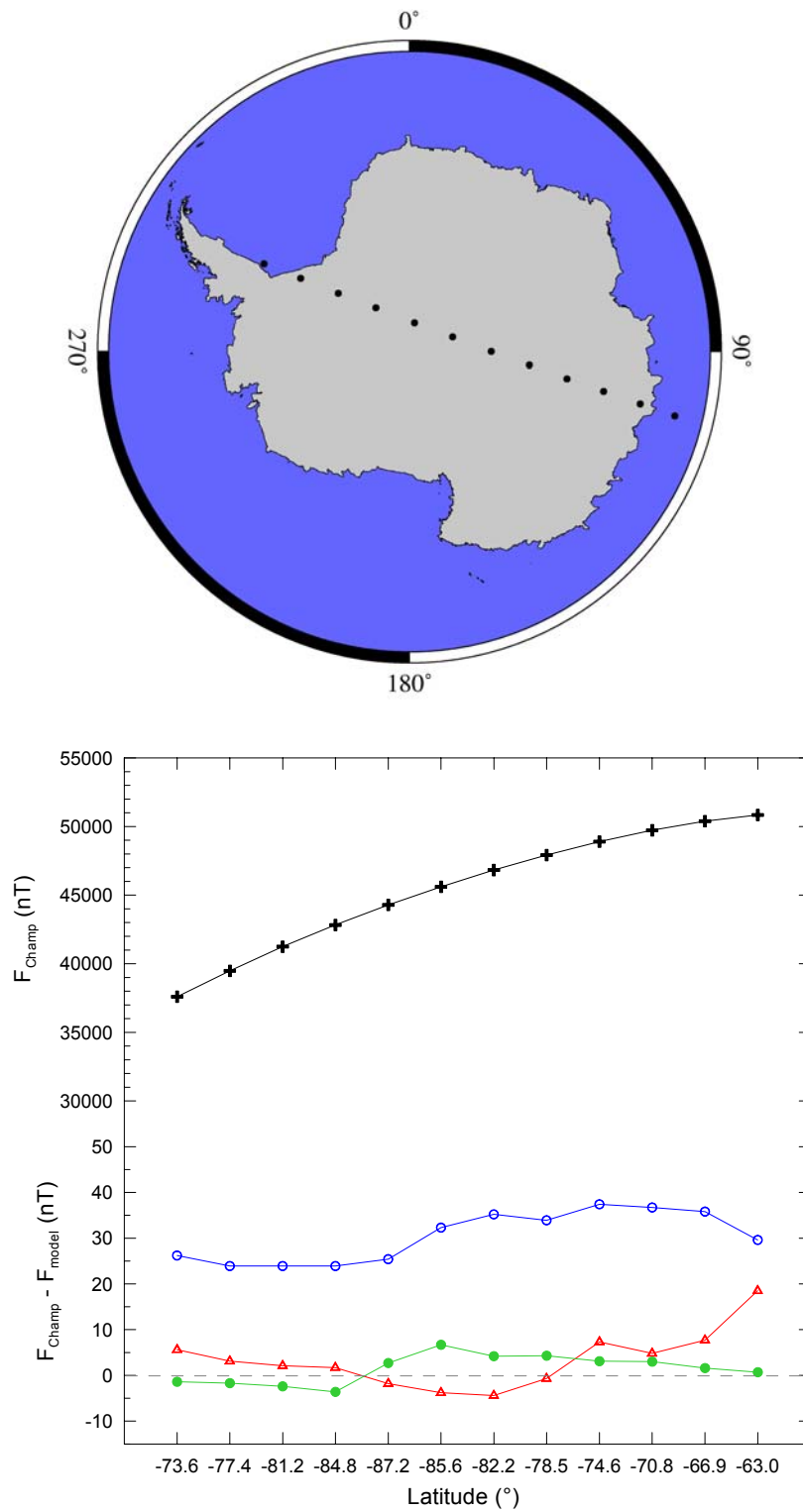


**Figure IV.7 (continued).** Total intensity measured during a track of Champ satellite mission (black crosses), and its differences with respect to the ARM (red triangles), IGRF (blue open circles), and CM3 (green solid circles) models. Track shown in the top half of the figure.

After a visual inspection of the behaviour of ARM for some selected tracks, the study of the spatial evolution of the satellite residuals can give important information about both the quality of the data and the model. Figure IV.8 shows the residuals between the measured total field and that given by ARM for OGO-6, Ørsted, and Champ as a function of the dipole colatitude  $\theta_{\text{dip}}$ . This is a more useful representation than that with respect to the geographic latitude. It consents to study the behaviour of the model for all latitudes, but also allows to identify the presence of possible external fields in the data. Largest residuals for high values of  $\theta_{\text{dip}}$  could be due to the influence of ionospheric currents in the data. As can be seen in figure IV.8, there is no a clear dependence between the amplitude of the residuals and the colatitude for Champ and Ørsted satellites, whereas the fit of a 4<sup>th</sup> degree polynomial (red line) to the residuals show that some influence from external currents is still present in OGO-6 data. This fact has to be taken into account for future versions of the model.

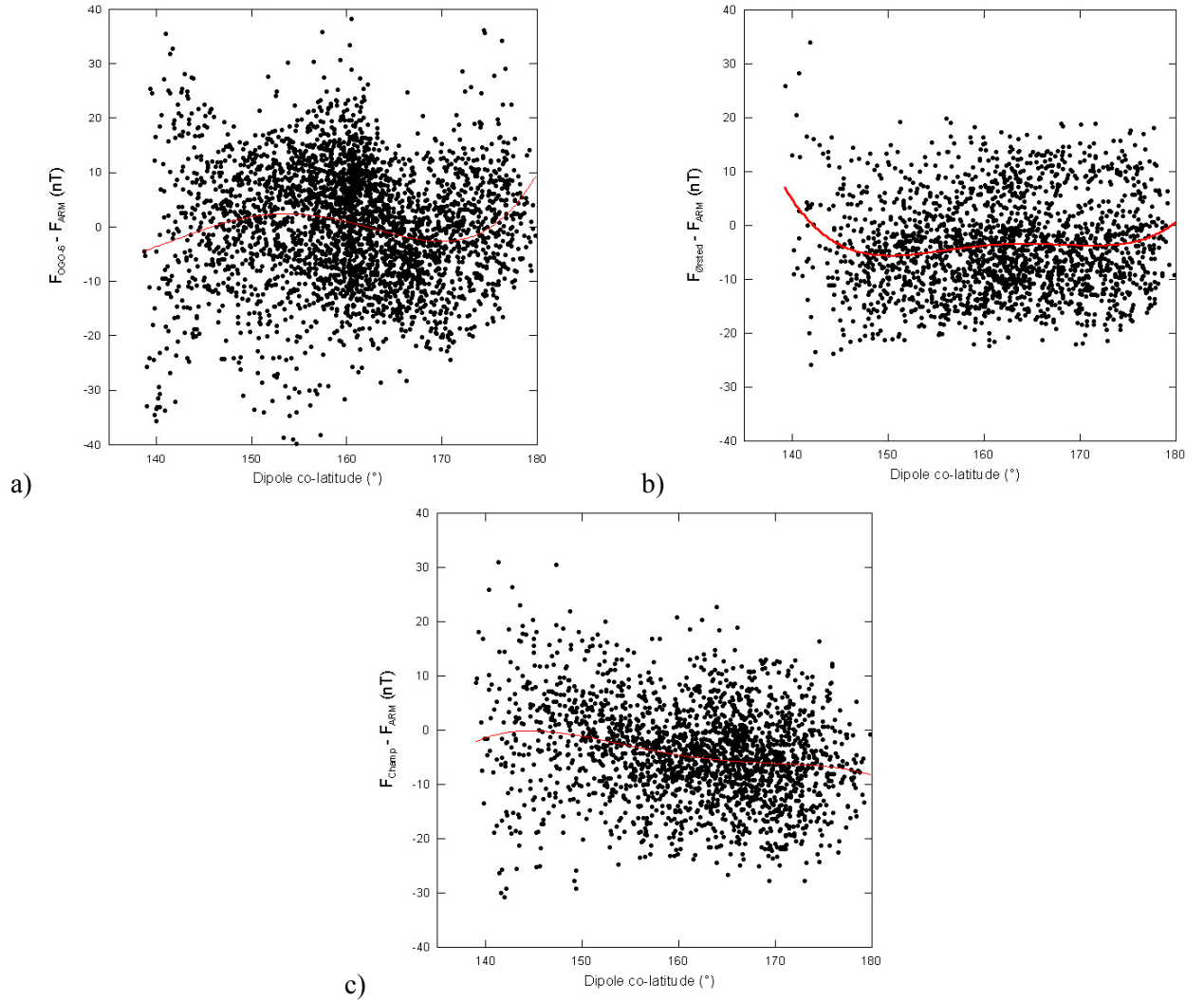


**Figure IV.8.** Evolution of the residuals between a) OGO-6, b) Ørsted, and c) Champ data and the ARM as a function of the dipole colatitude. Red line represents the fit given by a 4<sup>th</sup> degree polynomial.

The satellite data used to develop the model have been previously selected, according to the procedures described in the last chapter. By this reason, the residuals just shown between the satellite data and the values predicted by the model are more or less constant for any dipole colatitude. It is interesting to wonder how the model would appear if input satellite data would have not been selected according to the external fields.

To this aim, a SCHA model was developed using the observatory and stratospheric balloon data used for the ARM, and the original satellite data sets presented in table III.5, i.e. those data available before applying a more restrictive Kp selection, and without taking into account the values of AE and PC indices. Figure IV.9 shows the residuals between the values for Champ mission and those computed by this new model. As can be seen comparing the values to those shown in figure IV.8, the residual mean value has increased compared to the residuals found for Champ quiet data with respect to the values given by ARM (developed using quiet satellite data). Moreover, residual values increase for dipole colatitudes higher than  $160^\circ$ . This is due to the presence of external contamination in the data caused by the auroral electrojet. Figure IV.9 shows also for comparison the residuals of a SCHA model developed using synthetic data computed through the CM3 (see previous section IV.2), in this case synthetic values computed at the locations of the real Champ quiet data. There is no amplitude increase for the residuals between  $160^\circ$  and  $170^\circ$  dipole colatitude, since the synthetic data were computed using only the internal part of CM3 up to degree 13 (the larger amplitudes for low dipole colatitudes could be in this case explained by a lack of fit of the synthetic SCHA model for regions near the border of the spherical cap). This is another example of the fundamental role of data selection before the development of an internal field model.

### Secular variation of the model

Another property to be assessed is the behaviour of the model with regard to the secular variation. It has been shown that the fit to the input data is slightly better for ARM than for IGRF-9 for the case of the observatory data, whereas the fit is really improved for satellite data. The secular variation is however the most important feature to be assessed. The unrealistic secular variation pattern of models like the International Geomagnetic Reference Model results in anomaly mismatches at the edges of the surveys. Hence the original motivation to develop this Antarctic Reference Model was the possibility to have a useful tool to reduce magnetic surveys collected at different epochs.

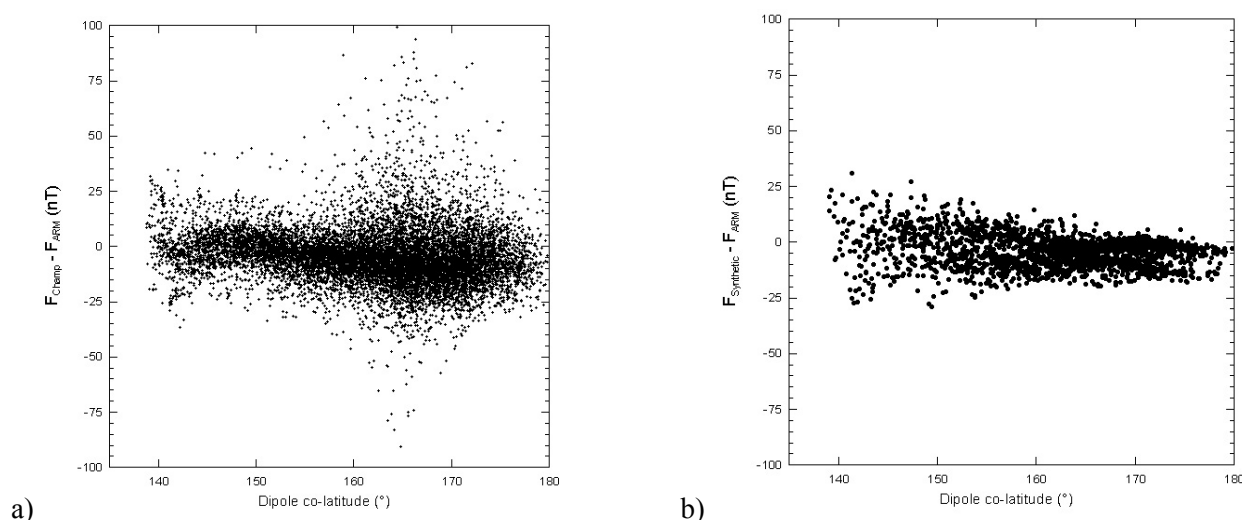


**Figure IV.9.** a) Residuals (nT) between the total intensity field measured by Champ and those values predicted by a SCHA model developed using satellite data non-selected from external fields. b) Residuals (nT) given by a SCHA model developed using synthetic data to synthetic data computed by CM3 at the locations of the real Champ quiet data.

Table IV.6 shows the comparison in terms of RMS of the input main field differences with those calculated from the SCHA, IGRF-9, and CM3 models for the overall observatory data set. The improvement relative to the IGRF-9 is around 22% for X component, 14% for Y, 29% for Z, and 31% for the total intensity field F. With respect to the CM3 the fit is almost equivalent for X and Y components, being ARM about 20% better for Z and F elements.

	RMS X (nT)	RMS Y (nT)	RMS Z (nT)	RMS F (nT)
IGRF-9	36.1	38.1	49.6	51.6
CM3	31.3	34.7	43.8	45.5
ARM	28.2	32.6	35.3	35.4

**Table IV.6.** RMS fit to observatory differences for IGRF-9, CM3, and ARM models.

The fit of ARM to each observatory is presented in table IV.7. The top value into the cell for each observatory represents for comparison the RMS between the differences relative to the respective means over the time interval and those computed from the IGRF-9; the bottom values indicate the RMS compared with the ARM predictions. It can be seen from this table that the secular change representation is improved when using ARM instead of IGRF for many of the observatories. The fit does not depend neither on the epoch nor on the position of the observatories. The Antarctic Reference Model could be interpreted to fail in the Dronning Maud

Land (region between  $0^\circ$  and  $30^\circ$  longitude approximately), because the fit to three of the observatories present in that area (SNA1, RBD2, and NWS) is better for the IGRF. However, it has to be taken into account that only two annual means are available for NWS and three for RBD2, as it was shown in figure III.2. In fact, the fit for other close observatories, like GVN2 or NVL, are altogether better when using the ARM.

Observatory	RMS (nT)				Observatory	RMS (nT)			
	X	Y	Z	F		X	Y	Z	F
ARC	15.2	23.2	10.7	5.4	RBD2	1.6	7.2	8.3	9.2
	10.9	13.9	16.0	15.6		1.1	8.8	14.9	15.1
LIV	3.1	2.0	5.4	3.7	NWS	1.5	.3	6.6	5.3
	36.2	30.0	24.5	43.8		2.2	4.3	25.1	22.7
AIA	26.6	23.7	49.0	44.6	GVN	13.9	83.1	37.6	21.9
	12.9	12.3	30.5	31.6		12.9	54.2	8.8	11.3
WIL	32.6	20.1	54.5	58.0	NVL	15.3	13.3	32.9	26.6
	20.7	17.6	13.4	10.4		14.2	17.9	25.3	22.5
CSY	70.7	29.5	81.5	80.2	HLL	12.8	21.2	9.2	10.0
	69.6	32.0	79.7	78.1		8.9	14.6	43.5	43.2
MIR	54.1	27.6	37.4	35.6	TNB	11.9	20.2	15.6	16.0
	27.5	14.6	18.1	15.3		18.3	16.9	23.7	22.3
DRV	12.9	11.1	48.9	48.4	EGS	11.5	4.1	15.9	12.1
	12.1	22.1	18.0	17.9		17.2	5.7	6.3	10.1
MAW	16.6	23.5	32.4	34.9	HBA	118.4	137.9	175.4	203.1
	30.2	16.2	15.0	14.5		34.3	107.6	101.6	100.5
MOL	51.1	38.1	43.1	48.8	SBA	12.9	20.4	27.3	21.0
	44.4	26.7	39.6	38.1		18.7	16.9	22.9	22.0
DVS	34.8	79.5	41.5	55.9	VOS	34.7	23.6	48.9	48.8
	37.5	80.5	47.8	62.3		27.7	18.3	35.7	34.2
SYO	14.6	42.1	56.0	52.2	PTU	1.7	8.7	62.5	59.8
	22.9	26.5	31.1	28.7		4.1	13.2	55.4	54.7
SNA1	7.8	11.9	12.0	10.9	BYR1	14.2	9.3	7.0	3.3
	18.8	16.9	5.8	10.8		.9	6.4	23.2	20.8
SNA2	20.9	50.2	16.9	12.9	BYR2	27.5	5.3	18.3	14.6
	16.6	64.5	10.8	8.9		5.1	17.6	20.9	18.6
SNA3	9.2	22.7	13.2	14.1	SPA	26.8	30.9	21.6	21.1
	14.1	25.1	13.0	13.4		21.9	46.7	47.1	38.7

**Table IV.7.** RMS fit to observatory differences. The top value into each cell corresponds to the RMS with regard to IGRF-9, the bottom one the RMS with respect to the ARM.



The precision of the fit to the secular change can be checked graphically. Figure IV.10 shows the fit of IGRF-9 and ARM to the differences relative to the means over all the period for four Antarctic observatories: Arctowski (ARC, red solid triangles), Syowa (SYO, blue squares), Scott Base (SBA, green clear triangles), and Vostok (VOS, orange circles). It can be seen that the values predicted from ARM (thick colour lines) follow better the real observatory data than those given by IGRF-9 (thin lines), independently of the location of the observatory.

Figures IV.11 to IV.14, on the other hand, show for a selected set of observatories the differences between the values of the real components relative to their respective means for each considered period and those relative means obtained from the Antarctic Reference Model and from the IGRF-9 model. The six observatories presented in these figures (AIA, MIR, DRV, MAW, NVL, and VOS, ordered by descending latitude) were selected in order to be a good representation of all the Antarctic territory, and all the temporal range of validity of the model. The differences with the ARM are generally smaller than the IGRF-9 for all six stations, and closer to the zero value.

An example of how ARM predicts the secular variation for all the considered Antarctic region can be found in figure IV.15, where the secular variation for 1995 for all three components and total intensity is shown. These figures were obtained from the differences found between the ARM values for epoch 1995.5 minus the values for 1994.5. The correlation of these maps with the measured secular variation (i.e. the difference between the corresponding annual means) is good for those observatories (a total of 13) that present annual mean values round about 1995.0.

With all these results in mind, it can be concluded that the Antarctic Reference Model represents the secular change better than the IGRF, with all the consequences related to the temporal reduction of overlapping magnetic surveys. The fact that ARM is a continuous model (i.e. the secular variation is defined in a continuous mode by a expansion by cosine functions) signifies an advantage with respect to a global model like the IGRF, in which the secular variation is assumed constant at five-years interval. It can be therefore expected that edge inaccuracies will not be present (or at least, they will be reduced) in merged surveys. This will be one of the subjects of next chapter.

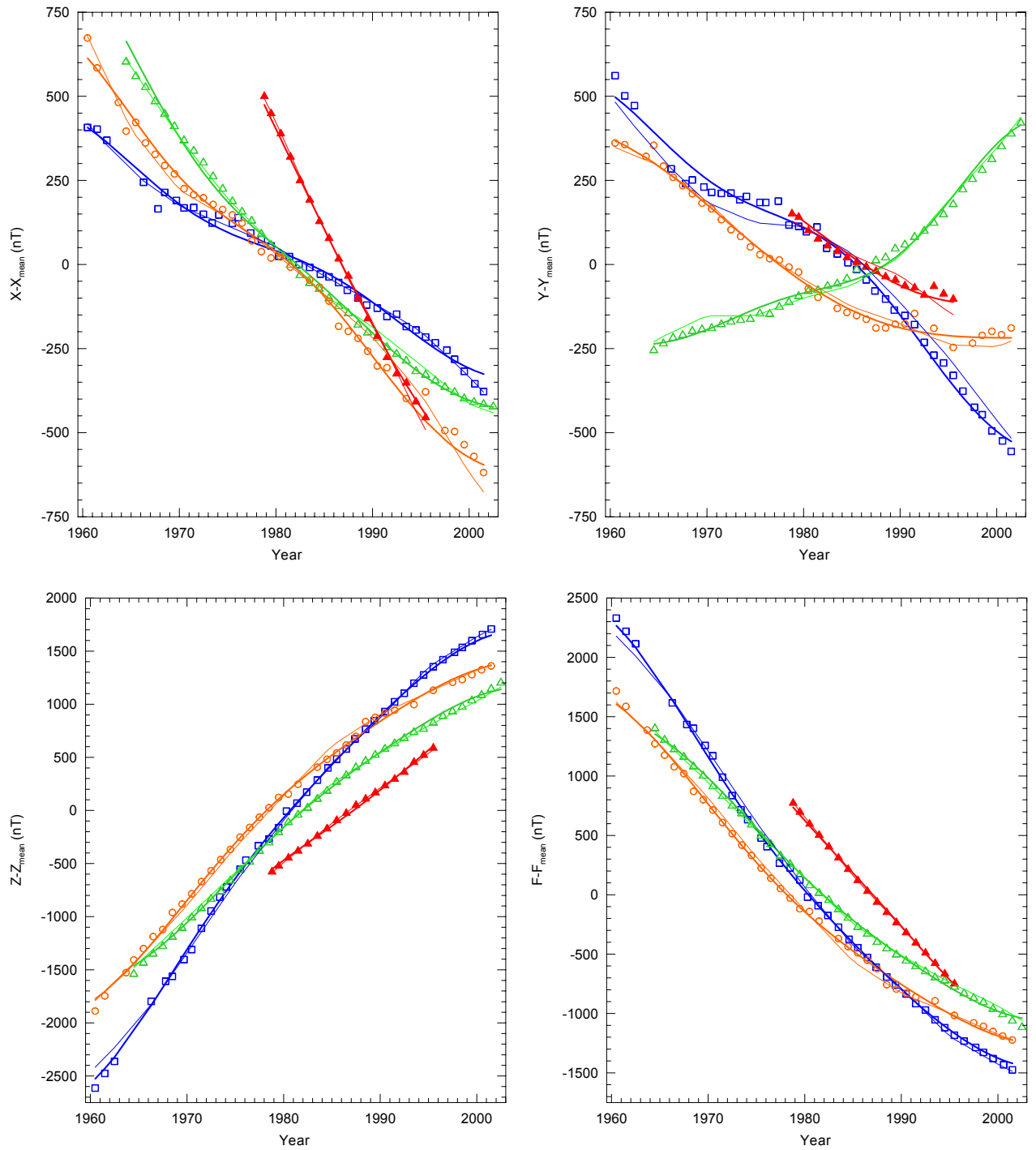


**Figure IV.10.**  $X$  (top left),  $Y$  (top right),  $Z$  (bottom left), and  $F$  (bottom right) annual means registered at ARC (red solid triangles), SBA (green clear triangles), SYO (blue squares), and VOS (orange circles) observatories relative to their respective mean values over the time period. The thick lines show the fit given by ARM, and the thin lines that by IGRF-9 (same colour code).

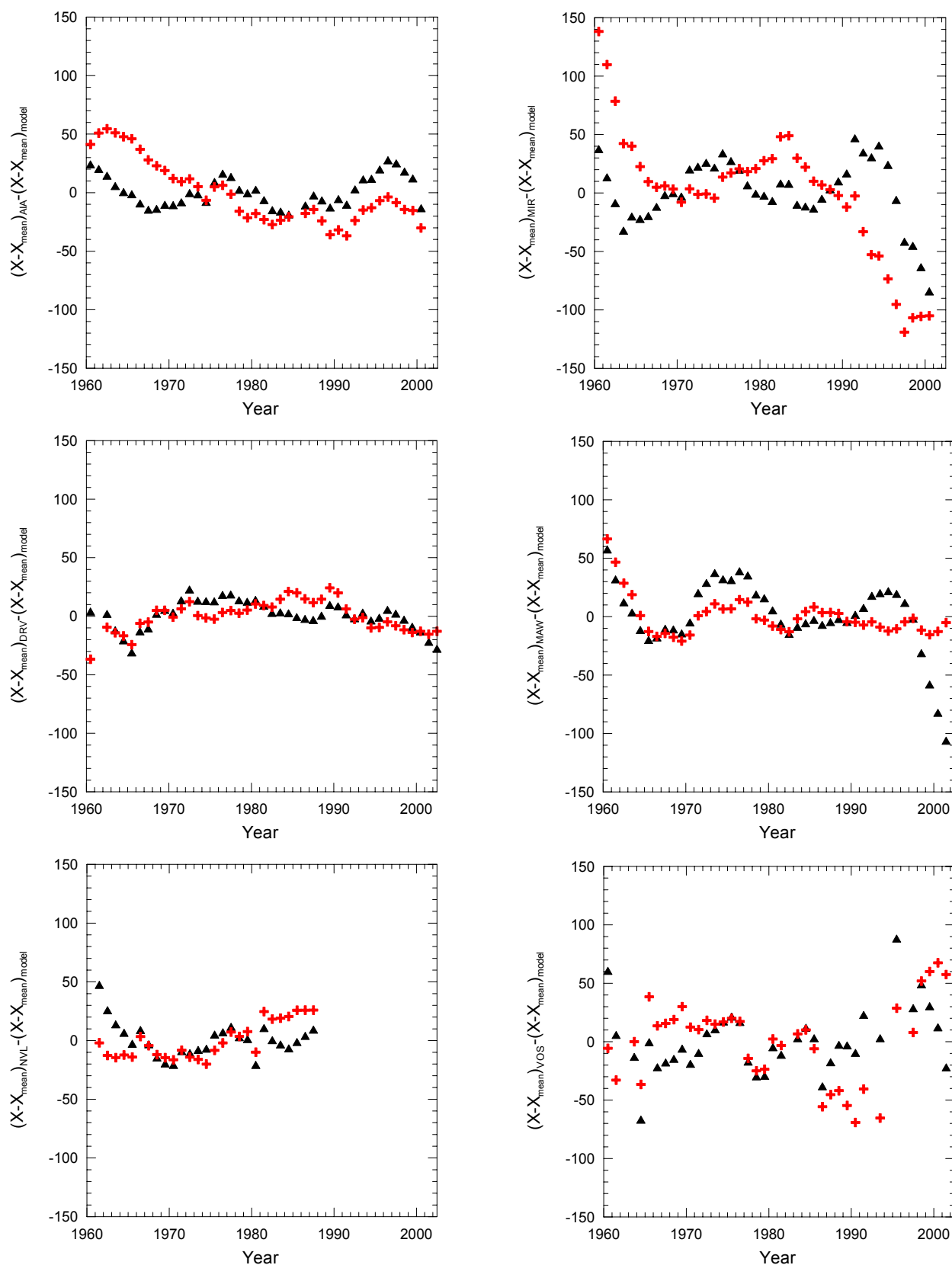


**Figure IV.11.** Comparison for a set of observatories of the differences between X component annual mean values relative to their respective means and the values predicted by IGRF-9 (red crosses) and ARM (black triangles).

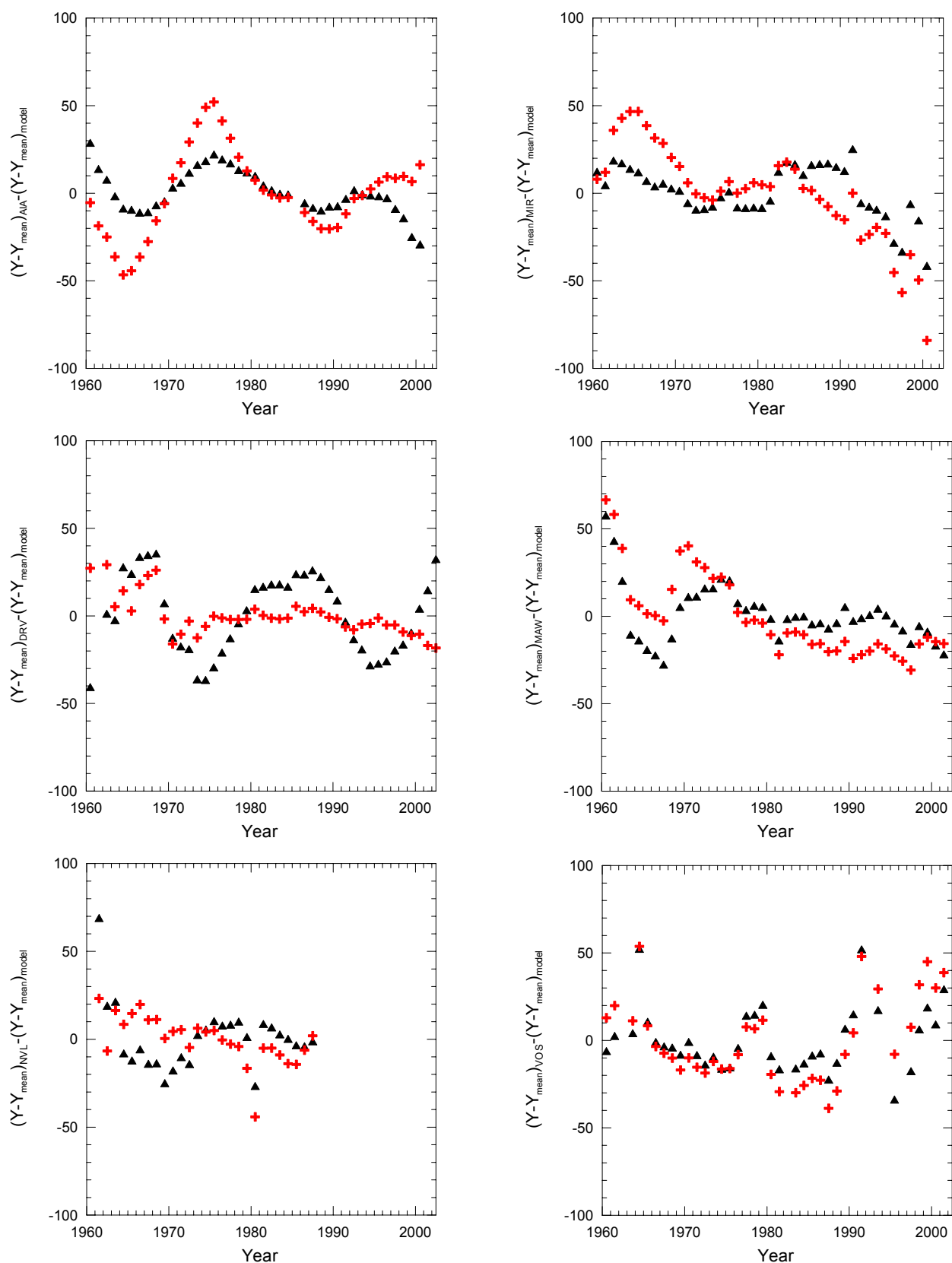


Figure IV.12. As figure IV.11 but for Y component.

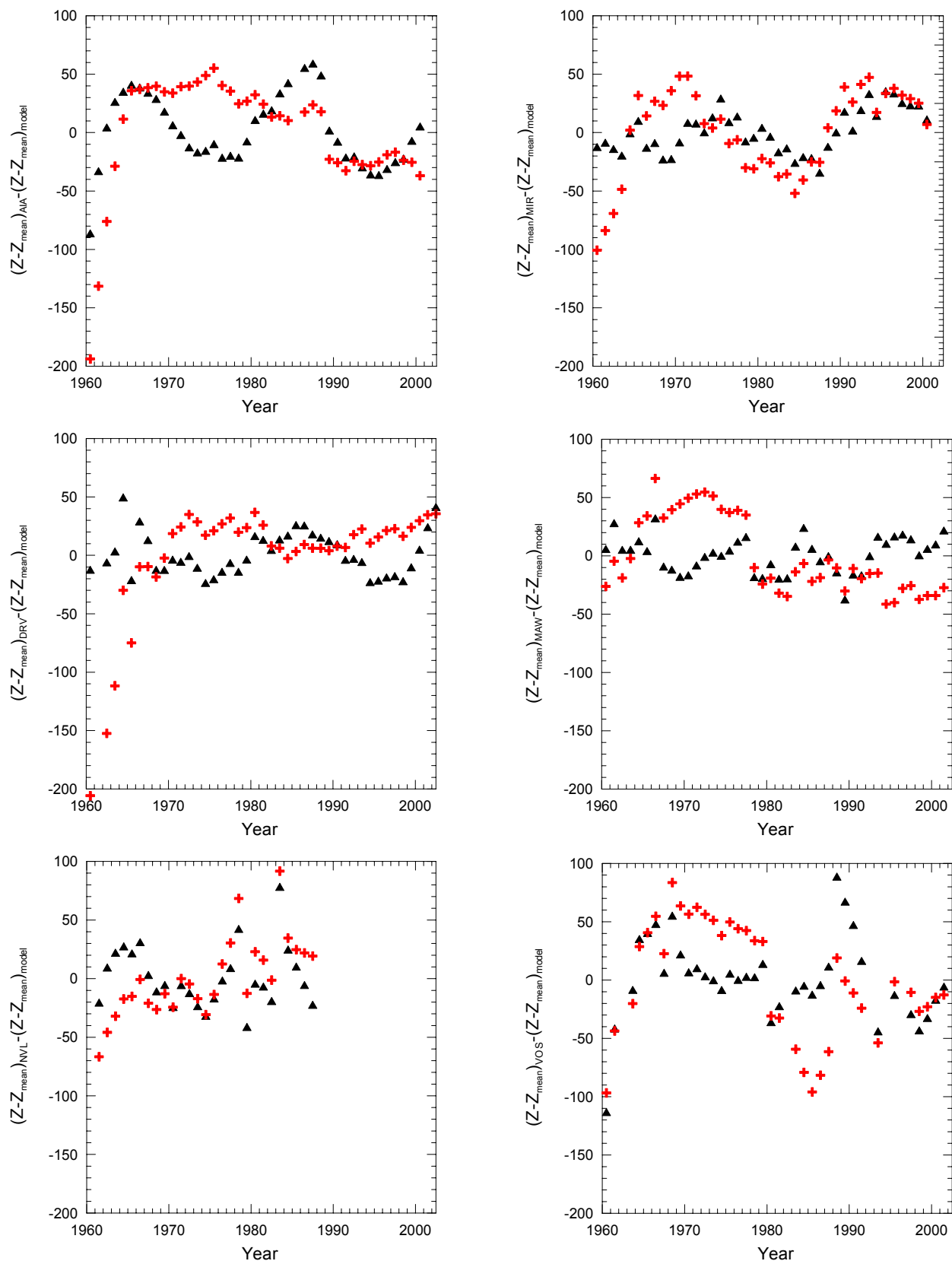


Figure IV.13. As figure IV.11 but for Z component.

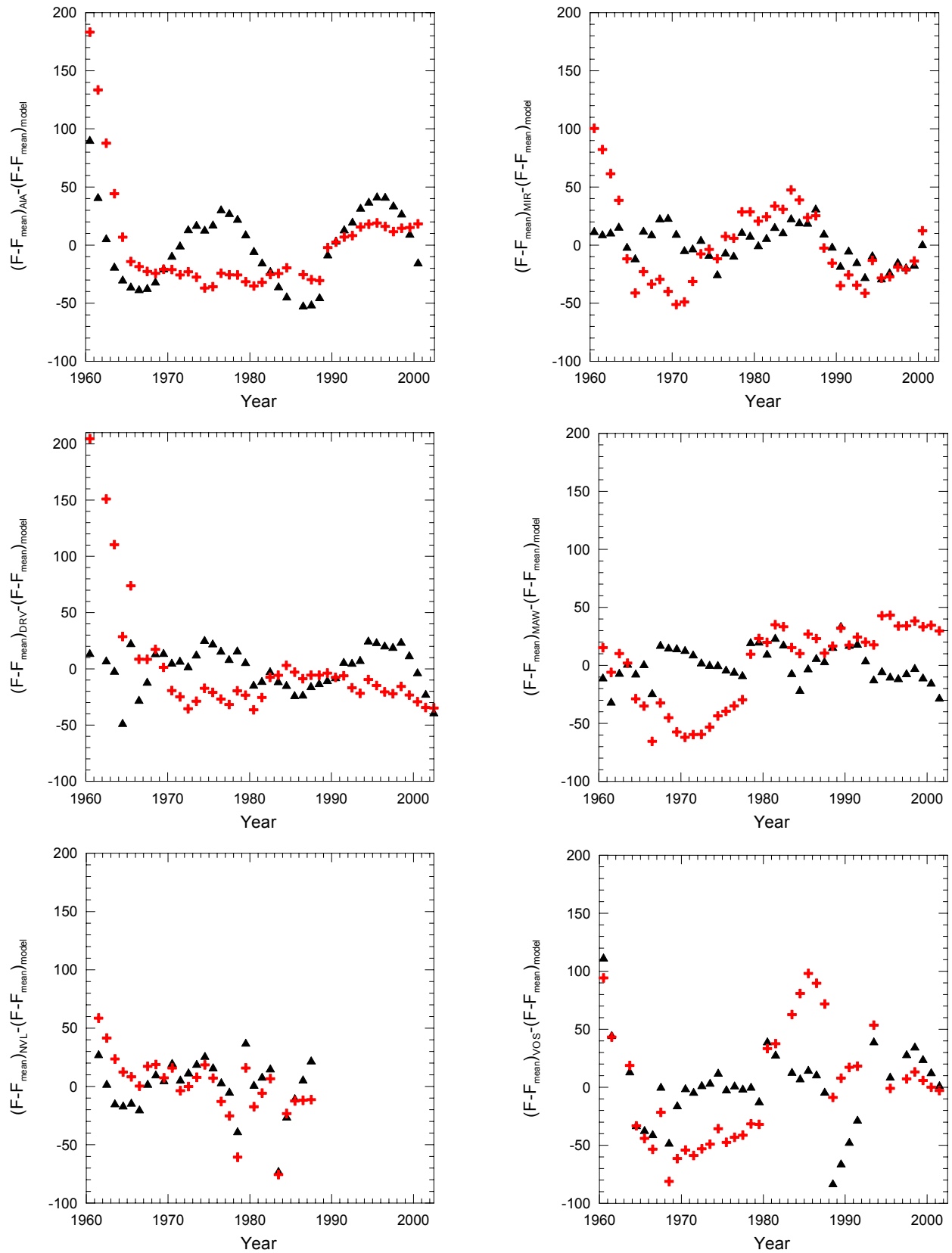
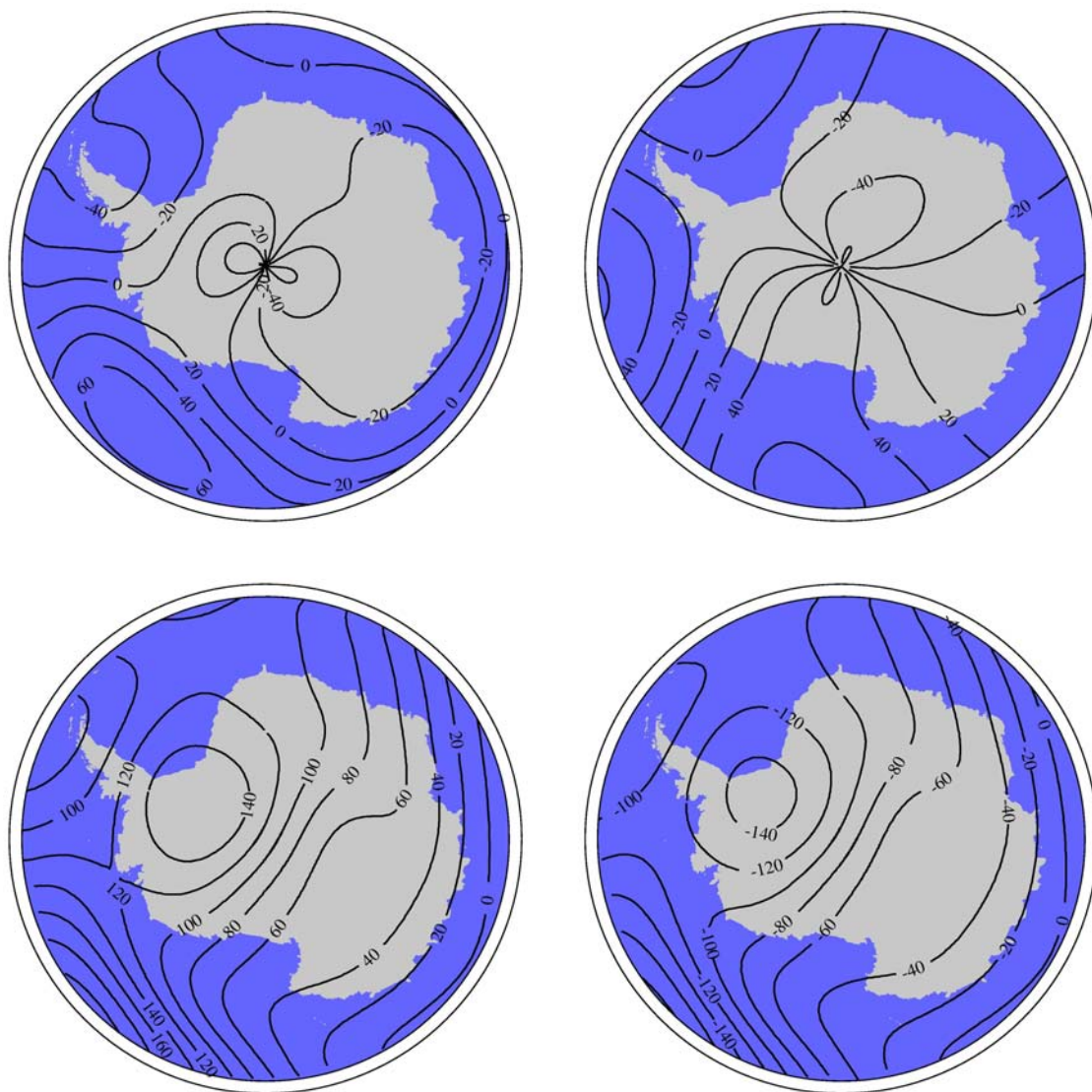


Figure IV.14. As figure IV.11 but for F element.



**Figure IV.15.** Secular variation predicted by ARM for epoch 1995.0 for X (top left), Y (top right), Z (bottom left), and F (bottom right) magnetic elements in nT/year. Contours (each 20 nT/year) were obtained as the difference between the values of the magnetic elements for epochs 1995.5 and 1994.5.

To check how different are the magnetic field values provided by ARM from those that would be obtained from IGRF, differences between both ARM and IGRF-9 values can be plotted for some given epochs. Figure IV.16 shows the differences for X, Y, Z, and F at sea level for 1980.0, roughly the central epoch of the analysis. It can be seen that there is not any defined pattern, but highs and lows alternate depending on the values provided by nearby observatories and that are followed by the ARM. As an example, differences for the total intensity oscillate between  $-200$  nT and  $125$  nT. The IGRF presents higher values than the ARM for the central part of the Antarctic continent, whereas the opposite situation is found for almost the complete coastline.



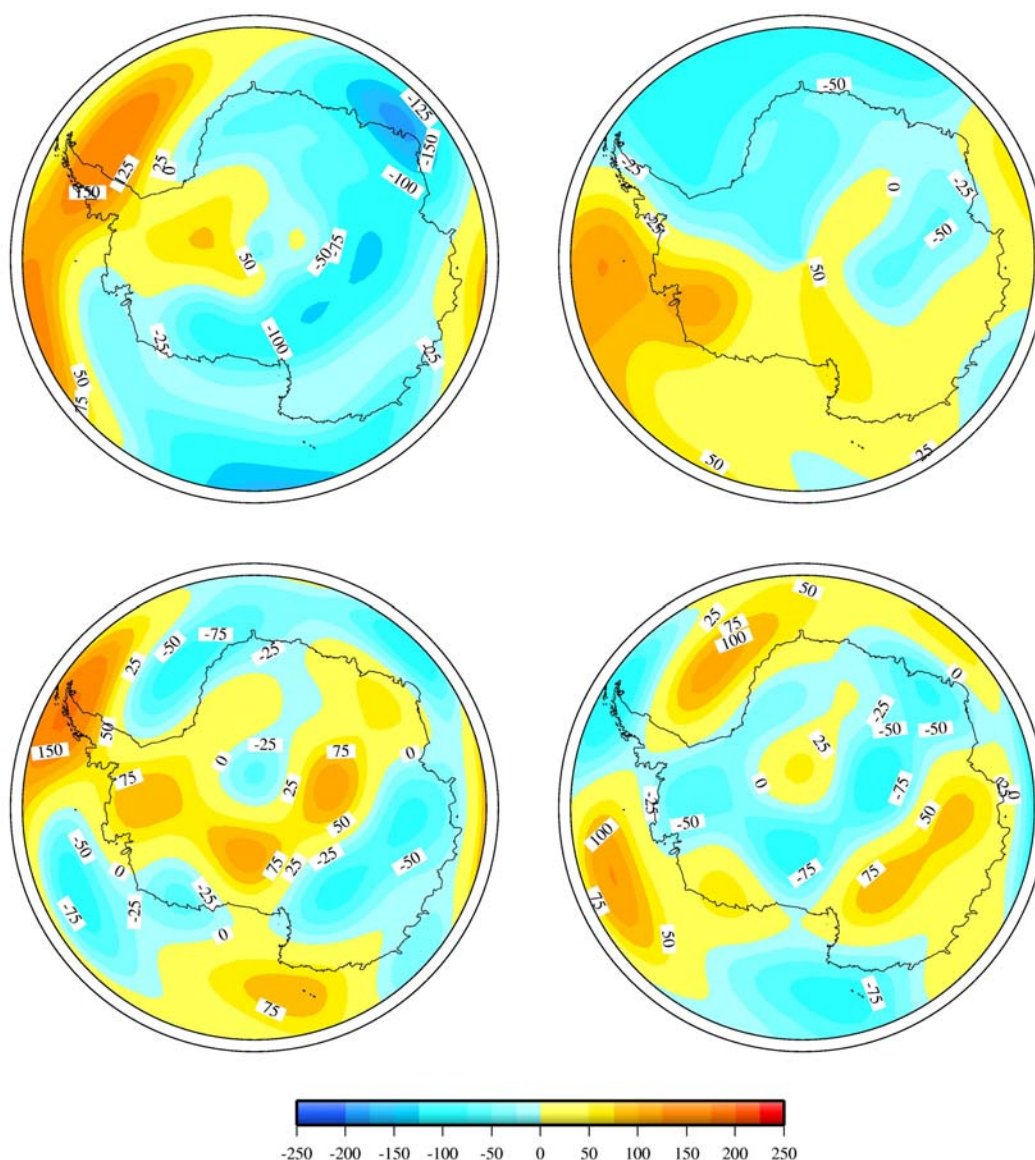


**Figure IV.16.** Differences at sea level between ARM and IGRF-9 for epoch 1980.0 for X (top left), Y (top right), Z (bottom left), and F (bottom right) magnetic elements.

In order to check if the differences plotted in this way have any physical significance, the same kind of comparison can be established between ARM and IGRF-9 but at satellite altitude. The resulting residual map can be compared to the satellite anomaly maps derived from satellite measurements that can be found in the literature. Figure IV.17a represents the differences between both models (ARM – IGRF-9) for the total intensity field for 1980.0 at 450 km height. On the other hand, figure IV.17b shows the map of the total anomaly field obtained from Champ satellite measurements at the same altitude [Kim *et al.*, 2004]. The blanked area is due to the lack of satellite measurements around the Geographic Pole. Some similar features are found between both maps. It is noteworthy the manifestation of highs in both maps on the Eastern part of the



Antarctic Peninsula (between  $300^\circ$  and  $0^\circ$  longitude), and on the South East Antarctic sector (between  $90^\circ$  and  $180^\circ$  longitude). It is also remarkable the appearance of lows over the Antarctic continent, and on the Ross Sea area ( $180^\circ$  longitude). So it can be affirmed that the residual map obtained from the differences between the total field values given by ARM and by IGRF-9 reflects approximately the lithospheric field between harmonic degree 10 and 25 (which is the maximum degree of ARM).

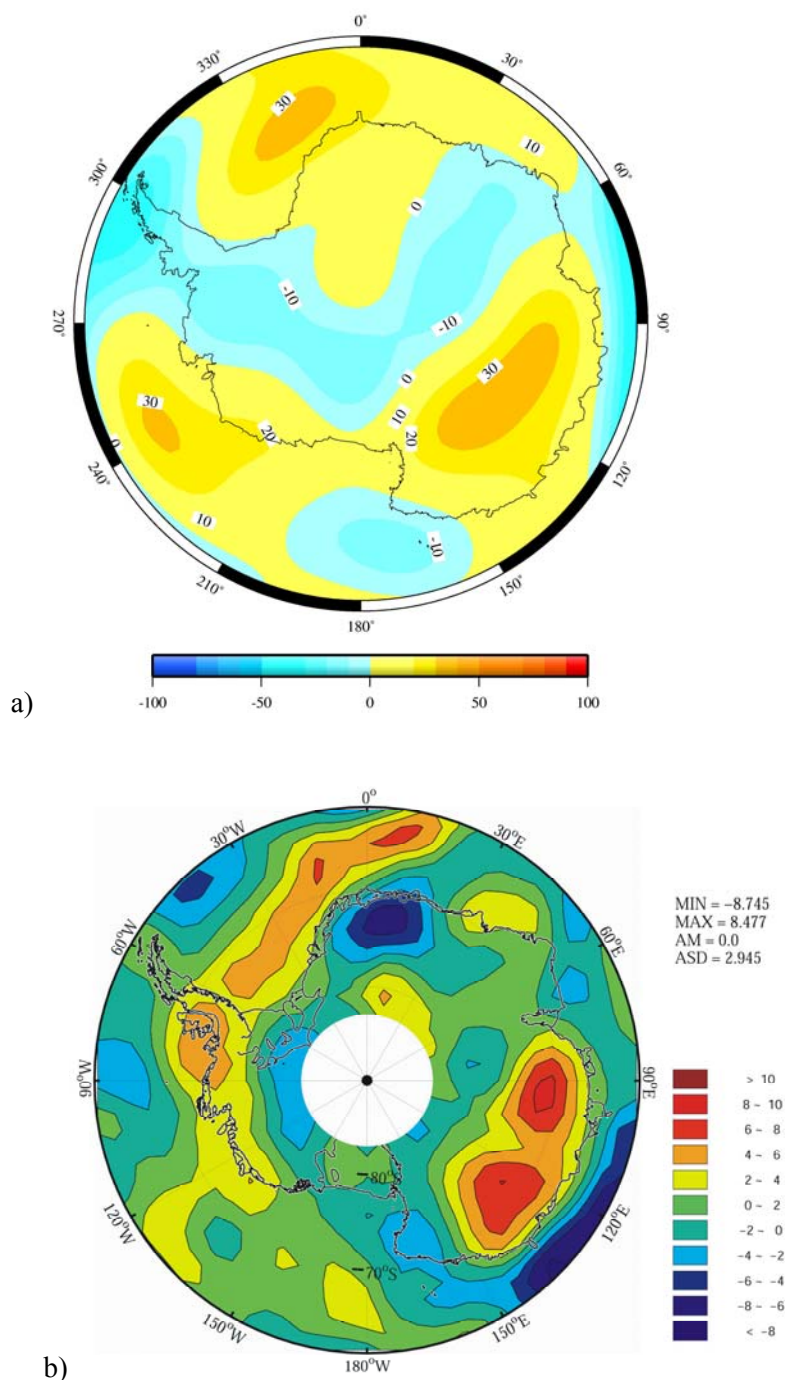


**Figure IV.17.** a) Differences (nT) between the total field values given by ARM and IGRF at 450 km.  
b) Champ magnetic anomalies of the Antarctic lithosphere at 450 km [Kim *et al.*, 2004].

## **V. Applications of the Antarctic Reference Model**

In the last chapter the Antarctic Reference Model has been presented, and its validity has been assessed. It has been shown that the model is able to represent the total field as well as its secular variation, improving for almost all cases the behaviour of the International Geomagnetic Reference Field model. Comparisons were carried on with respect to the IGRF, since it has been the model traditionally used for the reduction of magnetic surveys, and the final purpose of this work is to provide the scientific community with a useful tool to improve this procedure; and to the CM3, the model that represents the actual trend in magnetic field modelling. In this chapter some examples will be given about the use of ARM to reduce Antarctic magnetic surveys, together with other applications in which this Spherical Cap Harmonic model can be used.

### ***V.1. Online computation of the Antarctic Reference Model***

Before the strictly speaking applications, we would like to remark the importance given to the spreading of the work developed. One of the main aspects taken into account in the development of the Antarctic Reference Model was the idea to make it available to anyone in a simple way. Hence a website was developed to inform the scientific community about the latest developments of the model, and moreover to allow the user to obtain the values of the magnetic components for a given location and epoch. The electronic address of the website is <http://www.ingv.it/arm>. Both English and Italian versions are available, since most of the presented work was developed at the Istituto Nazionale di Geofisica e Vulcanologia, Italy. It is possible to look up for an introduction explaining the motivations that led to this work, to consult the present state of the work, and to compute online the values of the magnetic field through a simple form. Figure V.1 shows the appearance of the homepage of the ARM website.

### ***V.2. Magnetic maps***

In the same way that regional (global) models are used to produce regional (global) magnetic field charts, the Antarctic Reference Model has been applied to create maps of the magnetic field components at sea level from 1960.0 to 2005.0 at five-year intervals. These maps are presented in figure V.2. It is important to note that, with respect to previously developed versions of the model, maps for epoch 1960.0 and 2005.0 are now more reliable. Previous versions of ARM considered polynomials to represent the secular variation, and maps for the extreme epochs of the model presented some high frequency oscillations. Cosine functions avoid the fictitious undulations at the edge of the validity range of the model, like those shown in figure IV.1.

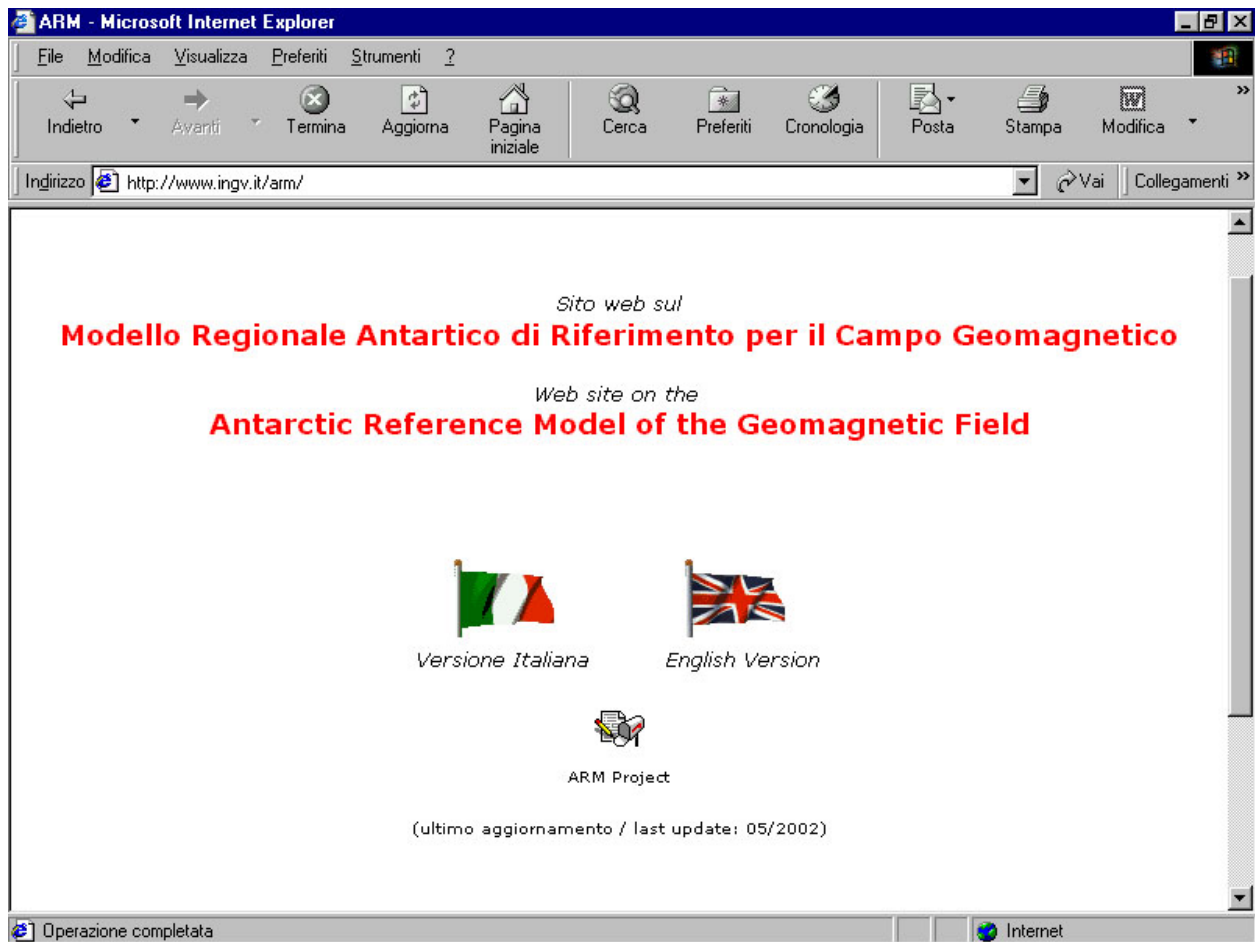


**Figure V.1.** Homepage of the Antarctic Reference Model website (<http://www.ingv.it/arm>).

Since satellite datasets were used to develop the model, magnetic maps at satellite altitude can also be produced. Figure V.3 shows maps for the total intensity at 500 km height for 1970.0, 1980.0, and 2000.0, approximately the epochs for which POGO, Magsat, and Orsted and Champ satellite data were respectively available. Again, it can be seen a smooth behaviour of the total magnetic field for all three epochs.

Some questions can be formulated about the behaviour of the ARM at intermediate heights, since only maps at ground and satellite height have been shown. Figure V.4 shows the evolution in height of the differences between the total field computed from ARM and IGRF models for a given epoch and different locations. The points chosen were located at  $-75^\circ$  latitude, with longitudes from  $0^\circ$  to  $270^\circ$  each  $90^\circ$ , and the epoch was fixed at 1980.0. The differences decrease smoothly from the Earth's surface towards the maximum considered height (500 km). This drop is probably due to the simple fact that the value of  $F$  is lower for satellite altitudes. The differences for the lowest and highest altitudes for the four considered points are coherent with the values that can be appreciated from figures IV.16 and IV.17.

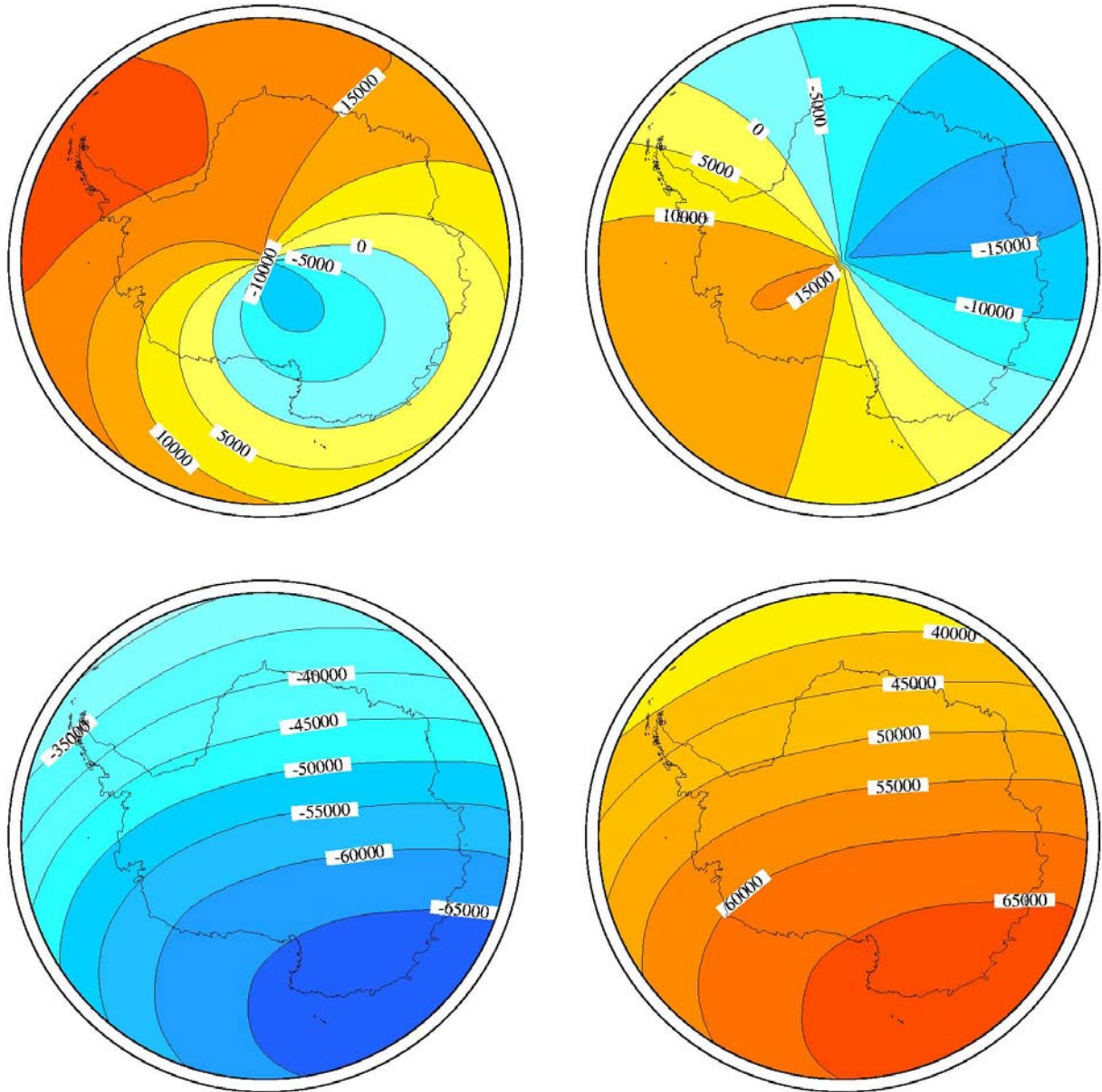


**Figure V.2.** Magnetic maps, in nT, produced by using the Antarctic Reference Model at epoch 1960.0 (sea level) for X (top left), Y (top right), Z (bottom left), and F (bottom right) magnetic elements.



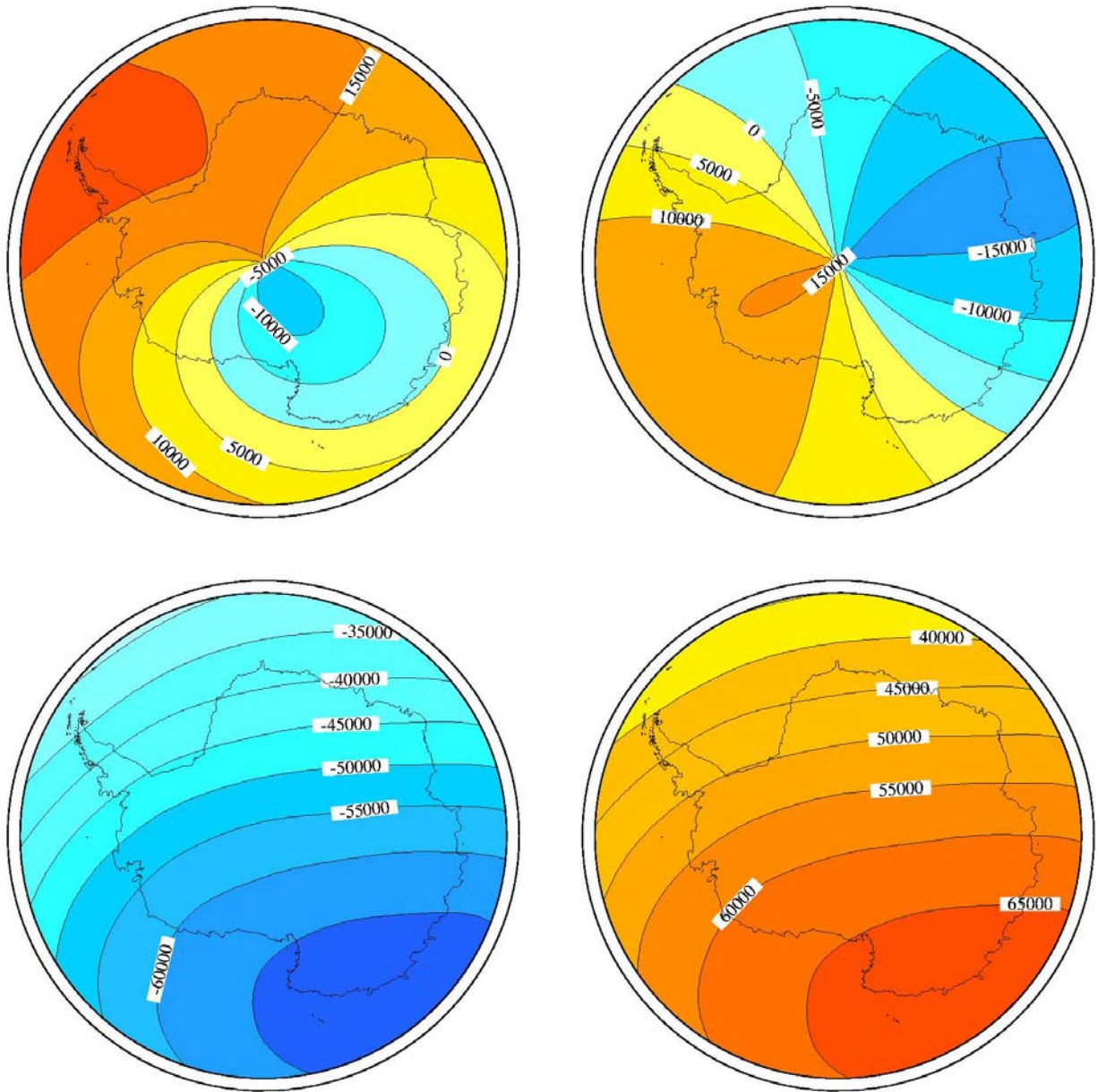


**Figure V.2 (continued).** Magnetic maps, in nT, produced by using the Antarctic Reference Model at epoch 1965.0 (sea level) for X (top left), Y (top right), Z (bottom left), and F (bottom right) magnetic elements.

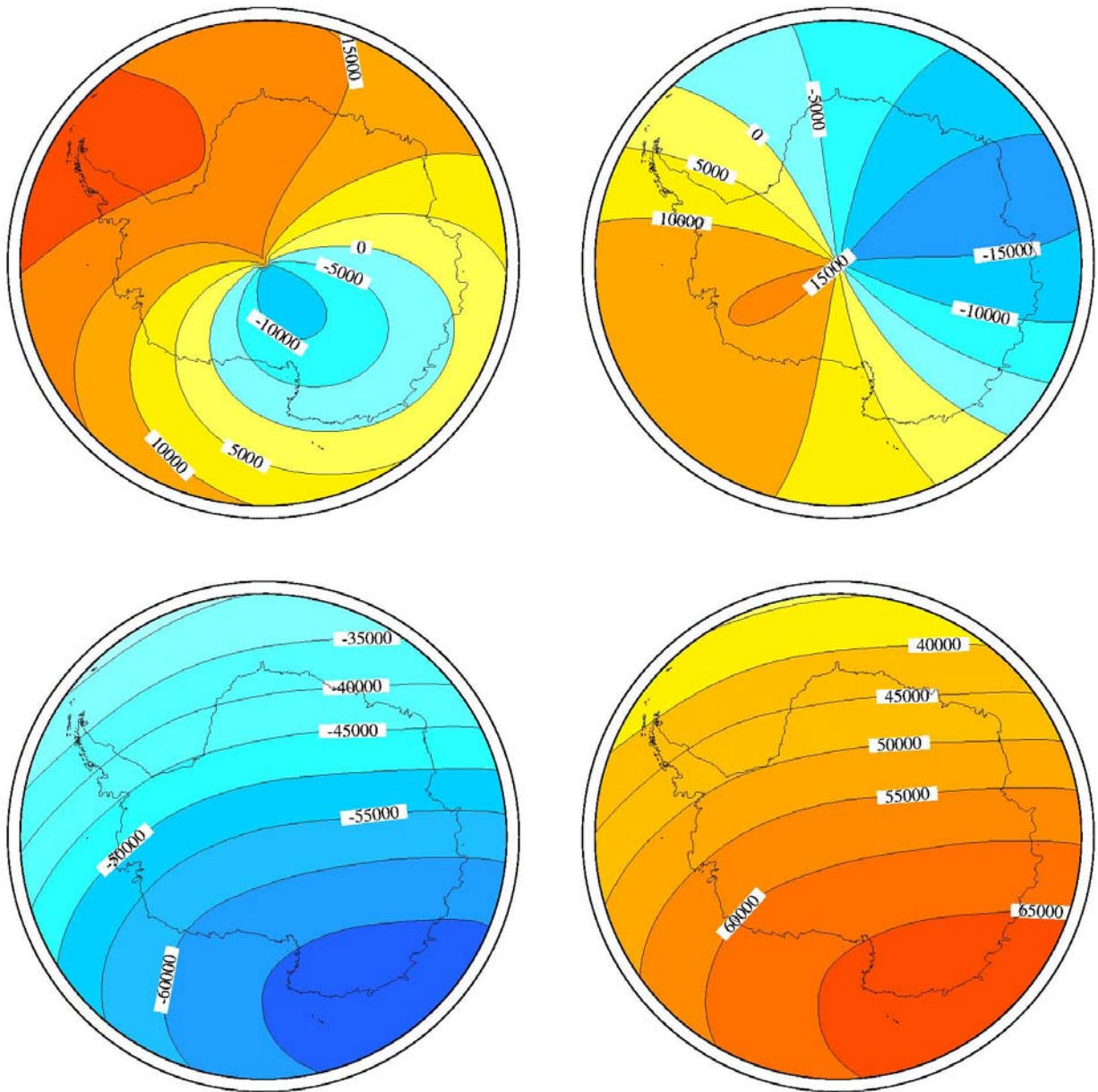


**Figure V.2 (continued).** Magnetic maps, in nT, produced by using the Antarctic Reference Model at epoch 1970.0 (sea level) for X (top left), Y (top right), Z (bottom left), and F (bottom right) magnetic elements.

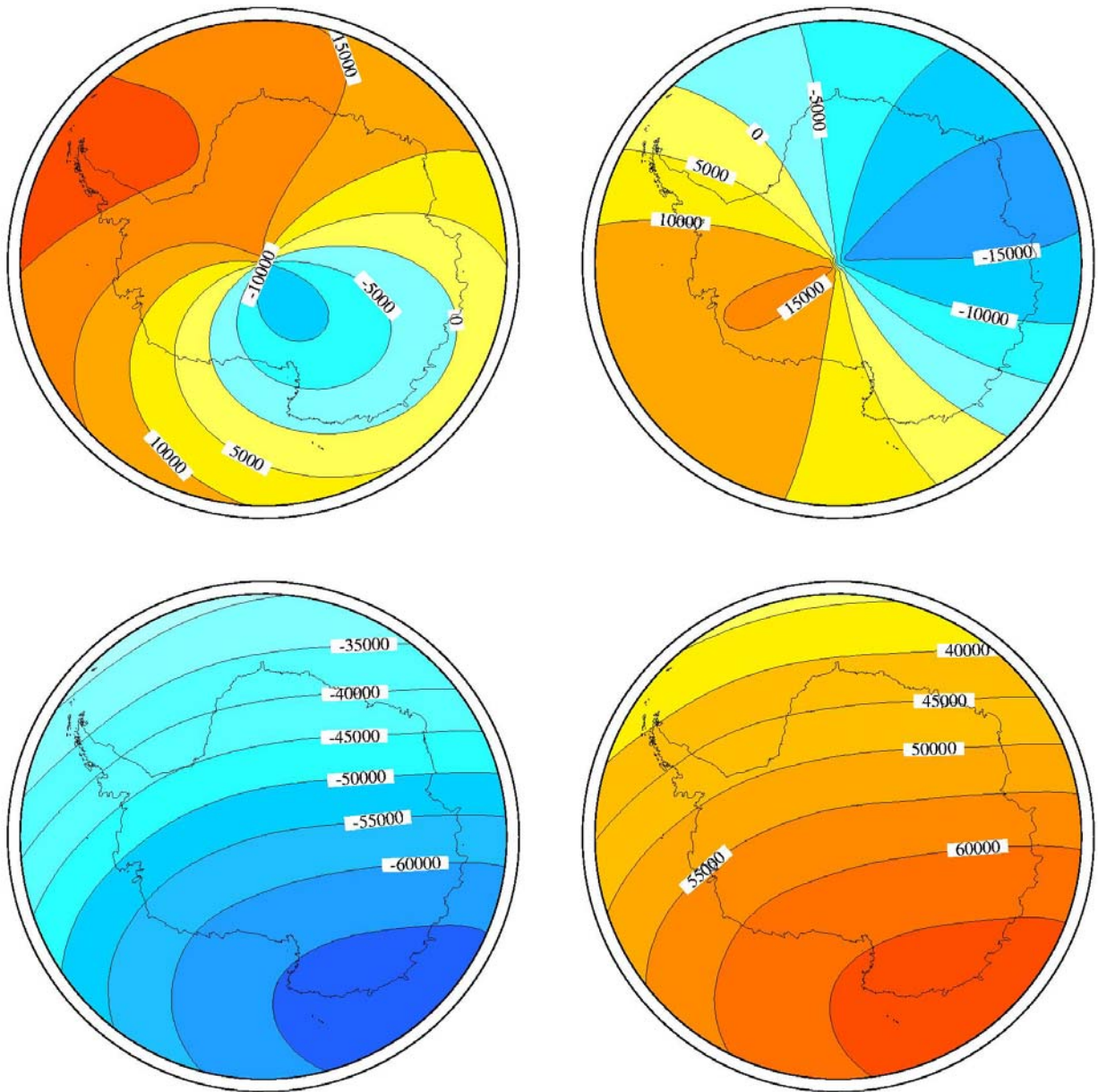


**Figure V.2 (continued).** Magnetic maps, in nT, produced by using the Antarctic Reference Model at epoch 1975.0 (sea level) for X (top left), Y (top right), Z (bottom left), and F (bottom right) magnetic elements.



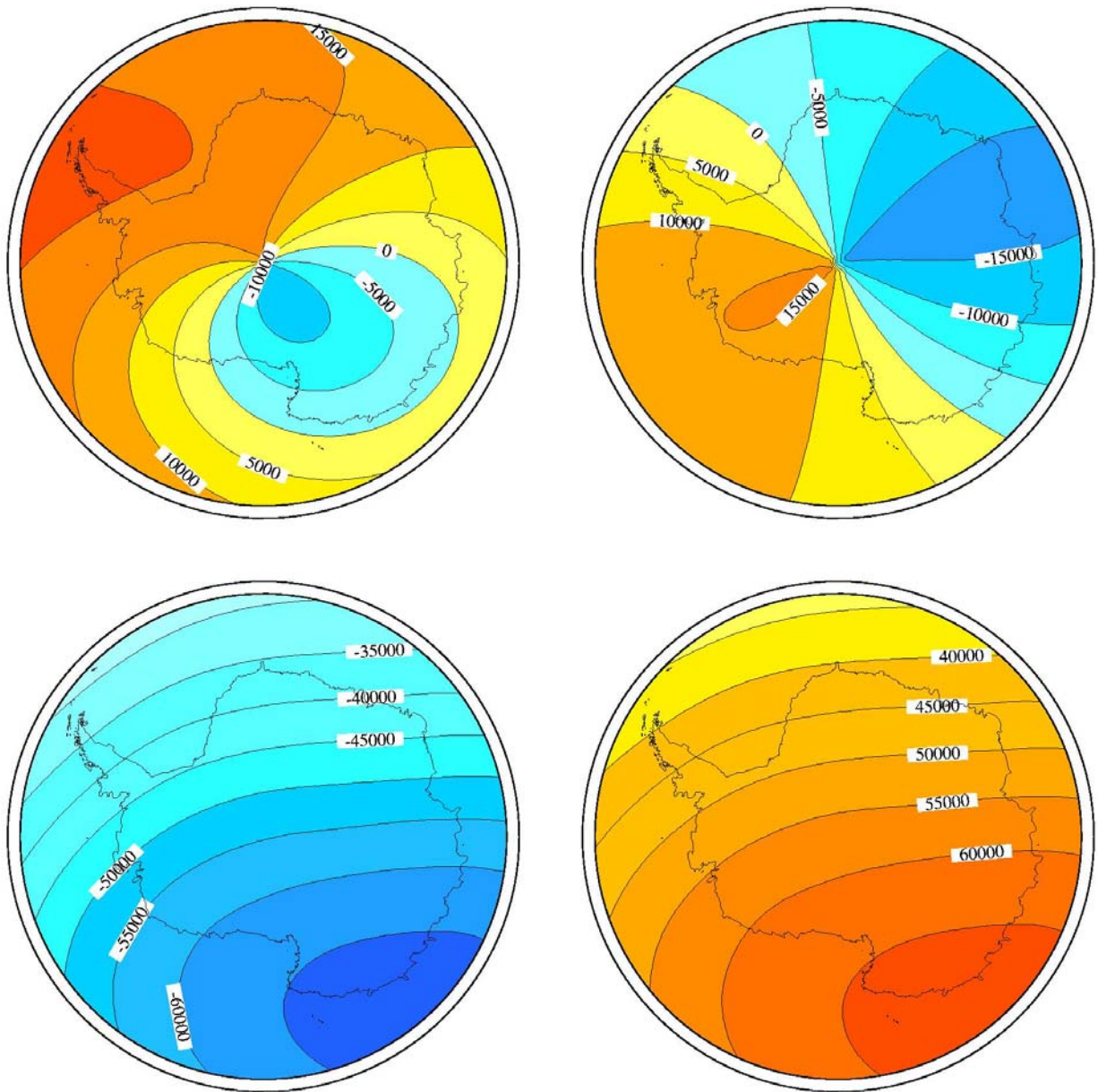


**Figure V.2 (continued).** Magnetic maps, in nT, produced by using the Antarctic Reference Model at epoch 1980.0 (sea level) for X (top left), Y (top right), Z (bottom left), and F (bottom right) magnetic elements.



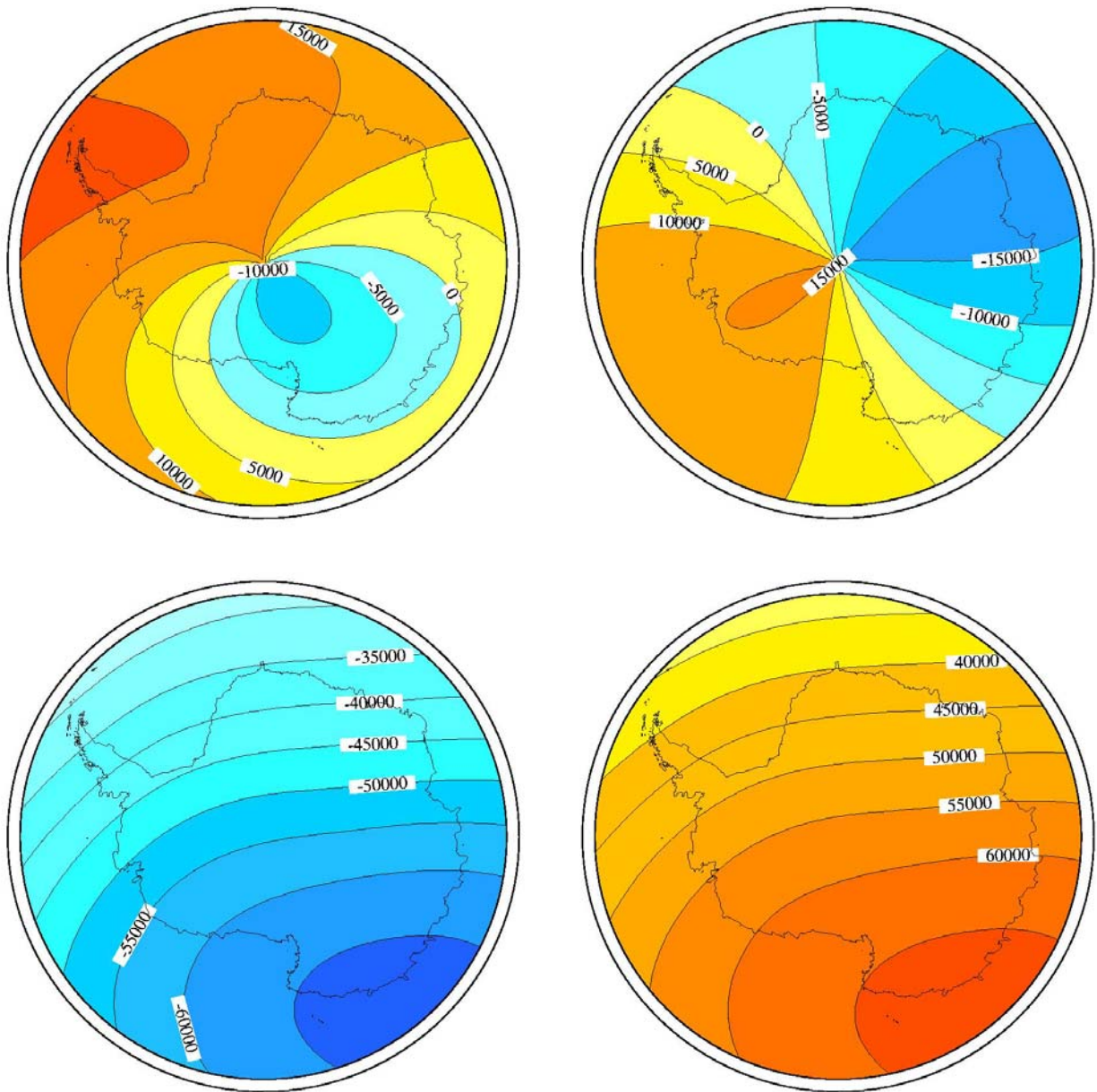


**Figure V.2 (continued).** Magnetic maps, in nT, produced by using the Antarctic Reference Model at epoch 1985.0 (sea level) for X (top left), Y (top right), Z (bottom left), and F (bottom right) magnetic elements.

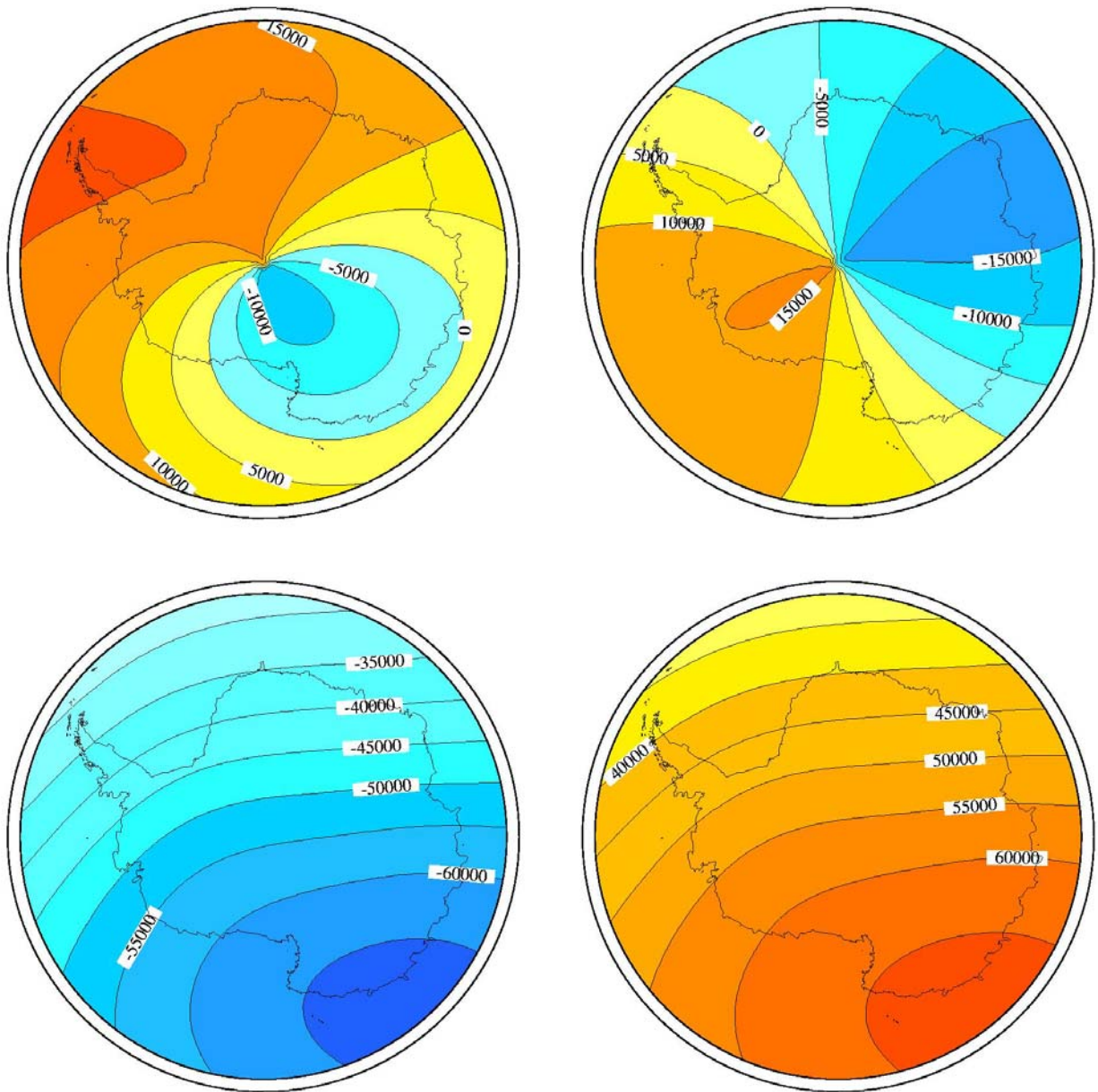


**Figure V.2 (continued).** Magnetic maps, in nT, produced by using the Antarctic Reference Model at epoch 1990.0 (sea level) for X (top left), Y (top right), Z (bottom left), and F (bottom right) magnetic elements.

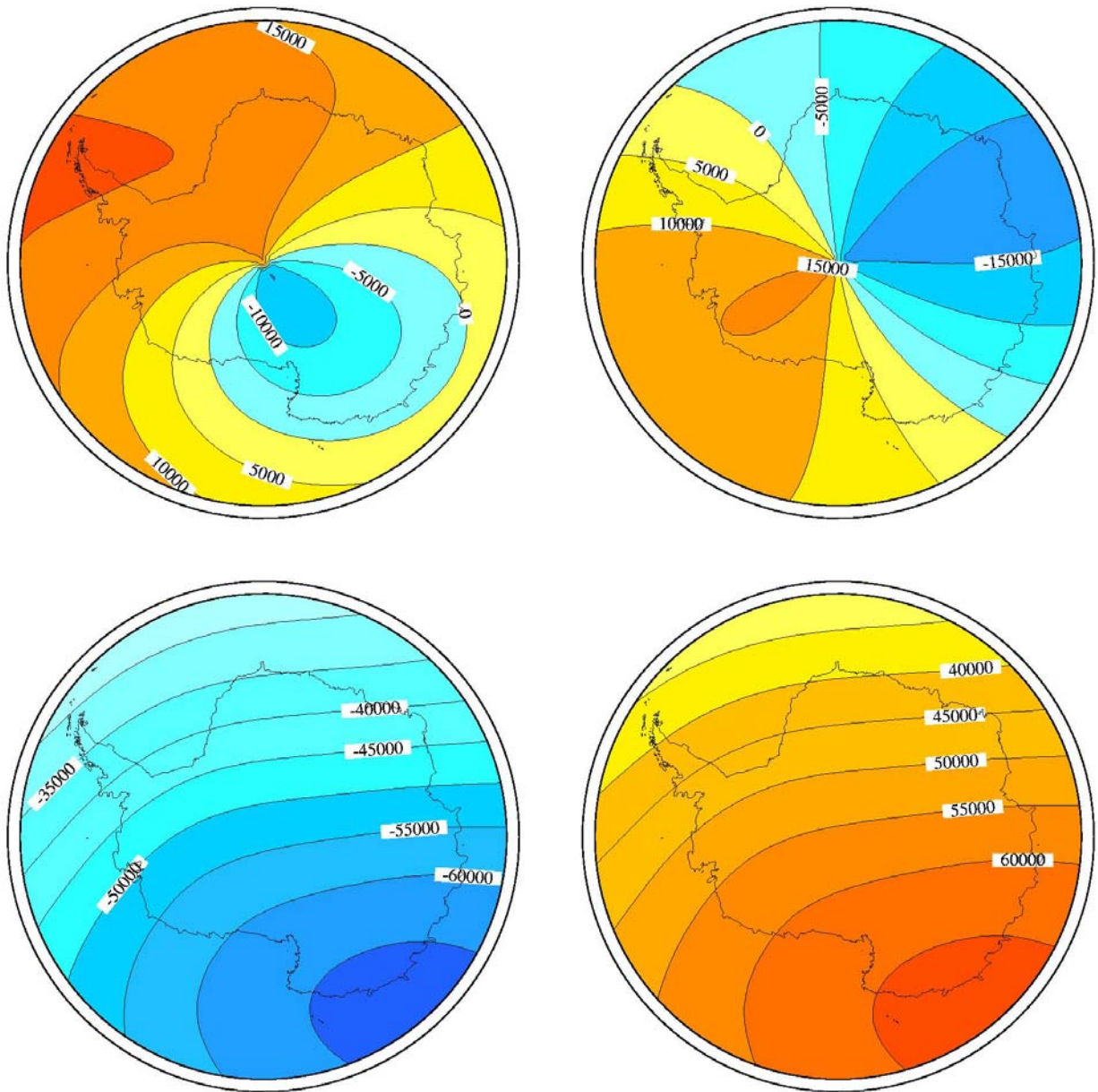


**Figure V.2 (continued).** Magnetic maps, in nT, produced by using the Antarctic Reference Model at epoch 1995.0 (sea level) for X (top left), Y (top right), Z (bottom left), and F (bottom right) magnetic elements.



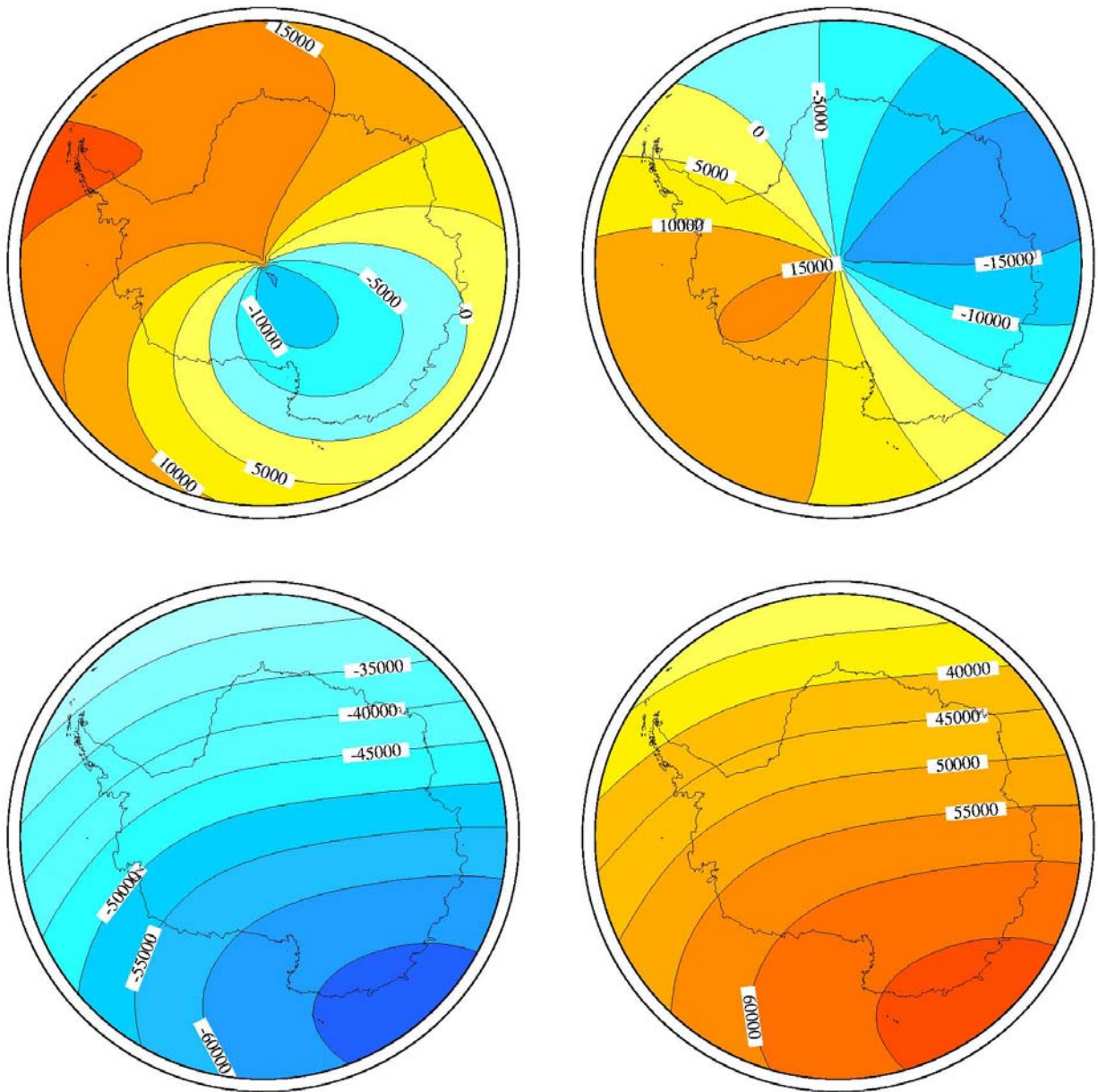


**Figure V.2 (continued).** Magnetic maps, in nT, produced by using the Antarctic Reference Model at epoch 2000.0 (sea level) for X (top left), Y (top right), Z (bottom left), and F (bottom right) magnetic elements.

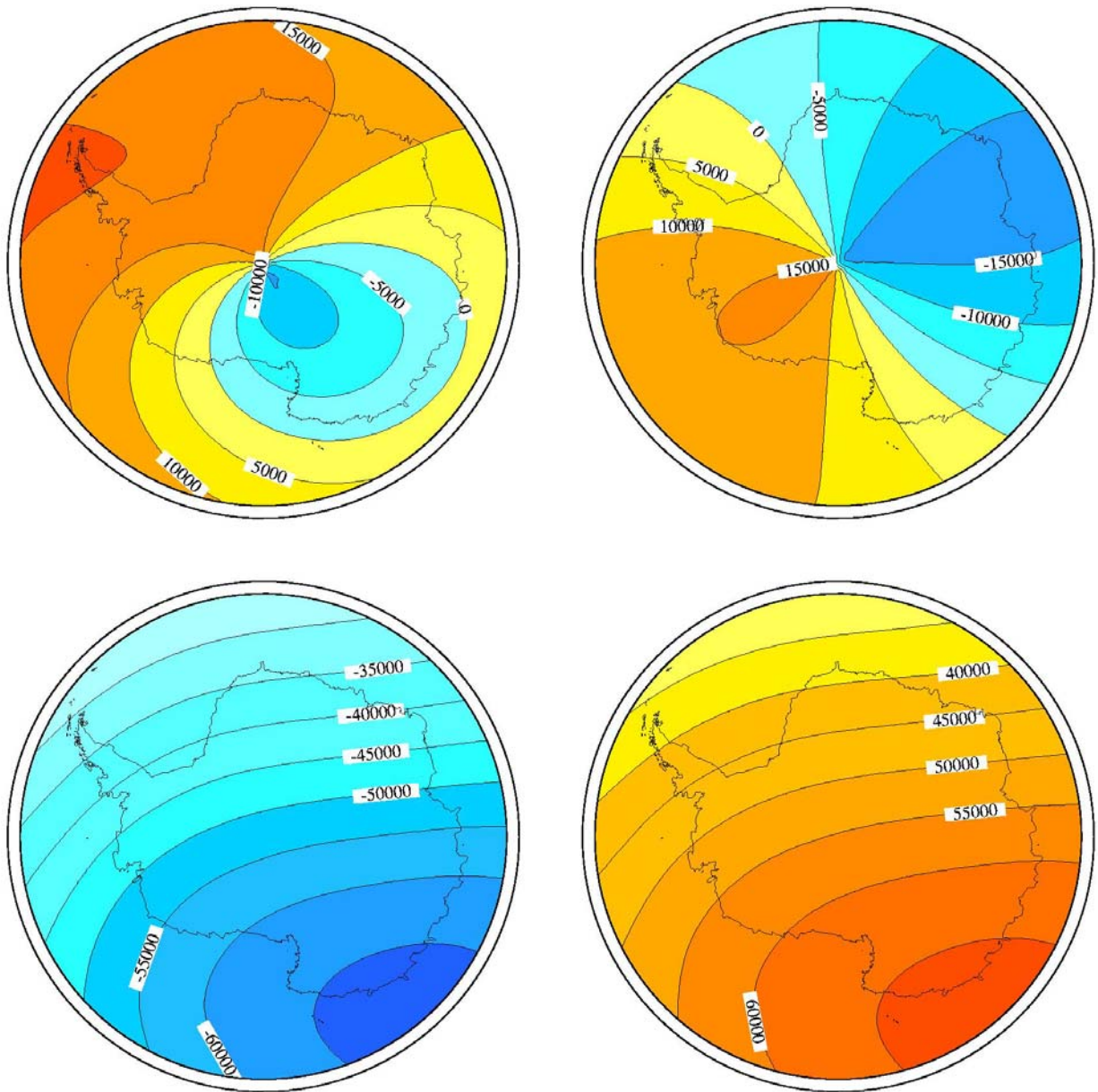


**Figure V.2 (continued).** Magnetic maps, in nT, produced by using the Antarctic Reference Model at epoch 2005.0 (sea level) for X (top left), Y (top right), Z (bottom left), and F (bottom right) magnetic elements.

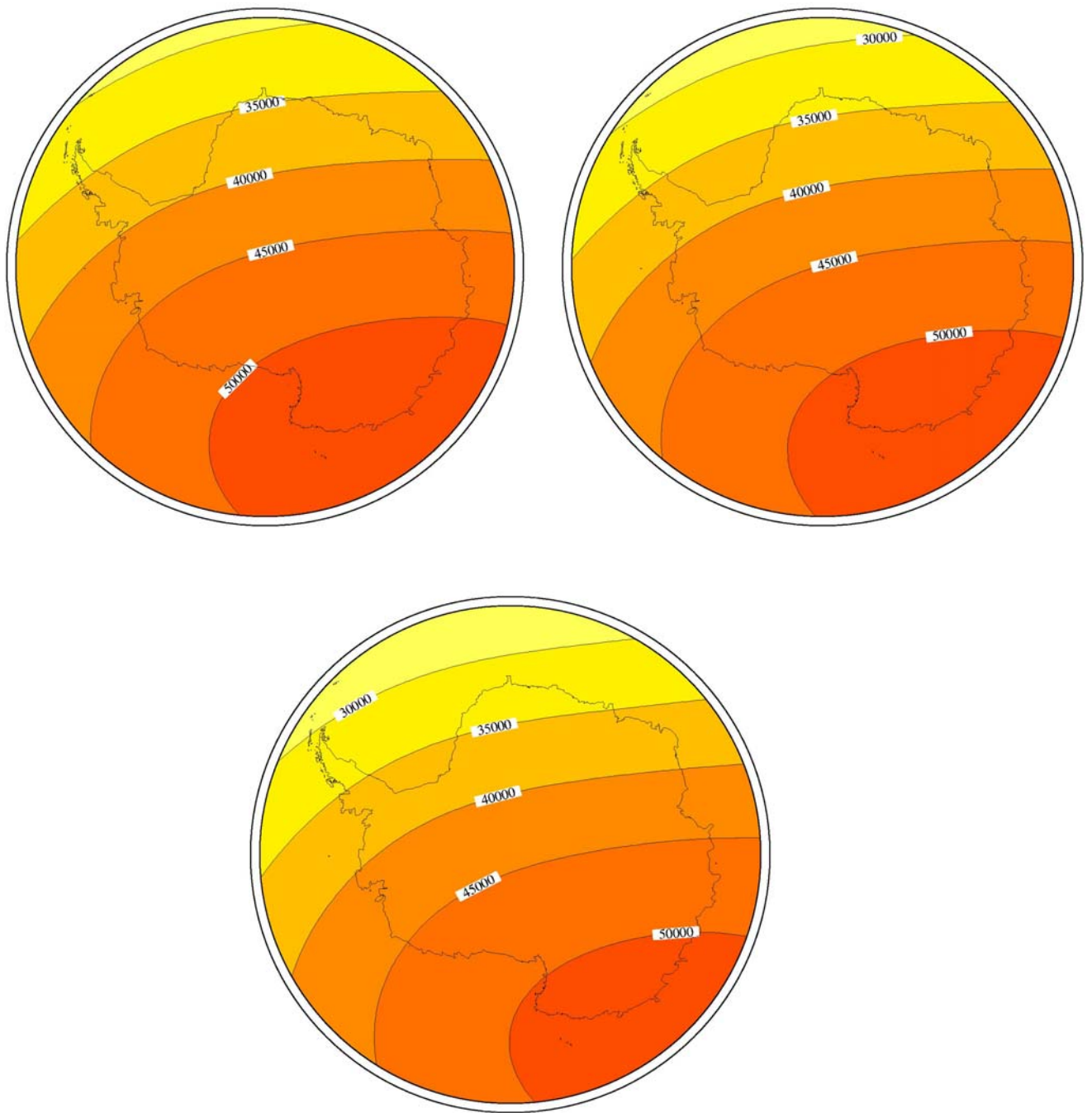


**Figure V.3.** Total intensity magnetic maps computed from ARM at 500 km height for epochs 1970.0 (top left), 1980.0 (top right), and 2000.0 (bottom).

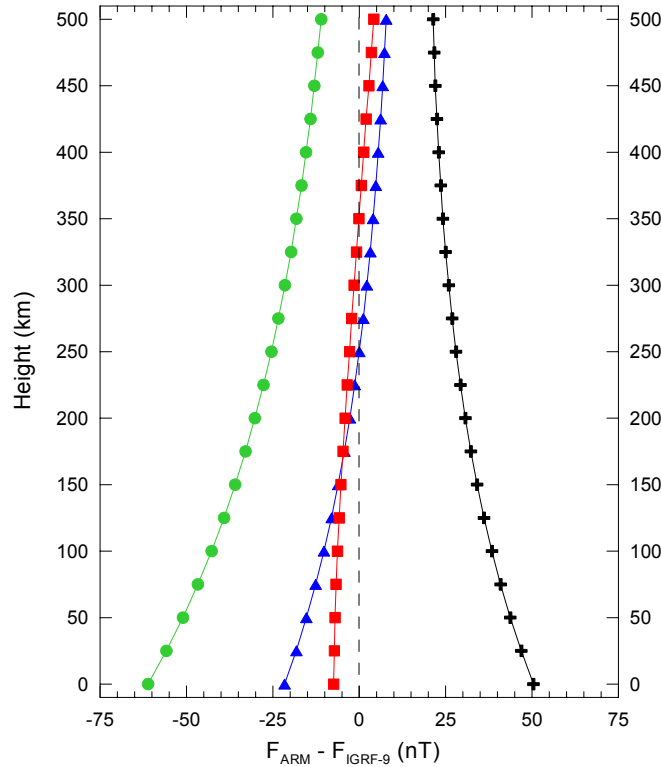


**Figure V.4.** Evolution in height of the total field differences between the ARM and IGRF-9 models for a given epoch (1980.0) and some given locations:  $-75^{\circ}\text{S}$ ,  $0^{\circ}\text{E}$  (blue triangles);  $-75^{\circ}\text{S}$ ,  $90^{\circ}\text{E}$  (black crosses);  $-75^{\circ}\text{S}$ ,  $180^{\circ}\text{E}$  (red squares); and  $-75^{\circ}\text{S}$ ,  $270^{\circ}\text{E}$  (green circles).

### V.3. Location of the magnetic pole

The considered region in which the Antarctic Reference Model has been developed has another main interest from a magnetic point of view: it contains the South Geomagnetic and Magnetic poles. The location of the first one is usually determined by the dipole part of the IGRF global model, whereas the second one is the point on the surface at which the magnetic field is vertical (i.e., inclination is  $-90^{\circ}$ ). As pointed out in a recent paper by Campbell [2003], the knowledge of the location of the Magnetic poles is not fundamental from a geophysical point of view, and it is more important to know the position of other “poles” (for example, those of the Earth’s eccentric dipole). Nevertheless, Barton [2002,2003] defends the scientific value of the study of the position and drift of the magnetic poles (to test the accuracy of global field models, for the work of cartographers, navigators, tourist operators, etc.).

We have computed the location of the South Magnetic Pole at 1-year interval through the Antarctic reference model. The change of position of the Pole from 1960.0 to 2005.0 is shown in figure V.5. The pole position associated to the first epoch is that one close to the Antarctic continent, and it agrees with the usual consensus that the location of the pole drifted out to sea



around 1960. These pole locations mostly coincide with those given by the International Geomagnetic Reference Field. To check quantitatively this agreement, one can compare the locations of the South Magnetic Pole given by both models with the experimental value found by Barton [2002] in December 2000. The mean observed position during a quiet interval for that period was  $64.67^\circ$  South latitude,  $138.12^\circ$  East longitude. The position given by IGRF-9 for that epoch is  $64.27^\circ$  South,  $138.06^\circ$  East, whereas the location provided by ARM is  $64.67^\circ$  South,  $138.19^\circ$  East, much closer to the “real” magnetic pole position. There are of course external, crustal, and induced fields to be taken into account that influenced the experimental determination of the pole position, but the proximity of the pole given by ARM to the experimental pole allows us to affirm that the Antarctic Reference Model is a good main field model also in this aspect.

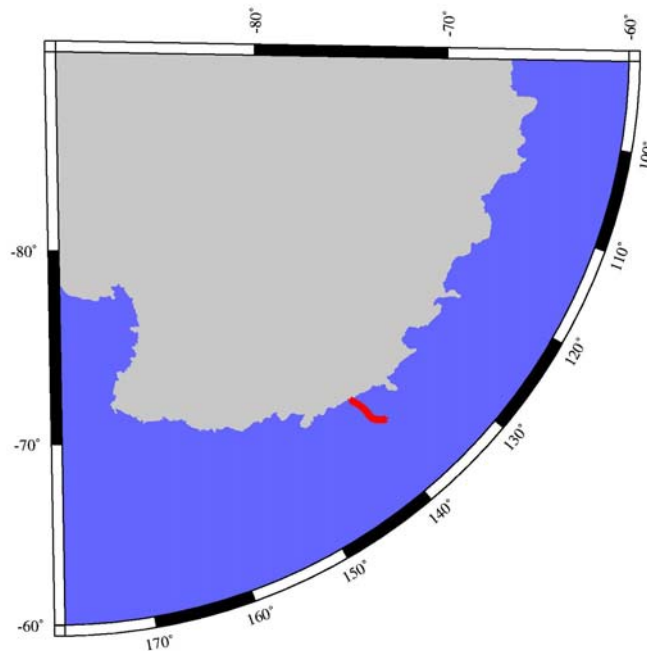


**Figure V.5.** Change of position of the South Magnetic Pole from 1960.0 to 2005.0 as given by the Antarctic Reference Model.

Once the location of the pole is computed for different epochs, the rate of this movement can be determined. Figure V.6 shows the annual velocity of the pole, computed as the distance between two consecutive annual positions (i.e. the arc of a great circle passing through both points). It can be seen that the velocity decreased during the studied period: the average speed since 1960 is around 6 km/year, whereas it is currently below 5 km/year. The velocity trend is similar to that given by IGRF-9 all over the period.



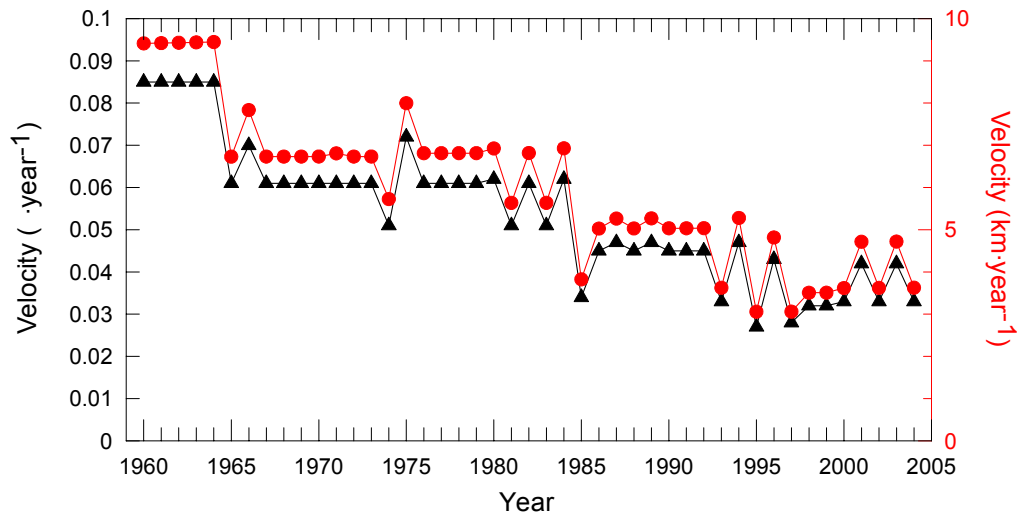


**Figure V.6.** Velocity of movement of the South Magnetic Pole in degrees per year (black triangles) and kilometres per year (red circles) as given by ARM.

#### V.4. Study of magnetic jerks

One of the most unusual features of the temporal change of the magnetic field, for a given element, is the rapid change in the secular variation slope that takes place in periods of one or two years; this phenomenon is called a geomagnetic jerk. More precisely, it is an abrupt change (a step-function) in the second time derivative (the secular acceleration) of the geomagnetic field. The fact that they represent a reorganization of the SV implies that they are of internal origin [Malin and Hodder, 1982] and their short time scale implies that they could be due to a change in the fluid flow at the surface of the Earth's core [Waddington *et al.*, 1995]. Two recent papers try to explain the physical origin of jerks. Bellanger *et al.* [2001] shows a correlation between geomagnetic jerks and the Chandler wobble (the motion due to the flattening of the Earth, that appears when the Earth rotation axis does not coincide with the polar main axes of inertia), whereas Bloxham *et al.* [2002] suggest that jerks can be explained by oscillatory flows (torsional oscillations) in the Earth's core. This latter work proposes also that the occurrence or not of a jerk depends on the morphology of the field: different characteristics of the field would imply that jerks would be observed in observatory records from which there is no evidence of a jerk event. From the historical magnetic records, there is evidence of some jerks (mainly at European observatories) occurred during the last forty-five years round about 1969, 1978, 1991, and 1999.

In a recent paper, Meloni *et al.* [2004] investigated the presence of jerks in Antarctica by means of both single and multi-station analyses applied to the longest available magnetic observatory time series. The existence of jerks was clear for some of the studied observatories, but not for all of them. The difficulties in the handling of Antarctic observatories (magnetic

measurements restricted in many cases to Austral summer and so on) mean a limit in obtaining high quality data, necessary for these kind of studies.

The presence of jerks was nevertheless studied in that paper also using the Antarctic Reference Model. In order to do this, the second derivative of the geomagnetic field was computed for different epochs using the Stirling formula:

$$\frac{d^2 B}{dt^2} = \frac{B(t + dt) - 2B(t) + B(t - dt)}{dt^2} \quad (\text{V.I})$$

being  $B(t)$  the value of a magnetic component  $B$  at time  $t$ , in our case computed using ARM. Maps for the secular acceleration were created for every year. Abrupt changes were found for years 1970, 1980, and 1990, whereas the acceleration values were very similar for all the other epochs in between. Figure V.7 shows for example the secular acceleration in the Y component of the magnetic field (the jerk is usually best defined for Y than for the other components) for years 1969, 1970, and 1971 (top); 1979, 1980, and 1981 (middle); and 1989, 1990, and 1991 (bottom). It can be appreciated a complex and highly irregular behaviour in the acceleration for the central year, being the pattern for the previous year similar to that of the year after. A possible explanation of this different behaviour for the central year is that the temporal part of the model is able to follow the slow secular variation for the 45 years of validity of the model, but it is not the case for the rapid variations like those represented by jerks. The model then fails for the years in which jerks occurred; for this reason sharp changes in the modelled secular acceleration appear. Hence although the model is unable to reproduce the expected features of a geomagnetic jerk (since the secular acceleration pattern seems to be the same before and after the year of occurrence of a jerk), it allows to discriminate the epoch of each event.

### **V.5. Application to magnetic surveys**

In this section the main utility of the Antarctic Reference Model will be shown. We will apply ARM to magnetic surveys carried on during different epochs and regions in Antarctica to obtain magnetic anomaly maps, and their features will be compared to those maps obtained using the IGRF as reference model.

Unfortunately it was not possible to do the test with the datasets previously shown in figure I.9. The originally measured total field values presented in that figure from Chiappini *et al.* [2002] were not available, and it was impossible to go back in the data processing to obtain the initial data because several operations were done to obtain the anomaly maps (hand levelling,

etc.). In some cases, much to our regret it was not obvious the procedure applied to the data to obtain the final anomaly data values, so we dismissed the use of those data to check the behaviour of ARM. Nevertheless some new aeromagnetic surveys have been conducted in the area of the McMurdo Sound – Victoria Land in the last years, among them two surveys developed in November 2003 in which the author of this work was involved. It is planned to reduce these recent surveys using ARM to obtain the new anomaly maps for the area.

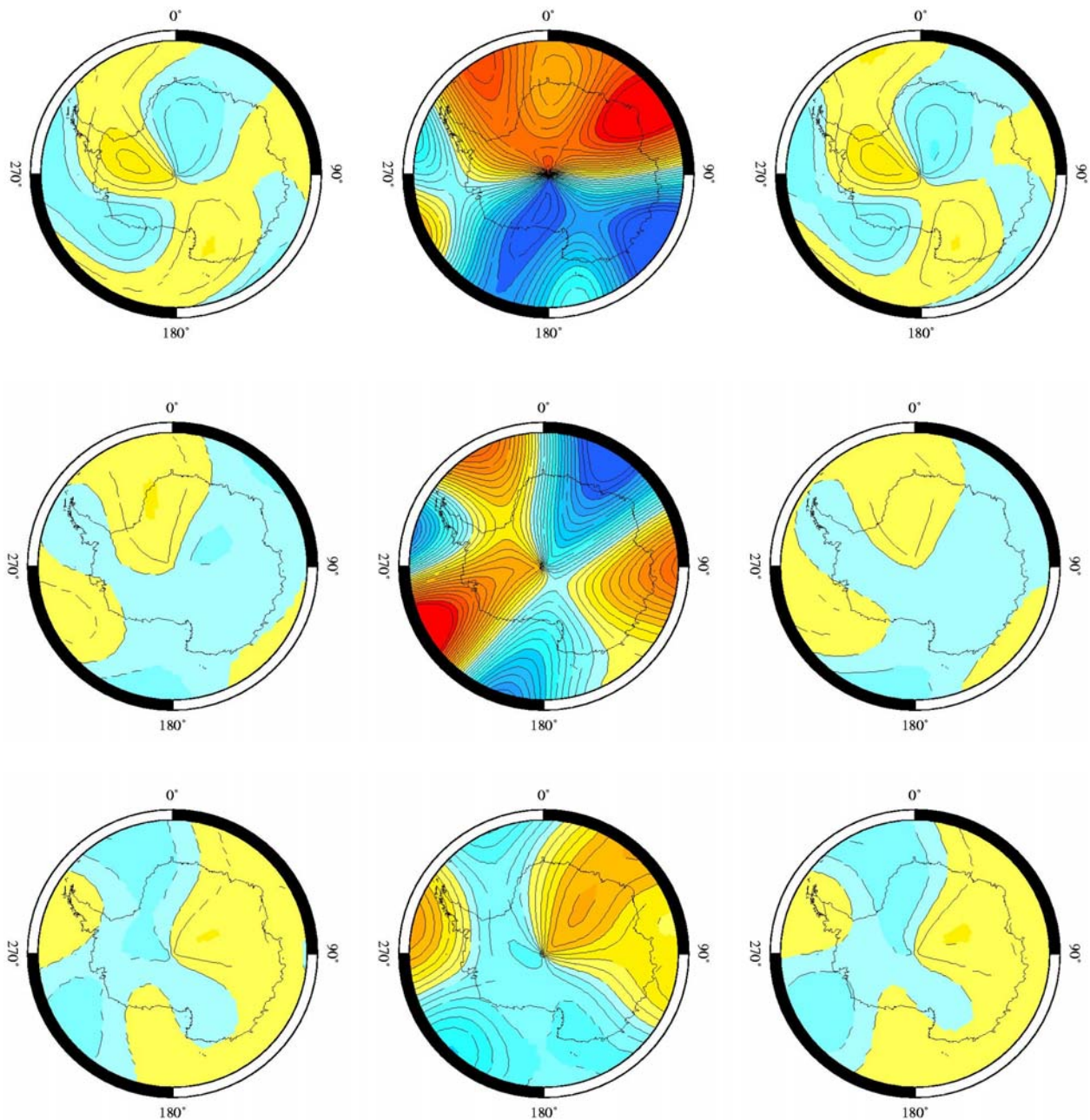


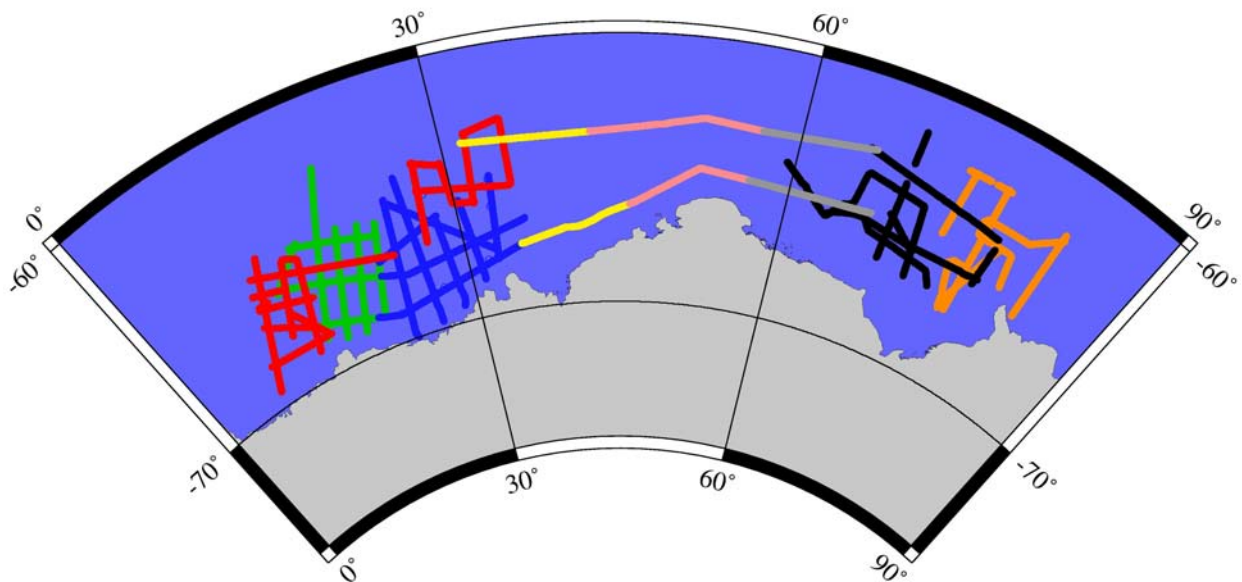
**Figure V.7.** Secular acceleration for Y magnetic component computed for different epochs as the second derivative of the magnetic field given by ARM. The epochs are, from left to right: 1969, 1970, and 1971 (top); 1979, 1980, and 1981 (middle); and 1989, 1990, and 1991 (bottom). Lines each 1 nT/year<sup>2</sup>.

On the other hand, other data sets were obtained to test the model. The surveys, provided by scientists involved in the ADMAP project, correspond to two different Antarctic regions, they were carried out in diverse epochs, and at different heights. Hence we can consider the results of these tests as an appropriate demonstration of the validity of ARM.

### Marine surveys from the Riiser-Larsen Sea and the Cooperation Sea

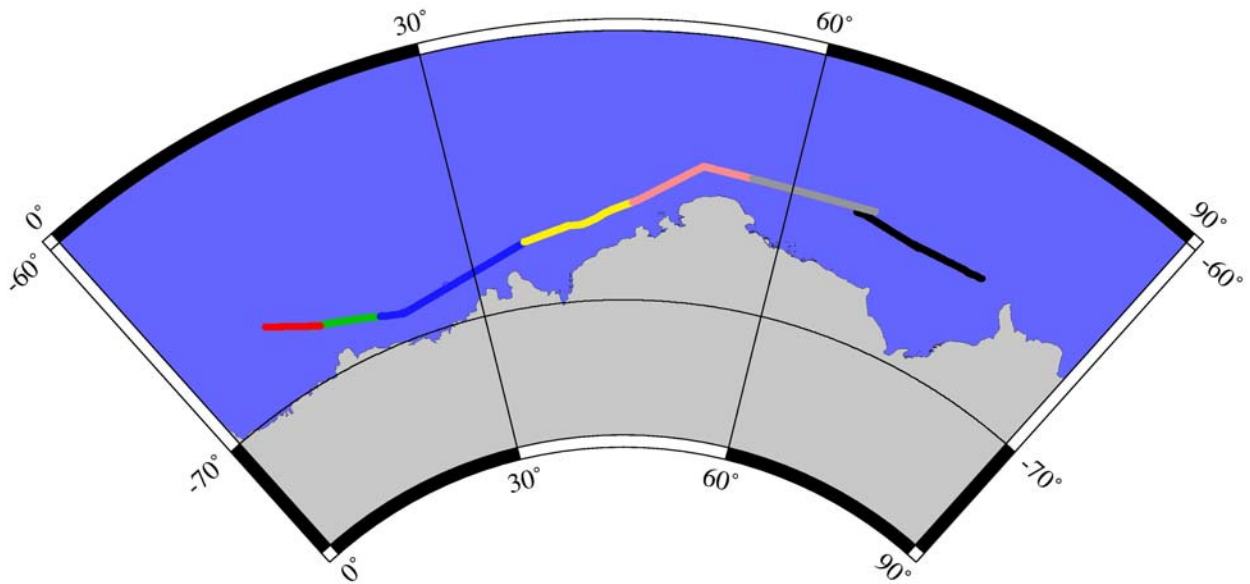
The first example shown corresponds to some marine magnetic surveys carried on by the Polar Marine Geological Research Expedition (Lomonosov, Russia) in the Riiser-Larsen Sea and Cooperation Sea regions between February 1994 and March 2002. Short wavelength diurnal variations were removed from the data, and a cross-over analysis show that they are of rather good quality [A.V. Golynsky, personal communication].

Figure V.8 shows the spatial distribution of these marine tracks, developed during eight different campaigns. The first survey was conducted during the Russian Antarctic Expedition cruise SAE-39 (orange tracks in figure V.8) in February 1994. The second survey (SAE-40, black tracks) spread over the first two months in 1995, whereas SAE-41 (green tracks), SAE-43 (blue tracks) and SAE-44 (red tracks) were conducted during February and March of 1996, 1998, and 1999, respectively. SAE-45 (yellow tracks), SAE-46 (magenta), and SAE-47 (grey) were carried throughout the first part of 2000, 2001, and 2002 in that order.



**Figure V.8.** Marine tracks from the Riiser-Larsen Sea and the Cooperation Sea. See text for details.

After a visual inspection of the survey tracks, it was noted the presence of a long profile that combined total intensity field data from almost all eight surveys (figure V.9). The epochs covered by this merged track extend from 1995 (SAE-40, easternmost survey) to 2002 (SAE-47, close to SAE-40). This long profile was selected to validate the Antarctic Reference Model, since the surveys overlapped properly at the join points. The starting and ending points for each survey were selected according to the closeness to the next survey.



**Figure V.9.** Profile line obtained from the previously shown marine surveys.

We must point that some doubts arose about the removal of the short period external variations from the considered surveys. There are three operative magnetic observatory close to the area covered by the marine surveys: Syowa ( $-69.0^{\circ}\text{S}$ ,  $39.583^{\circ}\text{E}$ ), Mawson ( $-67.6^{\circ}\text{S}$ ,  $62.883^{\circ}\text{E}$ ), and Davis ( $-68.583^{\circ}\text{S}$ ,  $77.967^{\circ}\text{E}$ ). It was not possible nevertheless to obtain minute values for all the covered epochs, neither from all three observatories. Only MAW and DVS provided total intensity minute values for part of the studied temporal range. These values were obtained from the SPIDR server of the National Oceanic and Atmospheric Administration (<http://spidr.ngdc.noaa.gov>). Furthermore, these observatories are too distant from some of the considered surveys, so a temporal reduction using the observatory magnetic records can not be applied.

Figure V.10 shows the anomaly field obtained from survey SAE-39 using ARM, compared (at the same scale) with the minute total field values recorded at DVS. It can be seen that some of the external variations registered in the observatory record (in form of sudden impulses) are still present in the anomaly field obtained from SAE-39 survey. For example, the low field during



February 6<sup>th</sup> with the following maximum peak for the next day; the behaviour of the field during February 13<sup>th</sup>; the low field values at the end of February 15<sup>th</sup>; etc. The probably presence of these external variations has to be taken into account when interpreting the obtained results. The importance of a close ground magnetic station for the temporal reduction of the survey data is clearly manifested.

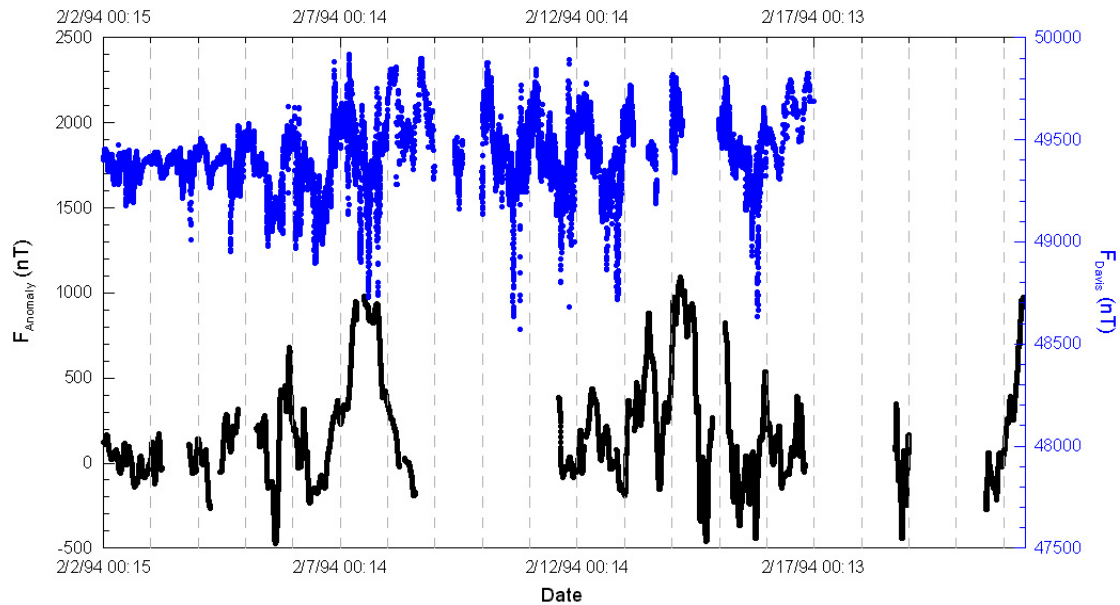


**Figure V.10.** Anomaly field obtained from SAE-39 survey using ARM as reference model (bottom, black line) compared with the total field values measured at Davis observatory for the same epoch (top, blue).

In order to correct the diurnal variation of the magnetic field as well as some of the external rapid variations, the usual procedure when observatory data are not available was applied, i.e. the removal of a reference field. Ionospheric and magnetospheric contributions from CM3 were subtracted from the marine profile data, and we assumed that the remaining field was representative of the main and crustal fields of the surveyed area. Total field values computed from IGRF-9, CM3, and ARM for each position and epoch were removed from the residual  $F$  values, and the corresponding anomaly profiles are shown in figures V.11 to V.13, respectively. Two anomaly profiles were obtained from CM3. The first one considered only the main field contribution from the model (degree  $n=13$ ), whereas an expansion up to  $n=25$  (equivalent to the degree represented by the ARM model) was considered in the second one. Since both results were similar, only one figure is presented for the anomaly field with respect to the CM3 (that one with  $n=25$ ).

The difference in the residual values at the join point between each couple of overlapping surveys reflect the suitability of the model used to reduce the data: better the model, lower the

difference found. Table V.1 shows the differences at the six join points for the four (IGRF, CM3 with  $n=13$  and  $n=25$ , and ARM) models used. It can be seen that the lowest differences are found when using ARM. The differences at point F are probably the most significant. It represents the union between the two most distant surveys, the first one developed in 1995 and the second one in 2002. Moreover, the daily Kp index (the sum of the 3-hour Kp indices for a given day) for the days in which overlapping measurements were taken was very low (10+ for February 5<sup>th</sup> 1995, and 6+ for March 16<sup>th</sup> 2002). Hence the external activity is expected to be low for these days. The proper continuation of both surveys given by ARM is a sign of the correctness of the model.

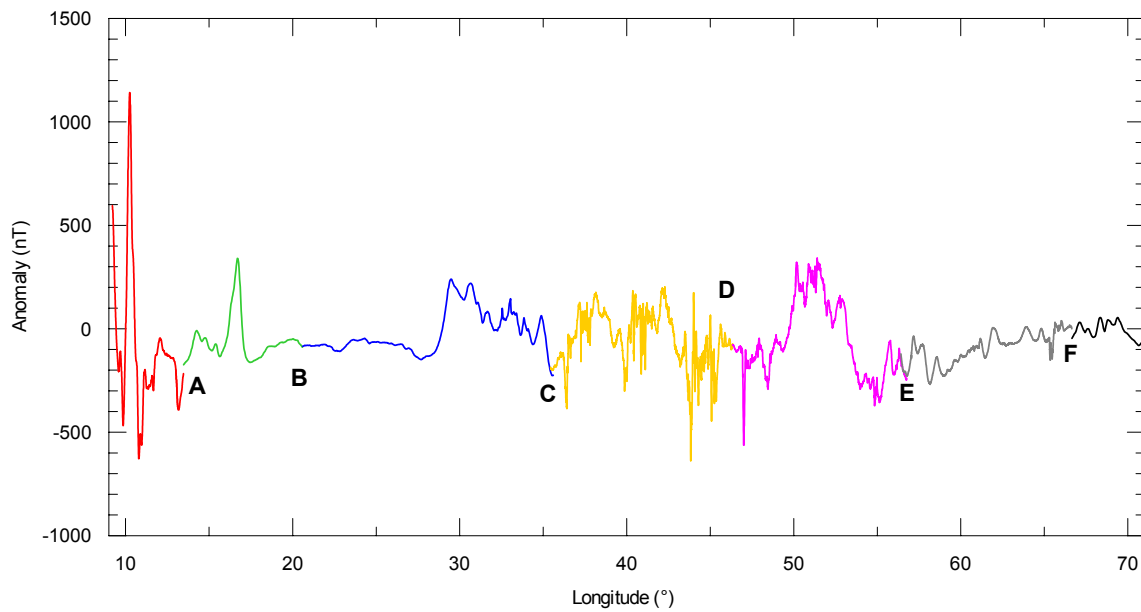


**Figure V.11.** Anomaly field obtained from the marine data using IGRF-9 as reference model.

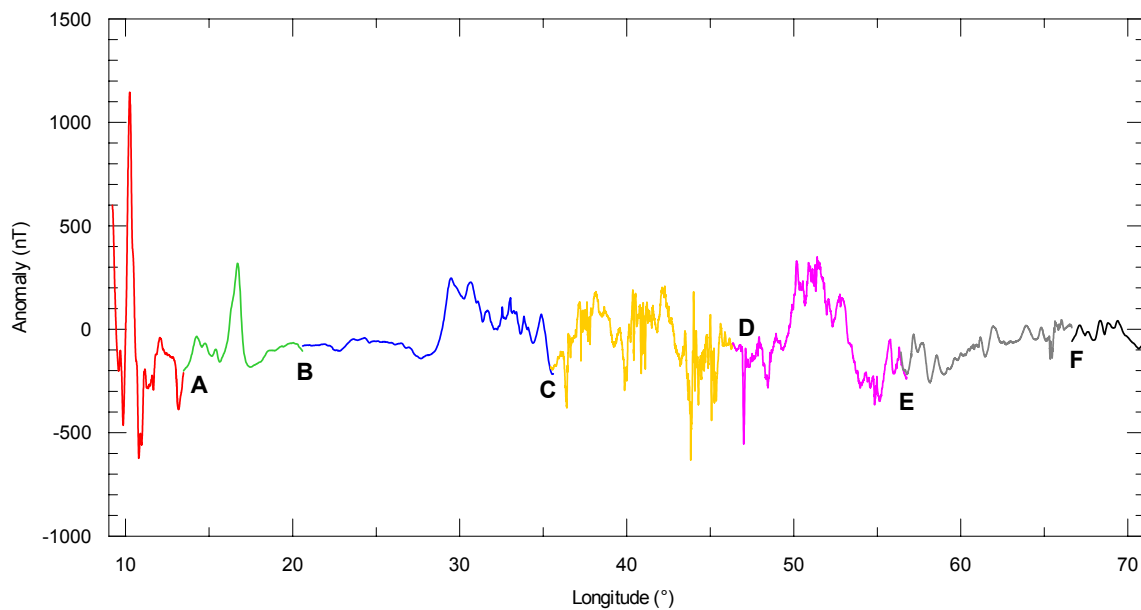


**Figure V.12.** Anomaly field obtained from the marine data using CM3 ( $n=25$ ) as reference model.

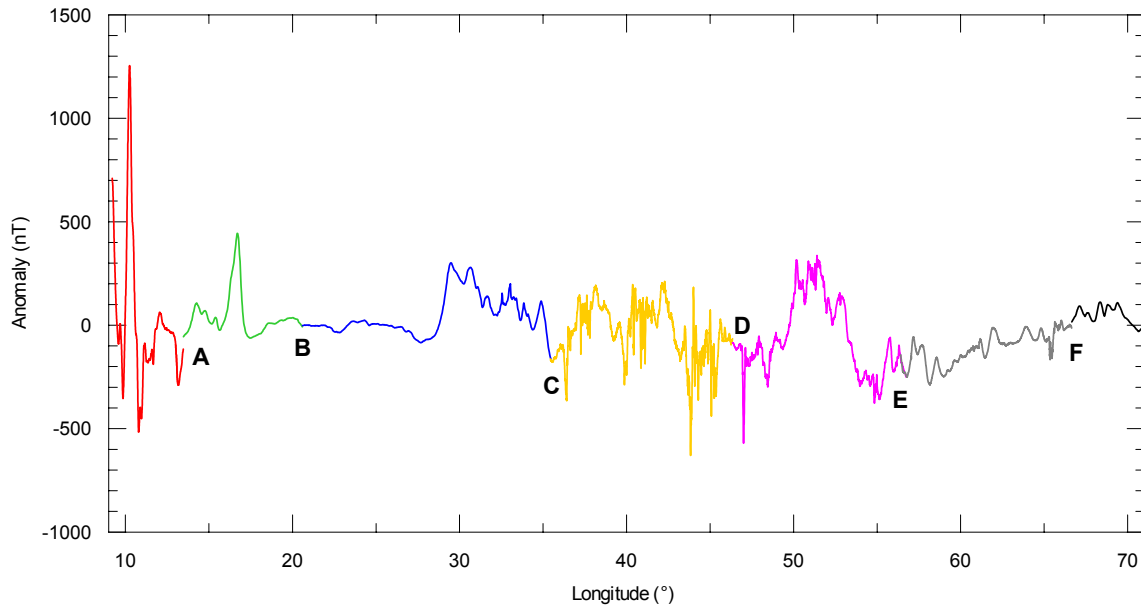


**Figure V.13.** Anomaly field obtained from the marine data using ARM as reference model.

Point	Model			
	IGRF-9	CM3 <sub>n=13</sub>	CM3 <sub>n=25</sub>	ARM
A	42.4	10.3	10.1	59.1
B	5.4	24.2	22.2	5.6
C	26.2	23.5	23.5	3.0
D	6.8	3.3	3.2	20.8
E	11.7	14.8	14.9	7.7
F	46.7	66.2	67.0	30.1
Mean	23.3	23.7	23.5	21.1

**Table V.1.** Differences (in nT) at the union points between the values of the anomaly field for couples of surveys obtained reducing the surveys with different models. The location of each union point can be checked in figures V.11 to V.13.

Finally, the bad correspondence found for ARM and IGRF-9 at points A and D could be influenced by the high external magnetic activity during some of the surveys (daily Kp equal to 37- for March 1<sup>st</sup>, 1999, and 35- for March 6<sup>th</sup>, 2000), so the evaluation of the connection at these points can not be taken so much into account. I would also like to point out that the IGRF 9<sup>th</sup> generation coefficients were published at the very late stage of this work, so although all the fits shown in this report were computed with respect to IGRF-9, all the rms had been previously computed with respect to IGRF-8. In particular, the mean difference found for the six union points just presented in table V.1 was up to 40 nT for IGRF-8. It is a clear demonstration of the improvement of IGRF-9 with respect to IGRF-8 for years between 1995 and 2005.



### Aeromagnetic surveys over the Antarctic Peninsula and Weddell Sea areas

The second example regards the aeromagnetic surveys held on the Antarctic Peninsula and central Weddell Sea areas in the framework of the USAC project [LaBrecque *et al.*, 1986]. The surveys were carried out between the second half of 1985 and the first months of 1989. Figure V.14 shows the survey lines covered by the available data separated by half years. As in the previous case for the marine data, no diurnal correction was made to the data [M. Ghidella, personal communication], so CM3 was again used to minimize the presence of external contributions into the measured total intensity field.

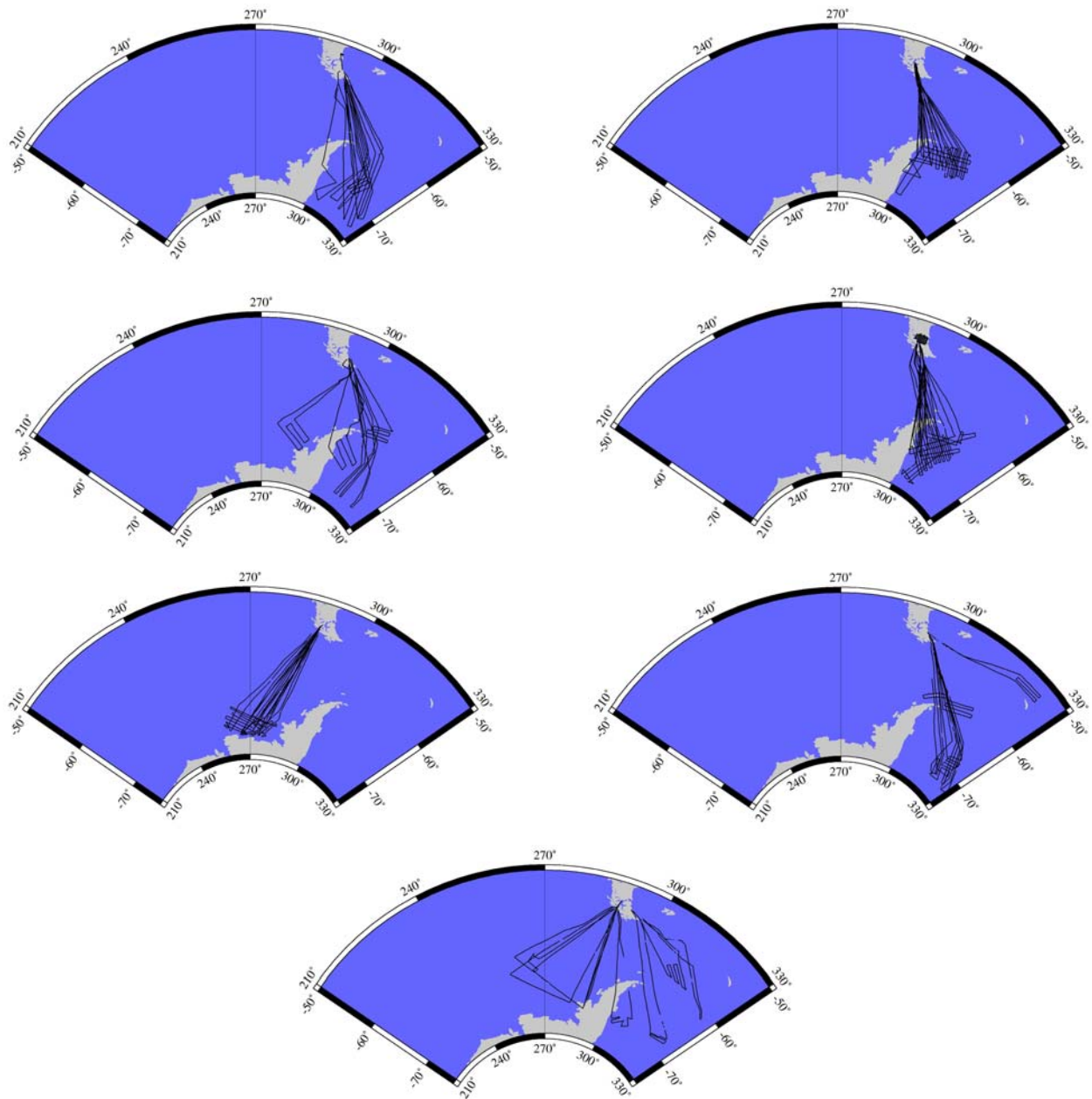


**Figure V.14.** USAC survey tracks distributed by half-years. From left to right and from top to bottom, figures correspond to 1985 (2<sup>nd</sup> half), 1986 (1<sup>st</sup> half), 1986 (2<sup>nd</sup>), 1987 (1<sup>st</sup>), 1987 (2<sup>nd</sup>), 1988 (1<sup>st</sup>), and 1989 (1<sup>st</sup>) surveys.

Track lines were visually inspected in order to find coincident passages, since the temporal reduction of the magnetic data from these lines could give another clue about the behaviour of the reference model used. Despite the high amount of available data presented in figure V.14, it must be taken into account that not all the surveys were flown at the same altitude. A major division can be done separating the surveys between those that were realized at high altitude (above approximately 6 km) and those carried out at low height (below 1.5 km). Therefore the number of tracks that overlies in all three coordinates (longitude, latitude, and height) is really low. An almost perfect correspondence was nevertheless found for two surveys, one carried out in December 16<sup>th</sup>, 1985 and other one in January 22<sup>nd</sup>, 1988. Again, a good reference model is supposed to give the minimum differences between the anomaly fields computed from both profiles. Figures V.15 to V.17 show the temporal evolution of the anomalies obtained using IGRF-9, CM3, and ARM. As can be seen, ARM is the reference model that brings one profile closer to the other. This difference was quantified for those couples of points (one for each profile) that were less than 10 meters distant in altitude. A total of 31 points which met this criteria were selected, and the mean differences found were 35.6 nT using IGRF-9, 28.5 nT using CM3; and 22.3 nT using ARM. So also in this case ARM appears to be the best reference model.

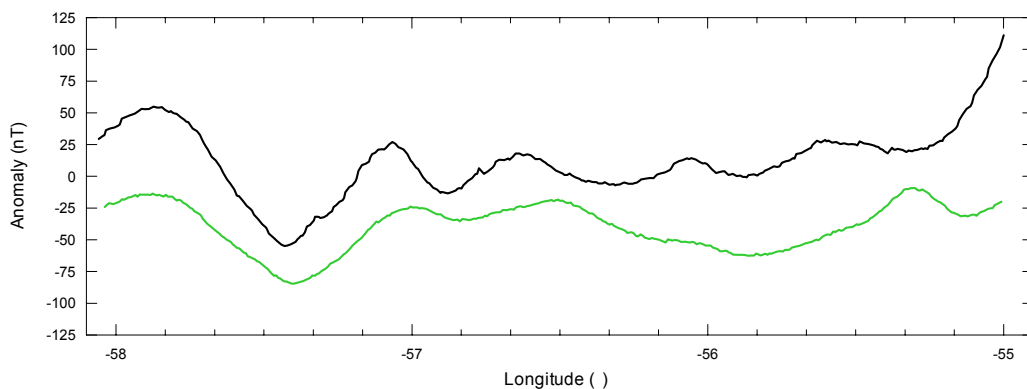


**Figure V.15.** Anomaly field obtained using IGRF as reference model from two different overlying profile lines, one carried out in December 1985 (black line) and the other one in January 1988 (green line).

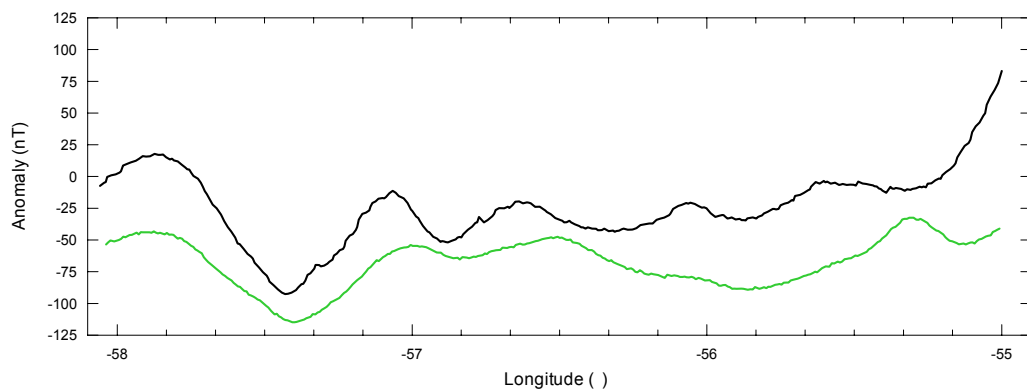


**Figure V.16.** As Figure V.15 but using CM3 as reference model.

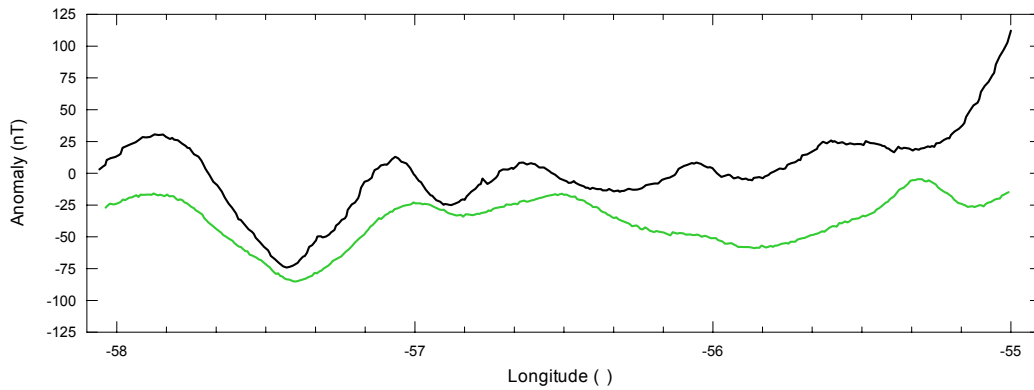


**Figure V.17.** As Figure V.15 but using ARM as reference model.

All the tests shown drive to conclusion that ARM is a model that represents properly the main magnetic field in Antarctica. As a final results, an anomaly map for the area covered by the aeromagnetic campaigns will be presented in what follows. Figure V.18 shows the location of the data points used to create the anomaly map. Only the measurements taken below 1 km were considered, and after applying a decimation the number of points was equal to 2196. Figure V.19 shows the plate-tectonic position of the area covered by the aeromagnetic data, as well as the geological interpretation of the Antarctic Peninsula region given by Johnson and Smith [1992] following the results of a previous aeromagnetic anomaly map. The knowledge of this region is fundamental in understanding the evolution of the West Antarctic neighbourhood. As can be seen, the northernmost region is dominated by an active transform fault and by a subduction linear batholith that give rise to the Pacific Margin Anomaly [Garret, 1990]. The central and southernmost regions are dominated by sedimentary basins.

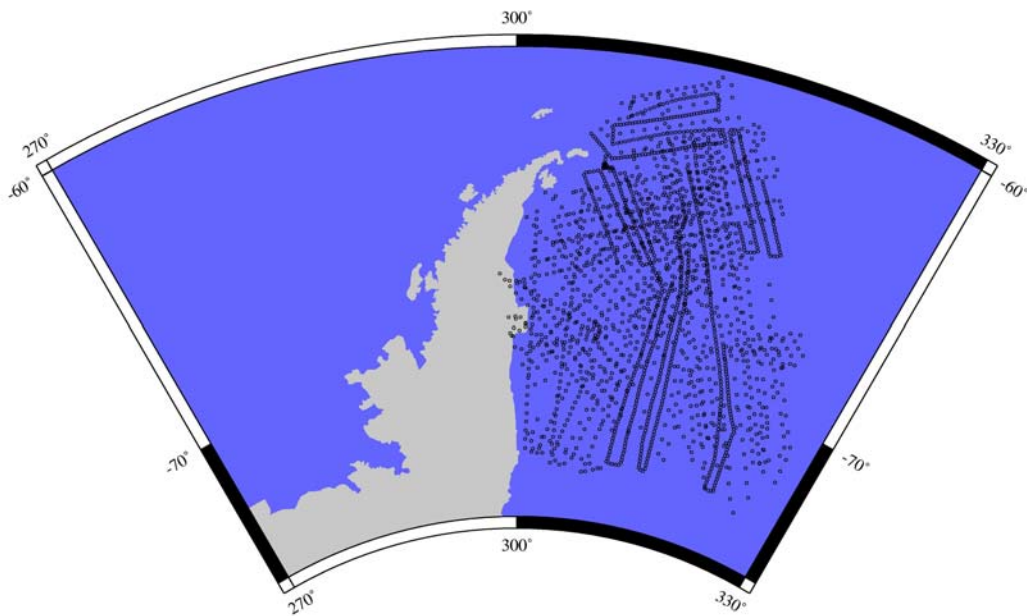


**Figure V.18.** Location of the data points used to obtain the final anomaly map presented in figure V.20.

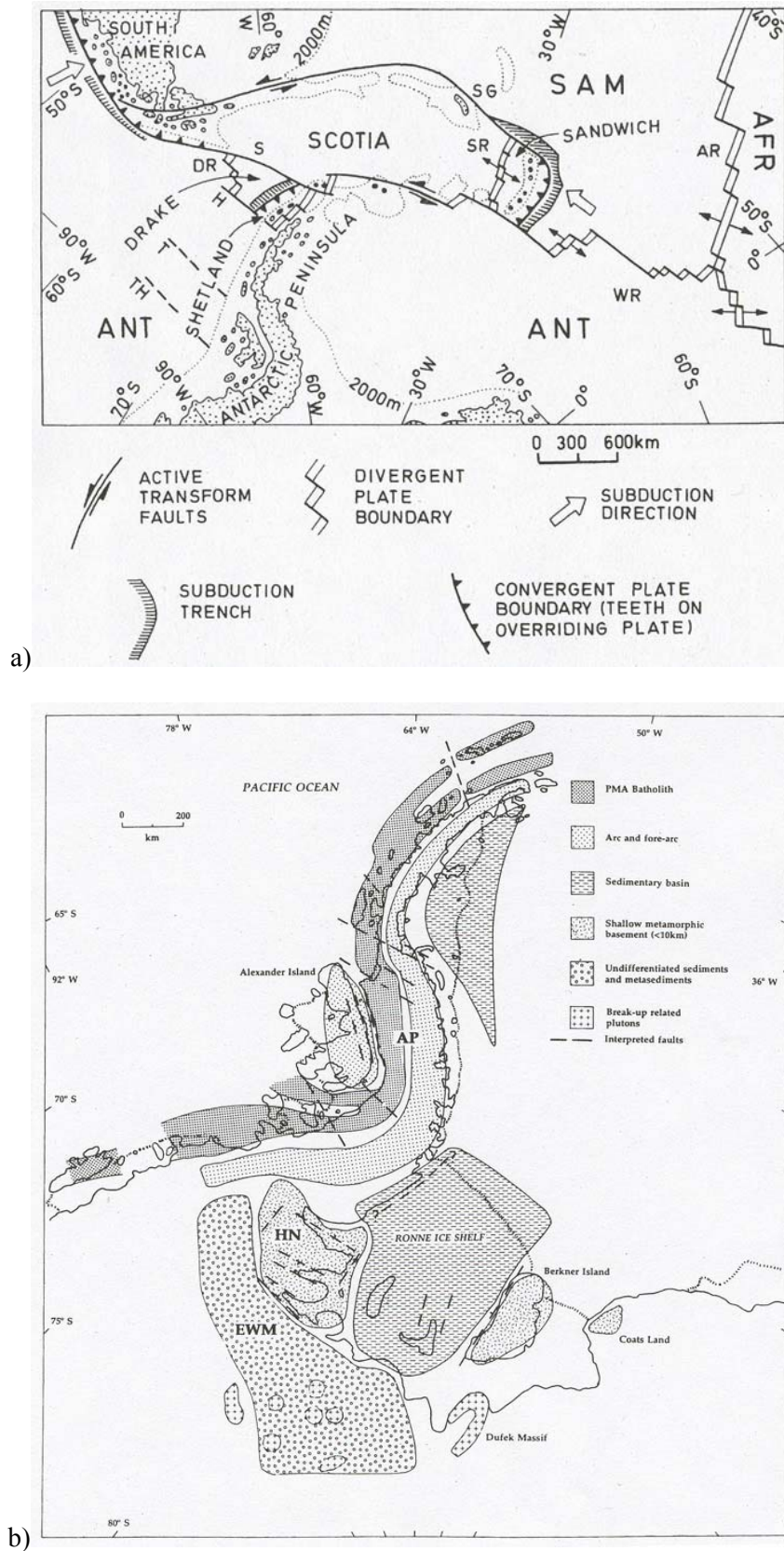


**Figure V.19.** a) Plate-tectonic location of the Antarctic Peninsula-Weddell Sea region [from Birkenmajer, 1992]. b) Geological interpretation of the Antarctic Peninsula area given by Johnson and Smith [1992] as derived from an aeromagnetic anomaly map.

The Antarctic Reference Model computed for each location at the epoch in which the measurement was taken was removed from the data. A first anomaly map in which all residuals are merged was then obtained. Since each one of these points had a different altitude, in order to bring all the anomaly data to a common altitude the method of equivalent sources was used [Mayhew, 1979]. Following this technique, the magnetic anomalies can be inverted to an equivalent layer magnetization model based on a dipole source array at the Earth's surface. The dipole magnetic moments are solved such that the field due to the array best fit the observed magnetic field above the grid.

An equally-area spaced array of dipoles was created. Each couple of dipoles were  $0.15^\circ$  distant in longitude, so the number of dipoles necessary to cover all the surveyed area was 5791. The dipole orientation was chosen that of the present magnetic field in the area, and they were placed 20 km depth below the Earth's surface. The equivalent source formulation leads to a mathematical model of the magnetic sources which gives rise to the observed anomaly field. The mean difference between the real anomaly field and that computed through the equivalent sources method is 1.5 nT. Differences are lower than 0.5 nT for 80% of the points. The magnetic anomalies can be therefore computed at a common height to produce the final anomaly map.

Figure V.20 shows the anomalies computed at 500 meters above sea level. The major features observed in the map are conserved when comparing it with previous anomaly maps for regions that included the area under study, maps that were generated using IGRF-8 as reference model [Golynsky *et al.*, 2002]. The highs that appear in the northernmost part of the map are related to the Pacific Margin Anomaly. The southern part of the map (the northern part of the Weddell Sea embayment) is dominated by a low in the anomaly field that spreads all over the area. This is related to the large thickness of the sediments in the region, so the magnetic anomaly signal is screened. Only one low-amplitude high is observed in that area, at around  $-70^\circ$  latitude, east-west aligned. This is known as the Orion Anomaly, and it is interpreted as a rift event at the Weddell Sea margin.

This map was created to show the utility of ARM, and not like a final map for geological interpretation. In this sense, no special attention was given for example to the high number of equivalent sources chosen to represent the field. More besides, the pre-process procedures involved in the analysis of aeromagnetic data (profile levelling, etc.) were avoided. All these considerations will be taken into account in the future step of this work, the development of a new magnetic anomaly map for Antarctica using ARM as reference model.



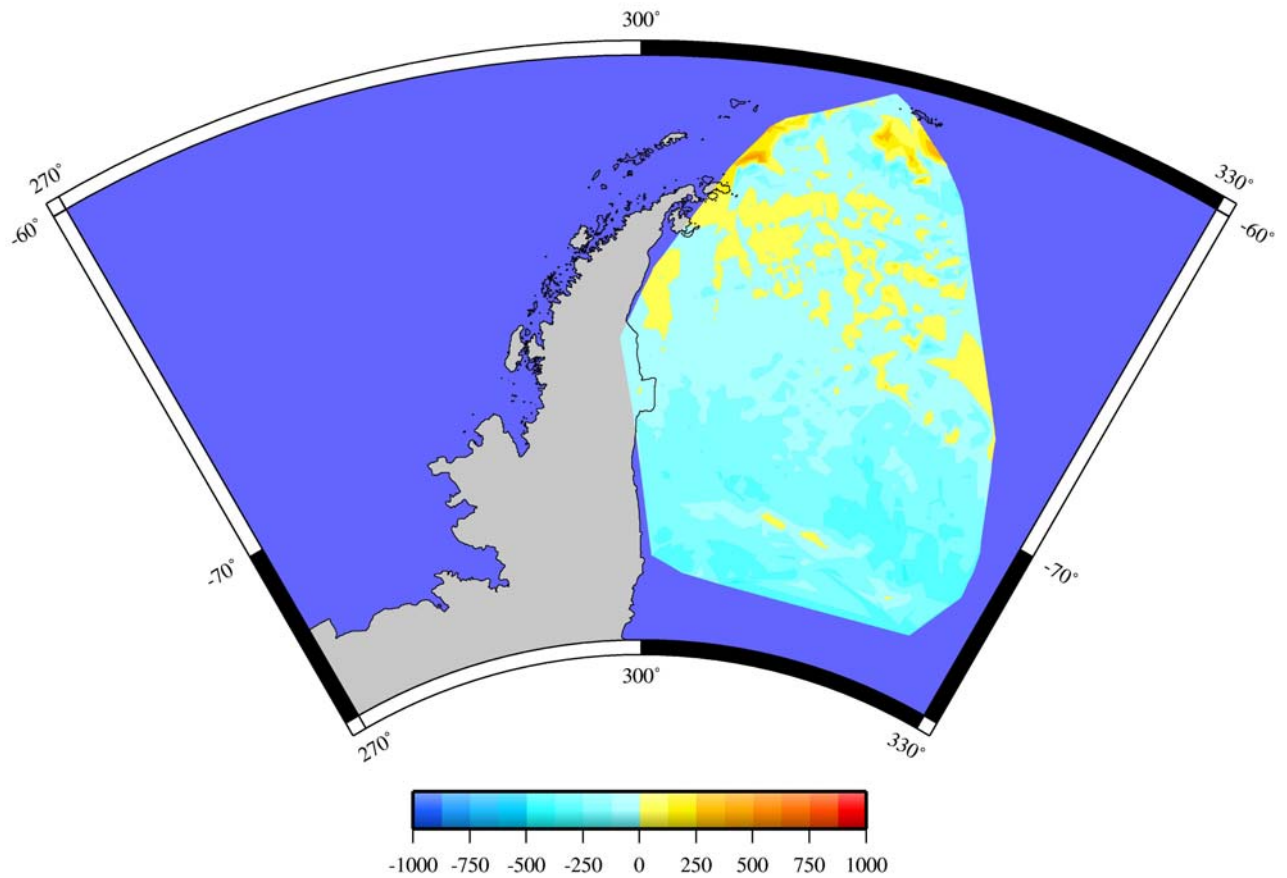


**Figure V.20.** Anomaly map computed at 500 meters height using the reference field given by ARM.

## VI. Conclusions

Through all the work presented in this thesis, I have attempted to analyse the geomagnetic field in Antarctica during roughly the last four decades, with all the useful available data I have found, with the purpose of obtaining a tool to reduce, as precisely as possible, the different magnetic surveys carried out in the region during the period of validity of the model. Independently of its main utility, the final result had to be an analytical representation of the main field and its secular variation (with the allowance for the longest wavelength part of the lithospheric field) over such a restricted portion of the Earth. To accomplish these objectives, a thorough study of the chosen technique (showing its capabilities and its limitations) on one hand, and of the data used on the other hand, has been undertaken and shown with all detail. Both technique and data have been scrutinized in order to allow for successive improvements or updates of the model.

The Antarctic Reference Model (ARM), at my knowledge the first full main field (i.e. main field plus its secular variation) geomagnetic model for Antarctica, has demonstrated to be a useful tool to develop magnetic studies below 60° South latitude. The model has been developed taking advantage of the last data sets available for the region. The database with the annual means from all obtainable Antarctic magnetic observatories has been updated. The inconsistencies found in some observatories series have been reported to the World Data Centers to avoid an incorrect use on the part of other users. A balloon mission has been studied to obtain a data set of magnetic measurements from stratospheric altitude. Special attention has been given to this mission since its magnetic measurements have been used for the first time in this work. Finally, data from six magnetic satellite missions have also been used, covering different epochs of the more than 40 years of validity of the model. These data have been selected according to different criteria to model only values corresponding to magnetically quiet periods.

Spherical cap harmonic analysis has been applied to develop the model. The technique has been reviewed, the improvements done since its introduction have been reported, and some of the major modifications have been considered to generate the coefficients of the model. The model is able to represent wavelengths down to 1600 km, and its validity has been assessed between 1960 and 2005. The model presents a smooth behaviour for the full temporal range of validity.

The model has been compared with the International Geomagnetic Reference Field 9<sup>th</sup> generation (IGRF-9) and with the Phase 3 of the Comprehensive Model (CM3) to check its

strength. The fit to both ground or satellite datasets, allows us to affirm that ARM represents properly the input data. The representation of the secular variation of the geomagnetic field has been improved with respect to the behaviour predicted by IGRF-9. The anomaly biases found with regard to the magnetic observatories are mostly comparable to the values obtained by the CM3. The fit of ARM to the input satellite data is better than the fit obtained by using IGRF-9 or CM3 models when only the internal contributions of this last one are considered. On the other hand, the maps for the magnetic components show that the Antarctic Reference Model presents also a proper performance in those locations or periods for which data are not available.

The maps for the magnetic components are one of the benefits of the developed model. Other profits have been the study of the location and movement of the magnetic pole, or the determination of the years in which magnetic jerks could have been occurred. All these tests have demonstrated moreover the validity of the model.

The final scope of this work, the development of a reference model able to reduce magnetic surveys better than IGRF, has been achieved. The validity of ARM has been furthermore demonstrated comparing it with data surveys that were not analysed in the model. The temporal reduction of marine and aeromagnetic data shown in this work let us to confirm that ARM can be used with guarantees to develop magnetic anomaly maps in which data coming from different periods are merged.

The future work related to this thesis will be focused in three fields: updating of the model, improvement of the satellite data selection, and improvement of the spherical cap harmonic analysis.

The model will be regularly updated as new datasets will be available. The website of the World Data Center at the British Geological Survey will be consulted periodically to obtain the latest observatory annual means. The fact that the author of this thesis belongs to a group member of the Ørsted and Champ scientific teams makes sure of having access to the newest satellite datasets.

These new satellite data, as well as the old data sets, will be selected not only assuming restrictive criteria in the magnetic conditions of a given period, but according to other selection procedures based on the static properties of the internal fields with respect to the variable appearance of the external fields. Such kind of procedure has been recently applied by Kim [2002] to study the Antarctic lithospheric field from satellite measurements, following the approach of Alsdorf *et al.* [1994b]. After separating individual passages into dawn and dusk



local times and by altitude, a first selection is done considering the variance of the residuals after the removal of a least-squares fit of the core field. The coherent and non-coherent features present in neighbouring tracks are finally isolated by using a Fourier correlation coefficient filter. It constitutes a finest way to select satellite data: several amounts of useful data are rejected when comparing satellite tracks against the geomagnetic indices, whereas in this procedure only data that appears to present magnetic contributions from internal origin are finally selected. In this sense, it is planned for the current year a visit of the author of this work to the Byrd Polar Research Center (Ohio, US) to meet the specialists in this analysis technique. The visit will be addressed to learn all the procedures to obtain a satellite magnetic field data set in which the external fields have been minimized.

The detailed study of the SCHA technique done in Chapter II can also give interesting results in this sense. We have seen how the improvement in the calculus of the associated Legendre polynomials meant in practice a better separation of the internal and external contributions of the analysed magnetic field. The same procedure can be applied to real satellite data coming from the newest missions. Ørsted and Champ satellites are providing us with a high amount of magnetic field measurements. These data can be divided into layers in altitude for periods with similar level of external activity (following magnetic indices, year season, etc.). A spherical harmonic expansion of the field can be therefore done on the Antarctic cap using both internal and external coefficients, in order to isolate the external contribution. We will begin the analysis using synthetic data from models like CM3, in which the separation of the external and internal components is known, to determine the parameters that best define each SCHA model. The real data will be then modelled to eliminate the systematic external fields.

With regard to the technique, spherical cap harmonic analysis will be revisited according to the procedure proposed by Korte and Holme [2003]. One of the main disadvantages of the mathematical procedure employed in this work is the rejection or acceptance of the coefficients of the model in accordance to their statistical significance, a method without a clear physical justification. This criteria selection can lead to situations in which a small variation in the parameters that define the model (e.g. a slight increment in the maximum spatial index of the model, or a change in the data weights) supposes a sharply change in the coefficient values. The above mentioned authors proposed a method in which a certain feature of the field (it can be the strength of the field over the surface of the spherical cap, or the mean square radial component of the vector field) is minimized. Following the authors, with this physical regularisation the individual coefficients become meaningful. Some preliminary tests have been actually carried

out by using the original software provided by the authors [M. Korte, personal communication]. More work will be also dedicated to the inversion procedure to solve the coefficients of the model.

To finish, all the achieved progresses will be reported at the ARM website (<http://www.ingv.it/arm>), where the state of the art of the work can be consulted. The possibility to access online to the model through a website, allowing the user to compute the values of the magnetic field for any place in Antarctica since 1960 onwards, makes the model available to anyone interested in it. Actually the model is being used by researchers at Goddard Space Flight Center [H.R. Kim, personal communication] as reference model to obtain the anomaly field from the newest satellite data. The model will be also used to obtain the new magnetic anomaly map of the Antarctic in the framework of the new Antarctic Digital Magnetic Anomaly Project [R.R.B. von Frese, personal communication].

## VII. References

- Alexandrescu M., Database of Geomagnetic observatory monthly means seeks contributors. *EOS, Trans. Am. Geophys. Union* **79**, 345, 1998.
- Alsdorf D.E., von Frese R.R.B., Arkani-Hamed J., and Noltimier H.C., Separation of lithospheric, external, and core components of the South polar geomagnetic field at satellite altitudes, *J. Geophys. Res.* **99**, 4655-4667, 1994a.
- Alsdorf D.E., von Frese R.R.B., and the Geodynamics Branch at GSFC, *Fortran programs to process Magsat data for lithospheric, external field, and residual core components*. NASA Technical Memorandum 104612, Greenbelt, Maryland, 1994b.
- An Z.C., Ma S.Z., Tan D.H., Barraclough D.R., and Kerridge D.J., A Spherical Cap Harmonic Model of the Satellite Magnetic Anomaly Field over China and Adjacent Areas. *J. Geomag. Geoelectr.* **44**, 243-252, 1992.
- An Z.C., Tan D.H., Xu Y.F., Golovkov V.P., Rotanova N.M., and Bondar T.N., Spherical Cap Harmonic Analysis of the Geomagnetic Field over East Asia. *J. Geomag. Geoelectr.* **46**, 789-795, 1994.
- Backus G. E., Non-uniqueness of the external geomagnetic field determined by surface intensity measurements. *J. Geophys. Res.* **75**, 6339–6341, 1970.
- Barton C., Survey tracks current position of South Magnetic Pole. *EOS, Trans. Am. Geophys. Union* **83**, 291, 2002.
- Barton C., Reply to “Comment on ‘Survey tracks current position of South Magnetic Pole’ and ‘Recent acceleration of the North Magnetic Pole linked to magnetic jerks’”. *EOS, Trans. Am. Geophys. Union* **84**, N. 5, 42, 2003.
- Blanco-Montenegro I., Torta J.M., García A., and Araña V., Analysis and modelling of the aeromagnetic anomalies of Gran Canaria (Canary Islands). *Earth Planet. Sci. Lett.* **206**, N 3-4, 601-616, 2003.
- Bellanger E., Le Mouél J.-L., Mandeia M., and Labrosse S., Chandler wobble and geomagnetic jerks. *Phys. Earth Planet. Int.* **124**, 95-103, 2001.
- Birkenmajer K., Evolution of the Bransfield basin and rift, West Antarctica. In *Recent Progress in Antarctic Earth Science*, ed. Y. Yoshida *et al.*, pp. 405-410. Terrapub, Tokyo, 1992.

- Bloxham J., Zatman S., and Dumberry M., The origin of geomagnetic jerks. *Nature* **420**, 65-68, 2002.
- Cain J.C., Daniels W.E., Hendricks S.J., and Jensen D.C., An evaluation of the main geomagnetic field, 1940-1962. *J. Geophys. Res.* **70**, 3647-3674, 1965.
- Cain J.C., Hendricks S.J., Langel R.A., and Hudson W.V., A proposed model for the International Geomagnetic Reference Field – 1965. *J. Geomag. Geoelectr.* **19**, 335-355, 1967.
- Campbell W.H., *Introduction to Geomagnetic Fields*. Cambridge University Press, Cambridge, 1997.
- Campbell W.H., Comment on ‘Survey tracks current position of South Magnetic Pole’ and ‘Recent acceleration of the North Magnetic Pole linked to magnetic jerks’. *EOS, Trans. Am. Geophys. Union* **84**, N. 5, 41, 2003.
- Chambodut A., Schwarte J., Langlais B., Lühr H., and Manda M., The selection of data in field modeling. *Proceedings of the 4th OIST meeting*, ed. Stauning *et al.*, pp. 31-34, Copenhagen, 2003.
- Chapman S., and Bartels J., *Geomagnetism*. Oxford University Press, Oxford, 1940.
- Chiappini M., von Frese R.R.B., and Ferris J., Effort to develop magnetic anomaly database aids Antarctic research. *EOS, Trans. Am. Geophys. Union* **79**, 290, 1998.
- Chiappini M., von Frese R.R.B., Behrendt J., Bell R., Bozzo E., Brancolini G., Damaske D., De Santis A., Ferraccioli F., Ferris J., Finn C.A., Ghidella M.E., Golynsky A., Gregori G.P., Grunow A., Ishihara T., Jewell C., Johnson A., Labrecque J., Lodolo E., Maschenkov D., Meloni A., Morris P., Nogi Y., Purucker M., Taylor P., Torta J.M., *Report on the II SCAR/IAGA Working Group on the Antarctic Digital Magnetic Anomaly Project (ADMAP)*. Pub. 601, Istituto Nazionale di Geofisica, Roma, 1999.
- Chiappini M., Ferraccioli F., Bozzo E., and Damaske D., Regional compilation and analysis of aeromagnetic anomalies for the Transantarctic Mountains – Ross Sea sector of the Antarctic. *Tectonophysics* **347**, 121-137, 2002.
- Cohen Y., Menvielle M., and Le Mouel J.L., Magnetic measurements aboard a stratospheric balloon. *Phys. Earth Planet. Int.* **44**, 348-357, 1986.
- Coles R.L., Magsat scalar magnetic anomalies at Northern high latitudes. *J. Geophys. Res.* **90**, N. B3, 2576-2582, 1985.

- Crill B.P., *A measurement of the angular power spectrum of the cosmic microwave background with a long duration balloon-borne receiver*. PhD thesis, California Institute of Technology, Pasadena, 2001.
- De Bernardis P., Ade P.A.R., Bock J.J., Bond J.R., Borill J., Bosaleri A., Coble K., Crill B.P., De Gasperis G., Farese P.C., Ferreira P.G., Ganga K., Giacometti M., Hivon E., Hristov V.V., Iacoangeli A., Jaffe A.H., Lange A.E., Martinis L., Masi S., Mason P., Mauskopf P.D., Melchiorri A., Miglio L., Montroy T., Netterfield C.B., Pascale E., Piacentini F., Pogosyan D., Prunet S., Rao S., Romeo G., Ruhl J.E., Scaramuzzi F., Sforza D., and Vittorio N., A flat universe from high-resolution maps of the cosmic microwave background radiation. *Nature* **404**, 955-959, 2000.
- De Santis A., Translated origin spherical cap harmonic analysis. *Geophys. J. Int.* **106**, 253-263, 1991.
- De Santis A., Conventional spherical harmonic analysis for regional modelling of the geomagnetic field. *Geophys. Res. Lett.* **19**, N. 10, 1065-1067, 1992.
- De Santis A., Decomposizione spettrale del campo geomagnetico in armoniche sferiche su calotta sferica. *Communication at the VII Workshop di Geoelettromagnetismo*, Padova, 1998.
- De Santis A., and Falcone C., Spherical cap models of Laplacian potentials and general fields. In *Geodetic theory today*, ed. F. Sansò, pp. 141-150, International Association of Geodesy Symposia, IUGG, 1995.
- De Santis A., and Torta J.M., Spherical cap harmonic analysis: a comment on its proper use for local gravity field representation. *Journal of Geodesy* **71**, 526-532, 1997a.
- De Santis A., and Torta J.M., Spherical cap harmonics and ordinary spherical harmonics. *Abstracts of the 8<sup>th</sup> Scientific Assembly of the International Association of Geomagnetism and Aeronomy (IAGA)*. Uppsala, 1997b.
- De Santis A., Kerridge D.J., and Barraclough D.R., A Spherical Cap Harmonic Model of the Crustal Magnetic Anomaly Field in Europe by Magsat. In *Geomagnetism and Paleomagnetism*, ed. F.J. Lowes *et al.*, pp. 1-17, Kluwer, Dordrecht, 1989.
- De Santis A., Battelli O., and Kerridge D.J., Spherical cap harmonic analysis applied to regional field modelling for Italy. *J. Geomag. Geoelect.* **42**, 1019-1036, 1990.
- De Santis A., Falcone C., and Torta J.M., Simple additional constraints on regional models of the geomagnetic secular variation field. *Phys. Earth Planet. Int.* **97**, 15-21, 1996.

- De Santis A., Chiappini M., Torta J.M., and von Frese R.R.B., Development of an improved geomagnetic reference field of Antarctica. *Annali di Geofisica* **42**, N. 2, 261-264, 1999a.
- De Santis A., Torta J.M., and Lowes F.J., Spherical Cap Harmonics revisited and their relationship to ordinary Spherical harmonics. *Phys. Chem. Earth (A)* **24**, N.11-12, 935-941, 1999b.
- De Santis A., Torta J.M., and Gaya-Piqué L.R., The first Antarctic geomagnetic Reference Model (ARM). *Geophys. Res. Lett.* **29**, N. 8, 33.1-33.4, 2002a.
- De Santis A., Barraclough D., and Tozzi R., Nonlinear variability in the geomagnetic secular variation of the last 150 years. *Fractals* **10**, N. 3, 297-303, 2002b.
- De Santis A., Gaya-Piqué L.R., Dominici A., Meloni A., Torta J.M., Tozzi R., Italian geomagnetic reference field: update for 2000 and secular variation model up to 2005 by autoregressive forecasting. *Annals of Geophysics* **46**, N. 3, 491-500, 2003.
- Draper N.R., and Smith H., *Applied regression analysis*. John Wiley & Sons, New York, 1966.
- Düzgit Z., and Malin S.R.C., Assessment of regional geomagnetic field modelling methods using a standard data set: spherical cap harmonic analysis. *Geophys. J. Int.* **141**, 829-831, 2000.
- Eckstaller A., Müller Ch., Nixdorf U., and Rogenhagen J., The geophysical observatory at Neumayer Station, Antarctica. In *The Antarctic Region: Geological Evolution and Processes*, ed. C.A. Ricci, pp. 1039-1048, Terra Antarctica, Siena, 1997.
- Friis-Christensen E., Lühr H., and Hulot G., *Swarm : A constellation to study the dynamics of the Earth's magnetic field and its interaction with the Earth system*. Proposal for ESA Earth Explorer opportunity missions, Danish Space Research Institute Report 1/2002, ISSN 1602-527X, 2002.
- Garrett S.W., Interpretation of reconnaissance gravity and aeromagnetic surveys of the Antarctic Peninsula. *J. Geophys. Res.* **95**, 6759-6777, 1990.
- Gauss C.F., Allgemeine Theorie des Erdmagnetismus. In *Resultate aus den Beobachtungen magnetischen Vereins im Jahre 1838*, p. 1-57, 1839.
- Gaya-Piqué L.R., De Santis A., and Torta J.M., Use of Champ magnetic data to improve the Antarctic Geomagnetic Reference Model. *Proceedings of the 2<sup>nd</sup> Champ Scientific Meeting*, 2004 (in press).

- Golynsky A.V., Chiappini M., Damaske D., Ferraccioli F., Ferris J., Finn C., Ghidella M., Ishihara T., Johnson A., Kim H.R., Kovacs L., Labrecque J., Masolov V., Nogi Y., Purucker M., Taylor P., and Torta J.M., ADMAP-Magnetic anomaly map of the Antarctic, 1:10 000 000 scale map. *British Antarctic Survey Misc.* 10, ed. Morris P., and von Frese R.R.B., Cambridge, 2001.
- Golynsky A.V., Morris P., Kovacs L.C., and Ferris J.K., A new magnetic map of the Weddell Sea and the Antarctic Peninsula. *Tectonophysics* **347**, 3-11, 2002.
- Haghipour A., *Sismotectonic map of the world*. Map 1:25.000.000. UNESCO, 2001.
- Haines G.V., Spherical Cap Harmonic Analysis. *J. Geophys. Res.* **90** (B3), 2583-2591, 1985a.
- Haines G.V., Magsat Vertical Field Anomalies above 40°N from Spherical Cap Harmonic Analysis. *J. Geophys. Res.* **90** (B3), 2593-2598, 1985b.
- Haines G.V., Spherical Cap Harmonic Analysis of Geomagnetic Secular Variation over Canada 1960-1983. *J. Geophys. Res.* **90** (B14), 12563-12574, 1985c.
- Haines G.V., Computer programs for spherical cap harmonic analysis of potential and general fields. *Computers & Geosciences* **14**, N.4, 413-447, 1988.
- Haines G.V., Regional magnetic field modelling: a review. *J. Geomag. Geoelect.* **42**, 1001-1018, 1990.
- Haines G.V., Modelling geomagnetic secular variation by main-field differences. *Geophys. J. Int.* **114**, 490-500, 1993.
- Haines G.V., and Newitt L.R., Canadian geomagnetic reference field 1985. *J. Geomag. Geoelectr.* **38**, 895-921, 1986.
- Haines G.V., and Torta J.M., Determination of Equivalent Currents Sources from Spherical Cap Harmonic Models of Geomagnetic Field Variations. *Geophys. J. Int.* **118**, 499-514, 1994.
- Haines G.V., and Newitt L.R., The Canadian geomagnetic reference field 1995. *J. Geomag. Geoelectr.* **49**, 317-336, 1997.
- Harrison C.G.A., The Crustal Field. In *Geomagnetism*, vol. I, ed. J.A. Jacobs. Academic Press Limited, London, 1987.
- Hildenbrand T.G., Blakely R.J., Hinze W.J., Keller G.R., Langel R.A., Nabighian M., and Roest W., Aeromagnetic survey over U.S. to advance geomagnetic research. *EOS Trans. Am. Geophys. Union* **77**, N. 28, 265-268, 1996.



- Holme R., Modelling of attitude error in vector magnetic data: application to Ørsted data. *Earth Planets Space* **52**, 1187-1197, 2000.
- Holme R., Lühr H., Rother M., and Gödderz K., Magnetic field modelling with CHAMP data: initial results. *EOS Trans. Am. Geophys. Union (Fall meeting suppl.)* **81**, N. 48, F346, 2000.
- International Association of Geomagnetism and Aeronomy (IAGA) Division V – Working Group 8, The 9th Generation International Geomagnetic Reference Field. *Phys. Earth Planet. Int.* **140**, 253-254, 2003.
- Jackson J.D., *Classical Electrodynamics*. John Wiley & Sons, New York, 1962.
- Jiancheng L., Dingbo C., and Jinsheng N., Spherical cap harmonic expansion for local gravity field representation. *Manuscr. Geod.* **20**, 265-277, 1995.
- Johnson A.C., and Smith A.M., New aeromagnetic map of the West Antarctica (Weddell Sea sector): introduction to important features. In *Recent Progress in Antarctic Earth Science*, ed. Y. Yoshida *et al.*, pp. 555-562. Terrapub, Tokyo, 1992.
- Kerridge D., Intermagnet: worldwide near-real-time geomagnetic observatory data. *Proceedings of the Workshop on Space Weather*, ESTEC, 2001.
- Kim H.R., *Antarctic lithospheric anomalies from Ørsted satellite and near-surface magnetic observations*. PhD thesis, The Ohio State University, 2002.
- Kim H.R., Gaya-Piqué L.R., von Frese R.R.B., Taylor P.T., and Kim J.W., CHAMP magnetic anomalies of the Antarctic crust. *Proceedings of the 2<sup>nd</sup> Champ Scientific Meeting*, 2004 (in press).
- Korte M., and Haak V., Modelling European Magnetic Repeat Station and Survey Data by SCHA in search of Time-Varying Anomalies. *Phys. Earth Planet. Int.* **122**, 205-220, 2000.
- Korte M., and Holme R., Regularization of spherical cap harmonics. *Geophys. J. Int.* **153**, 253-262, 2003.
- Kotzé P.B., Spherical Cap Modelling of Ørsted Magnetic Field Vectors over Southern Africa. *Earth, Planets and Space* **53**, 357-361, 2001.
- Kotzé P.B., Modelling and analysis of Ørsted total field data over Southern Africa. *Geophys. Res. Lett.* **29**, N.15, 5.1-5.3, 2002.

- LaBrecque J.L., Cande S., Bell R., Raymond C., Brozena J., Keller M., Parra J.C., and Yanez G., Aerogeophysical survey yields new data in the Weddell Sea. *Antarctic Journal of the United States 1986 Review* **21**, 69-70, 1986.
- Langel R.A., The magnetic Earth as seen from Magsat, initial results. *Geophys. Res. Lett.* **9**, 239-242, 1982.
- Langel R.A., *The Main Field*. In *Geomagnetism*, vol. I, ed. J.A. Jacobs, Academic Press Limited, London, 1987.
- Langel R.A., The use of low altitude satellite data bases for modeling of core and crustal fields and the separation of external and internal fields. *Surv. Geophys.* **14**, 31-87, 1993.
- Langel R.A., and Estes R.H., A geomagnetic field spectrum. *Geophys. Res. Lett.* **9**, 250-253, 1982.
- Langel R.A., and Hinze W.J., *The magnetic field of the Earth's lithosphere. The satellite perspective*. Cambridge University Press, Cambridge, 1998.
- Langel R.A., Ousley J., Berbert J., Murphy J., and Settle M., The Magsat mission. *Geophys. Res. Lett.* **9**, 243-245, 1982a.
- Langel R.A., Estes R.H., and Mead G.D., Some new methods in Geomagnetic field modeling applied to the 1960-1980 epoch. *J. Geomag. Geoelec.* **34**, 327-349, 1982b.
- Langel R.A., Sabaka T.J., Baldwin R.T., and Conrad J.A., The near-Earth magnetic field from magnetospheric sources and quiet-day ionospheric sources and how it is modeled. *Phys. Earth Planet. Int.* **98**, 235-267, 1996.
- Langlais B., and Mande M., An IGRF candidate main geomagnetic field model for epoch 2000 and a secular variation model for 2000-2005. *Earth, Planets, and Space* **52**, 1137-1148, 2000.
- Lanzerotti L.J., Langel R.A., and Chave A.D., Geoelectromagnetism. In *Encyclopedia of Applied Physics*, ed. G.L. Trigg. VCH Publishers, New York, 1993.
- Lawver L.A., Royer J.-Y., Sandwell D.T., and Scotese C.R., Evolution of the Antarctic continental margins. In *Geological Evolution of Antarctica. Proceedings of the Fifth International Symposium on Antarctic Earth Sciences*, ed. M.R.A. Thomson *et al.*, 533-539. Cambridge University Press, Cambridge, 1987.
- Lowes F.J., Mean square values on the sphere of spherical harmonic vector fields. *J. Geophys. Res.* **71**, 2179, 1966.

- Lowes F.J., Orthogonality and mean squares of the vector fields given by spherical cap harmonic potentials. *Geophys. J. Int.* **136**, 781-783, 1999a.
- Lowes F.J., A problem in using spherical cap harmonic analysis to separate internal and external fields. *Abstracts of the XXII General Assembly of IUGG*, GA1.07/W/03-B2. Birmingham, 1999b.
- Malin S.R.C., and Gupta J.C., The Sq current system during the international geophysical year. *Geophys. J. R. Astr. Soc.* **49**, 433-447, 1977.
- Malin S.R.C., and Hodder B.M., Was the 1970 geomagnetic jerk of internal or external origin? *Nature* **296**, 726-729, 1982.
- Mandea M., and Macmillan S., International Geomagnetic Reference Field – The Eighth Generation. *Earth, Planets and Space* **52**, 1119-1124, 2000.
- Mandea M., and Langlais B., Observatory crustal magnetic biases during Magsat and Ørsted satellite missions. *Geophys. Res. Lett.* **29**, N.15, 8003-8006, 2002.
- Mayaud P.N., *Derivation, meaning and use of geomagnetic indices*. Geophys. Monograph Am. Geophys. Union **22**, Washington D.C., 1980.
- Mayhew M.A., Inversion of satellite magnetic anomaly data. *J. Geophys.* **45**, 119-128, 1979.
- McLean S.J., Meyers K.D., Morris L.D., and Davis W.M., *A report on geomagnetic observatories*. World Data Center-A for Solid Earth Geophysics, Rep. SE-53, Boulder, 1995.
- Meloni A., Gaya-Piqué L.R., De Michelis P., and De Santis A., Some recent characteristics of geomagnetic secular variation in Antarctica. *Proceedings of the 9<sup>th</sup> ISAES meeting*, 2004 (in press).
- Needleman H.C., The NASA balloon program: conventional and long duration. *Adv. Space Res.* **17**, N. 9, 29-35, 1996.
- Neubert T., Mandea M., Hulot G., von Frese R.R.B., Primdahl F., Jørgensen J.L., Friis-Christensen E., Stauning P., Olsen N., and Risbo T., Ørsted satellite captures high-precision geomagnetic field data. *EOS Trans. Am. Geophys. Union* **82**, N. 7, 81, 2001.
- Olsen N., A model of the geomagnetic field and its secular variation for epoch 2000 estimated from Ørsted data. *Geophys. J. Int.* **149**, 454-462, 2002.
- Olsen N., Holme R., Hulot G., Sabaka T., Neubert T., Toffner-Clausen L., Primdahl F., Jørgensen J., Leger J.-M., Barraclough D., Bloxham J., Cain J., Constable C., Golovkov V.,

- Jackson A., Kotze P., Langlais B., Macmillan S., Manda M., Merayo J., Newitt L., Purucker M., Risbo T., Stampe M., Thomson A., and Voorhies C., Ørsted Initial Field Model. *Geophys. Res. Lett.* **27**, 3607-3610, 2000.
- Olsen N., Moretto T., and Friis-Christensen E., New approaches to explore the Earth's magnetic field. *J. Geodyn.* **32**, 29-41, 2002a.
- Olsen N., Holme R., and Luehr H., A magnetic field model derived from Ørsted, Champ, and Ørsted-2/SAC-C observations. (on-line talk) Virtual Session *New Magnetic Field Satellites*, *Am. Geophys. Union Spring Meeting*, 2002b (<http://www.dsri.dk/multimagsatellites>). Consulted January 31<sup>st</sup>, 2003.
- Olver F.W.J., and Smith J.M., Associated Legendre Functions on the cut. *J. Computat. Phys.* **51**, 502-518, 1983.
- Parkinson W.D., *Introduction to Geomagnetism*. Scottish Academic Press, Edinburgh, 1983.
- Press W.H., Flanning B.P., Teukolsky S.A., and Vetterling W.T., *Numerical Recipes. The Art of Scientific Computing*. Cambridge University Press, Cambridge, 1986.
- Purucker M., *Modeling of the Earth's magnetic field and its variations with Ørsted, Champ, and Ørsted-2/SAC-C: current status and future prospects*. Report of the Workshop after the 4<sup>th</sup> Ørsted International Science Team Meeting, Copenhagen, 2002.
- Purucker M., *Upcoming and proposed magnetic field satellites*. (on-line) Geodynamics Branch at Goddard Space Flight Center, 2003 ([http://geodynamics.gsfc.nasa.gov/research/mag\\_field/purucker/mag\\_missions.html](http://geodynamics.gsfc.nasa.gov/research/mag_field/purucker/mag_missions.html)). Consulted January 29<sup>th</sup>, 2003.
- Ravat D., and Purucker M., The future of satellite magnetic anomaly studies is bright! *The Leading Edge* **18**, 326-329, 1999.
- Ravat D., Langel R.A., Purucker M., Arkani-Hamed J., and Alsdorf D.E., Global vector and scalar Magsat magnetic anomaly maps. *J. Geophys. Res.* **100**, N. B10, 20111-20136, 1995.
- Rikitake T., *Electromagnetism and the Earth's Interior*. Elsevier, Amsterdam, 1966.
- Rishbeth H., History and Evolution of the World Data Center System. *J. Geomag. Geoelect.* **43**, 921-929, 1991.
- Rotanova N.M., and Odintsov S.D., Model of the Magsat Magnetic Anomaly Field over Europe using Spherical Cap Harmonic Analysis. *Phys. Chem. Earth (A)* **24**, N. 5, 455-459, 1999.

- Rotanova N.M., Odintsov S.D., Sas-Uhrynowski A., and Welker E., The Magnetic Anomaly Field over Poland and Adjacent Regions by using Magsat Satellite Data. *Acta Geophysica Polonica* **48**, N. 2, 223-240, 2000.
- Sabaka T.J., and Baldwin R.T., *Modeling the Sq magnetic field from POGO and Magsat satellite and contemporaneous hourly observatory data, phase I*. Contract Rep. HSTX/G&G-9302, Hughes STX Corp. For NASA/GSFC Contract NAS5-31760, pp. 100, Greenbelt, Maryland, 1993.
- Sabaka T.J., Olsen N., and Langel R.A., A comprehensive model of the quiet-time, near Earth magnetic field: phase 3. *Geophys. J. Int.* **151**, 32-68, 2002.
- Siebert M., and Meyer J., Geomagnetic activity indices. In *The Upper Atmosphere: Data analysis and interpretation*, ed. G.K. Hartmann and R. Leitinger, pp. 887-911. Springer-Verlag, Berlin, 1996.
- Stern D.P., and Bredekamp J.H., Error enhancement in geomagnetic models derived from scalar data. *J. Geophys. Res.* **80**, 1776-1782, 1975.
- Stevenson D.J., Planetary magnetic fields. *Rep. Prog. Phys.* **46**, 555-620, 1983.
- Thébault E., Schott J.J., and Mandeau M., Geomagnetic field modelling on small spherical caps. *EGS XXVII General Assembly*, EGS02-A-04673, SE6.07-1WE2A-003, Nice, France, 2002.
- Torta J.M., *Modelización regional del campo geomagnético sobre España: campo anómalo, variación secular y campo de referencia*. Memorias del Observatorio del Ebro 15, ISBN: 84-88253-00-1, 1992.
- Torta J.M., and De Santis A., On the Derivation of the Earth's Conductivity Structure by means of Spherical Cap Harmonic Analysis. *Geophys. J. Int.* **127**, 441-451, 1996.
- Torta J.M., García A., and De Santis A., New representation of geomagnetic secular variation over restricted regions by means of SCHA: application to the case of Spain. *Phys. Earth Planet. Inter.* **74**, 209-217, 1992.
- Torta J.M., García A., and De Santis A., A geomagnetic reference field for Spain at 1990. *J. Geomag. Geoelect.* **45**, 573-588, 1993.
- Torta J.M., Curto J.J., and Bencze P., Behavior of the Quiet Day Ionospheric Current System in the European Region. *J. Geophys. Res.* **102** (A2), 2483-2494, 1997.

- Torta J.M., Gaya-Piqué L.R., Solé J.G., Blanco I., and García A., A new geomagnetic observatory at Livingston Island (South Shetland Islands): implications for future regional magnetic surveys. *Annali di Geofisica* **42**, N. 2, 141-151, 1999.
- Torta J.M., Gaya-Piqué L.R., Riddick J.C., and Turbitt C.W., A partly manned geomagnetic observatory in Antarctica provides a reliable data set. *Contributions to Geophysics and Geodesy* **31**, N. 1, 225-230, 2001.
- Torta J.M., De Santis A., Chiappini M., and von Frese R.R.B., A model of the Secular Change of the Geomagnetic Field for Antarctica. *Tectonophysics* **347**, 179-187, 2002.
- Troshichev O.A., Dmitrieva N.P., and Kuznetsov B.M., Polar cap magnetic activity as a signature of substorm development. *Planet. Space Sci.* **27**, 217-221, 1979.
- Vennerstrøm, Friis-Christensen E., Troshichev O.A., and Andresen V.G., Comparison between the Polar Cap index, PC, and the Auroral Electrojet Indices AE, AL, and AU. *J. Geophys. Res.* **96**, N. A1, 101-113, 1991.
- Von Frese R.R.B., Kim H.R., Tan L., Kim J.W., Taylor P.T., Purucker M.E., Alsdorf D.E., and Raymond C.A., Satellite magnetic anomalies of the Antarctic crust. *Annali di Geofisica* **42**, N. 2, 309-326, 1999.
- Waddington R., Gubbins D., and Barber N., Geomagnetic field analysis-V. Determining steady core-surface flows directly from geomagnetic observations. *Geophy. J. Int.* **122**, 326-350, 1995.
- Walker J.K., Spherical cap harmonic modelling of high latitude magnetic activity and equivalent sources with sparse observations. *J. Atmos. Terrest. Phys.* **51**, N.2, 67-80, 1989.
- Wilkes R.J., Antarctic long-duration balloon flights: JACEE experience. *Adv. Space Res.* **21**, N. 7, 959-967, 1998.
- Wilkes R.J., Comments on Antarctic long-duration balloon flights. *Adv. Space Res.* **26**, N. 9, 1349-1352, 2000.

## Analytical index

### A

ADMAP Project; 17; 49  
 AE index; 74  
 Anomaly bias; 93  
 Associated Legendre functions; 10  
     computation; 41  
     orthogonality; 13  
 Auroral electrojet; 7  
 Autoregressive forecasting; 55

### B

Backus effect; 77  
 Balloon. *See* Stratospheric balloon data  
 Boomerang experiment; 61

### C

Champ satellite; 72  
 Comprehensive model (CM3); 34  
 Core field. *See* Main field  
 Crustal field; 5  
 Curie temperature; 5

### D

Definitive Geomagnetic Reference Field (DGRF); 20  
 Dst index; 73

### E

Equatorial electrojet; 7  
 Equivalent source; 144  
 External field; 5

### F

F-level; 28

### G

Geomagnetic field; 5  
     components; 10

    power spectrum; 12  
     wavelength; 28  
 Geomagnetic pole; 12; 130

### I

IAGA; 11; 49  
 International Geomagnetic Reference Field (IGRF); 11  
 International Geophysical Year (IGY); 49  
 Interplanetary magnetic field (IMF); 74  
 Ionosphere; 5

### J

Jerk; 132

### K

Kp index; 73

### L

Legendre polynomials; 13

### M

Magnetic anomaly; 15  
 Magnetic maps; 117  
 Magnetic pole; 130  
 Magnetosphere; 5  
 Magsat satellite; 28; 72  
 Main field; 5  
 Main field differences; 25  
 Maxwell equations; 9

### O

Observatory data; 48

### Ø

Ørsted satellite; 12; 72

### P

PC index; 74

POGO satellite; 71

## **R**

Remanent magnetisation; 16

## **S**

Satellite data; 68

Scalar potential; 9

SCHA. *See* Spherical Cap Harmonic Analysis

Secular variation; 8

Solar quiet variation (Sq); 7

Solar wind; 5

Spherical Cap Harmonic Analysis; 23

Spherical harmonics; 10

    expansion of potential; 10

    Gauss coefficients; 10

Storm, Magnetic; 6

Stratospheric balloon data; 59

Sunspot number. *See* Wolf number

## **T**

Temporal series expansion; 25

## **V**

Van Allen belts; 6

## **W**

Wolf number; 58

World Data Centers; 50